Preparation of electro-active self-assembled monolayers for the fabrication of advanced electronic devices

Maria Serena Maglione

Universitat Autònoma
de Barcelona

Preparation of electro-active self-assembled monolayers for the fabrication of advanced electronic devices

Maria Serena Maglione

Tesis Doctoral

Programa de Doctorado de Ciencia de Materiales

Directores

Dr. Marta Mas Torrent y Prof. Concepció Rovira Angulo

Tutor

Dr. Jordi Hernando Campos

Departamento de Química

Facultad de Ciencias

2018

La present memòria es presenta per aspirar al Grau de Doctor per:

Maria Serena Maglione

Vist i plau:

Dr. Marta Mas Torrent

Prof. Concepció Rovira Angulo

Dr. Jordi Hernando Campos

Bellaterra, 22 de Març de 2018

MARTA MAS TORRENT, Scientific Researcher, and **CONCEPCIÓ ROVIRA ANGULO**, Research Professor, of the Spanish Council of Research at the Materials Science Institute of Barcelona (ICMAB-CSIC)

CERTIFY

That **Maria Serena Maglione**, Master in Chemistry, has performed, under their management, the research work entitled **"Preparation of electro-active self-assembled monolayers for the fabrication of advanced electronic devices"**. This work has been performed under the mark of the Materials Science Ph.D. program of the Chemistry Department of the Autonomous University of Barcelona.

And in witness whereof this is signed by

Directors

Prof. Concepció Rovira Angulo   Dr.Marta Mas-Torrent

March 10, 2017

Abstract

The present Doctoral thesis is focused on the study of the switchable behavior on surface of specifically designed electroactive molecules by fabricating self-assembled monolayers (SAMs). Subsequently to the study on surface, the molecules were integrated into various devices in order to investigate the effects of the electroactive switch in more sophisticated systems. Four family of electroactive molecules were employed to reach these goals, namely antraquinones (AQ), ferrocenes (Fc), tetrathiafulvalenes (TTF) and polyclorotriphenylmethy (PTM) derivatives. The thesis is structured in such a way that each chapter is dedicated to a specific family of molecules, being the first part of the chapter focused on the description, the design and the synthesis of the molecule of interest. It follows the fabrication of the SAMs on indium tin oxide (ITO) or gold substrates, depending on the molecule functionality and, finally, the integration of the molecule in a specific device.

SAMs of PTM and TTF derivatives were fabricated on ITO and gold, respectively, and the investigation of their switching properties was carried out by cyclic voltammetry (CV) and using as read-out mechanism the optical, magnetic or capacitance response. In such a way, multi-state molecular switches with high potential in the field of memory devices were achieved. Furthermore, mixed SAMs of Fc and AQ derivatives were fabricated on patterned ITO//gold substrates, where the supramolecular interaction of the different redox species with β-cyclodextrin was used as a proof of the confinement of the surface properties.

The feasibility of the integration of electroactive molecules in devices was tested incorporating SAMs of AQ derivatives on specifically designed ITO electrodes in microfluidic chips. The redox activity of the AQ moiety was used as the driving force for the water actuation, realizing a micro electro-meccanical system operating at low voltage and, hence, with high potential in biological fields.

Finally, Fc, TTF and PTM derivatives were integrated in field effect transistors, by functionalizing the active channel, the gate contact or the dielectric, respectively. The presence of the electroactive molecules at the FET interfaces was proved to have a remarkable effect on the devices response, opening new perspectives for the future molecule-based technologies.

Nomenclature

AQ	Anthraquinone
Fc	Ferrocene
TTF	Tetrathiafulvalene
PTM	Polychlorotriphenylmethyl
SAM	Self-assembled monolayer
CV	Cyclic voltammetry
CE	Counter electrode
WE	Working electrode
RE	Reference electrode
$TBAPF_6$	Tetrabutylammonium hexafluorophosphate
EIS	Electrochemical impedance spectroscopy
FET	Field effect transistor
OFET	Organic field-effect transistors
EGOFET	Electrolyte-gated organic field-effect transistors
ITO	Indium tin oxide
THF	Tetrahydrofuran
ACN	Acetonitrile
DCM	Dichloromethane
CD	Cyclodextrin
CA	Contact angle
XPS	X-ray photoelectron spectroscopy
EPR	Electron paramagnetic resonance

MEMS	Micro electro-mechanical system
PL	Photoluminescence
IL	Ionic liquid
SPR	Surface Plasmon Resonance
BAMS	Bar-assisted meniscus shearing
EGaIn	Eutectic gallium-indium
HOMO	Highest occupied molecular orbital
LUMO	Lowest unoccupied molecular orbital
FT-IR	Fourier transform infrared spectroscopy
HMDS	Hexamethyldisilazane
XRD	X-ray diffraction
AFM	Atomic Force Microscope
HPLC	High performance liquid chromatography
APTES	(3-Aminopropyl)triethoxysilane
TMEDA	Tetramethylethylenediamine
DMAP	4-Dimethylaminopyridine
ToF-SIMS	Time-of-flight secondary ion mass spectrometry
LDI	Laser desorption/ionization
NMR	Nuclear magnetic resonance

Contents

1 Introduction and objectives 1

1.1 Molecular switches in nanotechnology . . . 1

1.2 Electrochemical switches . . . 3

1.3 Self-assembled Monolayer . . . 4

1.4 Electroactive Self-assembled Monolayers . . . 7

1.5 Electrochemical tools for SAMs characterization . . . 8

1.5.1 Cyclic Voltammetry . . . 8

1.5.2 Electrochemical Impedance Spectroscopy . . . 11

1.6 Field Effect Transistors . . . 14

1.7 General objectives . . . 17

2 Molecular switches based on anthraquinone and ferrocene derivatives 19

2.1 Objectives . . . 20

2.2 Introduction to the molecules . . . 21

2.2.1 Anthraquinone and its derivatives . . . 21

2.2.2 Ferrocene and its derivatives . . . 22

2.3 Design and synthesis of Anthraquinone derivatives AQSi and AQS_2 . . . 24

2.4 Preparation of switchable surfaces based on SAMs of AQ and Fc derivatives 26

2.4.1 Preparation and characterization of mono-component SAMs S_{AQSi}, S_{AQS_2} and $S_{FcC_{11}\ dil}$ . . . 26

2.4.2 Fabrication of the patterned ITO//gold substrate and formation of the bi-component SAM $S_{AQSi//FcC_{11}dil}$ . . . 32

2.4.3 Interaction between mono-component SAMs and β-CD . . . 34

2.4.4 Interaction between the bi-component SAM $S_{AQSi//FcC_{11}dil}$ and β-CD 40

2.4.5 Summary . . . 42

2.5 S_{AQSi} in microfluidics devices . . . 42

2.5.1 Introduction to digital microfluidics . . . 42

2.5.2 Static electrowetting studies on S_{AQSi} . . . 44

2.5.3 Water actuation on planar electrodes . . . 46

2.5.4 Integration of S_{AQSi} in microfluidic chips . . . 51

2.5.5 Preliminary studies with cells . . . 56

2.5.6 Summary . . . 58

2.6 Integration of a Fc SAM in field effect transistors based on MoS_2 monolayer 59
  2.6.1 2D MoS_2 Semiconductor 59
  2.6.2 Design, fabrication and functionalization of MoS_2 monolayers based FETs 62
  2.6.3 Liquid ionic gated FETs 65
  2.6.4 Summary 68

3 Molecular switches based on tetrathiafulvalene derivatives 71
3.1 Objectives 72
3.2 Introduction to tetrathiafulvalene 72
3.3 Design and synthesis of the TTF derivatives $TTFS_2$ and $BTTFS_2$ 74
3.4 Surface multi-state switch based on S_{TTFS_2} 77
  3.4.1 Multi-states switches 77
  3.4.2 Preparation and characterization of SAM S_{TTFS_2} 79
  3.4.3 Electrochemical Impedance Spectroscopy characterization of S_{TTFS_2} 82
  3.4.4 Summary 89
3.5 Integration of $TTFS_2$ in EGOFET devices by functionalizing the gate electrode 90
  3.5.1 Gate modification in electrolyte-gated field effect transistors 90
  3.5.2 Design and fabrication of the EGOFETs endowed with microfluidics 91
  3.5.3 Influence of the S_{TTFS_2} switch in the EGOFET: device characteristics 94
  3.5.4 Summary 102
3.6 $BTTFS_2$ as molecular rectifier 103
  3.6.1 Molecular wires and rectifiers 103
  3.6.2 Molecular rectifiers 104
  3.6.3 Preparation and characterization of S_{BTTS_2} 108
  3.6.4 Charge transport through S_{BTTS_2} 111
  3.6.5 Summary 114

4 Polychlorotriphenylmethyl derivatives 117
4.1 Objectives 118
4.2 Introduction to polychlorotriphenylmethyl radicals 119
4.3 Design and synthesis of the PTM derivatives αH-PTMsil, r-PTMsil and r-PTMpol 121
4.4 Switches on ITO surfaces based on $S_{\text{r-PTMsil}}$ 130
  4.4.1 Switchability study of $S_{\text{r-PTMsil}}$ 132
  4.4.2 Summary 134

4.5 Integration of r-PTMsil and αH-PTMsil in OFETs by functionalizing the dielectric . . . 135
  4.5.1 Functionalization of the dielectric in organic field-effect transistors . 135
  4.5.2 Design and fabrication of the OFETs devices . . . 137
  4.5.3 SAMs influence on the electric characteristics of the OFET devices . . 143
  4.5.4 Summary . . . 151
4.6 r-PTMpol as charge storage system . . . 151
  4.6.1 Electrochemical characterization of r-PTMpol . . . 152
  4.6.2 Summary . . . 156

5 Experimental methodologies **157**
5.1 Synthesis of the molecules used . . . 157
5.2 Reagents, solvents and substrates . . . 180
5.3 Procedures and apparatus . . . 181
  5.3.1 Fabrication of patterned ITO//gold substrates . . . 181
  5.3.2 Fabrication of planar electrodes on ITO substrates . . . 181
  5.3.3 Fabrication of ultra flat electrodes for EGaIn measurements . . . 181
  5.3.4 Preparation of self-assembled monolayers (SAMs) . . . 182
  5.3.5 Procedure for FET Fabrication . . . 183
  5.3.6 Spectroscopy and spectrometry techniques . . . 184
  5.3.7 Electrochemical techniques and FETs characterization . . . 186
  5.3.8 Other techniques . . . 187

6 General conclusions **189**

Bibliography **191**

1

Introduction and objectives

1.1 Molecular switches in nanotechnology

The evolution of civilization has always been strictly related to the development of the technology. Nowadays, “making things smaller” is one of the imperative technological requirement since the Nobel Laureate Richard Feynman in 1959 coined the term “miniaturization” as “a field, in which little has been done, but in which an enormous amount can be done in principle [...] because there is plenty of room at the bottom” [1]. The Feynman’s speech was a great incentive which led scientists to investigate the possibility of designing and constructing machines, motors and devices at the nanometer scale, in which the molecular level is included. Thus, in the last 60 years, many fields of technology, such as information processing, have benefited from progressive miniaturization of the device’s components, and a common shared prediction is that further progress in miniaturization will not only decrease the size and increase the power of computers, but could also open the way towards new technologies in the fields of medicine, environment, energy and materials [2].

The top-down approach used so far for the construction of miniaturized devices (Figure 1.1) is reaching fundamental and practical limits, which include severe cost limitations, for sizes below 50 nm [3]. Nevertheless the research on supramolecular chemistry has shown that miniaturization can be pushed further using molecules as convenient nanometer scale building blocks in a bottom-up approach, to construct ultra-miniaturized devices and machines [4, 5]. As an evidence of the importance of this topical research field, Jean-Pierre Sauvage, Sir J. Fraser Stoddart and Bernard L. Feringa won in 2016 the Nobel Prize in Chemistry "for the design and synthesis of molecular machines".

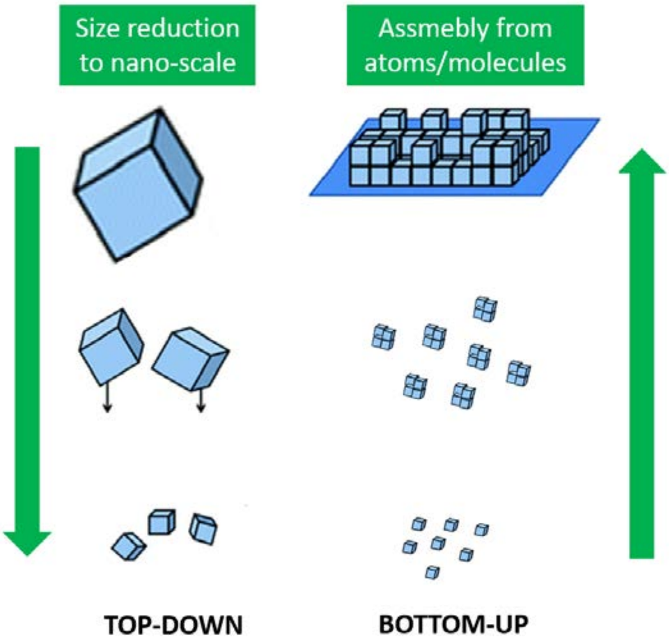

Figure 1.1: Schematic representation of the top-down and bottom-up approaches.

Therefore, nowadays one of the main targets in nanotechnology is to have full control at molecular level, aiming at predicting how the behavior of the key unit, that is the molecule, will affect the device properties. Controlling molecular properties means also being able to switch them as convenient. In past decades, scientists have been paying much attention to the design and fabrication of multifarious functional molecular switches which operate at the molecular level. A molecular switch is a molecule able to reversibly switch its physical and/or chemical properties between two or more states, by the application of an external stimulus (i.e., light, electrochemical or chemical reagents, etc).

Molecular switches are the key unit in various devices and smart materials, being responsible for the specific switch of the devices properties. So far, light-responsive molecules such as dithienylethene derivatives (Figure 1.2) [6, 7], spiropyran derivatives [8] and azobenzene derivatives [9] (Figure 1.2 a)), have played an important role in molecular sensing [10], controllable molecular self-assembly [11], photo-controlled biological systems [12, 13] and marrying molecular switches into solid-state electrical circuits [14]. Also mechanically interlocked molecules [15] have emerged as an important kind of molecular switches for the fabrication of molecular shuttles and motors [16] (Figure 1.2 b)).

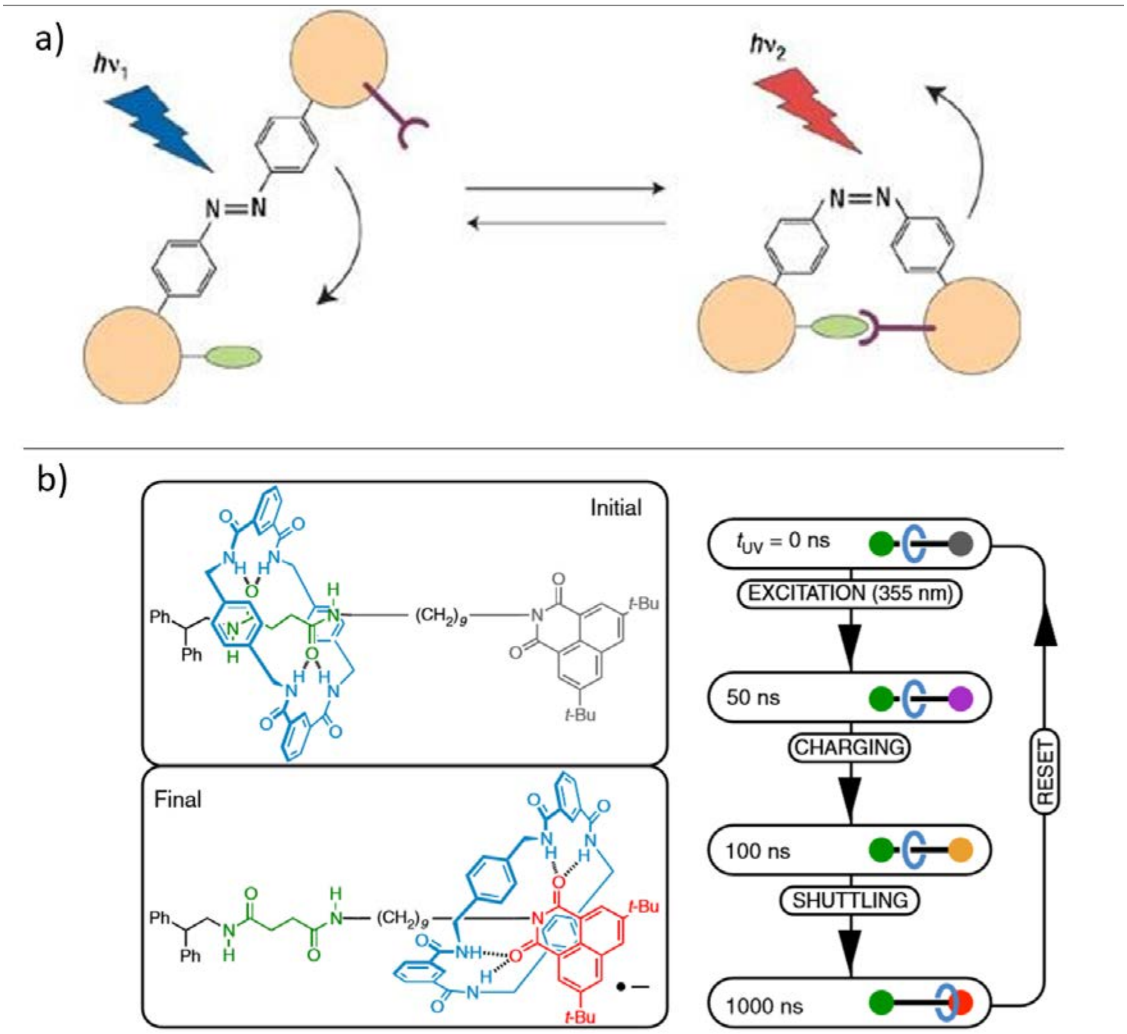

Figure 1.2: Example of a) azobenzene light induced conformational switch [17] and b) light-induced operation of rotaxane-based molecular shuttle [18].

1.2 Electrochemical switches

Molecules able to switch their physical/chemical properties between two o more different redox states by the application of an electric stimulus are called electrochemical switches. The possibility to modulate the molecular properties electrically is of great interest in the field of molecular electronics. The read-out mechanism for the electrochemical induced switch can be a signal of multiple nature such as an electrical, an optical, a magnetic and a capacitance response as well as a conformational change, depending on the molecule under study (Figure 1.3).

Electrochemical induced switches have been intensively investigated such as the supramolecular dyads combining commonly a rotaxane interlocked with a linear molecule both with electroactive units that undergo translational movements upon electric input [19, 20, 21]. Other interesting systems that have aroused much interest in this field are based on electrochromic molecules [22, 23, 24]. Recently also electroactive polymers characterized by the possibility of being oxidized and reduced in a reversible way [25] and others that show reversible mechanical deformation in response to an electric field have been subject of studies [26].

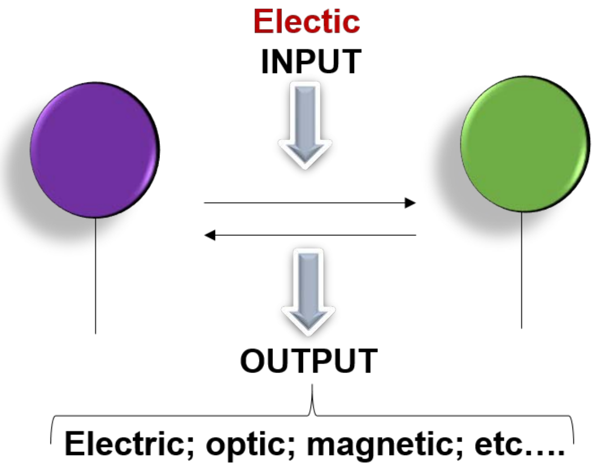

Figure 1.3: Schematic representation of an electroactive switch.

The immobilization of electroative molecules on solid supports is fundamental for their implementation in practical devices. The persistence of their properties and switching behavior on substrate is key for with the realization of electrochemical stimuli responsive devices [27]. One of the most versatile tools to address molecules on surfaces is by the preparation of self-assembled monolayers.

In this thesis four families of electroactive molecules were used as electroactive switches, namely anthraquinones, ferrocenes, tetrathiafulvalenes and polychlorotriphenylmethyl radicals. These molecules are able to be reversibly reduced or oxidized under the application of a low bias voltage and are very appealing since they can be optimally designed and synthesized having functional groups that allow the desired surface funtionalization.

1.3 Self-assembled Monolayer

Self assembly is a thermodynamically favorable process where the molecules spontaneously interact forming well organized structures. Molecular structures specifically designed can self-assemble on substrates forming Self-assembled

Monolayers (SAMs). In these molecules (or ligands) three main parts can be identified: the terminal, the spacer and the anchoring groups (Figure 1.4).

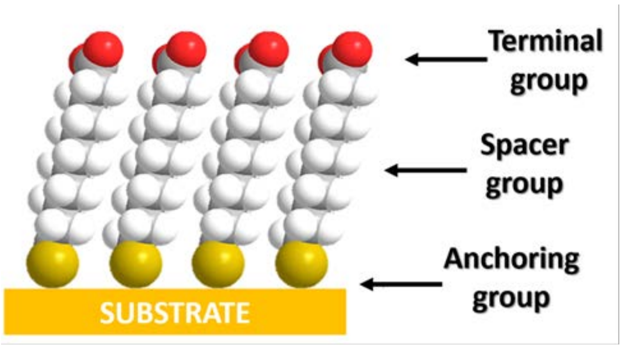

Figure 1.4: Schematic representation of a SAM.

1) Terminal group: it is also known as "head group" and largely defines the new air/substrate interface as well as the new functionality of the modified surface (for instance the electronic functionality).

2) Spacer group: it is the molecule backbone that bridges the terminal and the anchoring group defining the distance between the surface and the functional center. It has an important role during the self-assembly process. The inter-molecular forces between neighbor spacer groups can contribute to stabilize the SAM structure, favoring the assembly process and an efficient molecular packing. The bridge also controls the electron transfer rate (K_{ET}) between the head group and the substrate, for instance long length bridges are typically used to slow down the electron transfer rate.

3) Anchoring group: finally, the anchoring group is responsible for the interaction of the molecule and the surface. It needs to be considered in terms of its mechanical stability and also regarding its electrical and optical properties (i.e. transparency). There is a large number of anchoring groups that bind to specific substrates (as illustrated in Table 1.1), even if the most studied class of SAMs is derived from the absorption of alkanethiols on gold or silanes on oxide substrates [28, 29].

The choice of the terminal group is of great importance to ensure an efficient and reproducible adsorbate-substrate interaction, and is one of the key factor for the integration of molecules in advanced devices [30].

Table 1.1: The most used surfaces and anchoring groups for SAMs fabrication.

Substrate	Ligand or precursor	Interaction
Au	RSH; RSSR; RSR; RSeH; RSeSeR;	RS-Au; RSe-Au;
	RSO_2H; R_3P; R-CCH	RSO_2-Au; R_3P-Au, R-C=C-Au
Ag	RSH; RSSR; RSeH; RSeSeR	RS-Ag; RSe-Ag
Pd	RSH; RSSR	RS-Pd
Pt	RSH; RSSR; RCN	RS-Pt; RCN-Pt
Cu	RSH	RS-Cu
Fe	RSH	RS-Fe
Hg	RSH	RSH-Mg
Ni	RSH	RS-Ni
Co	RSH	RS-Co
GaAs	RSH	RS-GaAs
InP	RSH	RS-InP
SiO_2, glass	$RSiCl_3$; $RSi(OR)_3$	Siloxane
ITO	$RSiCl_3$; $RSi(OR)_3$; $RSiH_3$; $RSiCH_3$	RSi-ITO;
	RPO_3H	$RPO_3^{2-} \cdots M^{n+}$
Metal oxides	RCOOH; RCONHOH	$RCOO^{-} \cdots MO_n$; $RCONHOH \cdots MO_n$
Si/Si-H	$(RCOO)_2$; RCH=CH2; R-CCH	R-Si; RCH_2CH_2-Si; R-C=CH-Si
Si/Si-Cl	RLi; RMgX	R-Si
Mica	RPO_3H_2; $RPO(OH)_2$	$RPO_3^{2-} \cdots$ Mica

SAMs can be prepared from solution or vapor phase. The liquid approach is the most extensively used and, in this case, different parameters can affect the final structure of the monolayer, such as:

- Solvent. The solvent-substrate interaction and the molecular solvation affect both the thermodynamics and the kinetics of the self-assembly process.

- Temperature. The temperature is an important parameter that influences the kinetics of the SAM formation as well as the number of the defects in the SAM. The first minutes of the SAM formation seems to be the most sensible to the temperature effect [31].

- Molecular concentration and immersion time. The optimization of these two parameters will give rise to modified surfaces with high molecular coverage. Generally, for low concentrations long immersion times are required [32].

- Purity of the absorbate. Compounds with high purity (≥ 95%) are required for good SAM formation [33, 34].

- Substrate activation. One of the most important steps in the SAM preparation is the substrate pre-treatment, which includes the cleaning and the activation step. These parameters needs to be optimized depending on the substrate and on the molecule used. The typical procedures used for cleaning are washing with ultra pure solvents and with ultra strong acidic or basic solutions (i.e, piranha bath, hydrofluoric acid). The substrate exposure to oxygen or ozone plasma is also commonly used.

Once fabricated, a SAM is generally characterized by the combination of different techniques in order to get information about its chemical, physical and structural properties. In Table 1.2 the most used tools for SAMs characterization are reported.

Table 1.2: Most common techniques employed in SAMs characterization.

Technique	**SAM property**
Contact angle (CA)	Wettability
Atomic force microscopy (AFM) Scanning tunneling microscopy (STM)	Topographical properties
Infrared absorption spectroscopy (IRRAS) and Raman spectroscopy	Molecular composition, structure and interaction
Auger electron spectroscopy (AES), X-Ray photoelectron spectroscopy (XPS) and Synchroton X-ray absorption spectroscopy (XAS)	Elementary composition
Grazing incidence X-ray diffraction (GIXRD) X-ray reflectivity (XRR)	Molecular arrangement and packing
Time of flight secondary ion mass (ToF-SIMS) and Matrix assisted laser desorption time of flight spectrometry(MALDI-ToF)	Chemical composition

1.4 Electroactive Self-assembled Monolayers

As already mentioned, SAMs of electroactive molecules on conductive substrates provide an excellent and versatile model systems for the formation of electronic devices by self-assembly. Electroactive SAMs have been widely used in molecular electronics [35, 36, 37] and for the design of devices for applications such as (bio)sensors [38]. In particular SAMs of electroactive thiolated molecules have been investigated as model system for interfacial electron transfer events [29, 39, 40], as well as for the fabrication of memory devices, wherein the properties of the immobilized molecules are switched ON and OFF in response to the applied potential [41, 42].

A variety of redox species have been attached to SAMs, and include transition metal complexes (e.g., ferrocene, ruthenium pentaammine, osmium bisbipyridine, metal clusters) and other organic molecules. For instance, Di Bella and van der Boom reported SAMs based on redox metallic complexes whose switch was coupled with optical absorbance changes [43, 44]. Lindsey et al. realized a porphyrin-based charge-storage memory thanks to the specific characteristics of the porphyrins redox properties, which provide the basis for writing/reading the memory cell. Importantly, since porphyrins exhibit multiple cationic states that are accessible at relatively low potentials, these molecules afford multibit information storage with low power consumption [45]. Multiple examples of confined redox molecules were also provided by our group with the modification of ITO, gold, Pt and Ag substrates. Among all, it was demonstrated the possibility to confine on gold metallofullerene derivatives retaining their electrochemical/magnetic properties, by functionalizing the compound with a dithiolane group [46]. The electrochemical switching of SAMs of tetrathiafulvalenes [47], perchlorotriphenylmethyl radicals [48] and double decker complexes [49] have olso been subject of study. Furthermore, the use of a solid electrolyte (ion gel) to control electrochemically the redox molecular system was proposed as a tool for the integration of these systems in solid-state devices [50].

1.5 Electrochemical tools for SAMs characterization

A large variety of electrochemical techniques are suitable for characterizing and studying SAMs. Cyclic voltammetry, AC voltammetry, electrochemical impedance spectroscopy, and chronoamperometry are most commonly used.

In the work exposed in this thesis, we mainly employed cyclic voltammetry and impedance spectroscopy.

1.5.1 Cyclic Voltammetry

Cyclic voltammetry (CV) is a dynamic electrochemical method for measuring redox events. It can be used to study the electrochemical behavior of species diffusing to an electrode surface, interfacial phenomena at an electrode surface, and bulk properties of materials in or on electrodes [51]. The most used configuration for CV measurements is the three electrodes configuration. CV consists of cycling the potential of an electrode (the working electrode, WE) with respect to a reference electrode (RE), which is immersed in an unstirred solution (the electrolyte), and measuring the resulting current flowing towards the counter electrode (CE). The reference electrode must have a stable and well-known electrode potential, such as a silver/silver chloride electrode (Ag/AgCl). Furthermore, a supporting electrolyte is present to repress migration of charged reactants and products [52]. The controlling potential which is applied across WE and RE can be considered an excitation signal and it is applied as a linear potential scan with a triangular waveform. This triangular potential excitation signal sweeps the potential of the electrode between two values (the switching potentials) [53], generally, starting from a potential where no Faraday processes occur (initial potential) and moving to potential where reduction (E_{pc}) or oxidation (E_{pa}) of the studied solute occurs. After that, the direction of the linear sweep is reversed.

In a CV of a solution of a redox species, a peak is observed characterized by the peak height (I_p) and the potential at which the peak occurs (E_p). The formal redox potential ($E_{\frac{1}{2}}$) can be found as the mid-way between the two redox peaks comprising the voltammetry:

$$E_{\frac{1}{2}} = (E_{Pa} + E_{Pc})/2 \tag{1.1}$$

where E_{Pa} and E_{Pc} are the potential at which the anodic and cathodic peaks occur, respectively.

In Figure 1.5, the geometry of an electrochemical cell for cyclic voltammetry as well as an example of the CV response of an electroactive species are reported.

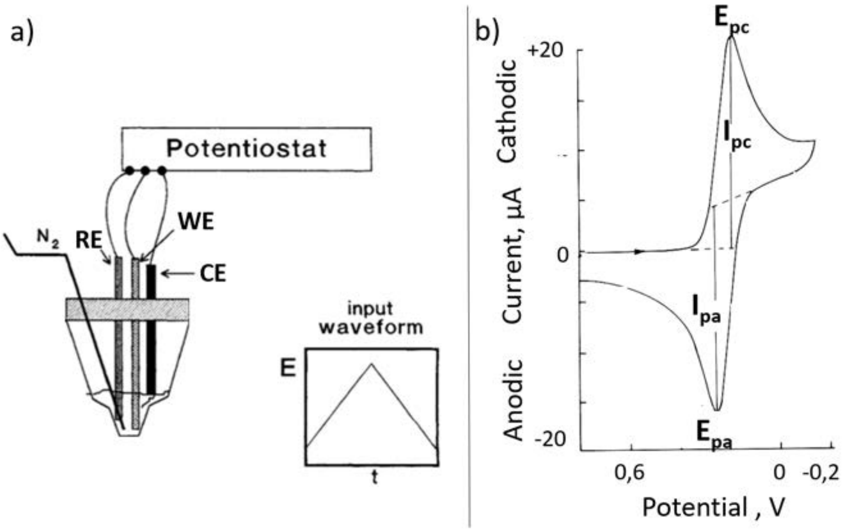

Figure 1.5: a) Scheme of a typical electrochemical cell for cyclic voltammetry. b) Example of the CV response of an electroactive species.

In the case of electroactive SAMs the species of interest are absorbed onto the WE. Figure 1.6 shows the typical shape of an ideal Nernstian electron transfer which consists in two symmetrical peaks where the charges (Q) for the oxidation and reduction (area under the peaks) are equal since all the absorbed species undergo reduction/oxidation. The current is symmetrical for both peaks and decays to zero because there is a fixed amount of reactant (diffusion does not play a role). The charge remains constant. The peak separation, ΔE_p, is calculated by $E_{pa} - E_{pc}$. In ideal Nernstian absorption, at slow scan rates the peak separation is 0, as scan rate increases peak separation increases in quasi-reversible process.

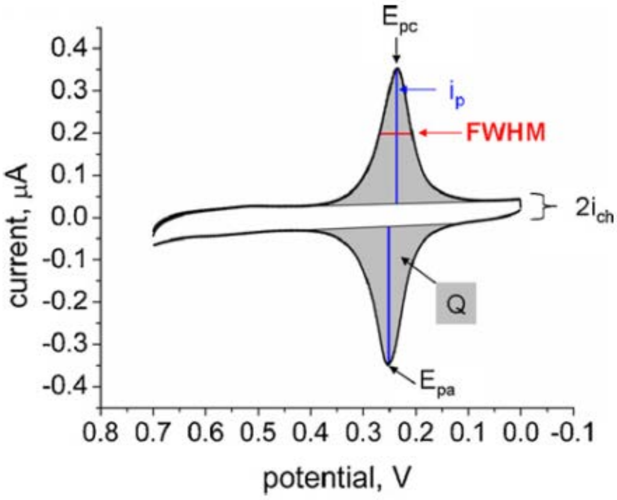

Figure 1.6: Relevant parameters of a CV of a surface-bound redox species. Parameters include: Epc, Epa, ich, ip, Q, and FWHM [39].

The background current (charging or capacitive current, I_{ch}) can be correlated to the thickness of the SAM while the faradaic current (I_p) is directly proportional to the scan rate,v, and the surface coverage, Γ, as showed in equation 4.1.

$$I_P = \frac{n^2 F^2}{4RT} v A \Gamma \tag{1.2}$$

Where n is the number of electrons transferred in the reaction, A is the area of the WE, R is the universal gas constant, T is the temperature (in Kelvin) and F the Faraday constant. Hence, Q, which is related to Γ, can be calculated from the integration of the peak area following the equation 1.3:

$$Q = nFAv\Gamma \tag{1.3}$$

The value of Γ is often compared to a theoretical maximum based on the molecular surface area of the adsorbate.

Moreover, the full width at half of the peak maximum (ΔE_{FWHM}) is given by:

$$\Delta E_{FWHM} = 3,53RT/nF \tag{1.4}$$

The shape of the peaks is indicative of the nature of the interaction between the surface confined species, generally broad peaks are associated with slow electron transfer kinetics and a non-ideal behavior of the adsorbed specie. While, the position of the peaks along the potential axis is indicative of the reversibility of the electron transfer process. As larger the ΔE_p, the more irreversible is the electron transfer.

1.5.2 Electrochemical Impedance Spectroscopy

Electrochemical impedance spectroscopy (EIS) is a measure of the ability of a circuit to resist the flow of electrical current and it is usually applied to investigate the interface between an electrode and a solution.

It overcomes the limits of the Ohm's low that, defining the resistance (*R*) in terms of the ratio between voltage (*E*) and current (*I*) (1.5), can be applied only in the case of the ideal resistor.

$$R = \frac{E}{I} \tag{1.5}$$

EIS is usually measured by applying a sinusoidal AC potential to an electrochemical cell and then measuring the current passing through the cell as function of time (see equation 1.6, where Et = E at time t; E_0 = amplitude of the signal; ω = radial frequency; f = frequency). Importantly, electrochemical impedance is normally measured using a small excitation signal. This is done so that the cell's response is pseudo-linear. In a linear (or pseudo-linear) system, the current response to a sinusoidal potential will be a sinusoid at the same frequency but shifted in phase (Φ) (1.7) . So, using an expression analogous to Ohm's Law it is possible to calculate the impedance of the system as in 1.8 in terms of a magnitude (Z_0) and a phase shift (Φ).

$$E_t = E_0 sin(\omega t) \;\; \omega = 2\pi f \tag{1.6}$$

$$I_t = I_0 sin(\omega t + \phi) \tag{1.7}$$

$$Z = \frac{E_t}{I_t} = \frac{E_0 sin(\omega t)}{I_0 sin(\omega t + \phi)} = Z_0 \frac{sin(\omega t)}{sin(\omega t + \phi)} \tag{1.8}$$

The impedance can be also represented as a complex function, $Z(\omega)$ composed of a real (Z_{re}) and an imaginary(Z_{im}) part, as expressed in 1.9.

$$Z(\omega) = \frac{E}{I} = Z_0 exp(j\phi) = Z_0(cos\phi + jsin\phi) \tag{1.9}$$

Plotting on the X-axis of a chart Z_{re} and on the Y-axis Z_{im}, a "Nyquist Plot" is obtained (see Figure 1.7 b)) [54]. Each point on the Nyquist Plot is the impedance at one frequency. The semicircle is characteristic of a single "time constant" process. Several semicircles can be expressed in a graph, although often only a portion of a semicircle is seen. Nyquist Plots have one major shortcoming: looking at any data point on the plot it is not possible to tell what frequency was used to record that point.

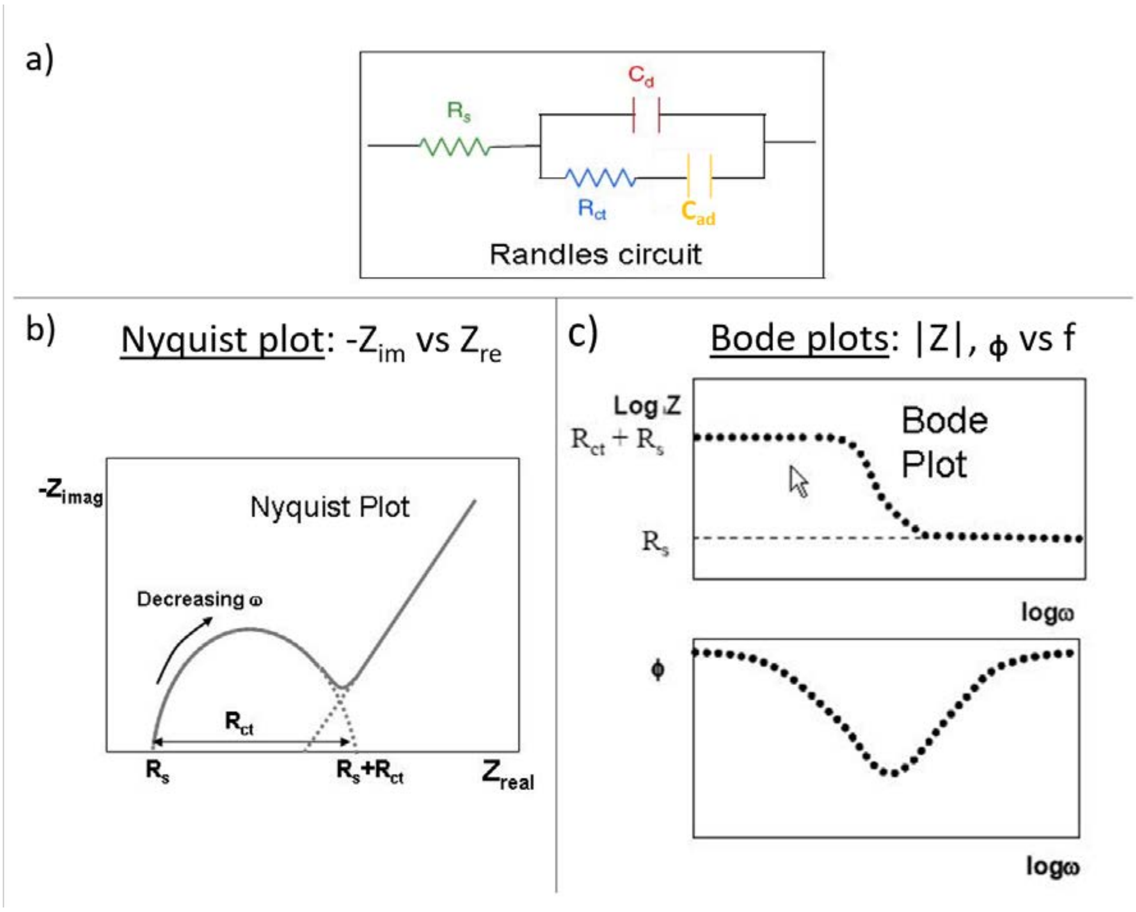

Figure 1.7: a) Randles circuit, b) Nyquist plot c) Bode plots.

Another common presentation mode of impedance is the Bode Plot, where the log frequency is plotted on the X-axis and both the absolute values of the impedance and the phase-shift on the Y-axis [54, 55] . Unlike the Nyquist Plot, the Bode Plot does show frequency information (see Figure 1.7).

The data can be rationalized as elements of an electric circuit that simulates the electrical behavior of the electrochemical system [56]. It is necessary to consider how the ionic charges are involved in the passage of the current. The Randles circuit (Figure 1.7 a)) is one of the simplest models for describing the electron transfer phenomena in redox species close to conductive substrates in an electrolyte with a resistance R_s, known as the ohmic solution resistance. At the electrode/solution interface some ions are used to adjust the ionic environment to balance the charge between the electrode surface ad the solution. This is equivalent to the charge/discharge of a capacitor with capacitance C_{dl}. Simultaneously, redox attached species undergo an electron transfer with the electrode, this yield a faradaic current whose magnitude reflects the rate of the electron tranfer process. This is equivalent to a resistor (charge transfer resistance R_{ct}) in series with a capacitor (charge/discharge of the electrochemical monolayer C_{ad}). The solution resistance is determined by the solution conductivity and the geometry of the cell. the double layer capacitance reflects the electrostatic interplay between the electrode and the electrolyte and depends on the nature and the area of the electrode and on the electrolyte ionic strength and permittivity. Rct represents the charge transfer kinetics and can be thought as the ratio of overpotential to current in absence of mass transfer limitation.

In SAMs EIS, to avoid the need to fit the acquired data to a specific circuit [39], it is possible to convert the complex impedance function $Z(\omega)$ into a complex capacitance function $C(\omega)$. This methodology consists in acquiring the information from measurements at specific electrode potentials and allows a better understanding of the different contributions in the current response as well as the establishment of a more robust means of segregating faradaic contribution of the response from the capacitive background [57].

1.6 Field Effect Transistors

The integration of SAMs in field effect transistors (FETs) is of great interest to control the chemico-physical properties of these electronic devices. In this thesis work we also investigated the possibility to integrate electroactive SAMs in FETs by functionalizing different device components.

The theory of the field effect transistors (FET) come from the ideas proposed by Lilienfield in 1926 and Heil in 1935, which patented the firsts three-electrode amplifying device based on semiconductors.

The FET consists of a semiconductor channel, which is the active part of the device where charge carriers flow, with metallic conducting electrodes at either end, referred to as the drain (D) and the source (S). A third electrode called the gate (G) is placed in very close proximity to the channel. In one of the widely used typology of FET, the semiconductor and the gate are separated each other by a thin insulating layer known as dielectric (generally silicon oxide). The working principle of a FET is the following: a voltage applied to the gate modifies the charge carrier density in the semiconductor in between source and drain, which therefore modulates the source-drain current. In this way, the gate of the FET controls the flow of carriers flowing from the source to drain. As it is only the electric field that controls the current flowing in the channel, the device is said to be voltage operated. There are two kinds of charge carriers: electrons (e) and hole (h) for n or p type semiconductors, respectively. This gives rise to two categories of FET known as n-Channel and p-Channel FETs.

Numerous FET geometries are described, among which the gate can be on top of the semiconductor (top-gate) or at the bottom of the semiconductor (bottom-gate). Similarly, the source and drain can be deposited on the top (top-contact) of the semiconductor or before it (bottom-contact).

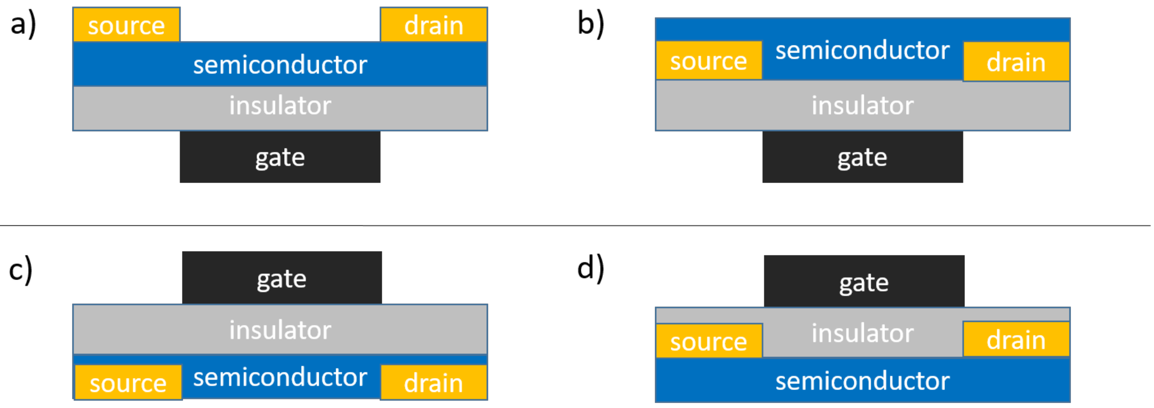

Figure 1.8: Bottom-gate a) top-contact b) bottom-contact and top-gate c) bottom-contact, d) top-contact FET geometries.

FETs can also be classified depending on the nature of the active material. In this thesis MoS_2 based FETs, where the active channel is a monolayer of the inorganic molybdenum disulfide, as well as Organic FETs (OFETs), where the semiconductor is an organic film (i.e. pentacene, fullerene, etc.) have been studied. Further, electrolyte-gated organic field-effect transistors (EGOFETs) which are OFETs where the organic semiconducting layer is in contact with an electrolyte instead of a classical dielectric, were also employed (Figure 1.9).

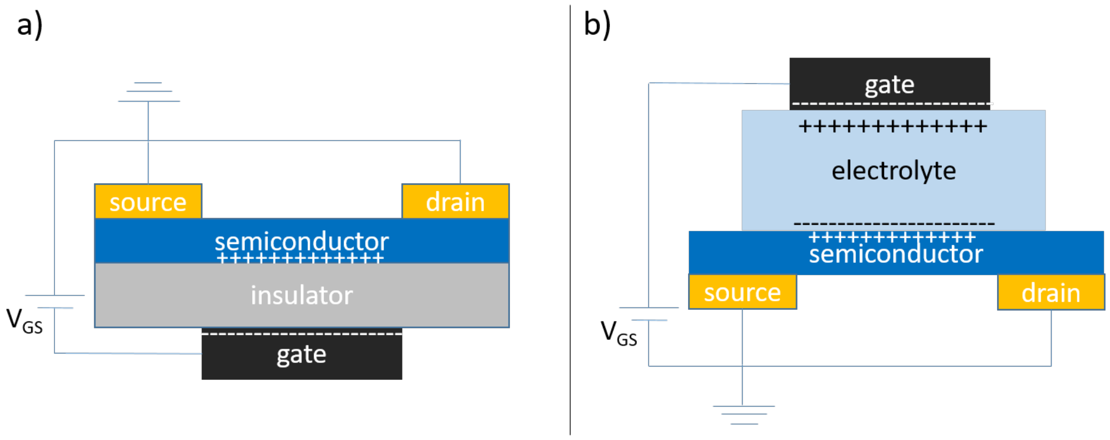

Figure 1.9: Schematic representation of a) an OFET and b) an EGOFET

To examine the transistor functions there are two principal ways: by means off applying a constant voltage V_{GS} and sweeping the drain-source voltage V_{DS} and measuring the drain current I_{DS} (output characteristics), and measuring the drain current while sweeping the gate voltage and keeping the drain voltage V_{DS} constant (transfer characteristics) (Figure 1.10).

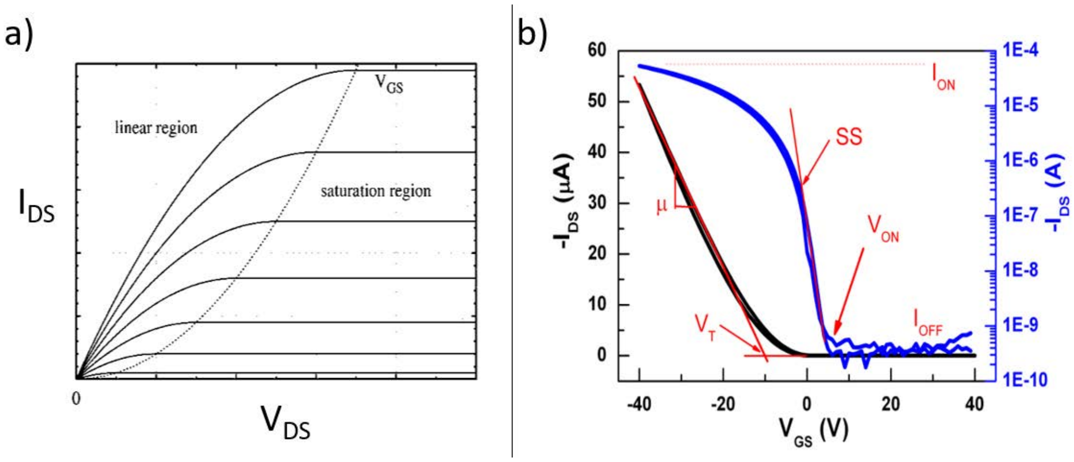

Figure 1.10: a) Example of output curves for different gate voltages. b) Example of transfer curves (blue line: log-lin, black line: lin-lin).

As it is possible seen from Figure 1.10 a), there are basically three regions in which FETs can operate:

1) Cut-off region: In this region the FET is in a non-conducting state (i.e. it is turned OFF). The channel current $I_{DS} = 0$. The gate voltage V_{GS} is less than the threshold voltage (V_{th}) required for conduction, being the V_{th} the minimum gate-to-source voltage V_{GS} that is needed to create a conducting path between the source and drain terminals. V_{th} is extracted as the intersection of the extrapolated linear part of the transfer characteristics and the V_{GS} axis.

2) Linear region. When $V_{GS} > V_{th}$ and $V_{DS} < (V_{GS} - V_{th})$ the transistor is turned ON, and a channel has been created which allows current between the drain and the source. The FET operates like a resistor, controlled by the gate voltage relative to both the source and drain voltages. In this linear region the current flowing through the channel is directly proportional to the V_{DS}. The equation describing the current-voltage characteristics in the linear region, $V_{GS} \gg V_{DS}$, can be simplified to:

$$I_{DS} = \frac{W}{L}\mu_{lin}C_i(V_G - V_{th})V_{DS} \tag{1.10}$$

where W and L are the width and length of the channel, respectively, and μ is the charge carrier mobility. μ (in units of cm^2 /V·s) is the average velocity of the charge carriers along the channel normalized to the longitudinal field and, in the linear regime, μ can be extracted from the slope of the transfer curve.

3) Saturation region. When $V_{GS} > V_{th}$ and $V_{DS} \geq (V_{GS} - V_{th})$ the FET is turned hard on. The channel is pinched off and the current cannot increase substantially anymore and saturates (I_{DSsat}). Then, the drain current is given by:

$$I_{DS} = \frac{W}{2L}\mu_{sat}C_i(V_G - V_{th})^2 \tag{1.11}$$

In the saturation regime, μ is calculated from the curvature, else from the slope of the linear trend in the plot of $\sqrt{I_{DS}}$ vs V_{GS}.

A FET device is characterized also by other parameters [58] such as:

- Turn-on voltage (V_{ON}). V_{ON} is the voltage at which a I_{DS} increases above the noise level of the off-current. The semi-logarithmic plot (I_{DS} vs V_G) is useful for extracting V_{ON}, SS and the ON/OFF ratio.

- On/off current ratio. It is an estimate of the amplification between the maximum and minimum value of the current I_{DS}. ON/OFF ratio is limited by the density of dopants and shallow traps.

- Sub-threshold swing SS. The sub-threshold swing SS (expressed in mV/decade) is a measure of how rapidly the device switches from the off state to the on-state and is extracted from the steep region of the I_{DS} trend.

1.7 General objectives

This Doctoral Thesis is framed inside the field of molecular switches and electronics and it is focused on the synthesis and the study of electroactive organic molecules for the fabrication of advanced electronic devices.

The main objective of the present thesis is the preparation of self-assembled monolayers (SAMs) on substrates, employing specifically designed electroactive molecules (i.e. anthraquinones, ferrocenes, tetrathiafulvalenes and polychlorotriphenylmethyl radical derivatives), with the aim of studying the switching behavior in surface. Once this target is achieved, the molecules will be be integrated in more complex devices to investigate the influence of their redox activity on the device performances.

The general objectives can be resumed as follows:

1) Design and synthesis of the electroactive molecules based on anthraquinones, ferrocenes, tetrathiafulvalenes and perchlorotriphenylmethyl radical with specific anchoring groups.

2) Preparation of self-assembled monolayers and investigation of their switching properties by CV and using as read-out mechanisms the optical, magnetic or capacitance response or the capability to form host/guest complexes.

3) Integration of the functional molecules in different electronics devices such as:

- FETs, OFETs or EGOFETs, by functionalizing the active material, the dielectric or the gate contact.
- Water actuator.
- Charge storage devices.

This thesis has been organized by dedicating each chapter to a specific family of electroactive molecules, being the design and the synthesis introduced as first. The second part of each chapter is devoted to the SAMs fabrication and characterization, and, finally, the implementation of the modified surfaces in more sophisticated devices is described.

2

Molecular switches based on anthraquinone and ferrocene derivatives

In this Chapter, anthraquinone (AQ) and ferrocene (Fc) derivatives will be presented and used as electroactive molecules. Then, switchability studies performed with these molecules on surface as well as in two different typologies of devices, will be deeply discussed.

In particular, 9,10-dioxo(triethoxysilyl)propyl)9,10-dihydroanthracene2carboxamide (AQSi) and 11(ferrocenyl)undecanethiol (FcC_{11}) molecules were selectively grafted in a patterned ITO//gold substrate with the aim of locally modulating the surface properties by the application of the appropriate electrochemical stimulus. By localizing on different areas of the substrate an acceptor (AQSi) and a donor (FcC_{11}) molecule we realized a three redox state system. Furthermore, we made use of the different binding interactions of an analyte (β-cyclodextrin) with the different redox states of the two molecules to validate the local modulation of the surface properties. Hence, depending on the voltage applied to the surface, we were able to trap the analyte on specific areas, demonstrating the confined modulation of the surface properties.

Moreover, the SAM of AQSi on ITO (S_{AQSi}) was reported as electrowetting system. AQ electrochemical features confer the capability of yielding a significant modulation of surface wettability of the functionalized ITO substrates as high as 25° when its redox state is switched. Hence, an array of planar electrodes for droplets actuation was fabricated and integrated in a microfluidic chip to perform some of the digital microfluidic operations such as droplet mixing, and splitting. Besides, the microfluidic device was employed in cell vehiculation by taking full advantage of surface electrowetting in culture medium.

Finally, the electrochemical switch of the ferrocene derivative 6(ferrocenyl)hexanethiol (FcC_6) was exploited to prove that complex thiolated molecules can be successfully employed to functionalize 2D MoS_2 semiconductors. This result open the way towards possible important future applications in the field of electronics and sensors.

2.1 Objectives

The objectives of this chapter are here itemized:

1) Design and synthesis of the anthraquinone (AQ) derivatives AQSi and AQS_2, shown in Figure 2.1 and characterization of the resulting SAMs (S_{AQSi} and S_{AQS_2}) and of the SAM $S_{FcC_{11}dil}$.

2) Fabrication and characterization of the bi-component SAM $S_{AQSi//FcC_{11}dil}$ on patterned ITO//gold substrate. Study of the supramolecular interactions between $S_{AQSi//FcC_{11}dil}$ and β-CD by switching the redox states of the confined molecules.

3) Integration of AQ and Fc derivatives in devices:

A) Incorporation of S_{AQSi} in microfluidic devices and study of the electrochemical actuation of aqueous droplets.

B) Implementation of FcC_6 in 2D Field Effect Transistors (FETs) by the functionalization of 2D MoS_2 semiconductor and study of the FcC_6 switch in ionic liquid gated FET.

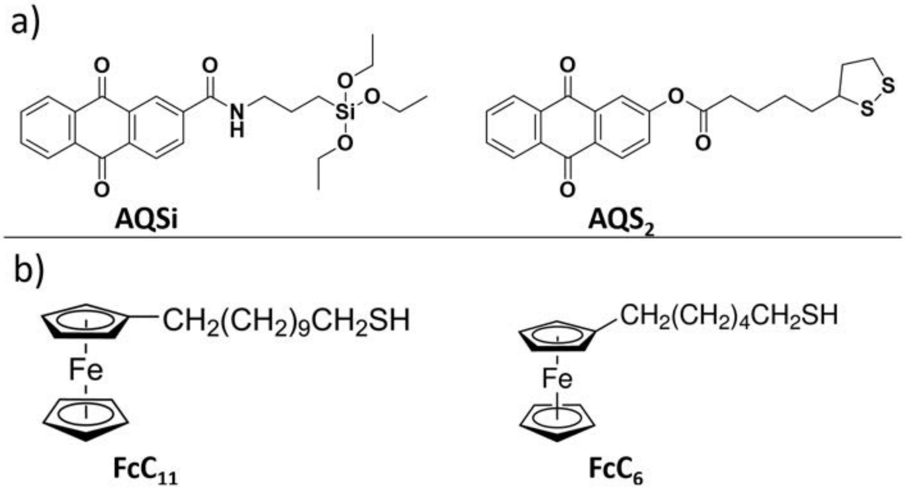

Figure 2.1: a) Anthraquinone and b) ferrocene derivatives used.

2.2 Introduction to the molecules

2.2.1 Anthraquinone and its derivatives

Anthraquinones (9,10-dioxoanthracenes; AQs) constitute an important class of natural and synthetic compounds with a large range of applications. Besides their application as colorants [59], anthraquinone-containing plants, for example aloe, have been used for centuries in folk medicine. Biological active anthraquinone derivatives have also been identified in bacteria, insects and fungi [60, 61]. Hence, anthraquinones are used as drugs in clinical practice with the role of laxative, anticancer, antibacteria, etc, where it has been observed that their biological activities are associated with their redox behavior [62, 63]. In addition to their use in medical applications, they serve as catalysts in many chemical and biochemical processes, such as reductive degradation of contaminants and hydrogen peroxide production [64]. Finally, within the last years they have been used in the emerging field of organic-based energy storage for the substitution of inorganic, scarce and polluting compounds [65, 66, 67].

AQs are aromatic compounds and their structure is based on the rigid planar three-ring aromatic anthracene system having two keto functions at positions 9 and 10 (Figure 2.2). 9,10-anthraquinone was synthesized for the first time in 1840 through oxidation of anthracene with nitric acid by Laurent [68]. However, it was Fitting in 1873 who attributed to the molecule the correct diketone structure [69].

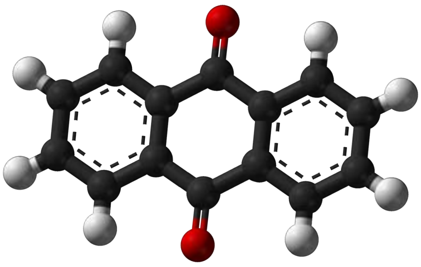

Figure 2.2: Molecular structure of anthraquinone.

Research on the electrochemistry of this compound has been actively pursued for many decades since the early 90's [70]. It has a long history, possible due to the complex electrochemical behavior that strictly depends on the medium.

In neutral aprotic media AQ undergoes two successive one-electron reduction steps to produce semiquinone ($AQ^{\cdot-}$) and quionone dianion (AQ^{2-}) generating two separate cathodic waves in Cyclic Voltammetry (CV) experiments. The first redox step is reversible and the second one is quasi-reversible at customary scan rates [71**? ? ?**] (Figure 2.3). The redox potentials of these redox species strictly depend on the stability of the reduced species. Hence, the polarity of the solvent, formation of hydrogen bonds, presence of basic or acid additives or the protonation-deprotonation equilibrium play a crucial role on them.

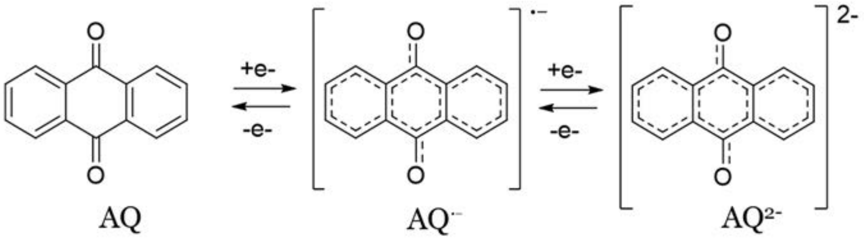

Figure 2.3: Redox processes of AQ in neutral aprotic media.

In aqueous buffer at acidic, neutral and alkaline pH, AQ undergoes one reversible two-electron reduction in which the reduction potential varies with the pH in a straightforward Nernstian manner. At acidic pH, the reduction is a single step two-electron two-proton process (Figure 2.4), while in alkaline pH the reduction is only a case of two-electron process [70, 71].

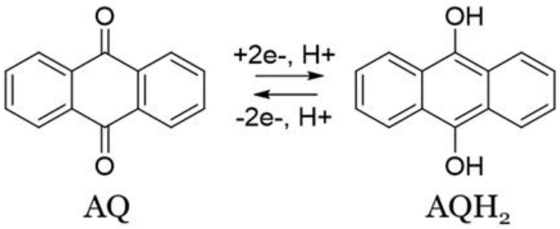

Figure 2.4: Redox process of AQ in acidic aqueous buffer.

The immobilization of this type of molecules on a surface has given rise to to a wide variety of applications within the field of molecular electronics. SAMs of AQ derivatives have been used as molecular wires [72], (bio)-sensors [73, 74, 75], to achieve the modification of the hydrophobic properties of a surface [76], and as molecular switches [77, 78].

2.2.2 Ferrocene and its derivatives

Ferrocene (Fc) is an organometallic compound discovered in 1951 by Kealy and Pauson by accident during the oxidation of cyclopentadienylmagnesium bromide with anhydrous ferric chloride in ether solution [79]. At almost the same time Miller, Tebboth and Tremaine isolated that unknown compound from the reaction of cyclopentadiene vapor with reduced iron at 300°C [80]. Its structure was proved by Wilkinson and Fischer which were awarded with the Nobel prize in chemistry in 1973 "for their pioneering work, performed independently, on the chemistry of the organometallics so called "sandwich compounds", among which ferrocene. Its structure is defined as "sandwich" structure since two cyclopentadienyl rings are symmetrical with respect to the central iron atom. Importantly, many of the chemical transformations which ferrocene undergoes result from its aromatic character, first demostrated by Woodward [81].

Although, ferrocene and its derivatives do not have many applications in industry at large scale, it has interesting applications in cancer research [82] and, more generally, in the pharmaceutical field [83]. It is also employed as antioxidant and antiknock due to its robustness and redox characteristics.

Indeed, it is well known that ferrocene easily undergoes one electron oxidation to form ferricenium cation $Fe(C_5H_5)_2^+$ in a reversible manner (Figure 2.5) in organic and aqueous media [84, 85, 86, 87, 88, 89]. The redox reaction ferrocene/ferricenium has been deeply studied during years, to fully understand both its kinetic and thermodynamics. Importantly, since its redox potential is little influenced by solvents, Fc is usually chosen as probe fore non-aqueous system [90, 91].

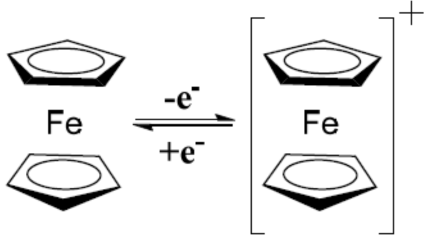

Figure 2.5: Structure of ferrocene and its reversible mono electronic oxidation.

Many works report Fc functionalizing surfaces, in particular gold [92, 93], to carry out studies of charge transfer [94], (bio)-sensors [95, 96] and molecular switches [97, 98].

The thiolated ferrocene derivatives here used FcC_{11} and FcC_6 have been purchased from Sigma-Aldrich and used without further purification.

2.3 Design and synthesis of Anthraquinone derivatives AQSi and AQS$_2$

Two molecules, namely AQSi and AQS$_2$, have been designed to confine the electroactive properties of the anthraquinone on ITO and gold, respectively. Specifically, the trietoxisilane was elected as terminal group in the case of AQSi, since it is able to covalently graft on ITO forming stable SAMs. In the AQSi structure, the trietoxisilane is linked to a short backbone chain of three carbon atoms that acts as a spacer separating the terminal group and the electroactive moiety of the molecule, finally connected by an amide bond. In the case of AQS$_2$ a disulfide terminal group was elected to form a thiolate gold bond, giving rise to a stable functionalization of the gold surfaces. The spacer was a backbone chain of four carbon atoms while the type of bond elected to connect the terminal and electroactive group was an ester bond.

Regarding the molecule preparation, AQSi was synthesized following the synthetic scheme showed in Figure 2.6 a) [99]. In the first reaction step, a solution of the commercial anthraquinone-2-carboxylic acid and thionyl chloride was heated at reflux temperature overnight under inert atmosphere, achieving the chlorination of the carboxylic acid. After that, the excess of thionyl chloride was removed flowing argon giving the anthraquinone-2-carbonyl chloride. The triethoxysilane terminal group was introduced through the formation of an amide bond. For that purpose the anthraquinone-2-carbonyl chloride was mixed with (3-aminopropyl)triethoxysilane (APTES) in dry toluene, with a catalytic amount of of triethylammine. After that, the mixture of reaction was concentrated under reduced pressure, the solid thus obtained was dissolved in chloroform and after cycles of precipitation (adding hexane) and filtration, the compound AQSi was obtained with a 70% of yield.

The compound thus obtained was characterized by different techniques such as Infrared spectroscopy (IR) and Laser Desorption/Ionization Mass Spectrometry (LDI-MS) (see experimental section). The formation of the amide bond was particularly proved by IR, with the presence of one peak at 1644 nm, and by NMR, with the appearance of one proton peak at 6,86 ppm in ^{1}H NMR (400 MHz) and one carbon peak at 165,6 ppm in ^{13}C NMR spectrum.

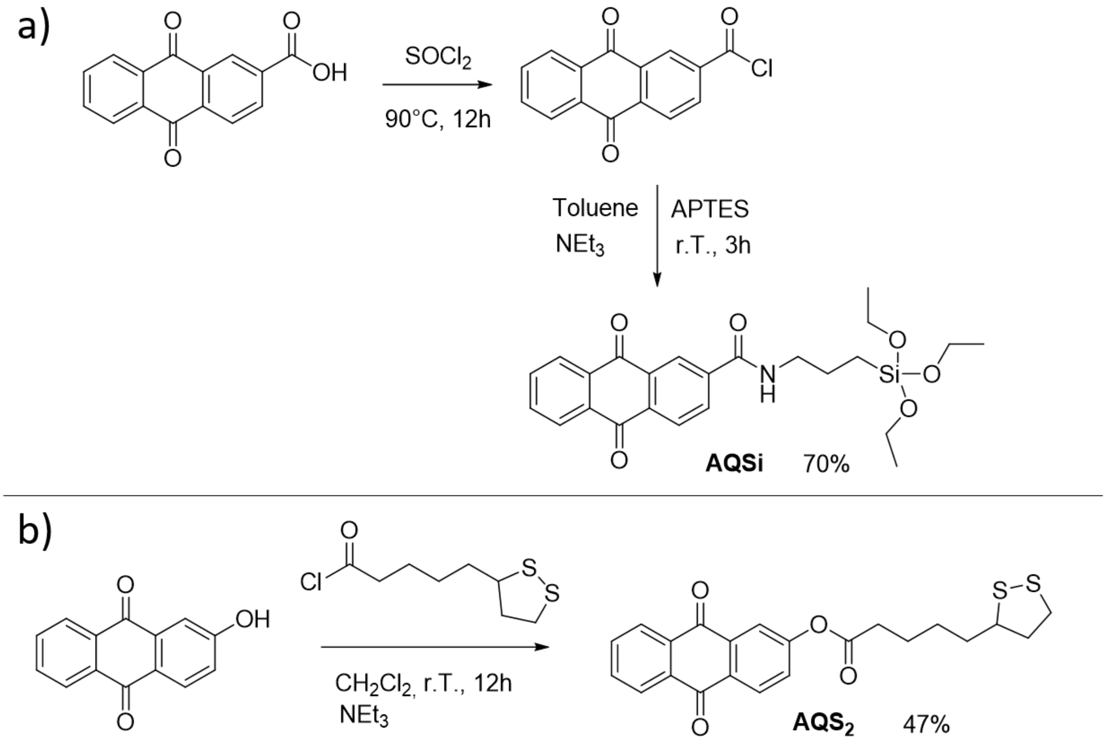

Figure 2.6: Synthetic scheme for the preparation of a) AQSi and b) AQS_2.

AQS_2 was synthetized in one step reaction (see Figure 2.6 b)). A solution of 2-hydroxyanthraquinone and α-lipoic acid chloride in presence of triethylammine in dichloromethane was left with under stirring overnight under inert atmosphere. AQS_2 was thus obtained with 47% yield. Also in this case, the characterization of the molecule was done through IR, LDI-MS and NMR spectroscopy (see experimental section). The peak related to the ester formation was observed at 172,8 ppm in ^{13}C NMR and at 1753 nm in the IR spectrum.

Finally the electrochemical properties of both AQSi and AQS_2 molecules were tested by cyclic voltammetry technique using ammonium hexafluorophosphate 0,1 M in dichloromethane/acetonitrile 9:1 as electrolyte. A silver wire and two platinium wires were used as reference, counter and working electrode, respectively. In the conditions used, just the first reduction process corresponding to the reduction of AQ to $AQ^{\cdot -}$ was observed at $E_{1/2}$= -1,0 V vs Ag(s) and at $E_{1/2}$= -1,4 V vs Ag(s) in the case of AQSi and AQS_2 , respectively (Figure 2.7).

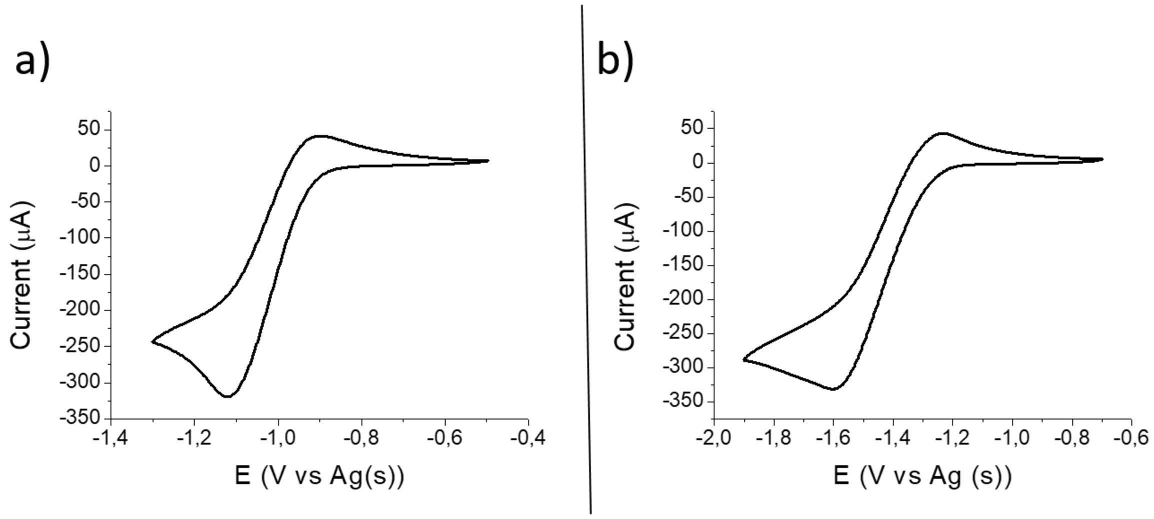

Figure 2.7: CV of a) AQSi and b) AQS_2 molecules. F_6H_4NP 0,1 M in dichloromethane (DCM)/acetonitrile (ACN) 9/1 was used as electrolyte. A silver wire and two platinum wires were used as reference, counter and working electrode, respectively. The scan rate was 0,5 Vs^{-1}.

2.4 Preparation of switchable surfaces based on SAMs of AQ and Fc derivatives[1]

2.4.1 Preparation and characterization of mono-component SAMs S_{AQSi}, $S_{AQS_2}$and $S_{FcC_{11}\,dil}$

Before of the preparation of the mixed SAMs, our final goal, a rigorous study on mono-component SAMs of the thiolated ferrocene derivative FcC_{11} on gold diluted with alkanethiols ($S_{FcC_{11}dil}$), and of the anthraquinone derivative AQSi on ITO (S_{AQSi}) was performed. This was done with the aim of optimizing the final condition for the preparation of the bi-component SAM, and also for studying the properties of each component, ferrocene and anthraquinone derivatives, separately first (Figure 2.8). We defined these SAMs as mono-component since they consist solely of one electroactive species.

---

[1] This work was published in the journal Chemical Communication: Maria Serena Maglione, Javier Casado-Montenegro, Eva-Corinna Fritz, Núria Crivillers, Bart Jan Ravoo, Concepció Rovira, Marta Mas-Torrent, Chem. Commun., 53, 2018, 3038-3041.

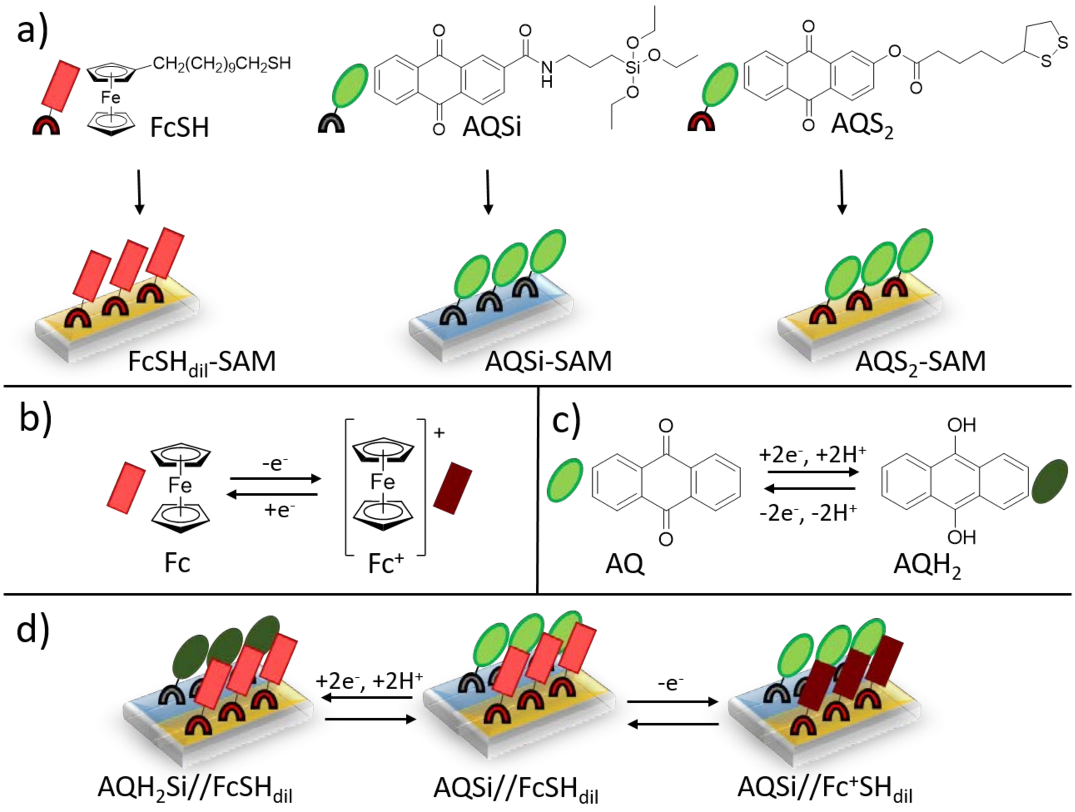

Figure 2.8: a) Molecular structure of the molecules used and scheme of the resulting SAMs. Redox processes of b) Fc and c) AQ in a protic media. d) Schematic representation of AQSi//FcC_{11dil} patterned SAM and its ternary switch as a result of the oxidation of ferrocene and the reduction of anthraquinone. For clarity, the alkanethiols present in the diluted FcC_{11dil} -SAM have been omitted

The preparation of the self assembled monolayers was carried out as follows. A commercial substrate of 50 nm of polycristallyne gold evaporated on glass adhesive layer provided by Phasis and a commercial substrate of 70 nm of ITO on glass bought from Delta Technologies were used. Both were washed with dichlorometane, acetone and ethanol HPLC pure grade solvent, sonicating for 15 minutes each. Then, they were dried under nitrogen flow and activated by UV-Ozone cleaner for 20 minutes. At this point the ITO coated glass substrate was immediately immersed in the solution containing AQSi molecule, while the gold substrate was firstly immersed in ethanol HPLC pure grade for 15 min and, finally, put in the solution of the corresponding molecule to reach the desired functionalization. The exact conditions used for the funcionalization are reported in Table 3.1. All the SAMs were prepared at ambient temperature, under inert atmosphere and with light exclusion. Once obtained, they were characterized by cyclic voltammetry (CV), contact water angle (CA) and X-ray photoelectron spectroscopy

(XPS), as described below. Importantly, the SAM of ferrocene $S_{FcC_{11}dil}$ was prepared diluted with the alkanethiol 1-decanethiol ($C_{10}SH$) to avoid creating a too dense monolayer where the steric hindrance of the ferrocene terminal group could impede the complex formation with the β-CD. In particular, the dilution 1/9 $FcC_{11}/C_{10}SH$ was used as suggested from literature [100]. For simplicity and clarity of the figures here reported, the alkanethiols used for the dilution will never be represented in the schemes. On the contrary, it was observed that the dilution of Anthraquinone derivatives SAMs was not crucial for the interaction between AQSi (or AQS_2) and β-CD, therefore, SAMs of S_{AQSi} and S_{AQS_2} were not diluted.

Table 2.1: List of conditions used for SAMs formation.

Substrate	**SAM**	**Solution**	**Immersion Time**
ITO	S_{AQSi}	0,5 mM of AQSi in toluene	4h
Gold	S_{AQS_2}	0,5 mM of AQS_2 in THF	40h
Gold	$S_{FcC_{11}dil}$	2 mM of $FcC_{11}/C_{10}SH$ 1/9 in ethanol	18h

The cyclic voltammetry of $S_{FcC_{11}dil}$ (Figure 2.9) was done using a conventional three-electrode setup with the modified gold substrate used as the working electrode, a platinum wire as counter electrode and a silver wire as quasi-reference electrode. A phosphate buffer solution at pH~ 6,9 was employed as electrolyte. The redox wave of the system is observed at $E_{1/2}$ = +0,26 V and the current is in linear dependence with the scan rate, confirming the confinement of the electroactive species to the electrode surface. The surface coverage was estimated by integrating the cathodic peak at 0,1 V/s in a CV experiment where ammonium hexafluorophosphate 0,1 M in dichloromethane (DCM)/acetonitrile (ACN) 9/1 was used as electrolyte, obtaining a value of 1,2 x 10^{-10} mol/cm^2. This value is lower than that obtained for SAMs of undiluted ferrocene derivatives and is in agreement with the coverage of mixed alkanethiols SAMs terminated with ferrocene diluted in the same proportion with analogous alkanethiols [100].

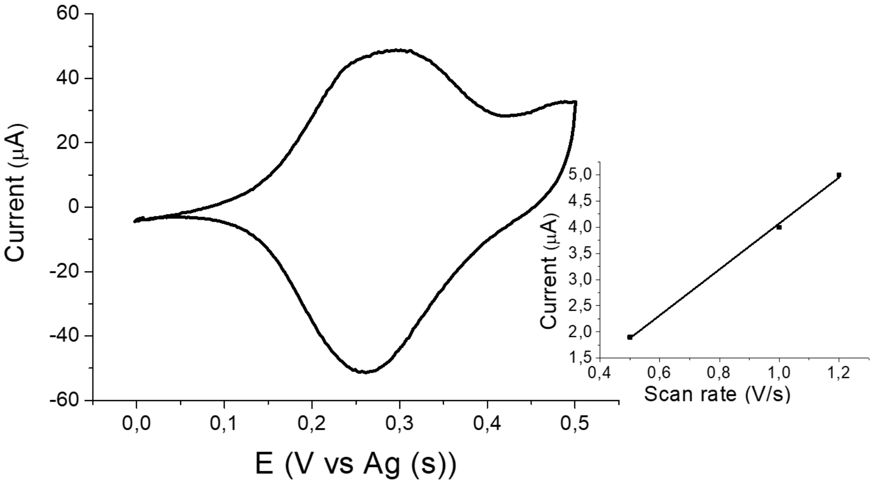

Figure 2.9: Cyclic voltammetry of $S_{FcC_{11}dil}$. The modified gold is used as working electrode while platinum and a silver wire as counter and quasi-reference electrodes, respectively. Phosphate buffer solution at pH~ 6,9 is employed as electrolyte. Inset: linear dependence between current and scan rate.

$S_{FcC_{11}dil}$ was also characterized by CA, giving a value of 103,7 ± 1, 1°. This value is higher than that obtained for a SAM of undiluited FcC_{11} (78 ± 3,4°) and is in agreement with the more hydrophobic character of the alkanethiol $C_{10}SH$ [101]. The XPS characterization is reported in Table 2.2

Table 2.2: XPS values of $S_{FcC_{11}dil}$.

Core Level	Binding Energy (eV)	Type of Bond
C1s	284,8	C-C/C-H
$S2p_{3/2}$	161,9	S-Au
$S2p_{1/2}$	163,1	S-Au

The electrochemical characterization of SAM S_{AQSi} was done in the same conditions described above for $S_{FcC_{11}dil}$. The CV shows a peak at $E_{1/2}$ = -0,64 ascribed to the reduction of the anthraquinone moiety to its corresponding anthrahydroquinone reduced form. Also in this case, the linear dependence between current and scan rate is observed (Figure 2.10).

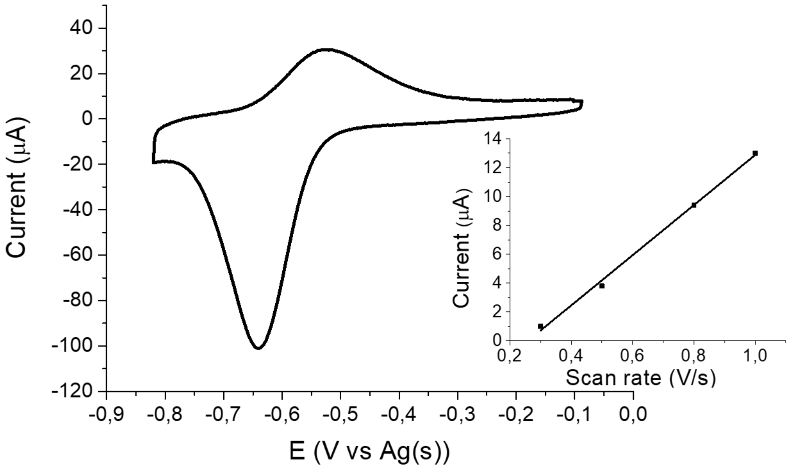

Figure 2.10: Cyclic voltammetry of S_{AQSi}. The modified ITO is used as working electrode while platinum and a silver wire as counter and quasi-reference electrodes, respectively. Phosphate buffer solution at pH~ 6.9 is employed as electrolyte. In the inset is reported the linear dependence between the current and the scan rate is shown.

For the subsequent preparation of the bi-component SAM, it was crucial to investigate the kinetics of the formation of SAM S_{AQSi}. Thus, the SAM formation was monitored after 2, 4, 8 and 48 hours of immersion in the solution of AQSi (Figure 2.11). A good coverage (1,6 x 10^{-10} mol/cm^2) was obtained starting from 4 hours of immersion. It was observed that a further increase in the immersion time did not significantly improve the coating.

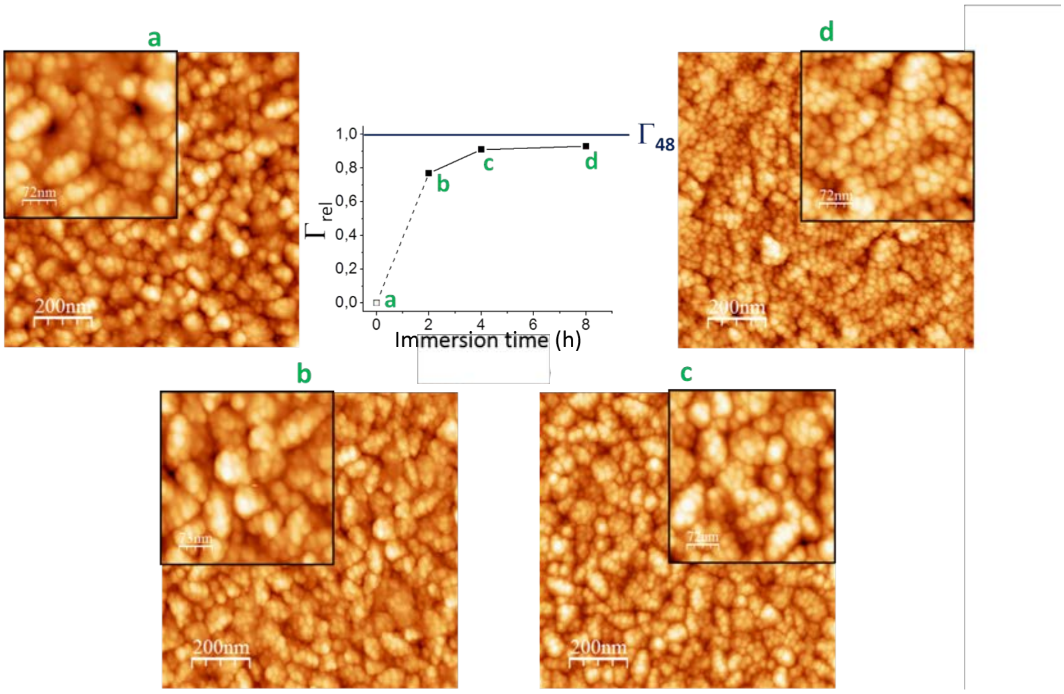

Figure 2.11: Variation of the relative surface coating (Γrel) of S_{AQSi} with increasing the immersion time of the substrate in the AQSi solution during b) 2, c) 4, and d) 8 hours. AFM topography images (1x1 μm^2) of S_{AQSi} on ITO (b-d) and of the unfunctionalized ITO substrate (a).

The minimization of the immersion time is important since later on $S_{AQSi//FcC_{11}dil}$ had to be prepared by subsequent immersion in two different solutions: the first one of AQSi and the second one of FcC_{11} /$C_{10}SH$, as it will be described in detail in Section2.4.2. Precise indication about the minimum immersion time required for a good formation of the SAM S_{AQSi} is crucial to ensure a good coverage of the ITO part of the patterned substrate without decreasing the reactivity of the gold part of the substrate that may be caused by a prolonged immersion in the first solution.

The contact angle observed for S_{AQSi} was 61,1 ± 1,5º and the XPS characterization is reported in Table 3.2.

Table 2.3: XPS values of S_{AQSi}.

Core Level	Binding Energy (eV)	Type of Bond
C1s	283,9; 285,3; 287,9; 288,7	C-Si/C=C; C-C/C-H; O=CN/SiO-C; C=O
O1s	530,4; 531; 532,1; 533	metal oxide; Si-O; C=O
Si2p	102,5	Si-ITO

In addition to these two SAMs a third SAM based on AQS_2 was fabricated on gold substrates giving rise to S_{AQS_2} . This SAM had been already studied and characterized in our group as reported in literature [102] (Table 3.1). The water CA was around of 83,1 ± 1,38º and it is close to those of other reported monolayers on gold exhibiting an exposed phenyl group. The CV data reveled a peak at -0,8 V vs Ag(s) when NBu_4PF_6 in acetonitrile was used as electrolytre. S_{AQS_2} was here employed in SPR measurements where a gold substrate was required, as elucidated later.

2.4.2 Fabrication of the patterned ITO//gold substrate and formation of the bi-component SAM $S_{AQSi//FcC_{11}dil}$

Once the mono-component SAMs were prepared and characterized, we moved to the fabrication of the bi-component SAM $S_{AQSi//FcC_{11}dil}$. Patterned substrates with ITO and Au areas were prepared following two approaches. The first one was aimed to realize a patterned ITO//gold substrate at micrometer scale. Stripes of 50 μm width were drawn by a Computer-aided design program (CAD) and transferred to an ITO coated glass substrate by a photolithographic process followed by thermal evaporation of gold. Through that protocol we were able to prepare a well defined pattern that allowed us to have an extremely high control on defined patterns at micrometer dimensions. Unfortunately, we were unable to use those substrates for our purpose since unexpectedly the gold showed fluorescence (see Figure 2.12), possibly attributed to the nanostructuration of the gold in the conditions used for its evaporation. In fact, it has been reported that gold nanoclusters can lead size-dependent fluorescence [103]. To avoid the gold fluorescence was crucial, since we aimed to use fluorescence microscopy as technique to visualize the interaction between the SAMs and the β-CD (as described in the next section).

The realization of reproducible substrates with free gold fluorescence was proved to be not easy. We were forced to simplify the manufacturing of the substrate in such a way that we could fabricate a larger number of substrates in a shorter time. To do that, we simply evaporated gold using a mask. Specifically, patterned surface with ITO//gold regions was finally realized by gold evaporation on an ITO-coated glass substrate using a metallic mask with 3 cm width stripe design. 15 nm of Cr and 75 nm of gold were deposited though thermal evaporation using the system Auto 306 from Boc Edwards. In this way, even if some of the substrates still exhibited fluorescence, we managed to manufacture also a number of useful surfaces for our purpose.

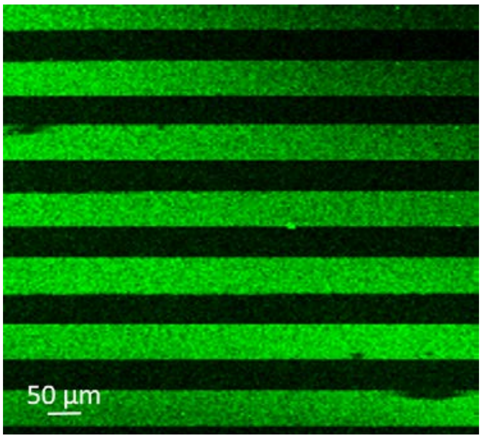

Figure 2.12: Bare ITO//gold patterned substrate realized by photolitography and gold evaporation. The green lines are due to the gold fluorescence.

The surface functionalization with AQSi and FcC_{11} was carried out in two steps. Firstly, the freshly cleaned and activated substrate was immersed in a 0,5 mM solution of AQSi in toluene during 4 h, under inert conditions, to functionalize the ITO coated regions. Then, the substrate was rinsed with toluene to eliminate the phisisorbed molecules, dried under a nitrogen flow and immersed in the second 2 mM solution of $FcC_{11}/C_{10}SH$ 1/9 in ethanol in order to functionalize the gold surface. Finally, the substrate was rinsed with ethanol and dried with nitrogen. It is important to highlight here that the functionalization of ITO had to be realized first since the oxide has to be activated in an ozone cleaner chamber to promote the formation of reactive hydroxyl groups immediately before to its functionalization.

The resulting $S_{AQSi//FcC_{11}dil}$ was characterized by CV. As expected, two redox processes corresponding to the oxidation of Fc and reduction of AQ were observed, giving rise to a ternary switch in a voltage window within ± 0,8 V vs Ag(s) (Figure 2.13).

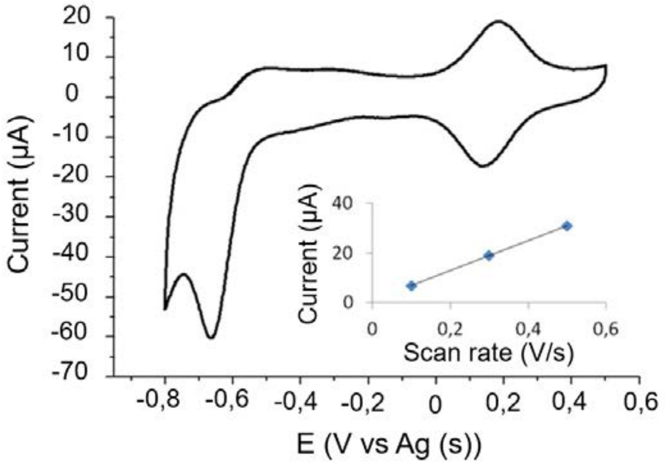

Figure 2.13: CV of the bi-component SAM $S_{AQSi//FcC_{11}dil}$. The modified ITO//gold patterned substrate is used as the working electrode vs Ag(s) and a Pt wire is used as the counter electrode in a phosphate buffer solution pH~ 6,9. Inset: linear dependence between the current and the scan rate when the oxidation of the ferrocene moiety is followed.

Importantly, through this methodology we reached to obtain a system with two significant figures of merits: on one hand, the molecules were confined in precise areas of the surface and, on the other hand, the combination of two different molecules, one donor and the other acceptor of electrons, yielded a system having an enhanced number of accessible redox states in a relatively small voltage window. Obviously, further engineering of the surface would be possible if more sophisticated patterns were required.

2.4.3 Interaction between mono-component SAMs and β-CD

Molecular recognition phenomena are fundamental in biochemistry and in the field of supramolecular chemistry [104]. The idea of exerting a direct control on molecular recognition has a biomimetic origin but its implications clearly extend into materials science. Having a full grasp over host-guest processes and get deep fundamental understanding of the intermolecular interactions responsible for binding, is required to realize molecular machines, sensors and responsive or smart devices [105, 106].

Cyclodextrins (CD) constitute one of the most famous class of natural hosts [107, 108]. They are cyclic oligosaccharides made up of six to twelve α-D-glucopyranose monomers connected at 1 and 4 carbon atoms. The CD with 6-8 α-D-glucopyranose units are known respectively as α, β and γ CD. They have a characteristic lampshade shape with a hydrophobic internal cavity and two hydrophilic external crowns crowded by hydroxyl groups. They are water soluble and can form inclusion complexes with non-polar guests, enabling, for instance, their solubilization in water. Several weak forces, including van der Waals, hydrophobic, dipole-dipole and hydrogen bonding interactions, cooperatively determine the inclusion complexes behavior of the cyclodextrin host. Furthermore, the cavity diameters of α, β and γ CD is from 0,45 to 0,95 nm and hence they can host specifically only guest molecules of the proper size.

CD form inclusion complexes also with redox active guests [109]. Interestingly, in this case, the strength of the host-guest interaction can be modulated according to the hydrophobicity of the redox states of the electro active molecules. Increasing their hydrophilicity, the formation of the complex becomes less favorable or even not possible, as in the case of viologens and cobaltocene [110, 111, 112, 113, 114, 115].

Also ferrocene and anthraquinone are reported as possible guests for β-CD. Throughout the years many groups have investigated a number of ferrocene derivatives complexing β-CD, finding that the one electron oxidation of the ferrocene moiety greatly diminishes the stability of the inclusion complex since results in charged molecules [116, 117, 118].

In the case of antraquinone, the antrahydroquinone reduced form is more hydrophilic, due to the replacement of two carboxyl groups with two hydroxyl ones. That is the reason why antrahydroquinone shows lower affinity with β-CD in comparison with the quinoid form [119, 120, 121, 122].

To prove the interaction between β-cyclodextrin and ferrocene or anthraquinone on substrates, Surface Plasmon Resonance (SPR), Contact Angle (CA), Cyclic Voltammetry (CV) and X-ray Photoelectron Spectroscopy (XPS) measurements were run on the mono-component SAMs of Fc on gold and AQ on ITO (or gold), separately first.

As a first step, we monitored the formation of the host-guest complexes in real time by SPR.

This technique is based on the phenomena that occur when polarized light is shone on a chip with a thin metal film on top, usually gold or silver [123]. On changing the angle of incidence, the intensity of the light reflected by the metal, passes through a minimum that is caused by the excitation of the surface plasmons. It means that photons of polarized light can interact with the free electrons of the metal layer, inducing a wave-like oscillation of the free electrons and, thereby, reducing the reflected light intensity. The angle at which the maximum loss of the reflected light intensity occurs is called resonance angle or SPR angle, and clearly depends on the refractive index of the media. When materials are adsorbed onto the metal, the local refractive index of the surface changes and so the surface plasmon resonance conditions. Hence, SPR is an excellent method to detect the adsorption of molecules on metal surfaces. It is also possible to monitor the changes in real time obtainig information on the kinetics of the adsorbing processes that are occurring on the surface.

Since for these experiments it is generally required to work on plasmonic gold surfaces, we employed the SAMs $S_{FcC_{11}dil}$ and S_{AQS_2}. The last one can be considered as the analogue of the system S_{AQSi} on ITO, but since AQS_2 bears a disulfide as terminal group it can react with gold forming SAMs compatible with SPR measurements.

The SPR measurements were done in collaboration with Prof. Bart Jan Ravoo from University of Münster, Germany.

The detected SPR curves are shown in Figure 2.14. The SPR response of the S_{AQS_2} is observed to increase during the addition of a solution of 1 mM β-CD in milliQ water for 18 minutes, indicating the formation of the host-guest complex. However, upon addition of a reducing agent (i.e., 2 mM $Na_2S_2O_4$) the signal decreases due to the release of β-CD that takes place when the reduced species AQH_2S_2 is formed. Afterwards, β-CD was injected again resulting in a steady SPR signal, which confirms that in this redox state the complex is not formed (Figure 2.14 a)). In the case of the SAM $S_{FcC_{11}dil}$ a similar experiment was performed (Figure 2.14 b)). Upon addition of a 1 mM solution of β-CD in milliQ water for 4 minutes to the functionalized surface a notable change of the SPR response was observed indicating the formation of the [β-CD][Fc] complex. Subsequently, a 1 mM solution of $FeCl_3$ was added for 2 minutes to oxidize the electroactive Fc units and to disaggregate the complex. Again, at this point further injection of β-CDs did not induce any increase of the SPR response since the formation of the complex was not favorable in this redox state.

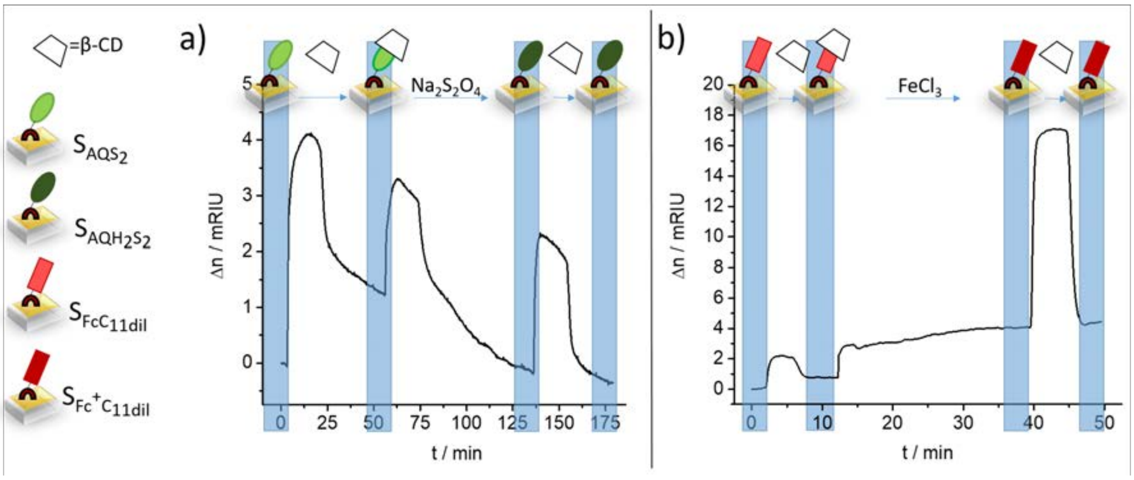

Figure 2.14: SPR measurements of a) S_{AQS_2} and b) $S_{FcC_{11}dil}$ related to the formation of the host-guest complexes with β-CD. Flow: 100 µL/min.

To further corroborate the formation of the host-guest complexes, $S_{FcC_{11}dil}$ and S_{AQSi} were immersed in a solution of β-CD (9 mM in ultra-pure water). The functionalized substrates were left during 3 h to achieve the complexation. Afterwards, they were rinsed with 50 mL of ultrapure water, to eliminate the free β-CD, and finally dried under a nitrogen flow. The so-treated surfaces were characterized by CA, CV and XPS and the results thus obtained were compared with those obtained with no treated surfaces.

It was noted that the water contact angle value changes approximately 20° after the formation of the complex, going from from 61,1 ± 1,5° to 39,9 ± 2,1° in the case of S_{AQSi} and from 103,7 ± 1,1° to 84 ± 1,5° in the case of $S_{FcC_{11}dil}$. As expected, the surfaces become more hydrophilic after having been exposed to cyclodextrin which has many hydroxyl group.

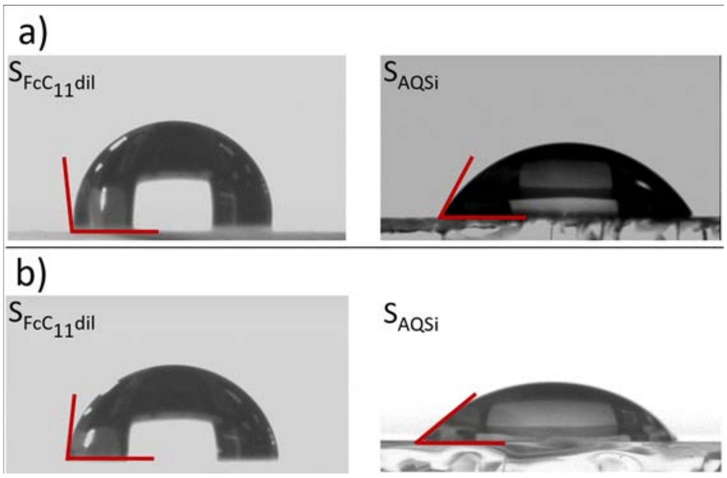

Figure 2.15: CA of $S_{FcC_{11}dil}$ and S_{AQSi} before and after the treatment with β-CD.

CV measurements were also performed before and after the formation of the complexes. It is assumed that the ferrocene and the anthraquinone bound to β-cyclodextrin are not electroactive anymore [109]. It means that the direct electrochemical oxidation (or reduction) of the inclusion complexes is less favorable, suggesting the electron transfer from (or to) the inclusion complex must be thermodinamically and/or kinetically hindered. As shown in Figure 2.16, the complexation of Fc and AQ units with β-CD is detected experimentally by a decrease in the current peaks intesity.

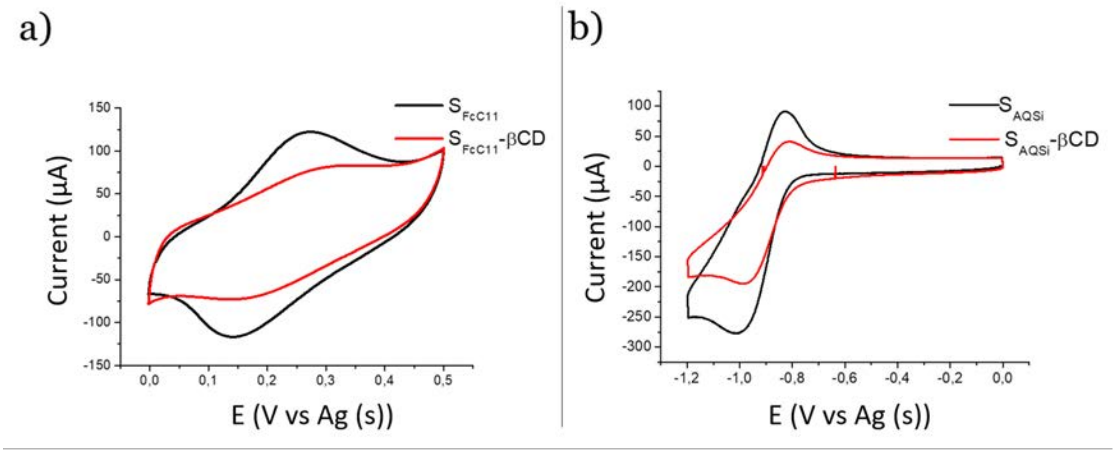

Figure 2.16: CV measurements of a) $S_{FcC_{11}dil}$ and b) S_{AQSi} before (black line) and after (red line) the treatment with β-CD.

Finally, in the XPS of the $S_{FcC_{11}dil}$, the complex formation is proved by the appearance of the peaks at binding energies around 286 and 288 eV for the C1s and 533 eV for the O1s coming from the β-CD (Figure 2.17).

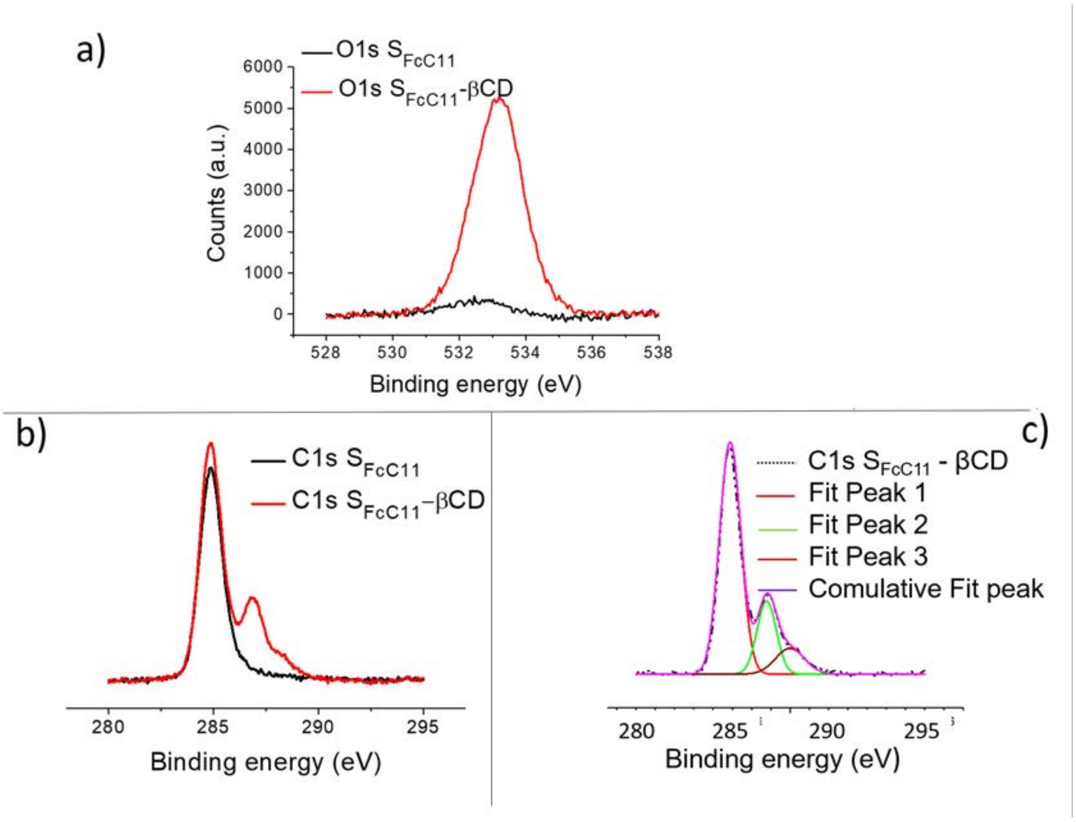

Figure 2.17: XPS analysis of S_{FcC11} before and after the treatment with β-CD a) for O1s and b) for C1s. c) Deconvolution of the C1s peaks coming from the β-CD.

In the S_{AQSi} the new peaks around 286 and 533 eV confirm the presence of β-CD on the surface (Figure 2.18, Figure 2.19).

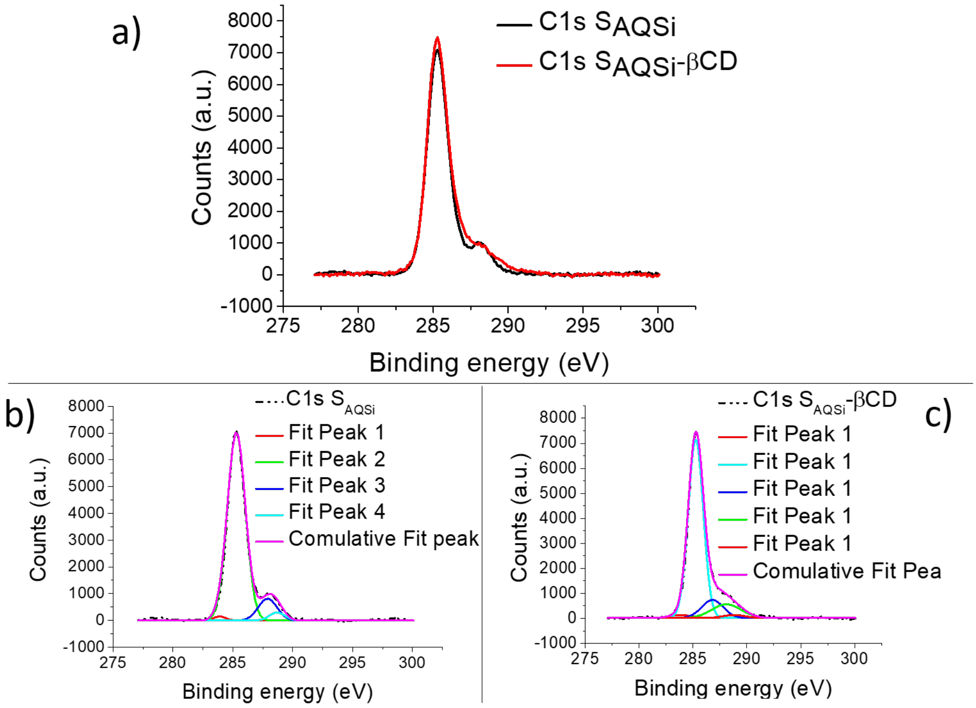

Figure 2.18: a) XPS analysis of S$_{AQSi}$ before and after the treatment with β-CD for the C1s. Deconvolution of the C1s peaks coming from b) S$_{AQSi}$ and c) S$_{AQSi}$- β-CD complex.

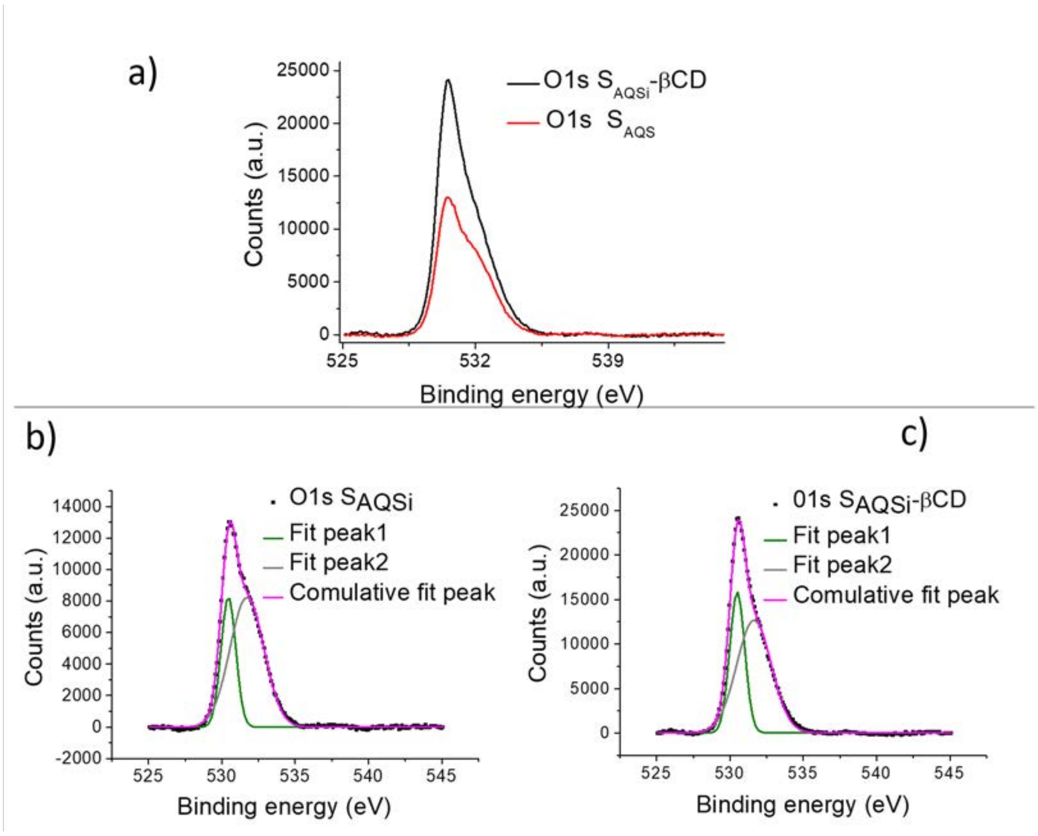

Figure 2.19: a) XPS analysis of S_{AQSi} before and after the treatment with β-CD for the O1s. Deconvolution of the O1s peaks coming from b) S_{AQSi} and c) S_{AQSi}- β-CD complex.

Considering all above, it can be firmly stated that both, Fc and AQ derivatives anchored on surface can form complexes with β-CD.

2.4.4 Interaction between the bi-component SAM $S_{AQSi//FcC_{11}dil}$ and β-CD

The last step to achieve our final goal was to prove the controlled trapping of β-CD on a specific location depending on the voltage applied on the patterned SAM $S_{AQSi//FcC_{11}dil}$. For this propose, fluresceine functionalized β-cyclodextrins (F-β-CD) was used as analyte in order to be able to visualize the molecular interactions by confocal microscopy. The substrates were immersed in an electrochemical cell filled with a phosphate buffer solution at pH~ 6,9 containing 60% m/v of F-β-CD. The patterned substrates were used as working electrodes in the following chronoamperometry experiments. The counter and the quasi-reference electrode were a platinum and a silver wire, respectively. A constant potential of +0,6 V vs Ag(s) was applied to oxidize the Fc units for 300 s, so the redox process [AQ//Fc] - $e^- \rightarrow$AQ//Fc^+ occurred and, as a consequence, the F-β-CD in the electrolyte medium could only interact with AQ moieties located on the ITO stripe. On the other hand, when a potential of -0,8 V vs Ag(s) was applied to reduce the AQ units, the redox process $[AQ//Fc] + 2H + 2e^{-} \rightarrow AQH_2//Fc$ took place and hence, the formation of the host-guest complex was promoted only between F-β-CD and the Fc units present on the gold coated regions (Figure 2.20). All these experiments were examined by confocal fluorescence microscopy (Figure 2.20 b) and c)). Clearly, it was observed that depending on the applied voltage the fluorescence derived from F-β-CD could only be seen on the ITO or gold areas, confirming that the host-guest supramolecular interactions can be electrochemically steered and locally addressed.

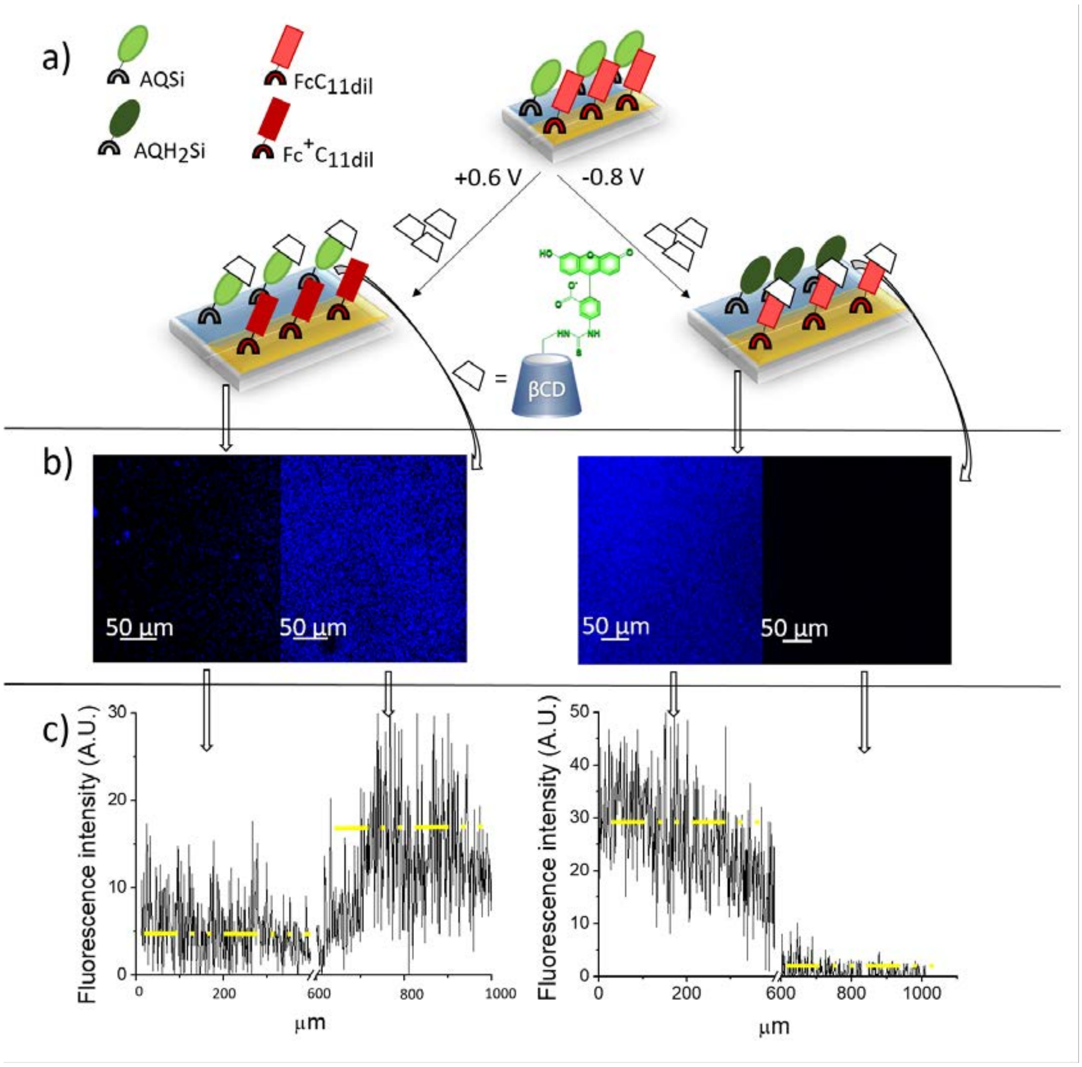

Figure 2.20: a) Schematic representation of the electrochemically guided interaction between F-β-CD and SAM $S_{AQSi//FcC_{11}dil}$. b) Confocal images of the substrate $AQSi//Fc^{+}C_{11}dil$ on the left and $AQH_2Si//FcC_{11}dil$ on the right after promoting the selective interaction with F-β-CD. c) Plot of the fluorescence intensity along the surface. For clarity the $C_{10}SH$ molecules used for diluting the Fc SAM are omitted.

2.4.5 Summary

In summary, we employed ITO//gold patterned surfaces to confine electroactive molecules with specific anchoring groups (SH and $SiOEt_3$) on defined surface regions. In this way, we realized a substrate exhibiting three stable redox states confining SAMs of an electron donor (i.e., Fc) and an electron acceptor (i.e., AQ) molecules. Further, we showed that the electroactive units anchored on the substrate form host-guest complexes with β-CD via supramolecular interactions only on their initial redox state. Hence, by applying the appropriate electrical signal the formation of the supramolecular interactions and hence the selective trapping of the β-CD, has been locally guided on the surface. This study represents a proof of concept of how it is possible to address important grasp on a system tuning the surface properties in a strictly controlled way. This response-stimulus control could be exploited in various fields of interest such as for sensors and in bio-applications by an appropriate interface engineering.

2.5 S_{AQSi} in microfluidics devices[2]

2.5.1 Introduction to digital microfluidics

Digital microfuidics concerns the manipulation of fluids on solids substrates. Having the control over the movement and the flow of droplets on surfaces and, in particular, of aqueous microdroplets, is of great interest to many industrial and medical applications [124].

It has been known for over a century that the interfacial energy between two immiscible media can be controlled by applying an electrical potential across them [125]. However, only during the last 20 years the surface tension force began to receive serious attention in engineering thanks to the advent of microelectromechanical systems (MEMS).

Within the field of digital microfluidics, micropumping by thermal control of surface tension was reported first [126], however the electric control of surface tension is significantly more promising for microdevices. The forces resulting from an electrical input started to be an attractive proposition in designing micromechanical devices able to replace the standard mechanical pumping of aqueous samples.

Different physical phenomena can be exploited for this purpose, such as

---

[2] The work here presented was published in the journal Small: Maria Serena Maglione, Stefano Casalini, Stamatis Georgakopoulos, Marianna Barbalinardo, Vitaliy Parkula, Núria Crivillers, Concepció Rovira, Pierpaolo Greco and Marta Mas-Torrent, Small, 2017, 1703344.

electro-osmosis [127, 128], electrowetting [129], electrohydrodynamic pumping [130, 131] and electrothermal flow [132, 133]. Within this context, electrowetting-on-dielectric (EWOD) [134] has been successfully implemented into microfluidics [135, 136, 137, 138, 139] because it permits the control over shape and flow of droplets by applying well-defined electrical fields [140].

In fact, EWOD is based on the application of a voltage between an electrode and a conductive droplet separated by a dielectric film (Figure 2.21). It was firstly reported by Berge in the early 1990s [141]. Berge introduced the idea of using a thin insulating layer to separate the conductive liquid from the metallic electrode in order to eliminate the problem of electrolysis usually present in electrowetting (EW), where the conductive liquid is in direct contact with the metal. The bias between the driving and counter electrode gives rise to the dielectric polarization, which promotes the droplet actuation. The presence of a net electrical charge at the interface makes the surface tension lower because of the repulsion between similar charges that decreases the work required to expand the surface area.

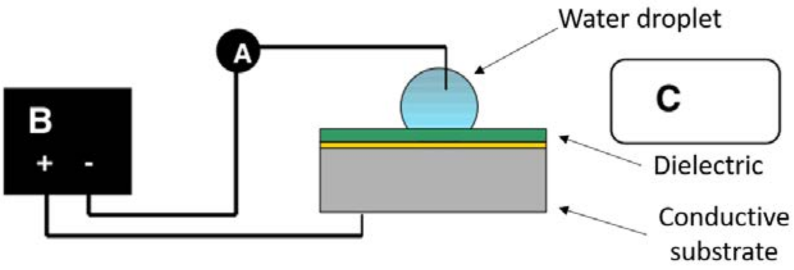

Figure 2.21: Schematic representation of an open EWOD experiment. A) Ampmeter; B) power supply; C) digital camera [142]

The mathematical relationship between the applied electrical potential (V) and the surface tension (γ) is the Lippmann's equation (2.1).

$$\gamma = \gamma_0 - \frac{1}{2} c V^2 \tag{2.1}$$

Where γ_0 is the surface tension at interface when no voltage is applied across the interfaces (no charge at the surface) and c is the capacitance per unit area, assuming that the charge layer can be modified as a symmetric Helmholtz capacitor. Since the electric field is applied at the metal-electrolyte interface, c corresponds to the capacitance of the electric double layer (EDL) formed at metal-electrolyte interface and γ needs to be interpreted as γ_{SL}, the surface tension at solid-liquid interfaces defined by the Young's equation (2.2). This equation can also be used to express the Lippmann's equation in terms of contact angle as in equation 2.3, called Lippman-Young's equation.

$$\gamma_{SL} = \gamma_{SG} - \gamma_{LG} cos\theta \tag{2.2}$$

$$cos\theta = cos\theta_0 + \frac{1}{\gamma_{LG}} \frac{1}{2} cV^2 \tag{2.3}$$

Where θ_0 is the contact angle when the electric field across the interfacial layer is zero, γ_{LG} is the liquid-gas surface tension and γ_{SG} the solid-gas surface tension. Thus, the contact angle is function of the applied voltage between the liquid and the electrode and, hence the surface wettability can be modified by the applied voltage.

Typically, the EWOD is achieved using two different configurations: i) the "single-plate" and ii) "two-plate" device [143]. Such devices have been studied a lot and consequently improved in the last decades, but one of the hot-topics within this field is still focused on lowering the driving potential in order to develop low-power and disposable actuators [144]. As a result, since the fabrication of the first devices, the driving potentials have been dramatically reduced from ± 100 V to 10 V [145].

In this context, and considering that electroactive SAMs are able to switch significantly the surface energy, and hence its wetting properties, at very low voltages [146], we considered to employ them as electrowetting systems as an alternative to EWOD. In particular S_{AQSi} has been used for this purpose.

2.5.2 Static electrowetting studies on S_{AQSi}

As already described, the electrochemical switch from AQ to AQH_2 leads to the replacement of two carbonyl groups with two hydroxyl ones. The consequence of this reaction on the wettability of the modified-ITO surface is supposed to be considerable in S_{AQSi}. The impact of that change was firstly checked by measuring the surface water contact angles (CA) before and after the electrochemical reduction of S_{AQSi}. As reported in Section2.4.1, the CA of a 5 µL drop S_{AQSi} is 61°. To measure the CA of the reduced system, the appropriate voltage (-0,6 V vs Ag(s)) was applied during 120 seconds in the electrochemical cell, using a phosphate buffer solution at pH 6,9 as electrolyte and platinum and silver wires as counter (CE) and reference (RE) electrodes, respectively. Then, the substrate was rinsed with ultra-pure water and dried with nitrogen. Finally, the

CA measurement was performed depositing 5 µL of water droplet on the dry substrate. The S_{AQH_2Si} SAM, gave a CA of 34°, as expected considerably lower than what S_{AQSi} exhibits (Figure 2.22).

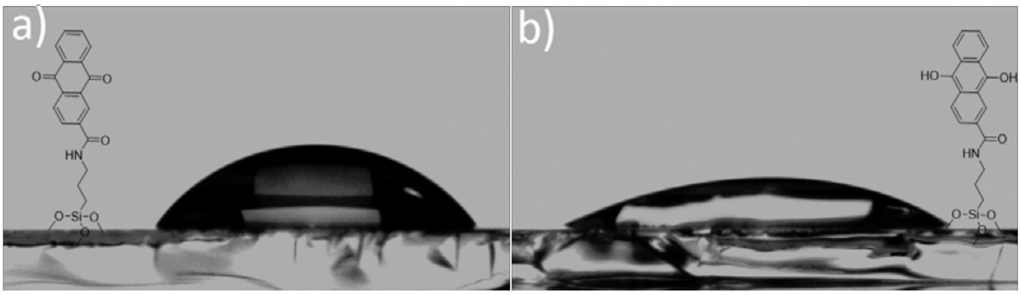

Figure 2.22: Water contact angle (5 µL drop) before and after the reduction of S_{AQSi}.

This marked surface energy difference allowed us to study the change of surface wettability "in-real time". As a result, a three-contact electrochemical cell was set directly into the aqueous droplet deposited on the S_{AQSi}. Both CE and RE were directly immersed in a buffered droplet (20 µL) located onto the functionalized ITO electrode used as working electrode (WE), as showed in Figure 2.23. The electrical ITO contact was realized by a standard probe micromanipulator and a linear sweep voltammetry (LSV) was carried out. A linear potential ramp was applied spanning from 0 V to -0,9 V vs Ag(s). The electrowetting onset occurred at -0,6 V in agreement with the CV of the SAM (Figure 2.10). As consequence of that, the spreading of the aqueous solution was clearly observed due to the formation of the anthrahydroquinone form. At this point a benchmark test was performed using a bare ITO electrode instead of the functionalized one. The same potential ramp used before was applied but no observable spreading of the water drop occurred. This cross-check enabled us to exclude any possible influence of the ITO polarization, confirming that in the potential window used the difference in surface energy came exclusively from the redox reaction.

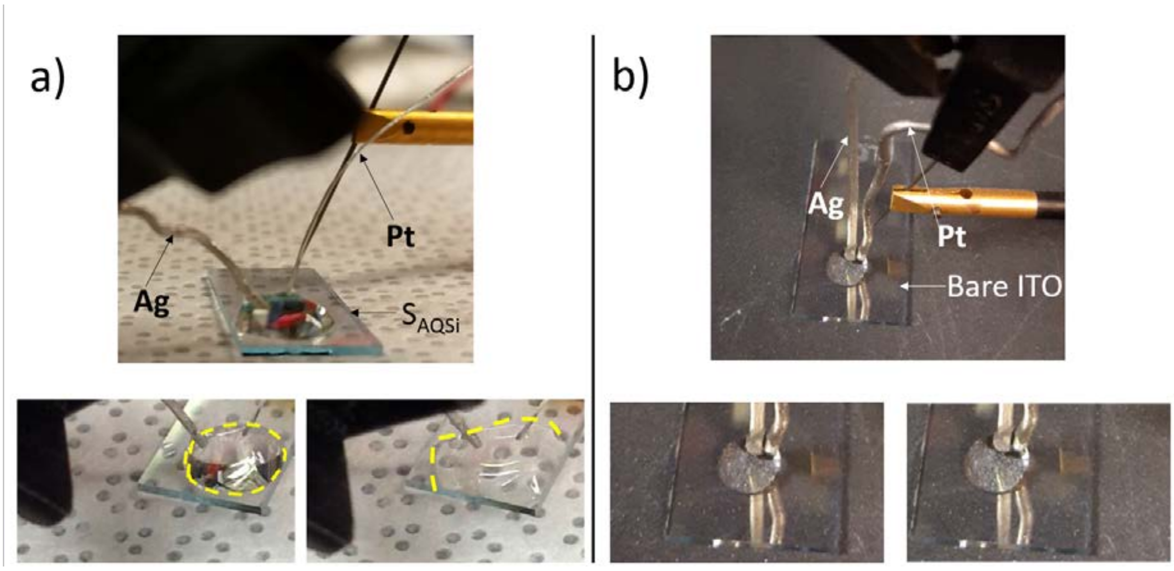

Figure 2.23: Initial (bottom left) and final (bottom right) state of the electrowetting onto a) AQSi-coated ITO and b) bare ITO. A dotted line has been drawn to mark the drop edges for clarity.

These first experiments do not move the droplet in a specific direction, because a sole SAM-coated electrode was conceived and, as consequence of that, when the reduction occurs the water spreads everywhere on the substrate.

In order to drive preferentially a water droplet towards a specific direction and so obtain a real water actuation, a more complex array of electrodes is required. The engineering of the system is fundamental to achieve more complex operations such as droplet water mixing, splitting and promoting directional flow.

2.5.3 Water actuation on planar electrodes

Different electrode arrays configurations were realized, according to the specific water actuation we wanted to obtain. All the electrodes were fabricated through a photolithographic process which is a high precision process used in microfabrication to pattern parts of a thin film or the bulk of a substrate. The steps involved in the followed photolithographic process can be resumed in:

1) Substrate preparation: it is intended to improve the adhesion of the photoresist material to the substrate. ITO-coated glass slides were firstly rinsed with HPLC pure grade acetone and isopropanol, and afterwards dried with a nitrogen stream.

2) Photoresist application: the photoresist, that is a light-sensitive material, was spin coated on the substrate. Specifically, the positive S1813 photoresist was spin-coated fixing the spinning speed at 4000 rpm and the spinning acceleration at 5700 rpm/s. After the deposition, soft-baking was needed to remove almost all of the solvents from the

photoresist coating. Soft-baking plays a very critical role in photo-imaging since the photoresist coatings become photosensitive only after this step. Hence, the substrates were annealed on a hot-plate at 100 °C for 60 s.

3) Exposure and development: the positive photoresist was exposed to the UV light. The electrode pattern, designed using computer aided design (CAD), were applied to the photoresist film using a laser-assisted writer (Durham magneto-optics, λ = 405 nm). As a consequence of the light exposure the photoresist changes its chemical structure becoming more soluble in the developer. The exposed resist was then washed away by the developer solution first (MF319 developer for 60 s) and then by ultrapure water, leaving windows of the bare underlying material. These are the steps where the pattern was effectively printed to the substrate.

4) Hetching: after the pattern was lithographically printed into the photoresist, it was transferred into the substrate. Hence, an acidic etching (namely HCl 32% v/v for 10 min) of the uncoated ITO was performed to define the designed electrodes.

5) Photoresist removal: when the etching was completed, the resist was finally removed by rinsing with acetone and isopropanol. Hence, the final pattern was achieved.

In Figure 2.24 a schematic representation of the photolithographic steps listed above is shown . In our case, the whole photolitographic protocol was carried out in a 10000 class cleanroom.

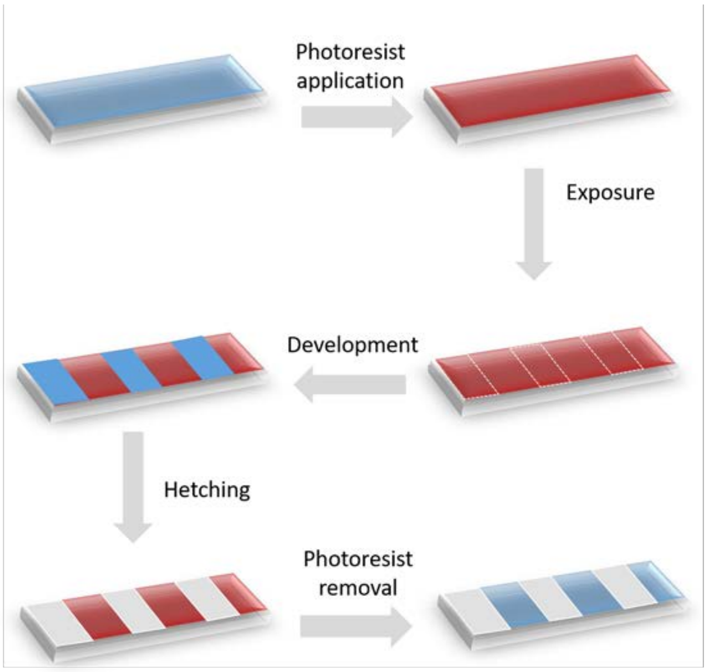

Figure 2.24: Schematic representation of the photolitography process used.

The simplest electrodes configuration used to achieve preferential motion of the aqueous droplets, consisted in two planar macro-electrodes (with an area equal to 12.5 mm^2) separated by a distance of 50 μm.

Both electrodes were functionalized with AQSi. Then, 20 μL of an aqueous electrolyte droplet (i.e. phosphate buffer solution pH~ 6,9) was located between the two, providing electric connection. In this configuration, the application of a voltage difference between the electrodes would promote the reduction of the AQSi molecules only on the negatively biased electrode. This would create a surface tension gradient that could provoke the droplet movement as illustrated in Figure 2.25.

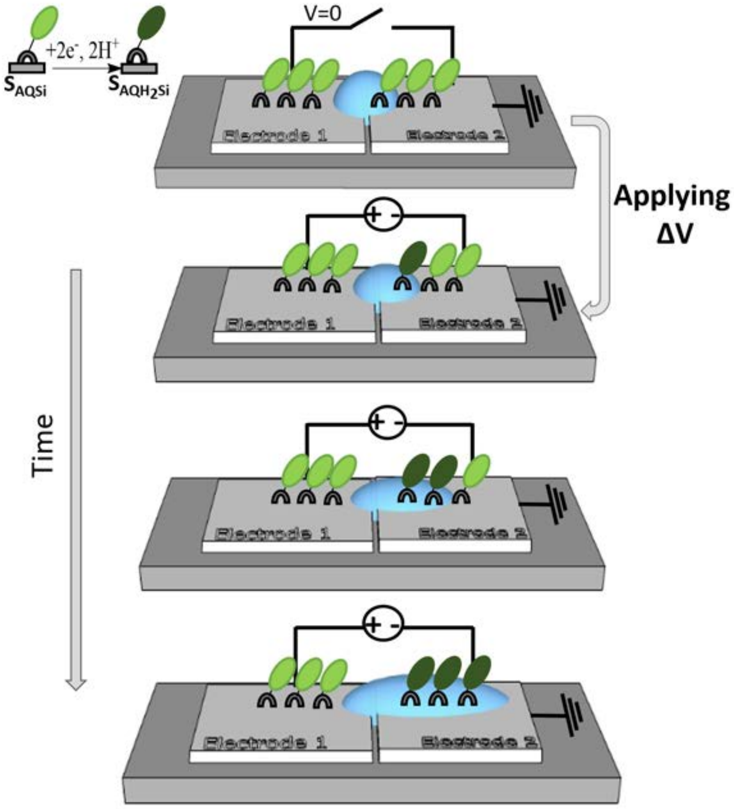

Figure 2.25: Schematic representation of the directional water actuation on two modified ITO electrodes.

Thus, a potential difference between 2,0 and 2,2 V was applied. As a consequence of that, the droplet located between the two electrodes moved towards the direction where the AQSi molecules were reduced to AQH$_2$Si (Figure 2.26). It should be noted that, while in the first electrowetting studies described in Section2.5.2, the electrical bias required to spread the droplet coincides with the potential value at which the reduction of the AQ group takes place in S$_{AQSi}$ (-0,6 V vs Ag)), in agreement with the CV measurements, here the voltage required to obtain the droplet motion is higher. The reason of this is the partial lose in the voltage control in the aqueous droplet due to the absence of a reference electrode. But importantly, the required voltage is still lower compared to the typical voltages used in EWOD systems [145] and, hence, S_{AQSi} SAM is undoubtedly attractive aiming at the fabrication of a low-power and disposable technology.

To confirm that the water actuation is exclusively related to the electrochemistry of the SAM, a reference test was performed. Thus, the same planar configuration was tested by using the non electroactive molecule 10-undecenyltrichlorosilane (UTCS) self-assembled on ITO (S_{UTCS}). This SAM was prepared following the conditions reported in Table 2.4.

Table 2.4: Conditions used for the fabrication of S_{UTCS}

Substrate	SAM	Solution	Immersion Time
ITO	S_{UTCS}	1 mM of UTCS in toluene	1h

This inert SAM provides a surface passivation and, as consequence, the application of a bias ranging from 2,0 V to 2,2 V between the two electrodes, did not result in the droplet movement (Figure 2.26). Thus, this experiment unambiguously proved that the capacitive processes are irrelevant for driving the aqueous droplets in the potential window used and it provides clearly all the evidences that the efficient actuation comes from the electrochemical switching properties of the anthraquinone derivative SAM.

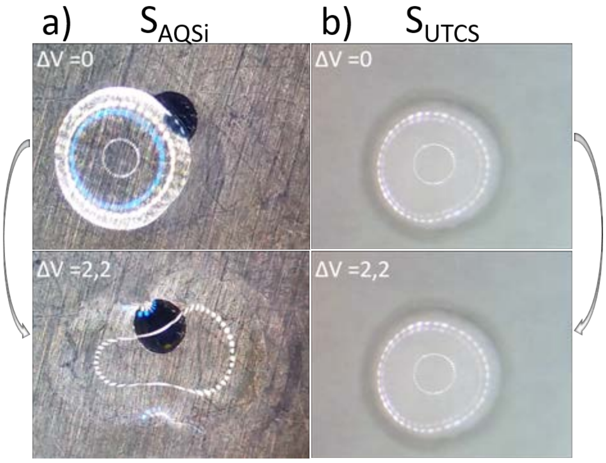

Figure 2.26: Optical images of an aqueous droplet deposited on a) S_{AQSi} and b) S_{UTCS} modified coplanar ITO electrodes, before (top images) and after (bottom images) the application of a potential difference of 2,2 V.

With the goal of achieving more complex actuations such as droplets merging, which is one of the basic actuations demanded for digital μ-fluidics, an array of three coplanar

ITO electrodes (E1, E2 and E3) was designed (Figure 2.27 a)). As usual, the electrodes were functionalized with AQSi and two buffer droplets were placed between them ensuring the closure of the electric circuit. This time, two well-known dyes, fluorescein and rhodamine, were added in the electrolyte solution in order to better visualize the droplet motion. E2 was grounded and a voltage equal to 2,2 V was applied to E1 and E3. Accordingly, E2 is the negative pole wherein AQH_2 is formed yielding a gradient of surface tension responsible for the droplets merging (Figure 2.27 b)). The threshold voltage for causing the droplets movement is 2,2 V, however, applying a slight higher bias such as 2,8 V, a faster water actuation is favored. Importantly, this experiment proves that the use of S_{AQSi} can be exploited to promote droplets merging, and we think that a proper engineering would permit the system to be able to carry out other operations as well.

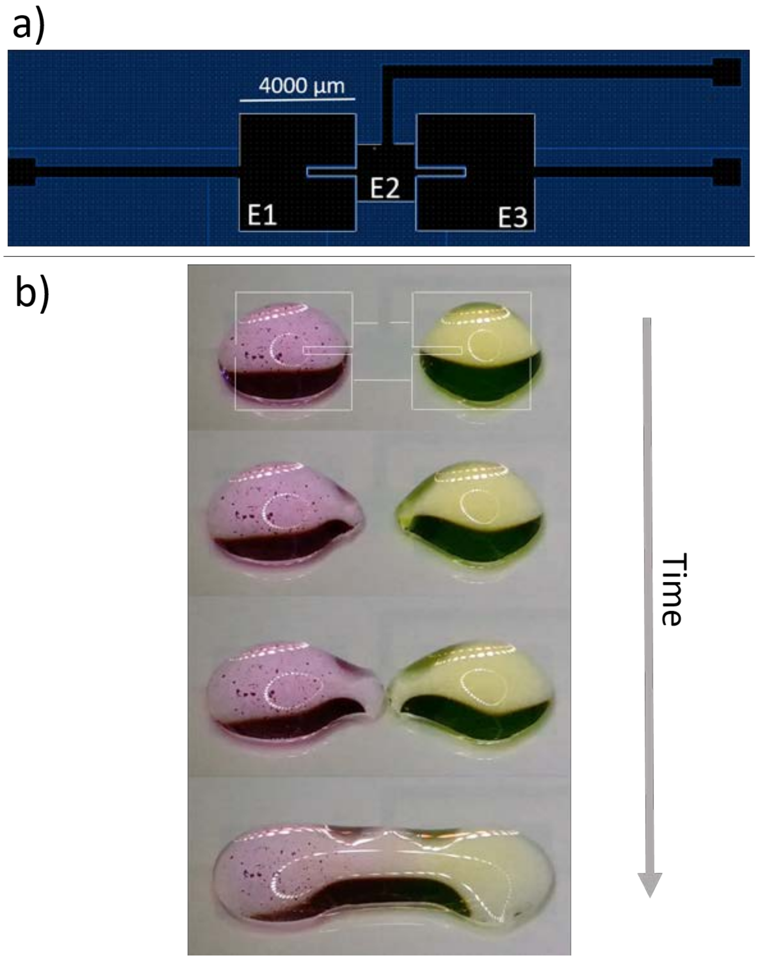

Figure 2.27: a) CAD drawing of the three-electrode array. b) Snapshots of the droplet merging when a voltage was applied between E1-E2 and E3-E2 (E2 was grounded).

Until now, we realized a system able to act as water actuator in a non controlled environment. It means that due to the dynamic equilibrium at the water/air interface, the droplet is subjected to water evaporation and small volumes cannot be managed. In addition, the system is clearly exposed to adventitious contamination.

Aiming at bio-applications, it is required an overall miniaturization of the system due to the need of using small volumes of biological samples and, of course, one of the central points is focused on avoiding possible contamination. For this reason, the next step was to design and fabricate a full-standing and compact chip encapsulated into a microfluidic system capable to manage few micro-liters of solution in a protected environment.

2.5.4 Integration of S_{AQSi} in microfluidic chips

In order to push the water actuator system through high technological and biological applications, it was endowed with a microfluidic chip. In such a way, the controlled environment was ensured avoiding the water evaporation and limiting the contamination with external agents. The design and the fabrication of the microfluidic chips were realized within the framework of a collaboration with the company Scriba Nanotechnology s.p.a. in Bologna (Italy).

The microfluidic chips are composed by a bottom and a top part. The bottom part was always a double-sided adhesive (90 µm thick) stuck onto the modified glass-coated ITO electrodes (Figure 2.28 a)). It defines the nominal volume of the micro-channels and their geometry. Different double-sided adhesive patterns were designed using CAD, according to the different channel geometries chosen. Then the designs were transferred to the adhesive by means of IR laser writer provided by Scriba Nanotechnology.

The top part of the microfluidic devices assures the controlled environment and a proper reservoir for the aqueous droplet. Two different materials were used to fabricate the top part, deriving in two typologies of microfluidic chips:

1) Polypropylene (90 µm thick). The shape of polypropylene was realized thermoforming the thermoplastic polymer by an hydraulic pump using a steel stencil designed by the IR laser writer (Figure 2.28 b)). That microfluidic ensures a complete isolation of the entire electrodes from the external environment.

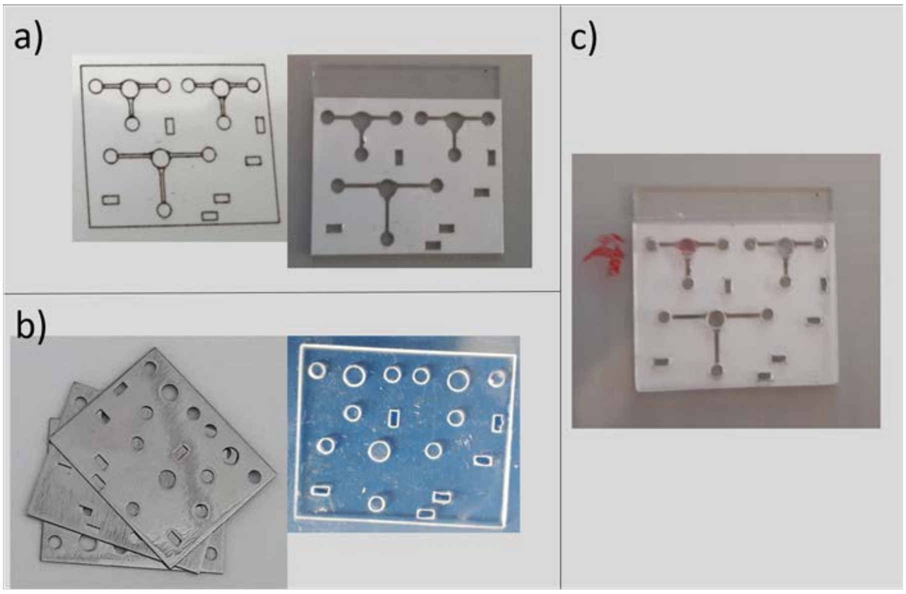

Figure 2.28: a) Double-sided adhesive freshly cut by IR-laser (on the right) and stuck onto the ITO modified electrode (on the left). b) Steel stencil used to thermoform the polypropylene sheet (on the right) and the thermoformed polypropylene sheets (on the left). c) Final microfluidic device, the micro-channels realized feature the following sizes: width 400 µm and length 4800/6800 µm.

2) Polyethylene terephthalate (PET) (7 µm thick) (Figure 2.29). In this case only the channels were protected from the external environment while the reservoir was a hole in the PET sheet fabricated with the IR laser writer.

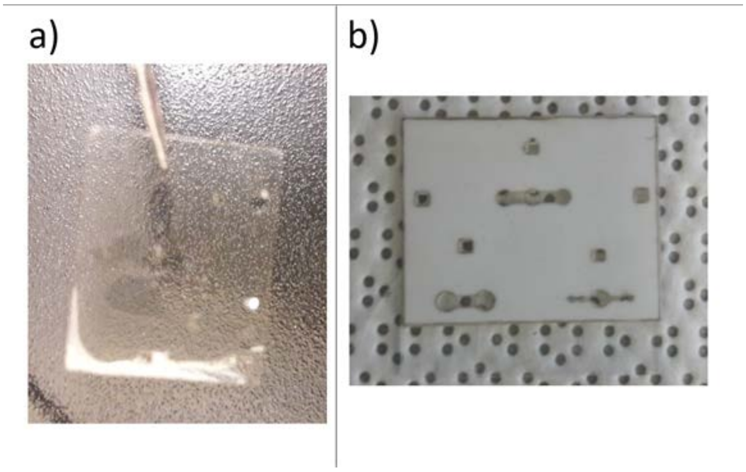

Figure 2.29: a) PET sheet used as top part of the microfluidic device. b) Final microfluidic device used.

The SAM-guided motion was verified again in the microfluidic chips where an increased friction into the micro-channels takes place due to the presence of the top part of the microfluidics devices. In particular the water actuation was tested moving the fluid towards one particular direction in the chips having the thermoformed polypropylene as top part. These devices are able to manage up to 10 µL of solution. Hence, two different microfluidic layouts that stand on the same electrode configuration were used. This unique electrode configuration is shown in Figure 2.30 and consists of four planar electrodes (i.e. E1, E2, E3, E4) separated each other by a distance of 50 µm. In the first geometry (see Figure 2.31 a)) three linear channels leave the central pool where the aqueous solution is located. Hence, by applying a voltage between the central electrode (E1) and one of the outer ones the liquid movement towards the selected outer channel was achieved (E3 in Figure 2.31 a)).

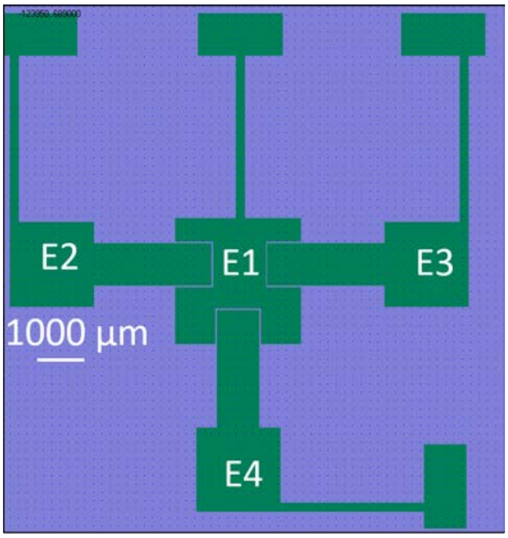

Figure 2.30: a) CAD drawing of the electrode array used to perform preferential water movement.

In the second layout the fluidic channel featured two sharp turns, with change of direction of the flow streamlines (Figure 2.31 b)). This new design forces the water flow along a contourted path, which could hamper it since the liquid could deviate along these additional paths. By applying a voltage between the electrodes E1 and E2, the water droplet was successfully guided towards the desired direction. This proves that the chip shows a higher control on the water motion with respect to a standard microfluidic system connected to a peristaltic pump.

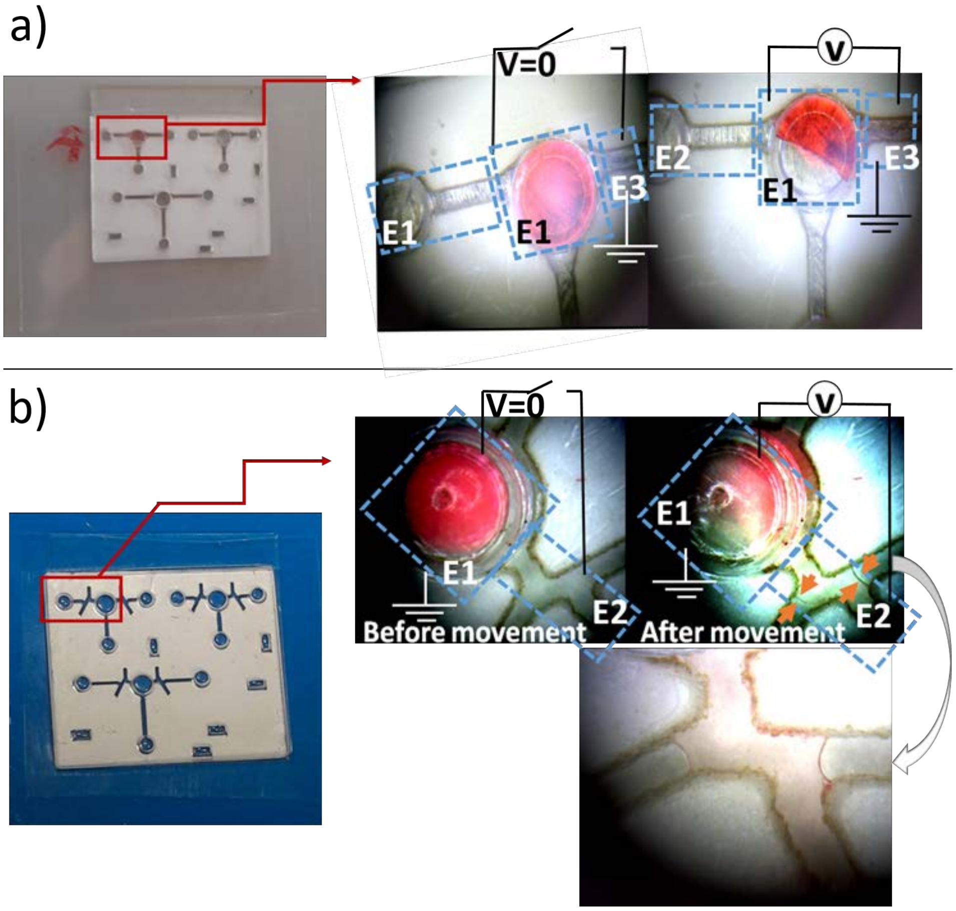

Figure 2.31: Pictures of the chips employed to achieve preferential water movement. Optical image of a) the SAM-guided droplet motion and b) the contorted flow along a contourted path. The orange arrows define the edge of the water droplet that coincides with the border of the electrode.

Also droplet mixing and splitting were performed in the microfluidics devices. For this kind of experiments two microfluidic chips, with PET as top part, were used. For splitting as well as for merging droplets, three planar electrodes were employed modulating their relative area according to the specific operation (Figure 2.32). In particular E1 was scaled down in the case of splitting (Figure 2.32 a)), in order to drive the water movement towards the outer electrodes on which the formation of AQH_2Si species will be promoted.

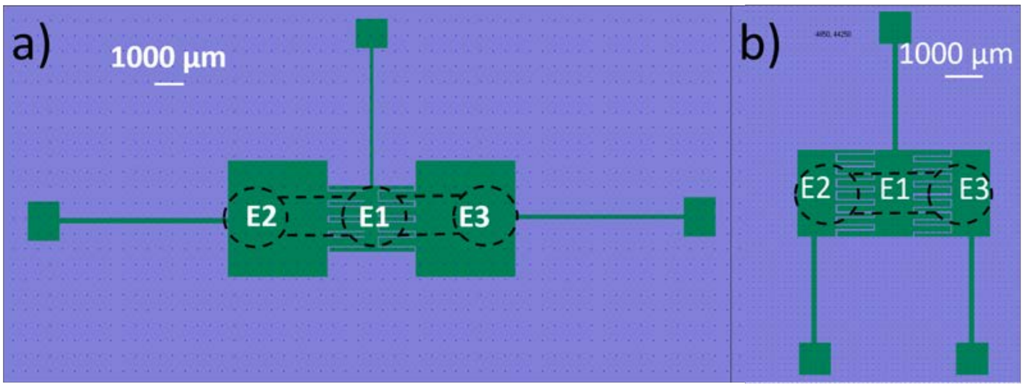

Figure 2.32: CAD drawing of the electrode array used to perform droplet a) splitting and b) mixing. Dotted lines: projection of the microfluidic channels used for these operations

The layout of the microfluidic channels used for this operation is shown in Figure 2.33 a) and consists in a central hole connecting two channels facing each other. The droplet deposited on E1 was simultaneously moved towards E2 and E3 applying a negative potential on them. Nevertheless, a residual droplet remains on E1, preventing it from drying completely. This problem can be addressed to the low hydrophobicyty of the SAQSi.

In the chip dedicated to the droplet merging the three electrodes have the same dimensions (Figure 2.32 b)) and a central channel connecting two outer holes is used as microfluidic lay out (Figure 2.33 b)). The experiment of mixing was successfully reached, applying a positive bias on E2 and E3 while keeping E1 grounded.

Importantly, this approach to fabricate microfluidics is versatile and transferable to many applications since the electrodes design can be easily modified in order to achieve more complex and different operations.

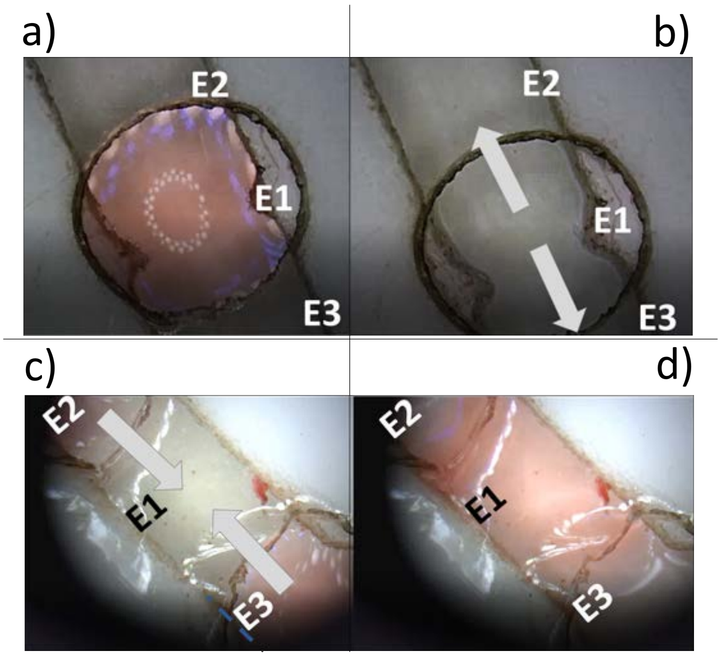

Figure 2.33: Optical images of the chips used to perform splitting and mixing operations a) before and b) after splitting; c) before and d) after mixing droplets.

2.5.5 Preliminary studies with cells

The successful implementation of our system in microfluidics devices prompted us to explore its application for a relevant actuation in biology. For this reason, we aimed at moving a medium containing cells instead of a simple electrolytic solution.

The cells line that was employed in this experiment is the NIH-3T3/green fluorescent protein (GFT) mouse embryonic fibroblast. The NIH-3T3 cells were purchased from Cell Biolabs and were cultured in Dulbecco's modified eagle medium (DMEM), supplemented with 10% (v/v) fetal bovine serum, 2 mM L-glutamine, 100 IU/mL penicillin and 100 mg/mL streptomycin. The cell line was maintained in standard culture conditions (37°C in a humidified atmosphere with 5% CO_2) and were periodically sub-cultured using Trypsin-EDTA solution 0,25% for detachment process.

Firstly, we performed preliminary test in order to ensure the biocompatibility of the system. Hence, the cell adhesion on chip for in vitro study was tested. We seed NIH-3T3 cells in complete medium (pH 7,4) with a broad range of concentrations, from 2500 to 10000 cells/cm^2, and with different incubation times of 5 min, 15 min, 6 h and 24 h. After 24 h, we observed that the cells remain attached to the device while retaining the morphology of fibroblasts. This result demonstrates that the SAM-coated substrate is not affecting the cells viability.

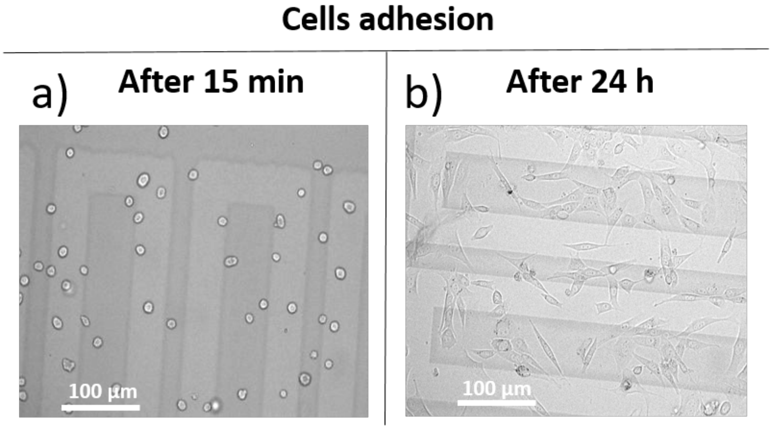

Figure 2.34: Cells in the microfluidics chip after a) 15 min and b) 24 h.

After that, liquid motion of the droplet containing cells was performed using the microfluidics array shown in Figure 2.35 and was followed by optical and fluorescence microscopy. When the usual appropriate voltage was applied, the actuation successfully occurred. The cells moved from the reservoir 1 to the channel until reaching the other reservoir localized in the opposite site of the channel. Furthermore, no differences were observed in velocity compared to the liquid without the presence of cells. Although viability and adhesion are rough proofs of the effective state of the cell health, they were conceived as preliminary tests that need to be implemented with further proofs of biocompatibility after the actuation, such as information on DNA damages, stress responses, etc. Remarkably, it has to be noted that the low range of potential required for the droplet actuation makes the system very compatible to cell culturing protocols. Furthermore, the voltage experimented by the cells during the actuation is always less than the applied one, indeed electrolysis of water is never observed. Within this view, the effective gradient of cells from the starting well up to the micro-channel can be safely assumed as a proof-of-principle of our chip efficiency. The use of electrochemically active SAM turns out to be a promising approach for a controlled cell migration, which is fundamental to many physiological processes, such as regeneration, tissue repair and protective immunity.

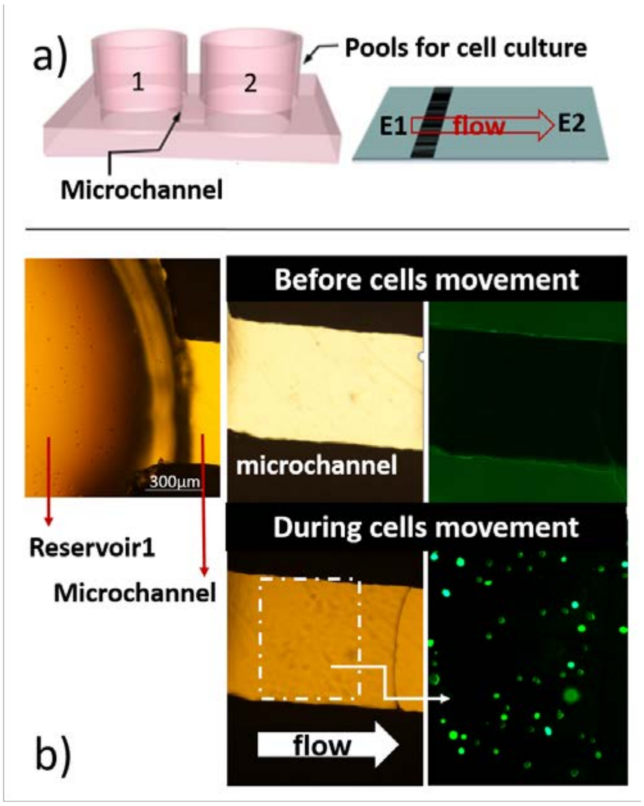

Figure 2.35: a) Microfluidic device used for cells manipulation. b) Movement of cells in the culture medium from one to the other reservoir upon the application of the electrowetting potential.

2.5.6 Summary

In summary, the electrowetting properties of AQSi based SAMs on ITO were successfully implemented into a micro-electromechanical system (MEMS). The two-proton two-electron redox reaction associated to the AQ core of the molecule functionalizing the ITO electrodes, is demonstrated to be the effective driving force for water actuation. The system we realized is based in switchable electrodes that can be easily subjected to further modification, reaching complex and technological targets required in the field of digital microfluidics. Further, we demonstrated that they can be successfully miniaturized and endowed with a microfluidic system. These smart electrodes reveal important figure of merits, such as transparency, robustness and biocompatibility. Importantly, the driving voltages they need to actuate are lower than the best digital microfluidics based on standard dielectrics. Thus, the functionalization of ITO-based chips with electroactive molecules constitute a promising platform to be implemented in digital microfluidics as an alternative option to conventional pumping systems or to EWOD-based devices composed of standard plastic dielectrics. Furthermore, the efficient actuation of cells medium makes our technology extremely promising towards bio-applications.

2.6 Integration of a Fc SAM in field effect transistors based on MoS_2 monolayer[3]

2.6.1 2D MoS_2 Semiconductor

Molybdenum disulfide (MoS_2) monolayer is an atomically thin semiconductor from the family of transition metal dichalcogenides (TMDCs). The basic unit of MoS_2 is composed of a molybdenum atom coordinated with six sulfur atoms. Each molybdenum atom is sandwiched between two sulfur atoms giving rise to an extraordinary thin material of only 6.5 Å that belongs to the large family of new 2D materials (Figure 2.36 a)). TMDCs 2D semiconductors have been subject of many research efforts within the last 5 years, principally thanks to their direct banding gap sizable between 1 and 3 eV, their high charge mobility (up to 100 $cm^2\ V^{-1}\ s^{-1}$) and their good mechanical flexibility. All these characteristics make them attractive for applications in the field of (opto)electronics and for sensor applications [147, 148]. Particularly, MoS_2 is the most investigated among all the 2D TMCDs, being the first one to be used as active layer in electronic switches and optoelectronic devices, such as solar cells [149].

The most commonly used production methods for MoS_2 monolayers are chemical vapor deposition (CVD) and mechanical exfoliation of the layered bulk material (Figure 2.36 b)) [150, 151, 152, 153]. Sputter growth atomic layer deposition [154] (ALD) of the precursor MoO_3 and subsequent conversion to the disulfide under reducing conditions and high temperature [155], as well as ALD process using H_2S and $MoCl_5$ or $Mo(CO)_6$ are others possibilities to prepare MoS_2 monolayers [156, 157] .

---

[3] This work was done in the framework of a secondment at University of Strasboug (France) in the group of Prof. Paolo Samorì at the Institut de Science et d'Ingénierie Supramoléculaires (ISIS) in collaboration with Dr. Simone Bertolazzi.

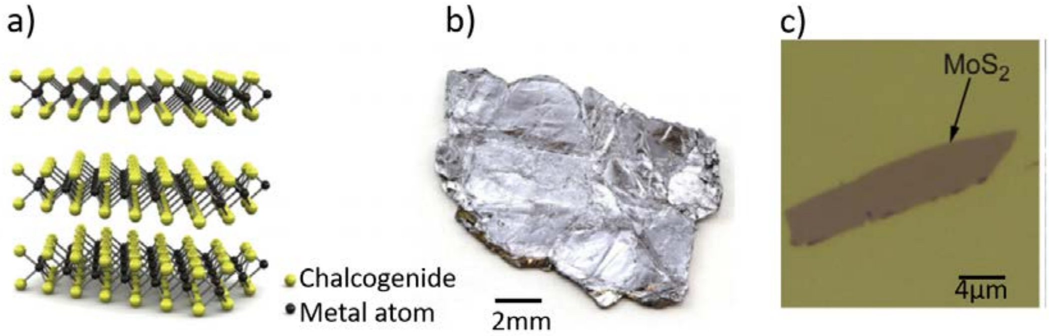

Figure 2.36: a) Schematic representation of the structure of a transition metal dichalcogenide material (TMDCs). b) Photograph of a bulk crystal of MoS_2 that can be used as a starting material for the exfoliation of single layers. c) Optical image of a monolayer of MoS_2 deposited on a SiO_2 surface [158].

The monolayers synthesized by each one of the possible fabrication methodologies lack of atomic perfection, even if in general the mechanical exfoliation approach using bulk MoS_2 can produce high-quality MoS_2 sheets with minimal defects [159]. The most common defects in this material are sulfur vacancies. Eliminating or at least reducing the adverse effect of such defects is imperative to improve the optoelectronics and conductive properties of MoS_2 . In fact, these defects are the major traps or scattering centers of charge carriers, leading to a relatively low mobility and low current level in field effect transistors (FETs) [160]. Thus, to mitigate the adverse effect of defects different strategies have been investigated within the last years, including exposure of MoS_2 to superacids or, more recently, exposure to thiols [161]. On the other hand, it must be considered that defects can provide new opportunities to tailor the physical and chemical properties of MoS_2 [162]. In general, if the MoS_2 sheets are free of dangling bonds it is difficult to attach functional molecules on their surfaces. However, sulfur-containing groups can be bonded to sulfur vacancies in MoS_2 [163]. So, such defects can also represent a good opportunity to greatly enhance the catalytic activity of MoS_2 for hydrogen evolution reaction, as already proved [164], or in view of possible applications in electronics devices, such as chemical (bio)sensors [165, 166, 167]. For this reason various approaches for modulating the density of sulfur vacancies have been reported in literature, namely electron irradiation, thermal annealing, plasma treatment, as well as bombardment with charged particles [168].

There are many works focused on introducing and repairing sulfur vacancies in few multilayer or even in monolayers of MoS_2 [161, 169]. Dong Min Sim et al. showed that the vacancy sites of 4-layers of MoS2 channel in FET can be artificially created by thermal annealing and can act as the binding sites for thiol-terminated molecules [170]. They showed that thiol-based organic molecules can be selectively chemisorbed and tightly bound on sulfur vacancies via the strong interaction between the thiol and the S-vacancy. They also studied how such thiolated molecules actually provide a surface charge transfer doping that affects the performance of the FET devices.

More recently, Bertolazzi et al. reported a systematic study concerning the measurement of critical field-effect devices parameters as function of sulfur-vacancy density in monolayer MoS_2 sheets serving as channel material in back-gated FETs [171]. Low-energy Ar-ion bombardment was used to introduce in a controlled way the sulfur vacancies. Hence, the changes in the electrical characteristics of the FETs were directly correlated to a well defined amount of sulfur vacancies (V_S) in the MoS_2 sheet. They demonstrated that the electron field-effect mobility μ_{FE} decreases as $1/V_S{}^2$ with increasing the density of vacancies up to V_S = 5%. Moreover, for V_S > 20% the transistor showed ambipolar behavior. Furthermore, they demonstrated that the electrical properties can be largely recovered by exposing the ion-irradiated devices to vapor of thiolated molecules such as butanethiols, confirming the previous results on chemisorption of thiols at sulfur vacancies [172].

Considering this background, we decided to investigate for the first time the possibility to functionalize sulfur vacancies previously introduced in a MoS_2 monolayer by treating it with an electroactive thiolated molecules (i.e., FcC_6) for two main purposes. Firstly, performing liquid gated FET measurements, we wanted to exploit the electrochemical behavior of the molecules that stay on the MoS_2 sheet to give a direct prove of the chemical functionalization of the sulfur vacancies. This result could open the way towards many interesting opportunities in the field of sensors. Secondly, we were interested in verifying if the electrochemical switch that Fc exhibits on the 2D semiconductor layer has some influence on the performance of the device.

It is important to underline here the reasons why the thiolated ferrocene derivative FcC_6 has been chosen for that kind of investigation. The complexity of the system is remarkable and at list three different aspects should be taken in consideration:

1) The molecule must be able to repair the sulfur vacancies without establish “parasite interactions” with the monolayer of MoS_2. Planar electroactive molecules such as tetracyanoethylene, tetrathiafulvalene, tetracyanoquinodimethane can be absorbed on the basal plane of MoS_2 thanks to non-covalent weak interactions with MoS_2 layers [173, 174].

2) The electrochemical behavior of the molecule has to be as simple and reproducible as possible. Furthermore, the molecule must be able to be reduced/oxidized in ionic

liquid (IL), that is an unconventional electrolyte for studies of electrochemical switch but useful for liquid gated FETs. The electrochemical behavior of ferrocene is little influenced by solvents and has been already reported in ionic liquid [50, 175].

3) Finally, the length of the spacer group that separates the electroactive core from the thiol terminal group, should not hinder the functionalization of the MoS_2 vacancies. Since the most used molecule in processes of sulfur vacancies repair is butanethiol, we chose an electroactive thiolated derivative having a backbone of six carbon atom, comparable with the four carbons backbone of a butanethiol.

2.6.2 Design, fabrication and functionalization of MoS_2 monolayers based FETs

The MoS_2 monolayers were grown on thermally oxidized heavily n-doped silicon substrates by mechanical exfoliation from commercially available molybdenite crystals and were identified by combination of optical and AFM microscopy (Figure 2.37), Raman and Photoluminescence (PL) spectroscopy.

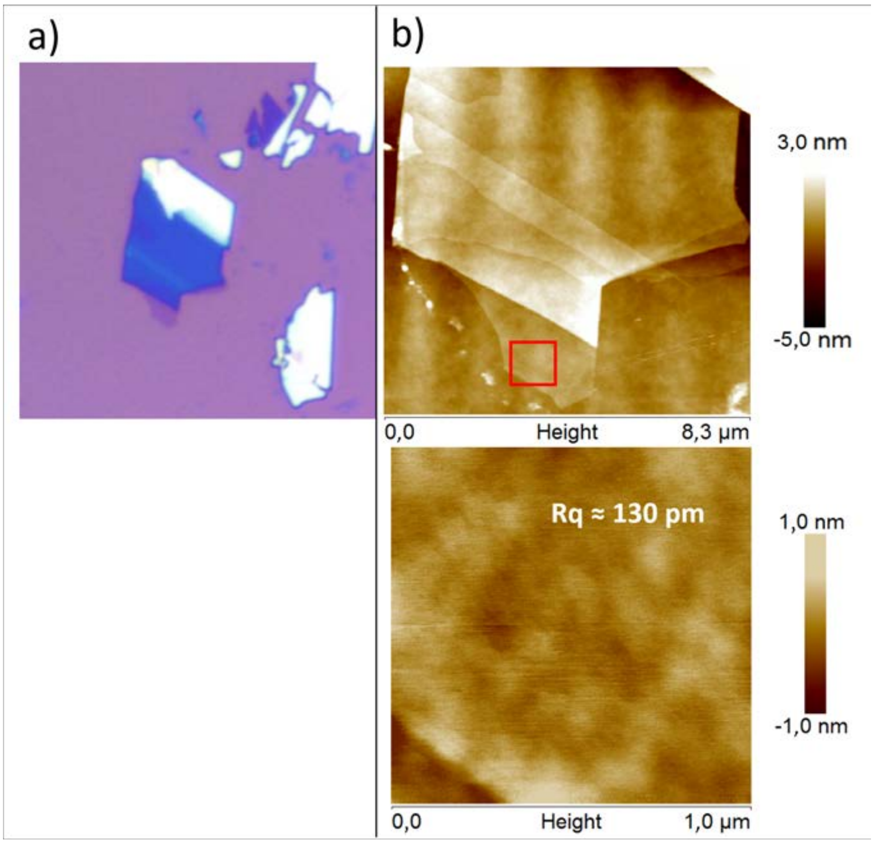

Figure 2.37: Optical and AFM images of a flake of MoS_2.

Then the electrodes were designed in order to contact the single layer of MoS_2, using CAD. The electrodes were transferred to the substrate by means e-beam lithography using as a resist a double-layer of polymethyl methacrylate. Subsequently, thermal evaporation of gold and lifting off in warm acetone concluded the fabrication step. LiF was deposited on the electrodes in order to avoid the deposition of thiolated molecules on gold during the process of functionalization (Figure 2.38).

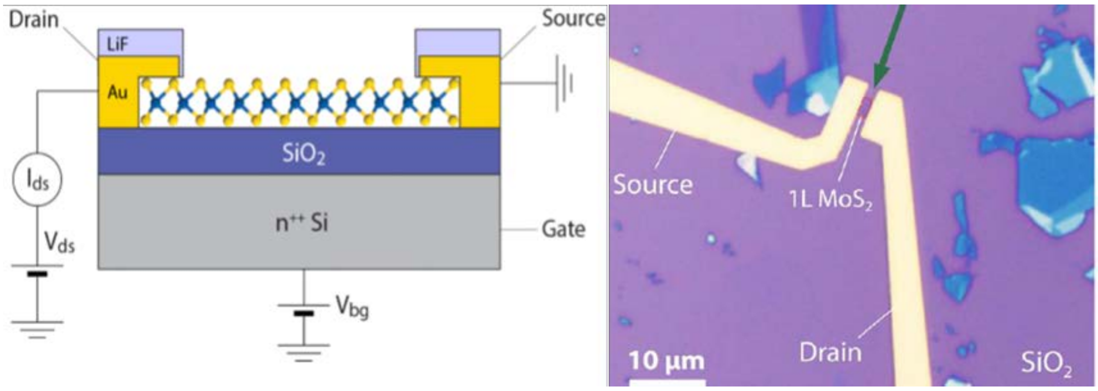

Figure 2.38: Schematic representation of the geometry of the devices (left) and optical image (right) of MoS_2 based FETs.

The device was subjected to ion bombardment with Ar-ion in order to introduce a density of vacancies equal to 3%. The bombardment was performed using a Thermo Fisher EX06 ion gun with acceleration voltage of 500 V. The angle between the ion beam and the substrate surface normal was around 58º.

Finally the MoS_2 vacancies were functionalized with FcC_6 molecules. A solution 0,1 mM of FcC_6 in dry toluene was prepared and heated at 70º C for 10 minutes. Then the freshly bombarded substrates were immersed into the solution and were left for 1 h at 70º C and them kept at room temperature overnight.

The day after the substrates were washed by immersion in three different beakers containing 20 mL of dry toluene each one. Subsequent washings were carried out by spin washing with other 40 mL more of dry toluene and, finally, the substrates were dried by spin-drying. The entire process was carried out in a glove box, under strictly protected atmosphere.

The MoS_2 flakes were characterized by Raman and photoluminescence (PL) spectroscopy before and after the functionalization. As it is possible to observe in Figure 2.39 both A and B exciton peaks of the PL spectra have a red shift after the functionalization. Furthermore, the broad peak around 1,75 eV associated to the disorder decreases, while the A an B peaks increase after the functionalization. The Raman spectra show a damping of the disorder-activated side bands together with a red shift of the A'$_1$ peak, consistent with the reduction of the sulfur vacancies. These results are in agreement with the data reported in literature for analogous systems [171].

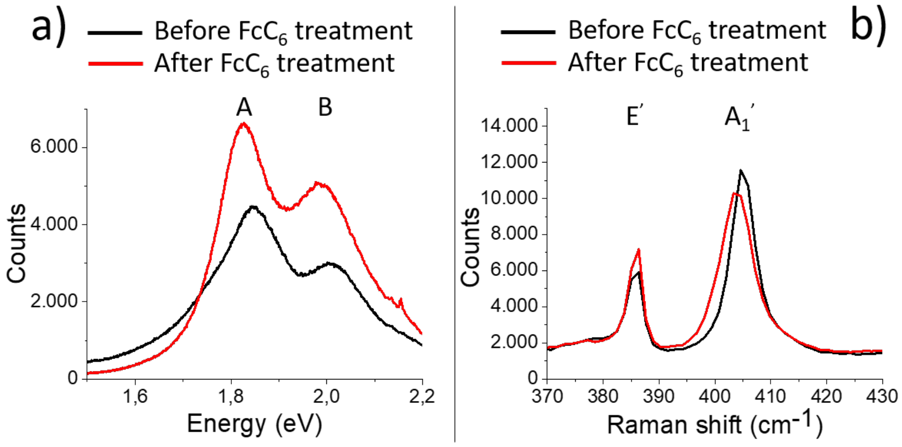

Figure 2.39: a) PL and b) Raman characterization of MoS_2 flakes before and after the functionalization with FcC_6 molecules.

The devices characteristics were also registered before and after the bombardment with heavy atoms and after the treatment with FcC_6 molecules.

Figure 2.40 portrays the drain–source current (I_{ds}) versus gate voltage (V_g) transfer characteristics of a typical monolayer MoS_2 FET that underwent the ion-bombardment procedure. After irradiating the device (blue curve) the mobility (μ) drops from ≈ 26 cm^2 V^{-1} s^{-1} to ≈ 0,0096 cm^2 V^{-1} s^{-1}, while the threshold voltage shifts towards positive values (from -38 V to 48 V). Defect states are responsible for reducing the fraction of mobile carriers in the conduction band; at the same time they increase the fraction of trapped carriers that do not contribute to charge transport, resulting in a degraded effective mobility [176]. As previously reported, the sulfur vacancies act as trap states [177].

After measuring the influence of ion-beam induced sulfur vacancies on the electrical transport properties of MoS_2 monolayer , we explored the possibility of performing a chemical treatment with FcC_6 molecules to repair these defects. We found that the treatment enhanced the I_{ON}/I_{OFF} ratio from ≈1,9 x 10^3 to ≈ 2,2 x 10^5 and the field-effect mobility from ≈ 0,0096 to ≈ 0,19 cm^2 V^{-1} s^{-1}. So even if the current was not entirely recovered after the treatment with the thiolated ferrocene FcC_6, a great improvement of the bombarded devices was observed and can be read as a clear proof of an effective coverage of the sulfur vacancies. To be sure that the effect was related to the use of the FcC_6 molecules, a blank test was performed immersing the devices in pure toluene instead of the solution of FcC_6 in toluene. As a result, no changes were registered in the tranfer characteristics of the device that were the same after the bombardment and after the toluene treatment, confirming that the thiolated molecules play an effective role on the repairing process.

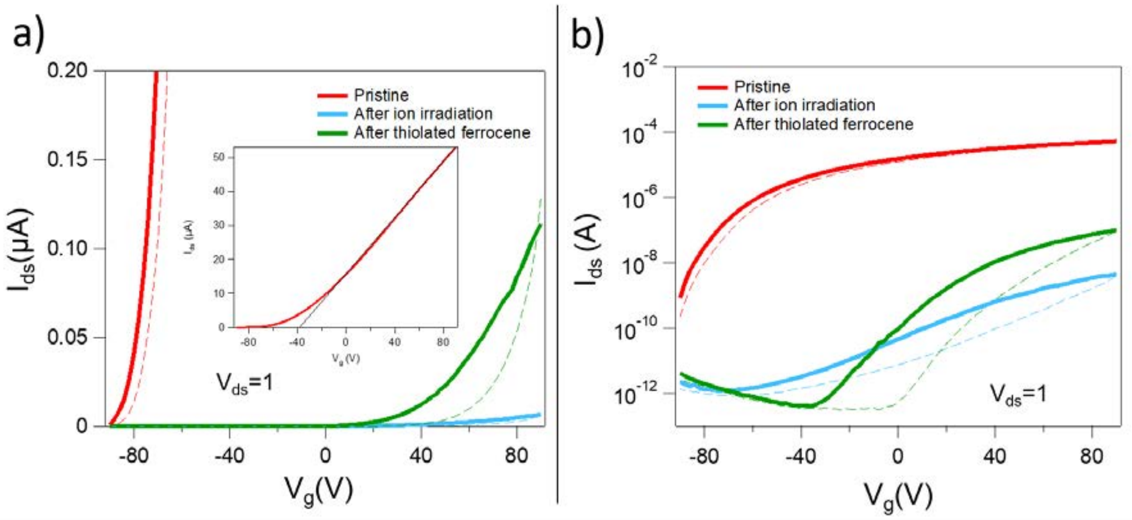

Figure 2.40: Transfer characteristics of MoS_2 based FET in a) lin-lin and b) log-lin scale at V_{ds} of 1V. Inset: transfer characteristic of the pristine MoS_2based FET.

2.6.3 Liquid ionic gated FETs

The last step was to test the system in ionic liquid (IL) gated FET conditions.

Ionic liquids are salts in which the ions are poorly coordinated, which results in being liquid below 100°C, or even at room temperature. In ILs at least one ion has a delocalized charge and one component is organic, which prevents the formation of a stable crystal lattice. The composition and associated properties of ILs depend on the cation and anion combinations. The methylimidazolium and pyridinium ions have proven to be good starting points for the development of ILs, but there are literally billions of different structures that may form an ionic liquid [178, 179]. ILs are described as having many potential applications that come from their physical properties: high thermal stability, high electrical conductivity and a large electrochemical window, which means a huge voltage range within they are inert towards electrochemical oxidation and reduction. Hence ILs show a wide range of applicability in the electronic/electrochemical field as electrolyte media [180, 181].

In the area of optoelectronics based on MoS_2 material, IL-gating has been used to improve the device performances and modulate the photoluminescence efficiency and photocurrent of monolayer MoS_2 flakes passivating the surface states and trapping charges that act as recombination centers [182]. In particular, transport measurements of IL-gated field-effect transistors consisting of few-layer MoS_2 indicate that the electron mobility in IL-gated devices exceeds significantly that of comparable back-gated devices. The observed performance enhancement, specifically the increased charged carrier mobility has been related to the reduction of the Schottky barrier at the source and drain electrode by band bending caused by the ultrathin IL dielectric double layer [183].

In our study N,N-diethyl-N-methyl-N(2-methoxyethyl)ammonium bis(trifluoromethanesulfonyl)imide has been chosen as IL. The FET devices based on MoS_2 functionalized with FcC_6 were measured in a dual gate configuration (Figure 2.41): 1) using the Si/SiO_2 as bottom gate/dielectric and 2) using Pt/IL.

In Figure 2.41 b) the transfer curve of the device using the back gate configuration is reported. Registering the Pt gate-source current (I_{ig}) vs. the gate voltage (V_{ig}) two peaks appear when a gate potential ramp is applied from -1 to +1 V. The two peaks are the analogue of the redox waves in a cyclic voltammetry measurement, considering that I_{ig} could give information on the electrochemical processes that happen in liquid gated devices, and can be attributed to the oxidation process of the ferrocene electroactive core. As it is possible to observe in Figure 2.41 c) the peak attributed to the ferrocene oxidation occurs when the V_g is -0,2 V. It is important to underline here that no reference electrode is used, and as a consequence, we do not have a full potential control in this media.

Furthermore, as reported in Figure 2.41 b) the switch of the molecule happens when the device is switched off. Due to that, it was not possible to measure the device in the two redox states of the Fc to observe the effect of the molecular redox switch. As a consequence, in these conditions it is not possible to verify which are the effects of the charge of the Fc molecules on the performance of the device.

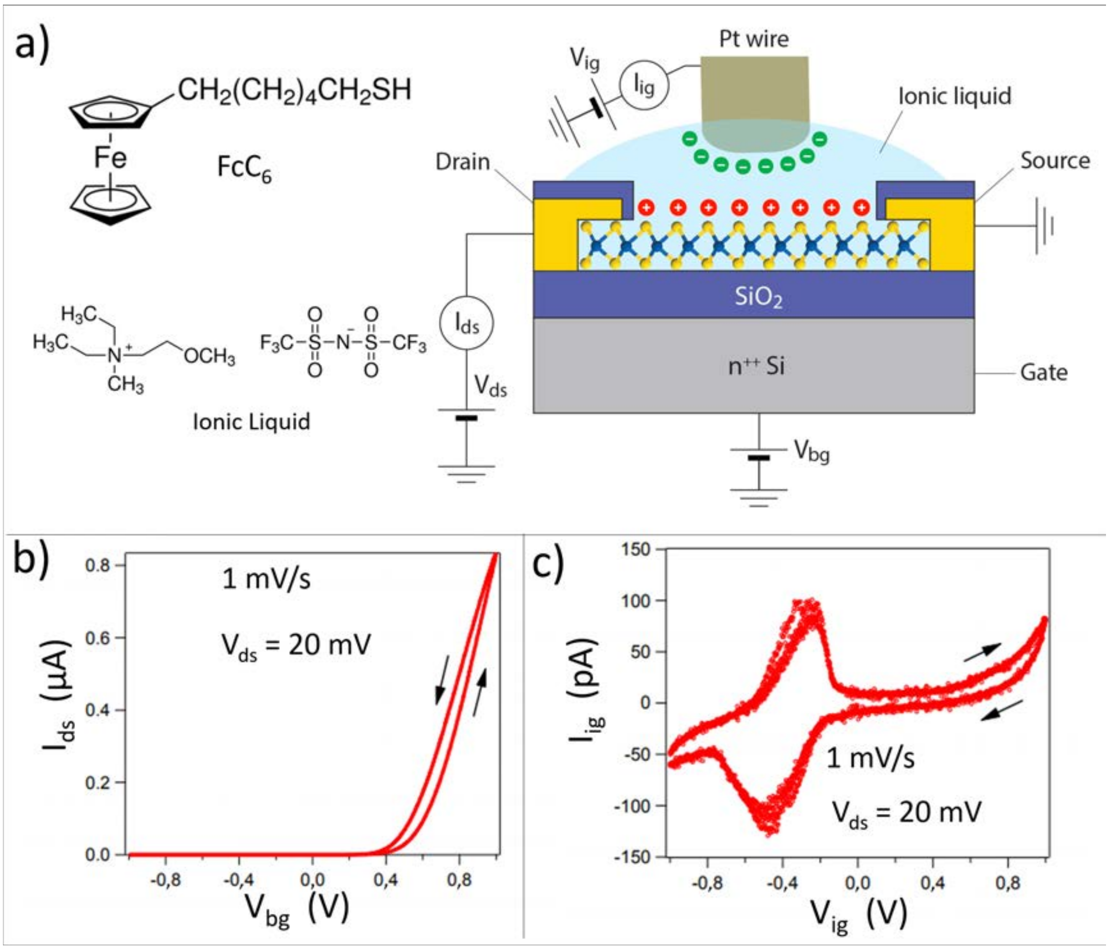

Figure 2.41: a) Schematic representation of the device geometry in the dual gate configuration used and representation of the FcC_6 molecular structure and IL used. b) Transfer characteristics in lin-lin scale for back gate measurements and c) I_{ig} / V_{ig} plot for IL gated measurements of MoS_2 based FET treated with FcC_6.

Finally, to confirm that Fc molecules are covalently linked to MoS_2 by insertion in the vacancies and they are not physisorbed, a blank test was performed using ferrocene without the thiol anchoring group. The IL gated measurements were run in the same conditions as above but in this case, as showed in Figure 2.42, in the I_{ig} / V_{ig} plot no peaks were observed. This result confirms that the thiols are key to fill the sulfur vacancies and are essential for the functionalization of the MoS_2 channel.

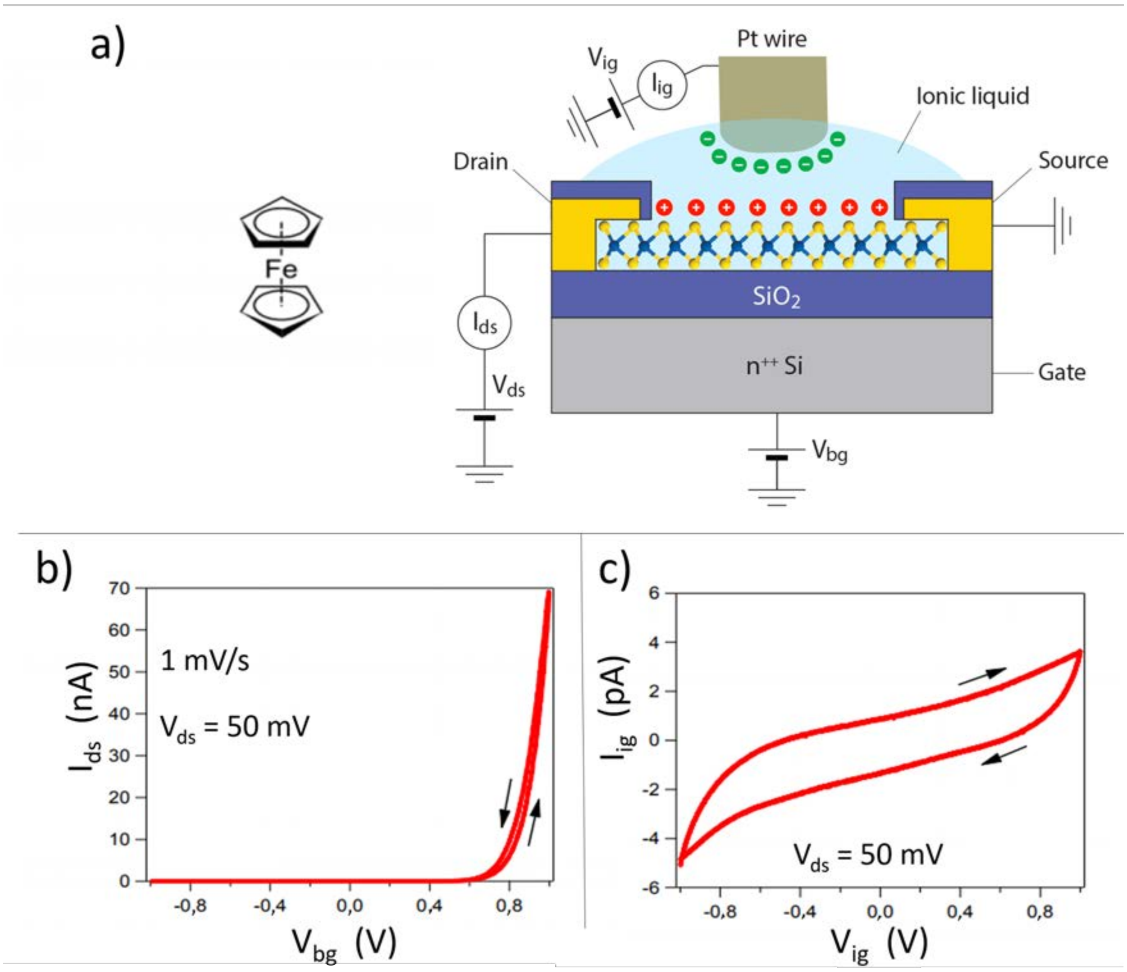

Figure 2.42: a) Schematic representation of the device geometry in the dual gate configuration used and representation of the ferrocene molecular structure. b) Transfer characteristics in lin-lin scale for back gate measurements and c) I_{ig} / V_{ig} plot for IL gated measurements of MoS_2 based FET treated with Fc.

2.6.4 Summary

In summary, we fabricated a MoS_2 based FET using a monolayer of MoS_2 as active channel. We introduced sulfur vacancies in the MoS_2 sheet by bombardment with heavy atoms in order to subsequently explore the possibility to functionalize the material with electroactive thiolated molecules. Specifically, the thiolated ferrocene derivative FcC_6 was chosen as electroactive probe. The FETs were measured in dual gate configuration using as a gate/dielectric 1) Si/SiO_2 and 2) Pt/IL before and after the functionalization. In the back gate configuration it is possible to observe an improvement of the performances of the devices once the functionalization occurred, as proof of the vacancies repair. In the IL-gate configuration, for the first time, the electrochemical switch of the Fc moiety was observed in the I_{ig} / V_{ig} measurements.

These results give a direct proof of the repair process of the sulfur vacancies with thiolated molecules and open the way towards future studies which could be of interest in the field of sensors or memories.

3

Molecular switches based on tetrathiafulvalene derivatives

This chapter is devoted to the work performed with two tetrathiafulvalene (TTF) derivatives: $TTFS_2$ and $BTTS_2$. Both molecules were employed to functionalize gold substrates forming the SAMs S_{TTFS_2} and S_{BTTFS_2}, respectively. Specifically, S_{TTFS_2} was fully electrochemically characterized with the main purpose of realizing a multi-state molecular switch. The SAM capacitance was monitored under the application of different specific bias voltage, obtaining a 4 state electrochemical switch operating with both electric input and output signals. Systems like this have potential applications as memory devices since they might implement the current binary system with quaternary logic storage platforms [184, 185, 186].

Moreover, $TTFS_2$ was successfully implemented into an an Electrolyte-Gated Field Effect Transistor (EGOFET) by modifying the gold gate electrode. The different response of the EGOFET depending on the redox state of the molecule anchored on the gate, was registered and investigated. A bias voltage able to convert $TTFS_2$ into $[TTFS_2]^{\cdot+}$ and vice versa, was systematically applied. The transfer characteristics of the device were recovered before and after each bias application. Hence, the effect of the molecular switch confined on the gate electrode was tested on the device performance. An increment of the transistor performance as well a threshold voltage shift and a transconductance change were observed once the TTF derivative was in its oxidized state.

Finally, the last part of the chapter is dedicated to the fabrication and the characterization of the SAM S_{BTTFS_2}. Such gold modified surface has been prepared with the aim of studying the charge transport properties through the SAM employing EGaIn electrodes. The results showed that this system exhibits a rectifying behavior and we are currently working on its rationalization.

3.1 Objectives

The objectives of this chapter can be resumed as follows:

1) Design and synthesis of thetetrathiafulvalene (TTF) derivatives TTFS$_2$ and BTTS$_2$, shown in Figure 3.1, and characterization of the resulting SAMs (S_{TTFS_2} and S_{BTTFS_2}).

2) Realization of a multi-state switch monitoring the SAM capacitance response as output signal.

3) Integration of the TTF derivatives in devices:

A) Incorporation of TTFS$_2$ in EGOFET devices by the functionalization of the gate electrodes and study of the device performance depending on the TTF redox state on the modified switchable gate electrode.

B) Realization of EGaIn junctions with S_{BTTFS_2} and study of the potential rectifier behavior of these molecules.

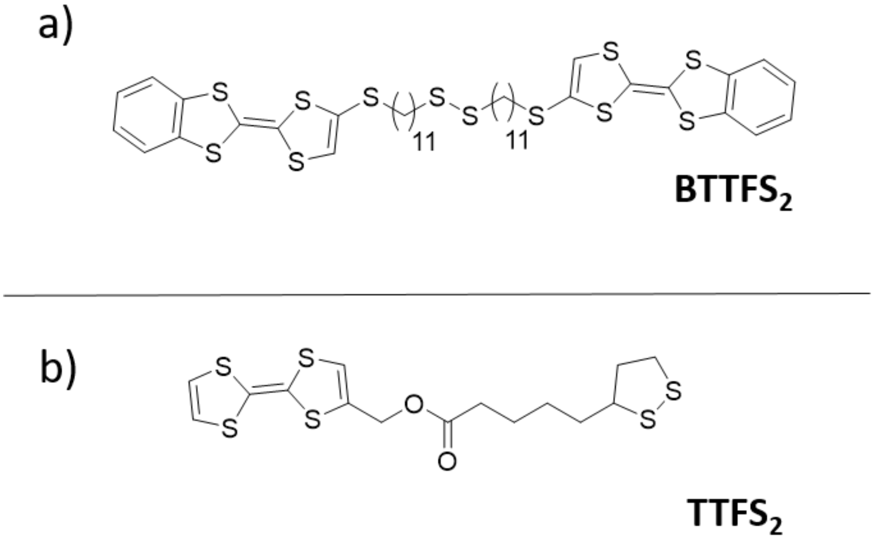

Figure 3.1: Molecular structure of the TTF derivatives used.

3.2 Introduction to tetrathiafulvalene

Tetrathiafulvalene (TTF) is a π-electron donor molecule synthesized nearly fifty years ago [187]. It is an electroactive molecule and its redox potentials are sensitive to the environment and to the chemical functionalization. TTF is a non-aromatic 14 π-electron molecule and can be easily and reversibly oxidized to its radical cation $[TTF]^{\cdot+}$ and dication $[TTF]^{2+}$ forms at accessible potentials (low $E^1{}_{1/2}$ and $E^2{}_{1/2}$ values) (see Figure 3.2). These cationic species possess aromatic character according to the Hückel rule, which is the reason why they are thermodynamically stable [188]. Considerable efforts have been devoted to the synthesis of TTF derivatives [189, 190, 191, 192]. Indeed, it is synthetically possible to introduce a large number of substituents in the 2, 3, 6, and 7 positions of the TTF core, with the aim of modifying the electronic and also the supramolecular characteristics of the TTF derivatives.

TTF has received great attention over the past years stimulated early on by the discovery of high electrical conductivity of the corresponding oxidized salt with chloride as counter anion [193]. TTF was the component of the first organic metal TTF-TCNQ [194] and superconductor [195]. Indeed, TTF derivatives have been found to be versatile building blocks to form supramolecular aggregates in the solid state stabilized by S··S and π··π interactions, with interesting conducting and magnetic properties [196]. TTF based complexes and ion radical salts exhibit unique structures and show interesting properties such as unusual electric conductivities, ferromagnetism, electrochromism, solvatochromism, and optical nonlinearity [197].

In the neutral state, TTF crystals and films have also shown to be promising organic semiconductors giving high field effect mobilities when integrated in Organic Field Effect Transistors (OFETs) [198, 199].

Many academic works report the electrochemical properties of SAMs of TTF derivatives in particular on gold [200, 201, 202]. Interestingly such TTF SAMs have been employed in (bio)sensing applications by using the TTF molecule as electroactive probe [203, 204, 205, 206]. Several reviews have addressed recent advances related to the application of TTF in material chemistry since in recent years TTFs system have received a renewed interest, particularly in the field of molecular electrochemical switches [207, 208, 209, 210].

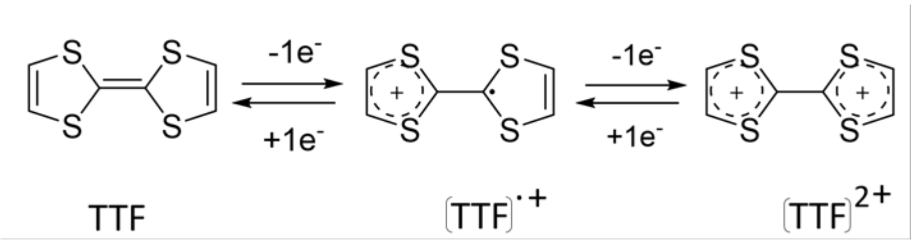

Figure 3.2: Reversible oxidations of tetrathiafulvalene (TTF).

3.3 Design and synthesis of the TTF derivatives $TTFS_2$ and $BTTFS_2$

The TTF derivivatives $TTFS_2$ and BTTFSH were designed with the aim of realizing SAMs of TTF on gold surfaces.

In the case of $TTFS_2$, a disulfide ensures two gold anchorage sites giving rise to a stable SAM. This terminal group was introduced on the TTF moiety through an ester bond reacting thioctic acid and a TTF alcohol derivative.

The synthesis of $TTFS_2$ was easily carried out following the route from Figure 3.3. The commercially available 2-formyltetrathiafulvalene was reduced with $NaBH_4$ to the alchol derivative **1** [211]. Then, the reaction of esterification between compound **1** and thioctic acid was performed in presence of N,N'-Dicyclohexylcarbodiimide (DCC) and 4-Dimethylaminopyridine (DMAP), giving $TTFS_2$ with 90% yield [200, 212]. The compound was characterized by NMR, Mass spectroscoy and IR, as reported in the experimental section.

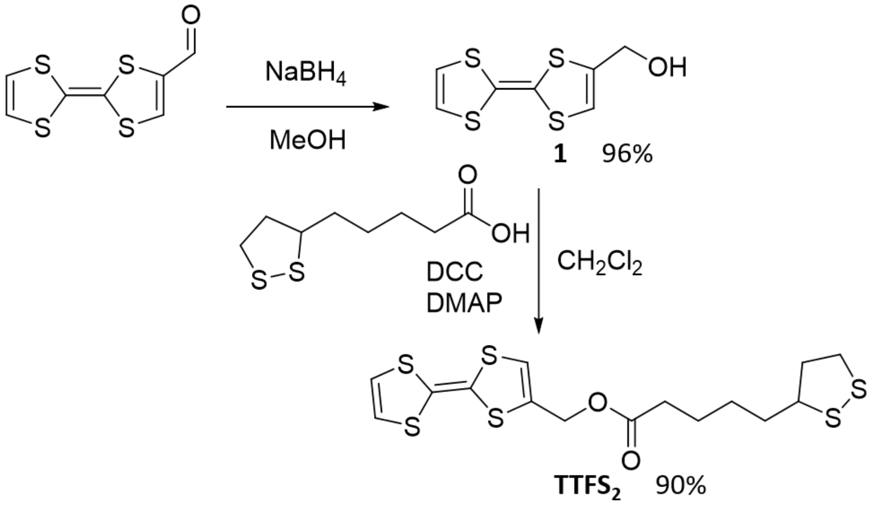

Figure 3.3: Synthetic pathway of $TTFS_2$.

BTTFSH (see Figure 4.6) was designed in order to realize a comparative study of the charge transport properties of a TTF SAM with those of a ferrocene (11(ferrocenyl)undecanethiol) SAM previously investigated [213], as explained in Section3.6. For this reason, we designed a TTF derivative bearing the same terminal group as well as the same spacer group than the above mentioned Fc derivative, namely, a sulfur and a C_{11} alkyl chain. However, the synthesis of BTTFSH could not be carried out successfully. Instead we obtained the dimerized compound, molecule $BTTFS_2$, as described below.

The synthesis of BTTFS$_2$ requires several steps as reported in Figure 4.6. First, the mono-substituted thione **2** was synthesized by the reaction between the commercially available bis(tetra-n-butylammonium)bis(1,3-dithiole-2-thione-4,5-dithiolato)-zinc complex with 3-bromoproponitrile in presence of pyridinium chloride [214]. Compound **2** was obtained with a yield of 60%. Subsequently, **2** was converted to **3** using mercury acetate with a 80% yield [215]. At this point, the coupling between **3** and **4**, which was synthesized from the salt 1,3-Benzodithiolylium tetrafluoroborate as reported in the scheme [216], was carried out with trimethylphosphite at reflux for 5 hours. This reaction gave rise to the benzo-TTF derivative **5** with a 79% yield. The TTF derivative **6** was obtained with a yield of 55% through nucleophilic substitution between the derivative **5** and the commercially available thioacetate S-(11-bromoundecyl) ethanethioate in N,N-dimetilformammide (DMF) with addition of CsOH in MeOH [217].

Subsequently, the deprotection of thioacetate was performed following the literature procedure [218], in order to obtain a thiol as terminal group. Hence, to a solution of **6** in a mixture of dry THF and MeOH EtONa was added. The mixture was stirred overnight under inert atmosphere. Finally, the reaction was neutralized adding ammonium chloride. Surprisingly, the thiol was not detected through ^{1}H NMR. Accordingly, mass spectrometry, confirmed that the synthesized molecule was not the BTTFSH derivative but the dimer BTTFS$_2$(see experimental section and Figure 4.6).

Since BTTFS$_2$, is also able to self-assemble on gold and actually presents some advantages compared with SH derivative, such as stability (thiol can be easly oxidized to disulfur) we chose to use this molecule for our studies.

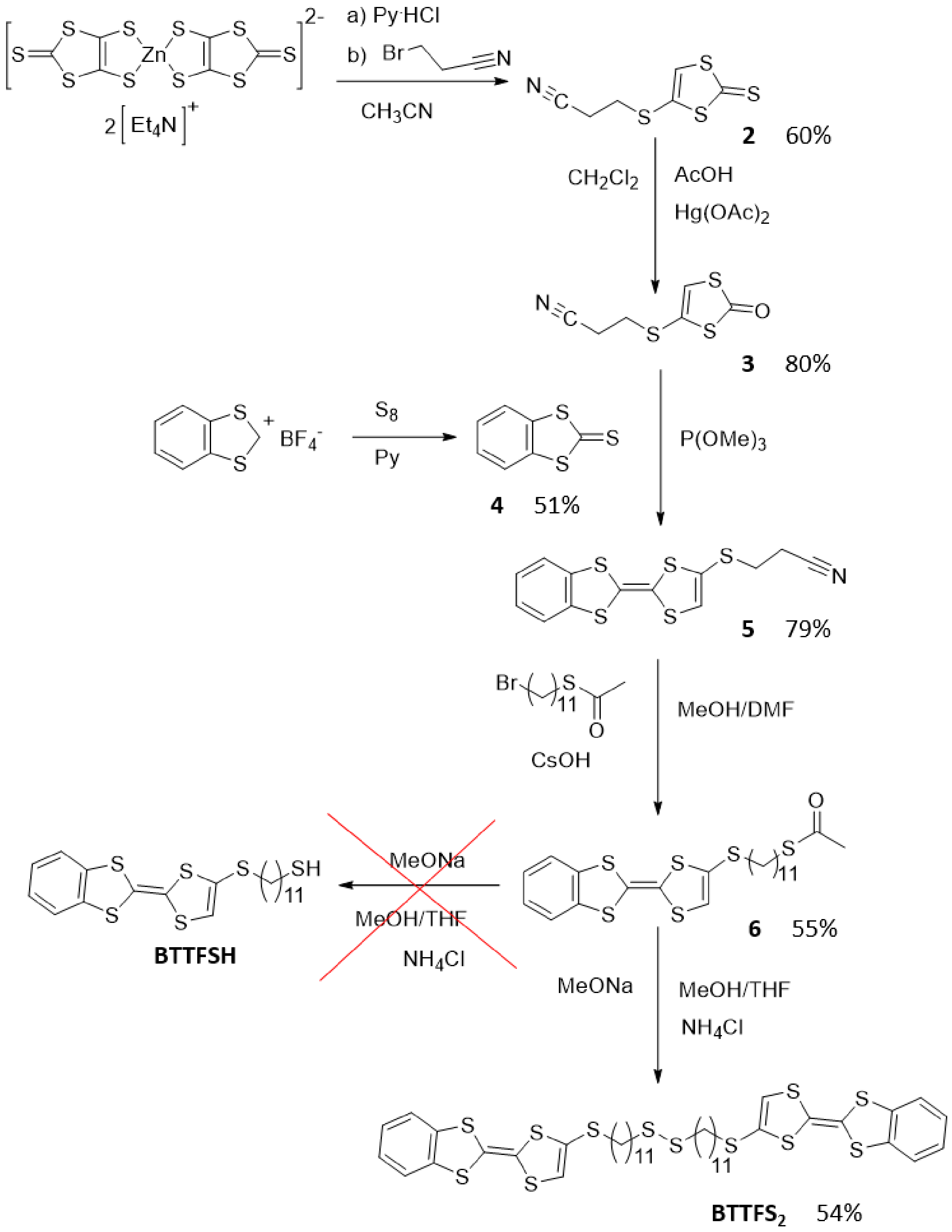

Figure 3.4: Synthetic pathway of BTTFS$_2$.

The electrochemical properties of both compounds TTFS$_2$ and BTTFS$_2$ were studied in solution using 0,1 M LiClO$_4$ in ACN/DCM 1/1 as electrolyte, a silver wire and two platinum wires as pseudo-reference, counter and working electrode, respectively (Figure 4.7). In the CV measurements of both molecules, two reversible redox waves were observed which were ascribed to the conversion of the TTF moiety to the radical cation

$[TTF]^{\cdot+}$ and dication $[TTF]^{2+}$. The redox processes occurred at $E^1{}_{1/2}$= +0,25 V and $E^2{}_{1/2}$= +0,60 V vs Ag (s) for $TTFS_2$, and at $E^1{}_{1/2}$= +0,56 V and $E^2{}_{1/2}$= +0,89 V vs Ag (s) for $BTTFS_2$.

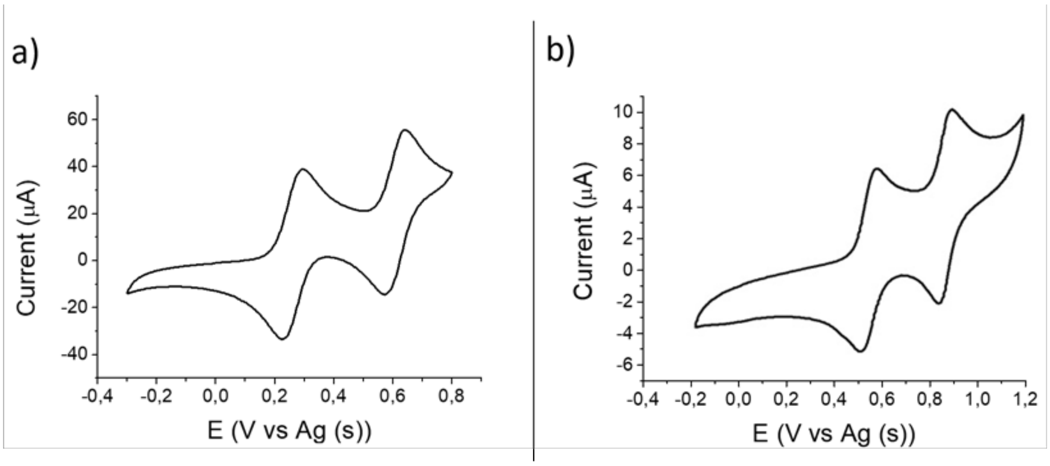

Figure 3.5: CV of a) $TTFS_2$ and b) $BTTFS_2$ molecules. $LiClO_4$ 0,1 M in ACN/DCM 1/1 was used as electrolyte, a silver wire and two platinum wires were used as pseudo-reference, counter and working electrode, respectively. The scan rate was 0,3 Vs^{-1}.

3.4 Surface multi-state switch based on S_{TTFS_2}[1]

3.4.1 Multi-states switches

In the field of molecular switches, it is of great interest to increase the number of different accessible states due to the potential of fabricating increasingly powerful memory devices.

There are different approaches in order to increase the number of accessible states of an electroactive system. One possibility is to employ molecules able to undergo more than one redox process. The problem encountered by this approach is that usually high potential voltages are required to access the multiple redox states. An alternative route is the realization of mixed SAMs combining donor and acceptor molecules on the same electrode (like in the case of the SAM $S_{AQSi//FcC_{11}}$ discussed in Chapter 2). Nevertheless, it has to be taken into account that, even if the operation bias could be low, the synthetic effort doubles up, as well as the costs of the production process, because two molecules are required instead of one. Finally, it is possible to select a read-out mechanism able to differentiate the response of the system not only before and after the redox process occurs, but also at different defined applied voltages. In this way, even when employing a monocomponent bi-stable electroactive SAM it is possible to obtain a multi-state switch.

---

[1] The work here presented was published in the journal RSC Advances: E. Marchante, M. S. Maglione, N. Crivillers, C. Rovira and M. Mas-Torrent, RSC Adv, 2017, 7, 5636-5641.

For instance, limiting the read-out response to the redox state of the molecule, the electrochemical stimulated switch of a TTF derivative anchored on ITO was previously followed monitoring its magnetic and optical response [47] (Figure 3.6). In the case of the magnetic output, the system was investigated by electron paramagnetic resonance (EPR) and gave rise exclusively to a 2-state switch. In fact, the TTF radical cation ($[TTF]^{\cdot +}$) is the only redox species with a magnetic moment, while the TTF as well as $[TTF]^{2+}$ do not produce any EPR response. When instead of the magnetic, the optical output was used the system gave three different responses for each accessible redox state. As shown in Figure 3.6 c) and d), by selecting a specific wavelength (i.e. 420 nm), three different levels of optical absorption could be distinguished corresponding to one redox state each.

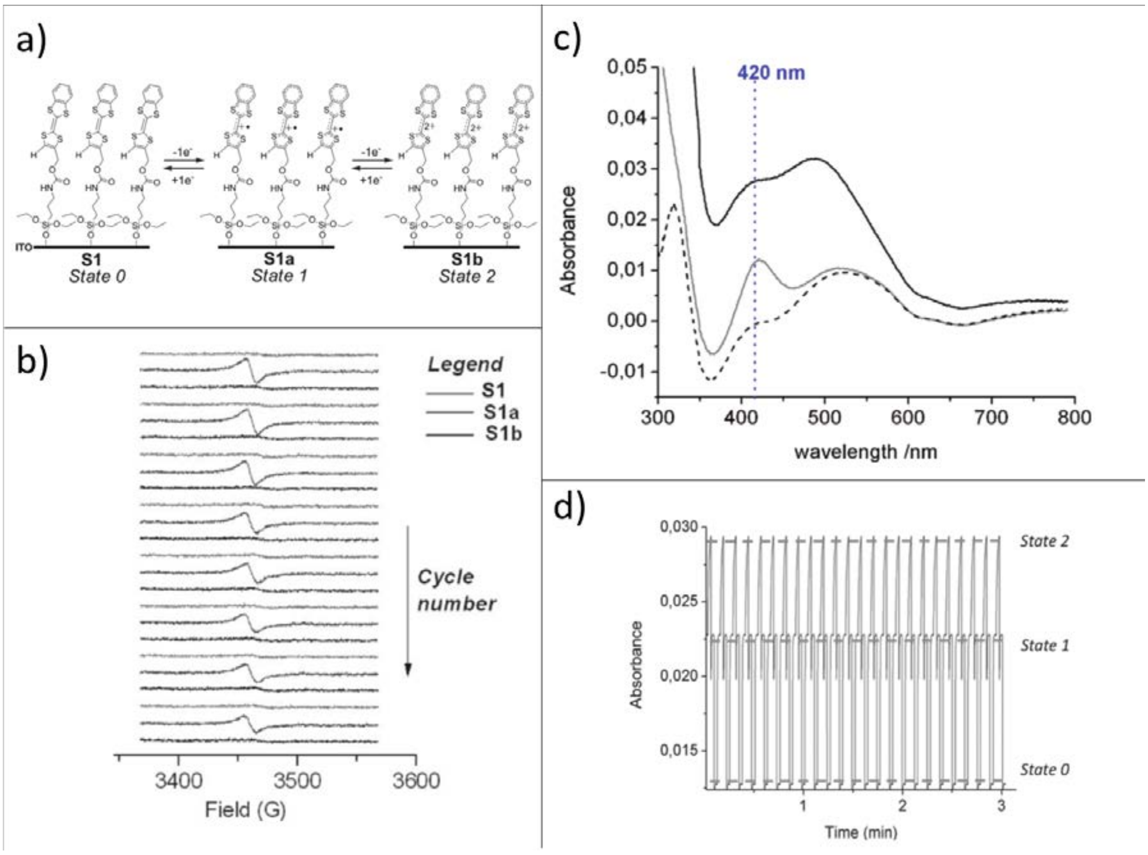

Figure 3.6: a) Schematic representation of the electrochemical tri-stability of a SAM of a TTF derivative on ITO (S1). b) EPR response of S1 monitored by EPR spectroscopy when a sequence of consecutive voltage pulses of -0,2, +0,9, and +1,5 V vs Ag (s) were applied to the substrate. c) UV-vis absorbance spectra of S1 (black dashed line), S1a (gray solid line), and S1b (black solid line) in a solution of 20 mM Tetrabutylammonium hexafluorophosphate (TBAPF$_6$) in acetonitrile. d) Optical absorbance of S1 at λ = 420 nm as a function of time upon consecutive application of a sequence of 2 s pulses at voltages vs Ag (s) of -0,2 V (state 0), +0,9 V (state 1), and +1,5 V (state 2) [47].

In the work here reported, studying the SAM S_{TTFS_2}, we aimed at obtaining a system where the definition of the number of states is not limited by the redox stability of the TTF species but it can be enhanced determining distinct levels of the output signal corresponding to specific input values. In other words, we planed to distinguish not only the various redox states of the molecules on the surface, but also the equilibria where more than one species coexist. To do this, we exploited the capacitance response of the SAM at defined DC applied potentials, following a procedure recently demonstrated in our group [50].

Another reason to choose capacitance response is that the use of electrical input/output signals is particularly appealing since they can be more easily integrated with modern technologies.

3.4.2 Preparation and characterization of SAM S_{TTFS_2}

The substrates used for the fabrication of SAM S_{TTFS_2} consist of 300 nm of Gold (111) on mica and were purchased from Georg Albert PVD-Beschichtungenwere. They were first rinsed with dichloromethane, acetone and ethanol HPLC pure grade, and dried under nitrogen stream. After, these substrates were cleaned in a UV ozone chamber for 20 minutes and afterwards immediately immersed in ethanol for at least 20 minutes, rinsed with ethanol and isopropanol and dried under nitrogen stream. Then, they were immediately immersed in the solution of $TTFS_2$ in tetrahydrofuran. The conditions employed for the SAM preparation are illustrated in Table 3.1. The SAM formation was carried out under light exclusion and under nitrogen atmosphere.

Table 3.1: List of conditions for S_{TTFS_2}preparation.

Substrate	SAM	Solution	Immersion Time
Gold	S_{TTFS_2}	1 mM of $TTFS_2$ in THF	72h

$S_{TTFS_2}$was successfully characterized by X-ray Photoelectron Spectroscopy (XPS). The binding energies are reported in table Table 3.2. The peaks at~ 532 and~ 533 eV, attributed to the oxygen-carbon bonds, as well as those at~ 162 and~ 163 eV for the sulfur-gold bond, give clear evidence of molecules bonded to the surface.

Table 3.2: XPS values of S_{TTFS_2}.

Core Level	Binding Energy (eV)	Type of Bond
C1s	284,8; 285,7; 288,9	C-C; C=C; O-C=O
O1s	532,2; 533,3	C-O; C=O
$S2p_{3/2}$	161,9; 163,6	S-Au; C-S-C
$S2p_{1/2}$	163,1; 164,7	S-Au; C-S-C

Also Time-of-Flight Secondary Ion Mass Spectrometry (ToF-SIMS) was used as characterization technique. The molecular peak, corresponding to the $[M]^+$ was observed at 422 m/z. Possible molecule fragmentations were visible as well (Figure 3.7).

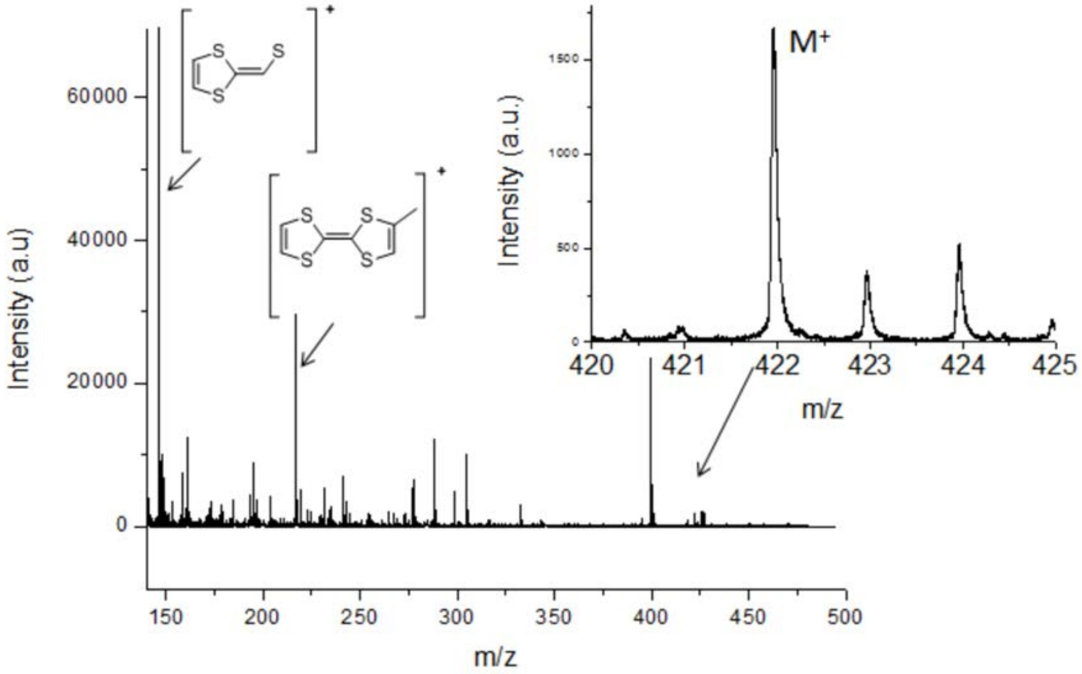

Figure 3.7: ToF-SIMS spectrum of S_{TTFS_2}.

Fnally the gold electrodes modified with $TTFS_2$ were characterized using electrochemical techniques. The voltammetric response is shown in Figure 3.8. A solution of $LiClO_4$ 0,1 M in acetonitrile was used as electrolyte, while the functionalized surface was used as working electrode and platinum and silver wires as counter and pseudo-reference electrodes, respectively. The two reversible one-electron processes corresponding to the oxidation to the radical cation and dication forms were observed at the formal potentials $E^1{}_{1/2}$= 0,26 V and $E^2{}_{1/2}$= 0,63 V vs. Ag (s), respectively. Moreover, during repeated electrochemical cycling no considerable differences in the CV were observed, confirming the stability of the SAM.

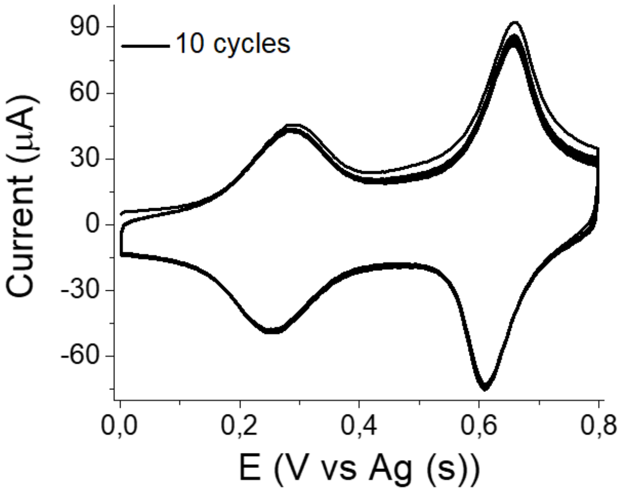

Figure 3.8: CV of S_{TTFS_2}. The functionalized surface was used as working electrode and platinum and silver wires as counter and pseudo-reference electrodes, respectively. The electrolyte was provided by a solution of $LiClO_4$ 0,1 M in acetonitrile. The CV measurement was repeated for 10 cycles.

Furthermore, there is a linear relationship between the anodic peak current intensity (I_{pa}) and the scan rate. This is in agreement with the presence of surface-confined redox-active molecules (see Figure 3.9). A further proof of that, is the small peak-to-peak separation ($\Delta E_p = E_{anodic} - E_{cathodic}$) found at low scan rates for the two redox processes. In particular, the first oxidation process presents a ΔE_{p1} of 27 mV while for the second one is ΔE_{p2} = 19 mV at scan rate 100 mV/s. Integrating the area under the cyclic voltammetry peak, the TTF surface coverage was estimated to be $2{,}2 \cdot 10^{-10}$ mol $\cdot$ cm^{-2} (at 100 mV $\cdot$ s^{-1} of scan rate).

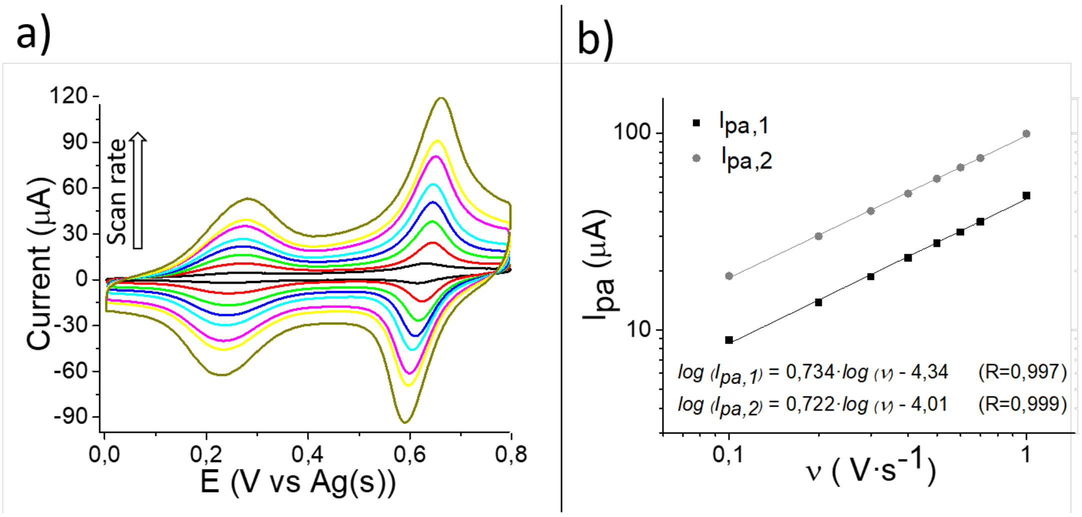

Figure 3.9: CV of S_{TTFS_2} at different scan rates (0,1; 0,2; 0,3; 0,4; 0,5; 0,6; 0,7 and 1 V/s). Linear relationship of the current peak (Ipa) vs the scan rate (ν). The functionalized surface was used as working electrode and platinum and silver wires as counter and pseudo-reference electrodes, respectively. The electrolyte was a solution of $LiClO_4$ 0,1 M in acetonitrile.

The full width at half maximum (FWHM) in a theoretical case, where an ideal Ernestine reaction under the Langmuir isotherm conditions (i.e., all adsorption sites are equivalents and there are no interactions between immobilized electroactive centers) occurs at 25 C, is ca. 90 mV. The deviations from the theoretical FWHM value gives hence information about the redox centers, especially related to the intermolecular interactions [219]. In this case, the FWHM value of the first redox peak was larger than 90 mV (i.e., 143 mV), whereas for the second redox peak was slightly lower than the theoretical value (i.e., 79 mV). This type of CV shape has been commonly observed in other TTF-based SAMs and is due to the intermolecular interactions between the TTFs [47, 201, 220].

Following, electrochemical impedance spectroscopy (EIS) was used to characterize electrical interfacial properties of our system.

3.4.3 Electrochemical Impedance Spectroscopy characterization of S_{TTFS_2}

In SAMs, electrochemical impedance spectroscopy (EIS) has mainly been previously employed to determine electron transfer rates in electroactive systems [221] or to investigate the ionic permeability through SAMs based of non-electroactive molecules [222]. However, EIS can be exploited to measure the capacitance of the different redox states of switchable SAMs, as recently reported in ferrocene SAMs [50]. Indeed, the complex impedance function $Z(\omega)$ can be converted into complex capacitance function

$C(\omega)$ by the following expressions:

$$Z(\omega) = Z_{re} - jZ_{im} \leftrightarrow C(\omega) = C_{re} - jC_{im} \tag{3.1}$$

$$C(\omega) = \frac{1}{j(2\pi f)(Z(\omega))} \rightarrow \begin{cases} C_{re} = \frac{1}{2\pi f}\frac{Z_{im}}{(Z_{re}^2+Z_{im}^2)}\frac{1}{A} \quad C_{im} = \frac{1}{2\pi f}\frac{Z_{re}}{(Z_{re}^2+Z_{im}^2)}\frac{1}{A} \end{cases} \tag{3.2}$$

Where Z_{re} and C_{re} are the real part and Z_{im} and C_{im} are the imaginary part of the impedance and capacitance complex function, respectively, f is frequency and A the electrode surface area.

This methodlogy is very powerful to characterize the capacitance of SAMs without the need of introducing equivalent electrochemical circuits.

To characterise the S_{TTFS_2}, impedance spectra were collected in the same conditions as the ones used in the CV experiments, between 200 kHz and 500 mHz with an AC amplitude of 5 mV (peak-to-peak) at three different voltages: before the redox process (10 mV), at the first redox peak potential (250 mV), and at the second redox peak potential (620 mV). Nyquist plots are reported in Figure 3.10 a) and look like vertical lines parallel to the y axis [223, 224, 225, 226]. In cases where a DC-current can be established, such as when an ion pair is present in the electrolyte solution, Nyquist plots typically display one or more semicircles [54]. Nevertheless, in the case of surface confined molecules under an inert electrolyte, as in the present case, a DC-current cannot be established, and the system shows capacitor behaviour. The capacitor like system is also shown by the Bode plots [227] that at low frequency region consist of straight lines with slopes close to 1, while the phase angles (Φ) approach 90° (Figure 3.10 b). So, at low frequencies the gold metal surface acts as one capacitor plate and the physisorbed ions at the SAM/electrolyte interface act as the other capacitor plate [228]. On the contrary, at higher frequencies (f > 10 kHz), the frequency-independent impedance and phase angle close to zero indicate that the system behaves as a resistor, that is, the total impedance is dominated by the solution resistance. This is due to the fact that at high frequencies, the capacitor behaves as a short-circuit element since there is no time to be charged, allowing the AC current to pass.

Noticeable, a significant modulation in |Z| is observed at the low frequency region depending on the DC voltage applied (i.e., on the SAM redox state), indicating that the performed impedance measurements could be successfully used as a readout of the molecular switch.

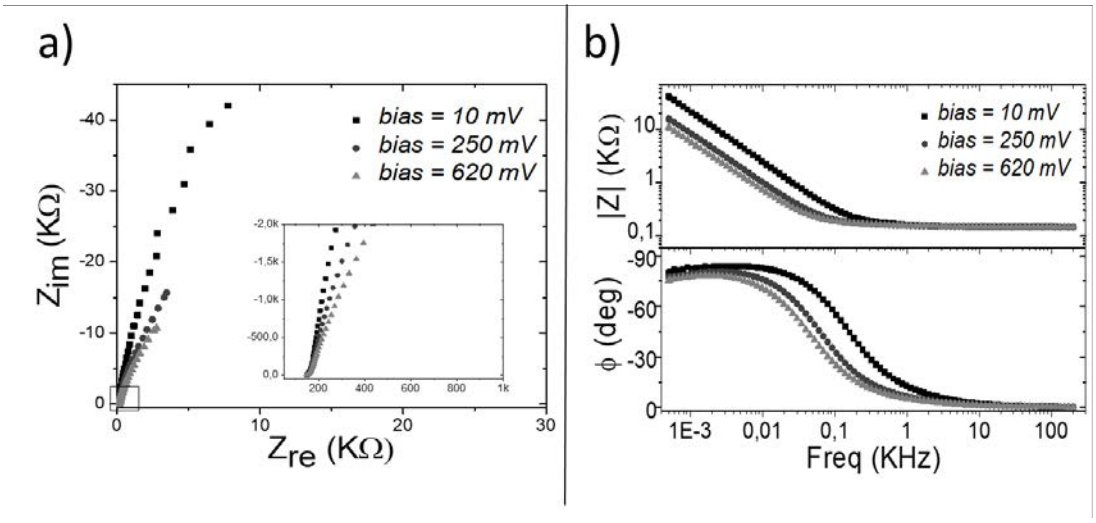

Figure 3.10: EIS characterization of S_{TTFS_2} at 3 different bias voltage: 10, 250 and 620 V vs Ag (s). a) Nyquist plot b) Bode plots.

Alternatively, the data can be analyzed by means of capacitance Bode plots by using the expressions 3.2 (Figure 3.11), providing very useful information for surface confined redox species [57, 229, 230]. Different processes with different time constants are occurring depending on the applied DC potential. The small semicircle recorded at a voltage outside the redox process (i.e., 10 mV) comes from the non faradaic terms dominated by the resistance of the electrolyte and the double layer capacitance. In the redox window potentials faradaic contributions are also present (i.e., a pseudo-capacitance for charging the monolayer and a resistance for the electron transfer).

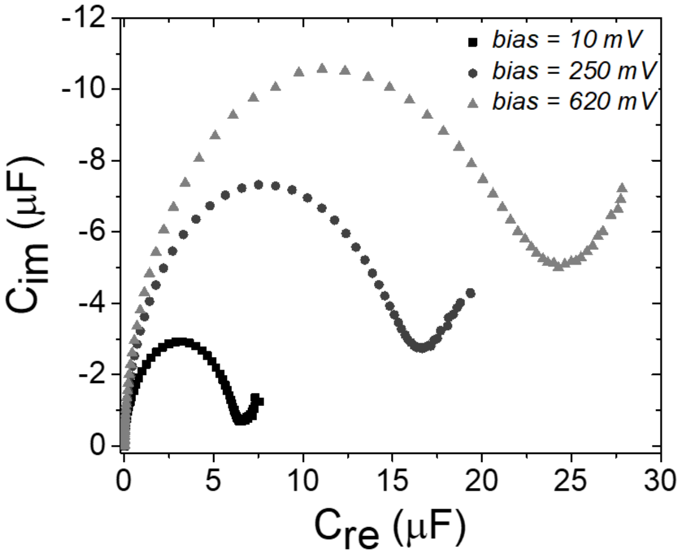

Figure 3.11: Capacitance plot for S_{TTFS_2} at 3 different bias voltage: 10, 250 and 620 mV vs Ag (s)

Noteworthy, the influence of applied potential on the capacitance spectra of bare Au was much smaller than when the gold is functionalized with the TTF electroactive monolayer (Figure 3.12), indicating that the observed effect is not simply due to the polarization of the metal but to the redox processes involved.

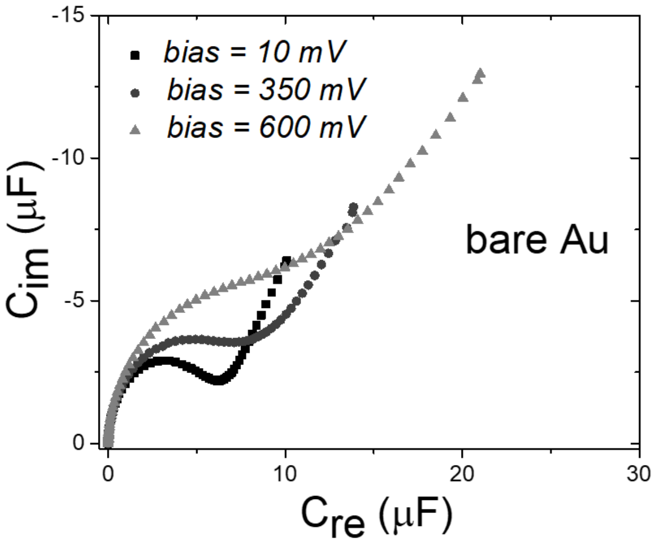

Figure 3.12: Capacitance plot of bare gold at the studied 3 bias voltages: 10; 350 and 600 mV vs Ag (s).

Furthermore, plotting the imaginary part of the capacitance for S_{TTFS_2} against the frequency at DC bias of 10, 250 and 620 mV (Figure 3.13 a)), it is possible to extract information about the kinetic parameters of the redox transfer. For this purpose, the appropriate data treatment is necessary. First of all, the solution resistance (R_e), which is easily extracted from the beginning of Z_{re} at high frequency in the Nyquist plot, should be subtracted from the spectrum by means of $Z_{re}(\omega)$ - R_e. Then, the blank response from the experimental data registered at 10 mV is also subtracted. In this way, we can gain information exclusively on the redox processes, free of parasitic signals. Figure 3.13 b) shows the final responses of the two C_{im} spectra that correspond to the first and second redox processes, respectively, after the subtraction of the response of the SAM outside the redox window.

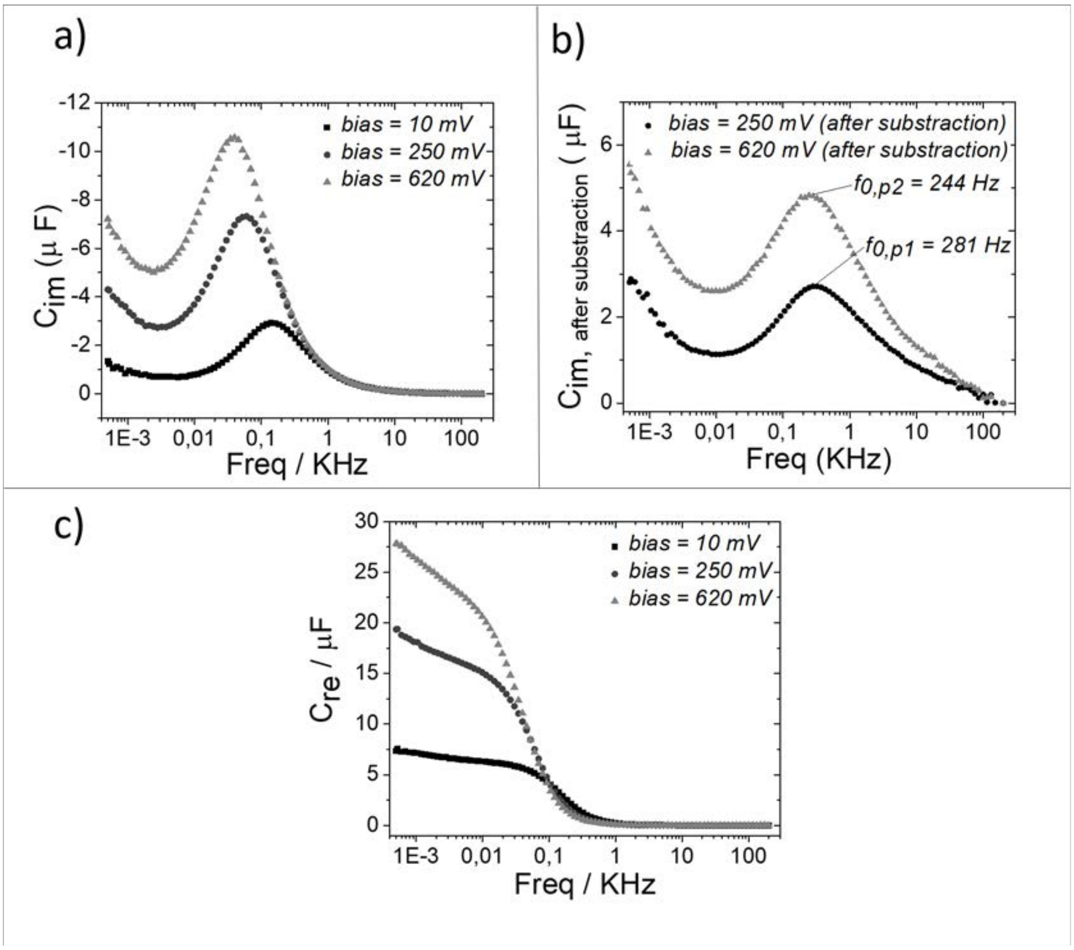

Figure 3.13: Capacitance Bode plots of S_{TTFS_2} at 3 different bias voltages: 10 mV, 250 mV, and 620 mV vs Ag (s). a) Experimental data of the imaginary part of the capacitance vs frequency, and b) after subtraction of the non-faradaic response. In c) the experimental data for the real part of the capacitance vs frequency is represented.

From these graphs, the rate constant for the electron transfer process (k_{ET}) can be estimated from the frequency (f_0) at the highest ordinate point using the expression 4.1

[227]:

$$K_{ET} = \pi f_0 \tag{3.3}$$

The k_{ET} values for the TTF / $[TTF]^{\cdot+}$ and $[TTF]^{\cdot+}$ / $[TTF]^{2+}$ redox processes were estimated to be 882 and 767 s^{-1}, respectively. Noticeably, previously reported transfer rates for TTF SAMs extracted from applying Laviron's formalism on the CV data gave a higher value for the second oxidation process than for the first one [231, 232]. This trend was attributed to environmental effects such as the formation of ion pairs between the oxidized TTF molecules and the electrolyte anions that accelerated the second redox process. However, here the transfer rates found for the two TTF redox processes by EIS are of the same order.

Further, the C_{re} vs frequency plot is illustrated in Figure 3.13 c). We found that at medium/high frequency range, the measured capacitance corresponds to the bulk capacitance, whereas at low frequency values a plateau is reached reflecting the interfacial double-layer capacitance [233]. Consequently, at this low frequency the capacitance is clearly dependent on the redox state of the molecule and, thus, on the applied DC voltage.

Therefore, the capacitance response of the switchable S_{TTFS_2} was investigated at low frequency. Taking into account the CV data, four different voltage inputs were selected: 10, 250, 450 and 620 mV vs Ag(s), respectively. Such voltages correspond, respectively, to four different $TTFS_2$ states. At 10 mV the molecule is in neutral state (state 1), at 250 mV is where the first oxidation process occurs, $TTFS_2 - e^- \rightleftharpoons [TTFS_2]^{\cdot+}$ (state 2), at 450 mV all the TTF surface-confined molecules should exist as $[TTFS_2]^{\cdot+}$ radical cation (state 3) and finally, at 650 mV is where the second oxidation process takes place, $[TTFS_2]^{\cdot+} - e^- \rightleftharpoons [TTFS_2]^{2+}$ (state 4) (see Figure 3.14).

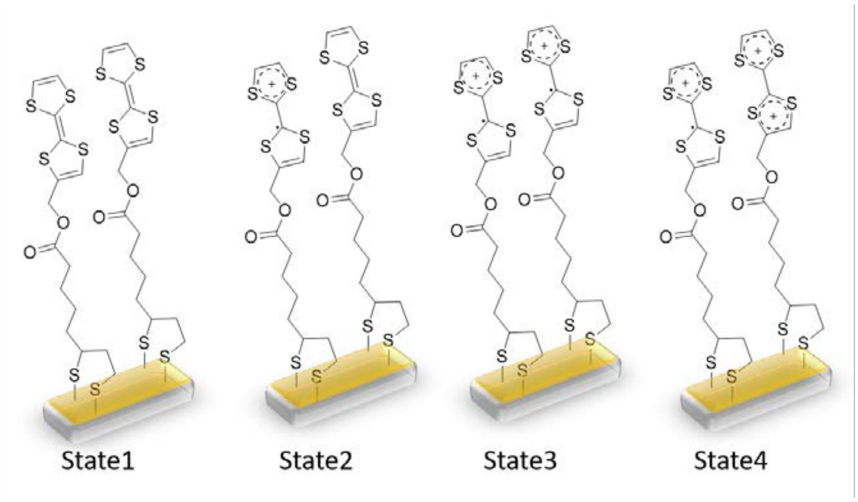

Figure 3.14: Schematic representation of the four $TTFS_2$ states at the bias potential of 10, 250, 450 and 620 mV vs Ag(s) (state 1, 2, 3 and 4, respectively).

Hence, EIS measurements were performed at 1 Hz at the selected DC potentials. The evolution of C_{re} in the four states is shown in Figure 3.15 a) over 20 cycles. The feasibility of using the SAM capacitance as output of the electrochemical switch was validated by finding capacitance values discernible and specific for each state with significant on/off ratio. After 20 cycles, the initial capacitance value decreased in 3%, 15%, 2% and 30% for states 1–4, respectively. As the values indicate, such variation is more pronounced at the states corresponding to the potential of the redox process and can be attributed to some molecular desorption caused by the bias stress. This is in accordance with the CV shape changes observed for the SAM before and after the impedance switching experiments. The switching response was studied in different samples after the application of 50 cycles and similar results were achieved (Figure 3.15 c)).

So, it can be affirmed that we were able to realize a 4-state surface confined molecular switch operating with both and electric input and output signals by making use of the SAM capacitance. Certainly, the weak point of our system is its robustness that is limited to the electrochemical stability of the sulphur–gold covalent bond. Such stability could be probably improved by avoiding extremely traces of humidity and oxygen. It can also be anticipated that SAMs such as silane derivatives on ITO, could be a more durable alternative.

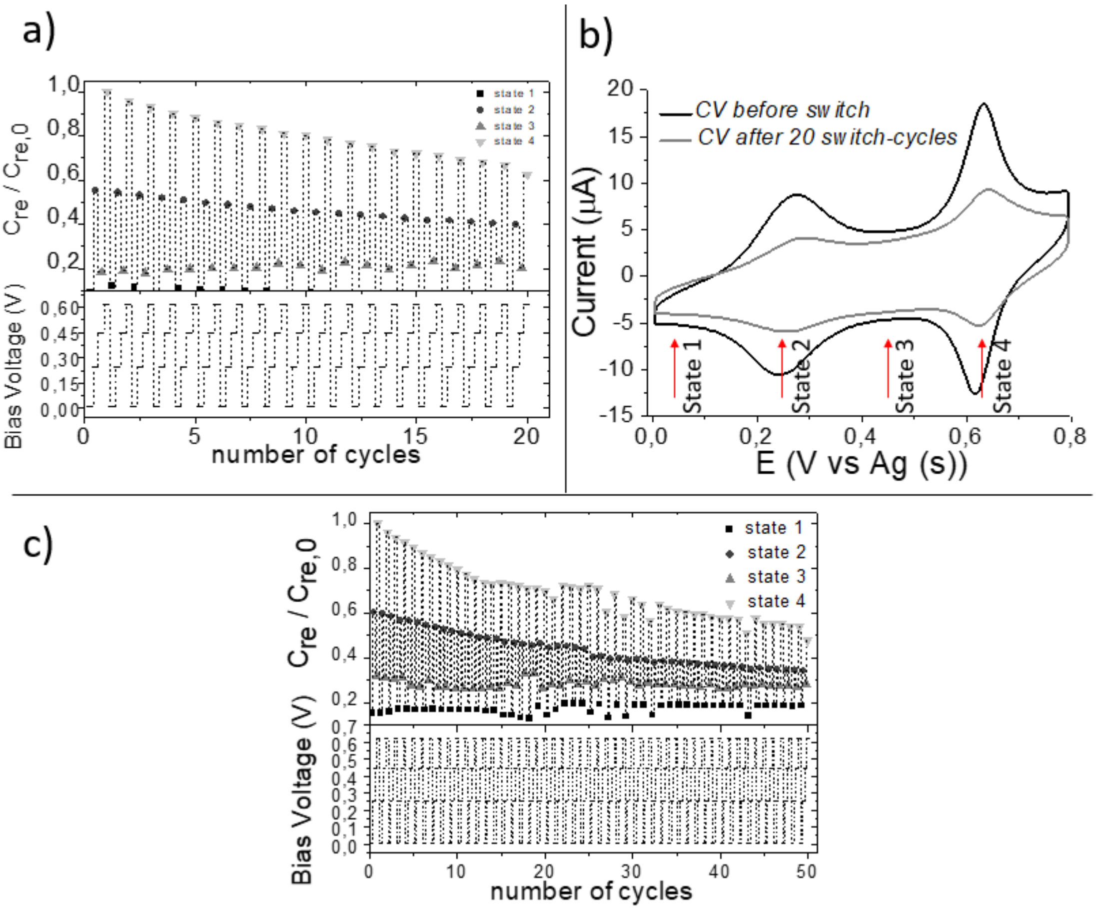

Figure 3.15: a) Four states switching of S_{TTFS_2}. At the bottom, applied bias voltage profile; at the top $C_{re}/C_{re,0}$(at 1 Hz) output, at the corresponding states: state 1 (10 mV); state 2 (250 mV); state 3 (450 mV); state 4 (620 mV). b) CV of S_{TTFS_2}in $LiClO_4$ before and after the 20 EIS cycles. c) Relative capacitance values ($C_{re}/C_{re,0}$) of S_{TTFS_2} during 50 switching cycles.

3.4.4 Summary

Resuming, the SAM S_{TTFS_2} on gold was prepared and fully characterized by EIS in order to determine the two electron transfer constants and the capacitance of the system at different applied voltages. Four different states were defined and the electrochemical switching response was successfully monitored employing the SAM capacitance as a read-out mechanism. Importantly, the number of states of the switch was not limited to the number of redox states of the molecule but instead it was determined by the output of the system at defined DC applied potentials. Complementary, high and comparable values of k_{ET} were obtained by EIS for the two redox process of the TTF. Thus, the results here reported might encourage the development of this type of electrochemical molecular switches for the future implementation in devices since quaternary logic storage platforms can easily match the present binary system as they can be decoded directly into two binary-digit equivalents.

3.5 Integration of TTFS$_2$ in EGOFET devices by functionalizing the gate electrode[2]

3.5.1 Gate modification in electrolyte-gated field effect transistors

The modification of the gate electrode is one of the hot topics within the field of electrolyte-gated organic-field effect transistors (EGOFET). This modification principally affects the work function of the metal as well as the capacitance of the double layer at the gate/electrolyte interface. This approach is of technological interest for the optimization of the device performance as well as for the realization of fundamental studies of transistor device physics. For instance, the effect of different gate electrode materials (Au, Pt, W, Cu, Ag and glassy carbon) using polymeric and a crystalline organic semiconductors as active materials was investigated [234, 235]. It was observed that by varying the gate electrode work function, a systematic threshold voltage shift can be measured, which follows the work function trend. Recently it has also been demonstrated that faradaic reactions at the gate/water interface can be responsible for the current increase in the device, as in the case of Zn gate electrodes [236].

Furthermore, it was demonstrated the dependence of source charge injection on the gate electrode work function by systematically investigating the contact resistance in electrolyte-gated OFETs. The possibility to control the charge injection by changing the gate electrode is a way to overcome a significant bottleneck to the transistor performance [237].

The functionalization of the gate electrode has been explored for the fabrication of (bio)sensors by immobilizing a specific receptor on the gate electrode. Devices with sensitivity comparable to state-of-the-art techniques, such as enzyme-linked immunosorbent assay (ELISA) or surface plasmon resonance (SPR), have been demonstrated [238, 239**?**].

Here we employ switchable TTFs to graft as a SAM on the gate electrode of EGOFETs in order to gain an additional parameter to control the device properties. The prepared devices could be appealing in applications as memory devices as well as in the field of sensors.

---

[2] The work here presented was done in collaboration with Vitaliy Parkula, Dr. Stefano Casalini, Qiaoming Zhang, Dr. Pierpaolo Greco and Prof. Fabio Biscarini.

3.5.2 Design and fabrication of the EGOFETs endowed with microfluidics

The EGOFET was fabricated on a silicon substrate with gold source and drain electrodes. The electrodes layout was photolithographically patterned by means of a micro-writer, while the gold (40 nm) was deposited by thermal evaporation (system Auto 306 from Boc Edwards) using chromium (5 nm) as adhesive layer. The electrodes were covered with an organic semiconductor. Specifically a solution of 2,8-difluoro-5,11-bis(triethylsilylethynyl)-anthradithiophene (diF-TES-ADT) mixed with polystyrene (Mw = 10000 g · mol^{-1}) in a ratio 4:1 in chlorobenzene was used. It was deposited through the Bar-Assisted Meniscus Shearing (BAMS) technique. This methodology was previously demonstrated in the group to give rise to highly crystalline films exhibiting high OFET performance [240, 241] (Figure 3.16).

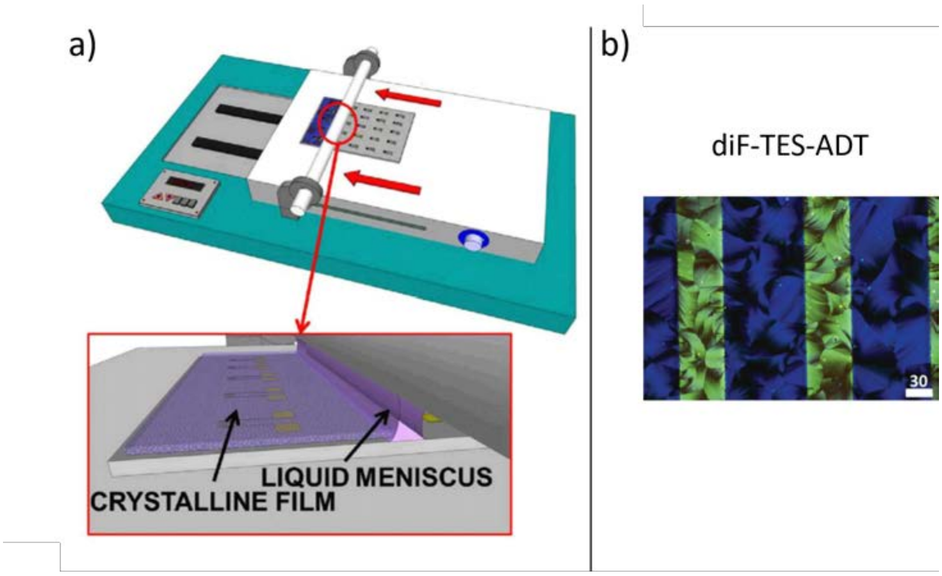

Figure 3.16: a) Representative sketch of BAMS [240]. b) Optical polarized microscopy image of a diF-TES-ADT:PS film which shows uniform crystalline domains.

The EGOFET used was endowed with a microfluidic chamber in order to allow the electrolyte replacement remaining in a controlled environment. A proper tailored microfluidic chamber was fabricated by Scriba Technology s.p.a. Its layout allows one an easy assembly onto the interdigitated electrodes. The upper part of the microfluidic chamber bears two well-defined holes, which enables a precise positioning of two Au gate electrodes (the working and the reference gate, as explained later). The flow of the aqueous electrolyte is guaranteed by a peristaltic pumping. Importantly, this design of a self-standing chip containing two different gate electrodes that can be connected and manipulated individually, allowed us a systematic comparison of the electrical performance of the same device by changing the chemical functionalization of one of the gates surface (i.e. working gate), but leaving always a bare gate electrode for control tests (i.e. reference gate). The geometry of the device together with that of the microfluidic chamber is schematically shown in the Figure 3.17 a), while in Figure 3.17 b), a real picture of the system is presented.

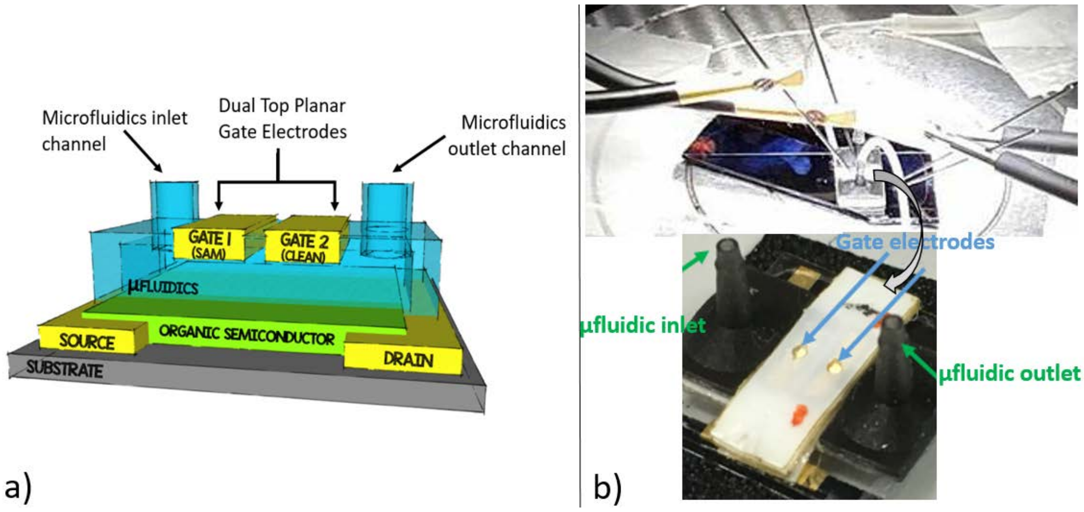

Figure 3.17: a) Schematic representation of the device structure. b) Real picture of the system.

The gate electrodes consisted of Si/SiO_2 and were prepared from a 4″ Si wafer (with a thickness of 525 ± 25 µm), which then were cut into 4 mm × 1 mm Si pieces. The silicon was strongly As doped (n-type), with a resistivity ranging from 1 to 6 mΩ·cm. A 50 nm thick gold layer was deposited on both sides of the Si/SiO_2 wafer using an electron beam evaporator (ULVAC EBX14D). A 5 nm thick chromium film was deposited as adhesion layer between SiO_2 and the Au layer. The double layer of gold with highly doped intermediate silicon layer provides a possibility for contacting the electrodes from top with electrical probe station.

In order to ensure the proper substrates decontamination, a rigorous cleaning protocol was followed before proceeding with the gate functionalization. First of all, the gate electrodes were immersed overnight into sulfuric acid. Then, they were rinsed with ultra-pure water, dried under nitrogen flow and sonicated into a sequence of different HPLC solvents (dichloromethane, acetone and ethanol) for 15 minutes each solvent. The substrates were then dried again, under nitrogen stream and were furthermore cleaned in a UV ozone chamber during 20 minutes. Afterwards they were immersed in ethanol for 25 minutes, rinsed with isopropanol and finally, dried under N_2 stream. The formation of the SAM S_{TTFS_2} was carried out following the protocol reported in Table 3.1.

In order to establish the behavior of $TTFS_2$ in an aqueous environment, CV measurements were performed on S_{TTFS_2} using an aqueous electrolyte (Figure 3.18). As usually, a three-electrode setup was used. The modified $TTFS_2$ substrate was employed as the working electrode (WE), while a platinum and a silver wires (0,5 mm of diameter each one) were the counter (CE) and quasi-reference electrodes (RE), respectively. Firstly, a 0,1 M of a buffer phosphate (pH 6,9) aqueous solution (PBS) was elected as electrolyte since it is the most used electrolyte in EGOFETs employed in biological applications. In these conditions the CV spectrum did not show any peak that could be attributed to the redox process of $TTFS_2$, as shown in Figure 3.18 a). The $[TTFS_2]^{\cdot+}$ species did not form probably because the aqueous media lacked of an appropriate counter ion for the stabilization of the TTF radical cation. Hence, in addition to the PBS another salt, namely sodium perchlorate, was used as electrolyte support in the ratio PBS/$NaClO_4$ 1/1, with the role of stabilizing the fixed charges arising from the $TTFS_2$ oxidation. In these new conditions the CV of S_{TTFS_2} showed an anodic peak centered at 0,27 V and a cathodic one at 0 V. The peak-to-peak distance was around 270 mV, so this means a quasi-reversible redox reaction, implying that the electron transfer between TTF and the gold surface is partially hindered (see (Figure 3.18 b)).

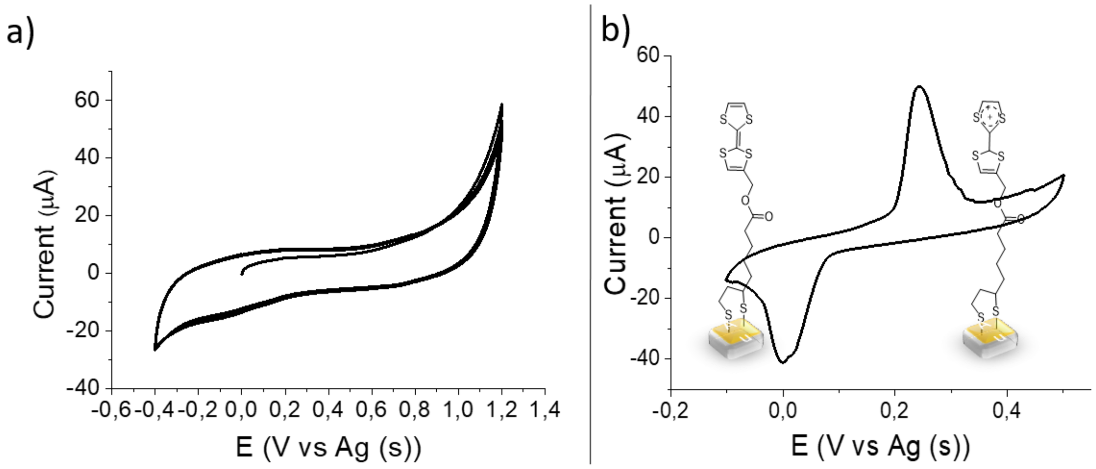

Figure 3.18: CV of S_{TTFS_2} at scan rate of 0,3 V/s. S_{TTFS_2} was used as working electrode, while a silver and platinum wire were used, respectively, as reference and counter electrode. As electrolyte it was used: a) an aqueous solution (100 mM) of a phosphate buffer solution (pH 6,9) b) a 100 mM solution of PBS and sodium perchlorate (1/1) in ultra-pure water.

The CV measurements enable us to choose the right electrolyte conditions to have a stable switch as well as the value of the bias potential needed to oxidize/reduce the $TTFS_2$ on the working gate. This information was necessary to perform the electrical measurements of our EGOFETs.

3.5.3 Influence of the S_{TTFS_2}switch in the EGOFET: device characteristics

The electrical characterization of the EGOFETs consisted of 5 steps listed here, that were systematically performed and repeated during many cycles of measurements.

1) Initial step: one electrical recording of the device connected to the reference gate and a further one connected to the $TTFS_2$ functionalized working gate was done. This latter measurement corresponds to $TTFS_2$ in its initial state.

2) Oxidation step: a potential difference equal to +0,6 V was applied for 15 seconds between the two gate electrodes (namely reference RG, and working WG) (RG was grounded). This electrical configuration allowed us to avoid any electrical stress at the organic semiconductor and to oxidize the $TTFS_2$ anchored on the WG to $[TTFS_2]^{\cdot+}$. It should be noticed that the selected potential is higher than that required for the oxidation/reduction to occur in the conditions seen above in the CV measurements. We elected to use a broad potential window considering the different setup as well as the absence of the reference electrode in the configuration used to perform the electrical characterization of the device.

3) Oxidation state recording: two I-V transfer characteristics were recorded. One using the WG with the SAM on its oxidized state ($[TTFS_2]^{\cdot+}$), and another one using the RG as a control test.

4) Reduction step: a pulse of -0.6 V was applied between WG and RG for 15 seconds. RG was always kept as ground terminal. In this way the $[TTFS_2]^{\cdot+}$ was reduced again to $TTFS_2$.

5) Reduction state recording: two I-V transfer characteristics were recorded using the WG and the RG.

Note: a single oxidation of $TTFS_2$ to $[TTFS_2]^{\cdot+}$ followed by the reduction of $[TTFS_2]^{\cdot+}$to $TTFS_2$ completes a single “oxidation – reduction cycle”.

The electrical performances of the devices using the two gate electrodes, WG functionalized by S_{TTFS_2} (WG-$TTFS_2$) and RG (bare Au) is shown in Figure 3.19. As it can be seen by looking at the figure, the two curves are shifted along the x-axis due to the fact that there is a difference in the device threshold value when the two gate electrodes are used.

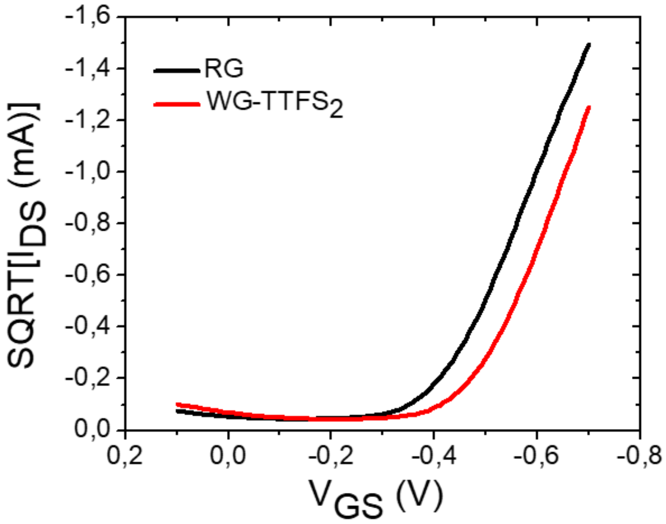

Figure 3.19: Transfer characteristic curves of the initial state recorded with RG (black) and WG-TTFS$_2$ (red) at V_{DS}= -0,4 V.

Subsequently, five whole oxidation-reduction cycles were performed, and the corresponding I-V transfer characteristics are shown in Figure 3.20.

The I-V transfer characteristics corresponding to the RG are substantially stable. On the other hand, when the TTFS$_2$ oxidation is carried out applying the positive voltage on the WG, an evident shift of the threshold voltage towards less negative values is observed in the EGOFET transfer characteristics, which leads to a clear increase of the drain-source current with respect to the reference gate. Further, when $[TTFS_2]^{\cdot+}$ is again reduced, the curves are shifted back giving again threshold voltages more negative than the one obtained with the reference gate at a fixed V_{GS}. Hence, at a specific fixed gate voltage, two different current intensity levels can be observed, one that corresponds to the WG with the S_{TTFS_2} in its neutral (reduced) state and one to its charged (oxidized) state. We can state that the devices are stable at least during some hours, namely for the whole time of the experiments.

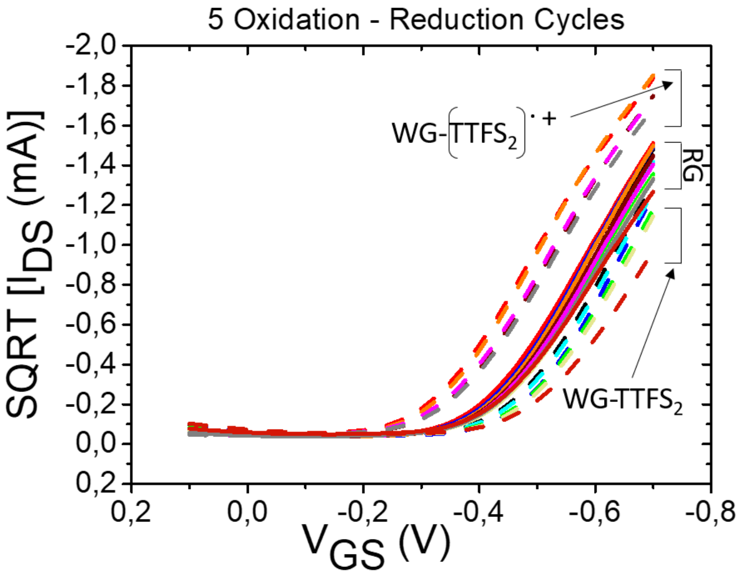

Figure 3.20: Overlay of transfer characteristic curves of a total of 5 oxidation-reduction cycles employing the RG (solid lines) and the WG (dashed lines) with V_{DS}= -0,4 V.

The molecular switch of the $TTFS_2$ changes the capacitance of the working gate, inducing the presence of additional charges onto the electrode surface. These charges strongly influence the double layer organization in the electrolyte/gate interface and, as a consequence, the capacitive coupling between the gate and the semiconductor. Thus, it is reasonable to observe a threshold voltage shift as the main effect in our devices. Specifically, a modulation in the V_{TH} of more than 200 mV is reached. Figure 3.21 represents the signal shift of the threshold voltage with respect to the reference bare gold electrode. Furthermore, the cycles show that the change of threshold voltage is reproducible and reversible, while the EGOFET performances related to the reference gate remain invariant throughout the experiment.

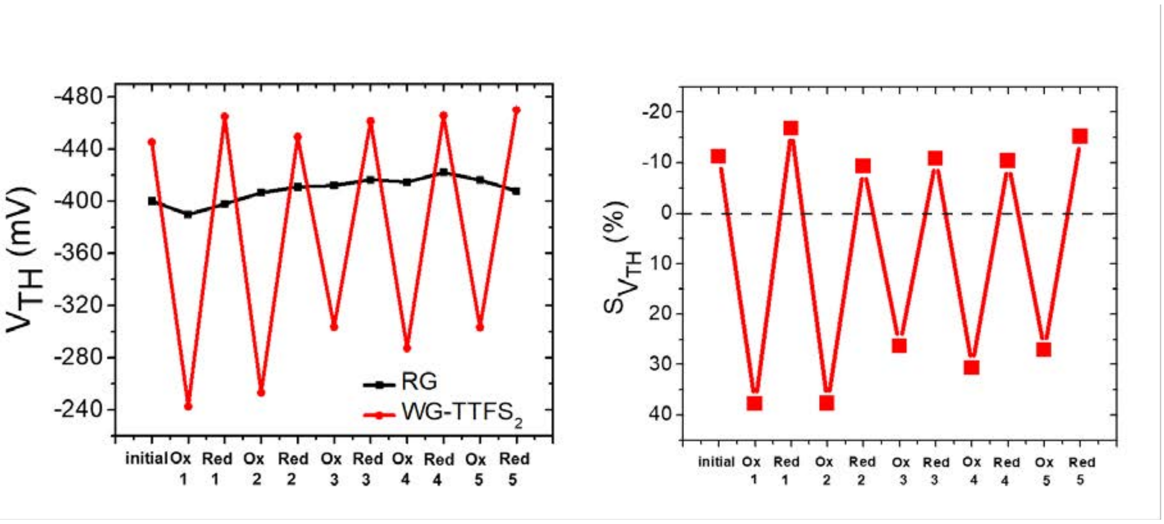

Figure 3.21: Left: threshold voltage shift of a total of five oxidation-reduction cycles. Right: percentage of the threshold voltage signal switch of WG-$TTFS_2$ with respect to RG.

Another approach to visualize the clear change of the electrical performances consists of extracting the transconductance. This parameter is the first derivative of the drain-source current with respect to the gate-source voltage. Transconductance gives a coherent result with respect to the one of the threshold voltage. This parameter is modified at 0,35 V up to 300% for the working gate, whereas the reference gate is almost invariable (see Figure 3.22).

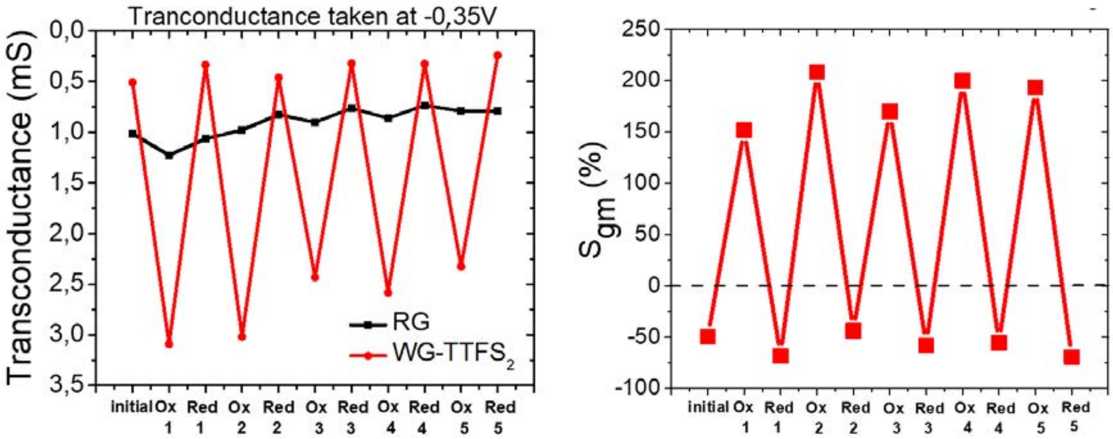

Figure 3.22: Transconductance voltage shift of a total of five oxidation-reduction cycles (left) and percentage of the transconductance voltage signal switch of WG-$TTFS_2$ with respect to RG (right).

In order to certify that the threshold voltage shift and the transconductance changes are ascribable only to the redox features of the TTF-based SAM, two cross-checks were performed. The former was the direct comparison between two bare Au gate electrodes. The latter consisted of using a SAM composed by an decanethiol, which guarantees the formation of a well-packed non electroactive SAM.

Hence, with regard to the first blank test, two gold electrodes were assembled to the EGOFET device within the microfluidics chamber. The protocol of the electrical measurements was performed without any change but now the WG and the RG were both bare gold electrodes without any functionalization. Figure 3.23 represents the initial state of the two bare gold electrodes, on which it can be seen that the current values, transconductance and threshold voltage are equal with both gates.

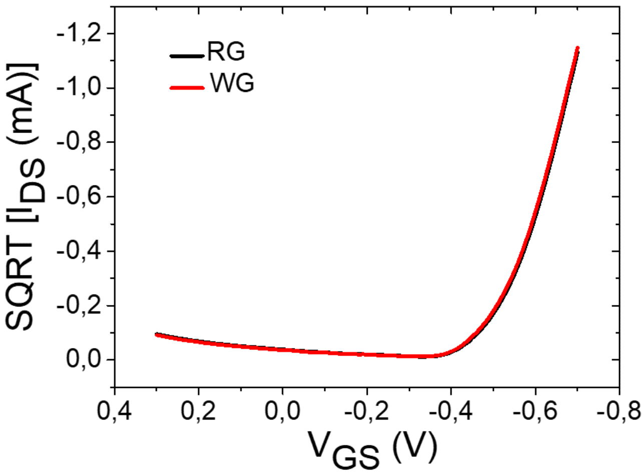

Figure 3.23: Transfer characteristics of the EGOFET with two bare gold electrodes with V_{DS}= -0,4 V.

The same electrical switch cycles were performed as previously described and the threshold voltage and transconductance values obtained throughout three oxidation-reduction cycles are represented in Figure 3.24.

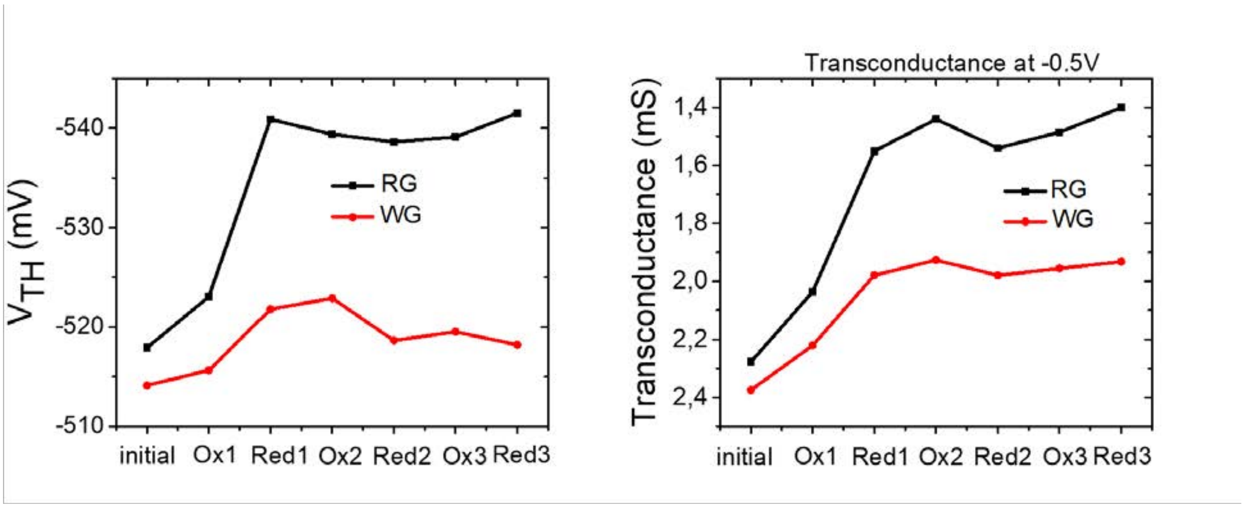

Figure 3.24: Threshold voltage (on the right) and trasconductance (on the left) values found for 3 oxidation-reduction cycles using bare Au electrodes as RG and WG.

As it is possible to observe, the electrical behavior of the threshold voltage and transconductance are coherent between each other and no significant changes are recorded as consequence of the different bias application. In fact, the fluctuation of the threshold voltage is around 5 mV, which is consistent with the normal fluctuation of this device. Transconductance is changing in less than 0.5 mS. This experiment proves that the previous effects observed with the WG functionalized with S_{TTFS_2} are not simply due to the polarization of the metal electrode.

In the last cross-check performed, the WG electrode was functionalized with 1-decanethiol instead of using $TTFS_2$, while the RG was bare gold as usual. The conditions reported in Table 3.3 were used to achieve the functionalization.

Table 3.3: List of conditions for the gate functionalization with 1-decanethiol.

Substrate	SAM	Solution	Immersion Time
Gold	$S_{1\text{-decanethiol}}$	1 mM of 1-decanethiol in ethanol	1h

The transfer characteristic curves were taken employing both of gate electrodes within each step of the oxidation-reduction cycle, following the usual protocol. Since 1-decanethiol does not have a redox-active group, no changes in the threshold voltage neither in transconductance should be observed throughout the oxidation-reduction cycles. As it can be seen in Figure 3.25, initially there is a clear difference between the currents of both electrodes, where the WG -decanethiol has a lower current value in comparison to the bare gold. Moreover, it shows the same threshold voltage shift of the initial TTF-based SAM gate, in comparison with the bare gold electrode. This proves the intrinsic relationship between the interfacial charges present at the gate surface and the threshold voltage. Once adsorbed an organic material onto the gate electrode, a negative shift of the threshold takes place due to a capacitive weakening between the gate electrode and the organic semiconductor.

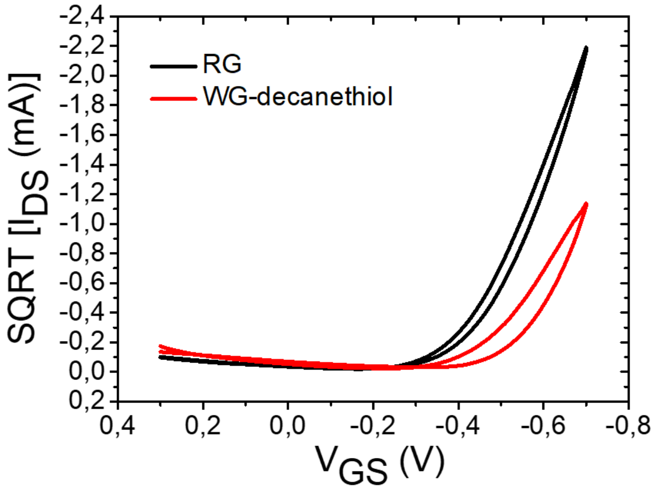

Figure 3.25: EGOFET transfer characteristics in the initial state, where the red line corresponds to the decanethiol functionalized gate and the black line to the RG. V_{DS}= -0,4 V.

Importantly, as observed in Figure 3.26, within the redox cycling no significant changes are occurring. By extracting the threshold voltage and transconductance values it can be observed that there are almost no variation of the values between the “oxidised” and “reduced” state simulation (i.e., by applying positive and negative voltages pulses to the WG with respect to RG before recording the transfer curves).

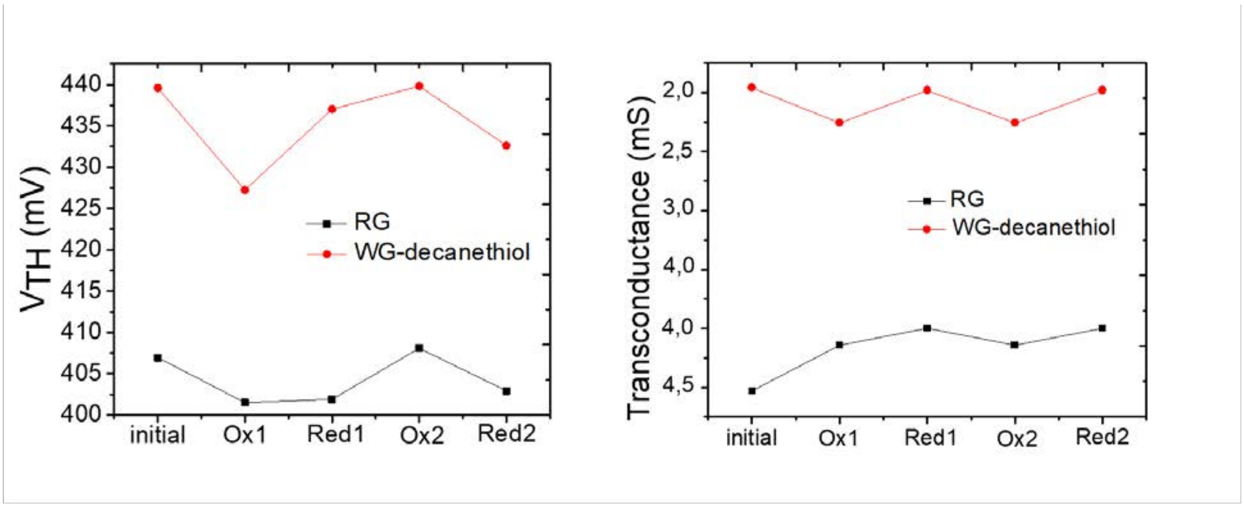

Figure 3.26: Threshold voltage (left) and trasconductance (right) values within two oxidation-reduction cycles employing RG and WG functionalized with 1-decanethiol.

For comparison, the data taken from the WG-decanethiol simulated switch experiment with the data obtained from the switch of WG-TTFS$_2$ have been overlapped in Figure 3.27. It appears clear that the changes in the threshold voltage as well as the gain in the transconductance are exclusively present in the case of WG-TTFS$_2$ molecule, while the changes with the WG-1-decanethiol experiment are almost negligible. Hence it can be stated that the TTF moiety is the only responsible for the electrical changes observed in the previous experiments, which are ascribed to the redox switching of the S_{TTFS_2}.

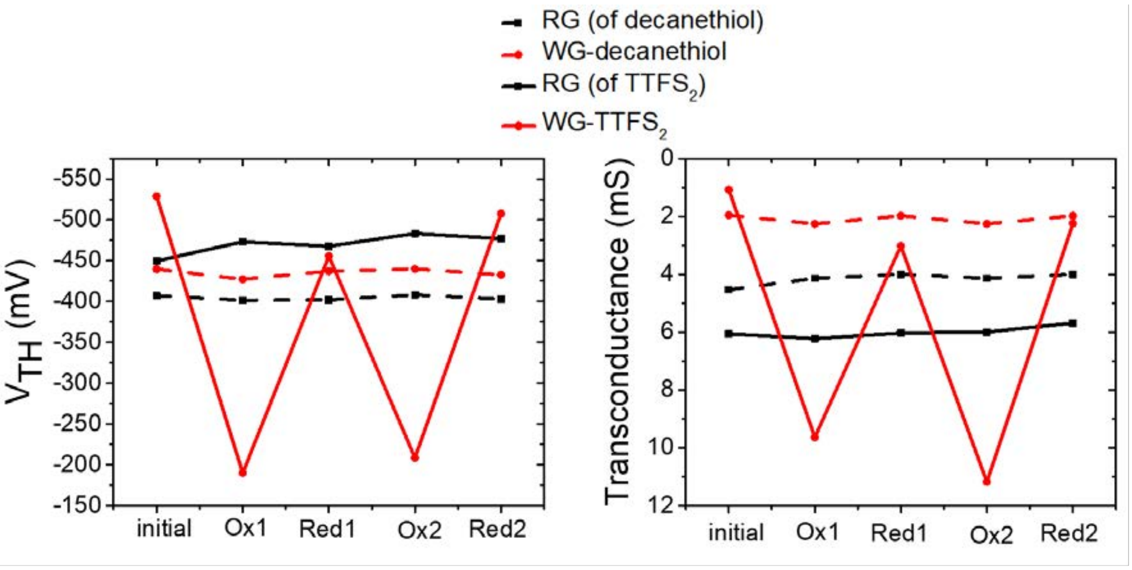

Figure 3.27: Overlap of the threshold voltage (left) and trasconductance (right) values within two oxidation-reduction cycles using the WG electrodes functionalized with 1-decanethiol and TTFS$_2$ with their corresponding RG.

3.5.4 Summary

Resuming, a full-standing EGOFET encapsulated on top by a customized microfluidic chamber was fabricated. Thanks to the presence of two top gate electrodes, this chip allowed us to study the effect of the functionalization of one gate electrode but having always a control gate to make sure of the proper operation of the device. The working gate electrode was functionalized with an electroactive TTF-based SAM and the response of the EGOFET was investigated in the two redox states of the SAM. The results showed unambiguously that WG-TTFS$_2$ yields a switchable electrolyte-gated organic field-effect transistor. Test experiments proved that the redox properties of TTFS$_2$ are the solely responsible for our switchable devices. Thus, we showed for the first time that by introducing electroactive molecules on the gate electrode of an EGOFET we have an additional parameter to control the device properties. This high control level can open new perspectives for their application in sensors or in memory devices, considering each switch state as one bit memory.

3.6 BTTFS$_2$ as molecular rectifier [3]

3.6.1 Molecular wires and rectifiers

The study of molecular charge transport is of great importance in the field of molecular electronics. The interest lies on the future technological implications that it could have the production of electronic devices of sub-nanometric dimensions [242]. In order to carry out these investigations, the fabrication of devices made by an organic molecule trapped between two electrodes is required. This kind of studies face countless difficulties principally related to presence of numerous contributions to the global charge transport of a molecular system. In fact, it must be considered the influence of the molecular structure along which the charge flows, but also the phenomena that occur at the interfaces metal-electrode/molecule.

Different approaches are reported to realize these three component devices (i.e. electrode/molecule/electrode). The important requirement is the realization of stable junctions with the final goal of having the control over the properties that such molecular devices show.

One of the possible approaches for the exploration of the molecular transport properties consists in the use of SAMs on metals instead of single molecules. The use of SAMs present numerous advantages in comparison with the single molecular junctions principally due to the simpler fabrication steps, which make their application in organic electronics more promising.

In these systems the substrate where the SAM is grown acts as one of the electrode, while the second electrode can be realized by 1) an Atomic Force Microscope (AFM) [243, 244] or Scanning Tunneling Microscope (STM) tip [245, 246, 247]; 2) a metal, generally gold, that is evaporated on the SAM; 3) a conductive polymer, such as poly(3,4-ethylenedioxythiophene) polystyrene sulfonate (PEDOT:PSS) [248] or polyaniline (PANI); 4) a liquid metal, such as Hg or the liquid eutectic of gallium and indium (EGaIn), the so-called “EGaIn” electrode (Figure 3.28).

In particular, the use of liquid metals is specially appealing since it ensures a soft non-damaging contact at room temperature. It presents also other numerous advantages such as:

1) the minimization of the contact force that could have influence on the charge transport and that is always present when an AFM tip is used [249, 250];

2) the metal droplet does not penetrate into the SAM as it could happen in the case of

---

[3] This work was done in collaboration with Prof. Christian A. Nijhuis.

evaporated gold electrodes [251];

3) it does not interact with the SAM, while a interaction could happen when conductive polymers are used [252];

4) it allows the formation of well defined structures metal/molecule/metal;

5) finally, it permits to record a large number of data ensuring by on statistical analysis the validity of the results.

Liquid electrodes were proposed by Whitesides that used mercury first [253, 254] and EGaIn eutectic later on [255]. The EGaIn eutectic has advantages over the use of mercury since the latter needs to have a protective layer, usually formed by a SAM of a short alkyl chain, to confer stability to the electrode. This protective layer can add resistivity [256]. On the other hand, the drop of eutectic EGaIn reacts spontaneously with oxygen present in the air forming a thin layer of Ga_2O_3, which enables the drop to remain stable and conical under ambient conditions ensuring a better contact with the SAM [213]. In addiction to that, EGaIn electrode is not toxic, is commercially available, is easy to manipulate (can be deposited with a pipette or syringe without applying high temperatures or vacuum) and has a low vapor pressure.

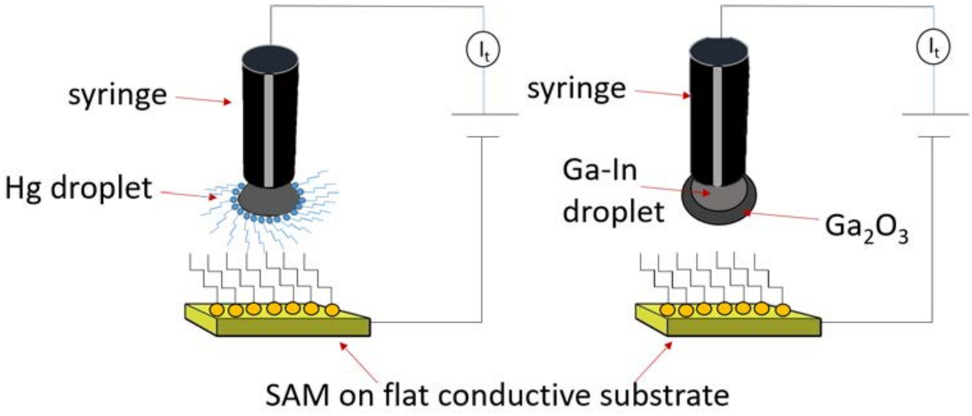

Figure 3.28: Illustration of a liquid metal setup. A syringe containing a liquid metal is brought into contact with a surface . The metals used are mercury coated with a SAM on the left, and the mixture of Ga and In alloy on the rigth. Electrical characterization is carried out using the back of the syringe to contact the metal drop.

3.6.2 Molecular rectifiers

The concept of molecular rectifier was born in 1974 from a theoretical idea of Aviram and Ratner [188], and actually it was one of the first steps initiating the field of molecular electronics. In their article published in Chemical Physics Letters, Aviram and Ratner defined an organic rectifier as an organic molecule having roughly the properties of a p-n junction. They started from the knowledge that, by the use of substituent groups on aromatic systems it is possible to increase or decrease the π-electron density within the molecule and hence to create sub-units with electron poor (p-type) or electron rich (n-type) character. Hence, they proposed as theoretical molecular rectifier, molecules connected between two electrodes having both, a donor and an acceptor site (D-A) effectively insulated from each other. The separation was accomplished by the use of a sigma-electron system (insulating bridge) between the D-A sub-units. In that molecular junction, electrons would be expected to pass only from cathode to acceptor, from acceptor to donor and finally from donor to anode, with unidirectional electron flow and, therefore, showing the rectification of current.

So, accordingly to the theoretical model described by Aviram and Ratner, a rectifying behavior can be achieved in acceptor-bridge-donor systems (A-B-D), where the presence of a bridge is responsible for the isolation of the two units (D and A) so they do not interact with each other.

Based on this idea, many groups devoted great efforts to the study of the properties of transport in D-A systems to get current rectification [257, 258].

Nevertheless, Nijhuis et al. have reported systems with rectifier behavior even if they were formed by an insulating part (alkylic chain) and a single electroactive part (ferrocene) [213].

In these systems, the rectification, R, was evaluated at ± 1 V in unions based on SAMs on flat Ag of derivatives of alkanethiols functionalized with ferrocene "$Ag^{TS}SC_nFc$ // Ga_2O_3 / EGaIn", where | J (V) | is the absolute value of the current density (A / cm^2) as a function of the voltage:

$$R = \frac{|J(-V)|}{|J(V)|} \tag{3.4}$$

The charge transfer through the SAMs was systematically studied by Nijhuis et al. using the EGaIn method. In these studies, the influences of the length of the insulating bridge as well as the proximity of the electroactive moiety (ferrocene or bi-ferrocene) to each electrode (Figure 4.32) was investigated.

In such way, they explored two effects: they varied the shape and width of the tunnelling barrier presented by these SAMs and, in addition, they varied the electronic coupling of each electrode with the highest occupied molecular orbital (HOMO) of the ferrocene (Fc) or bi-ferrocene (Fc_2) units. By changing the coupling between the HOMO and the electrodes, they verified the mechanism of rectification proposed by William et al. and Baranger et al. [259, 260] according to which in non symmetric systems, the HOMO is strongly coupled to one electrode while it is not equally coupled to the other one. Therefore, it becomes easily accessible exclusively in one direction of polarization. Accordingly, they reported that in the case of simple alkanethiols chains as well as in SAMs where the electroactive moiety is exactly in the middle of the chain (symmetric systems), no rectification is obtained. However, when the Fc or Fc_2 groups are at the end of the alkyl chain a rectification of $R > 10^2$ was registered. Thanks to these experiments it is possible to state that to obtain a system with rectifier behavior, an electroactive moiety as well as a certain degree of asymmetry is required.

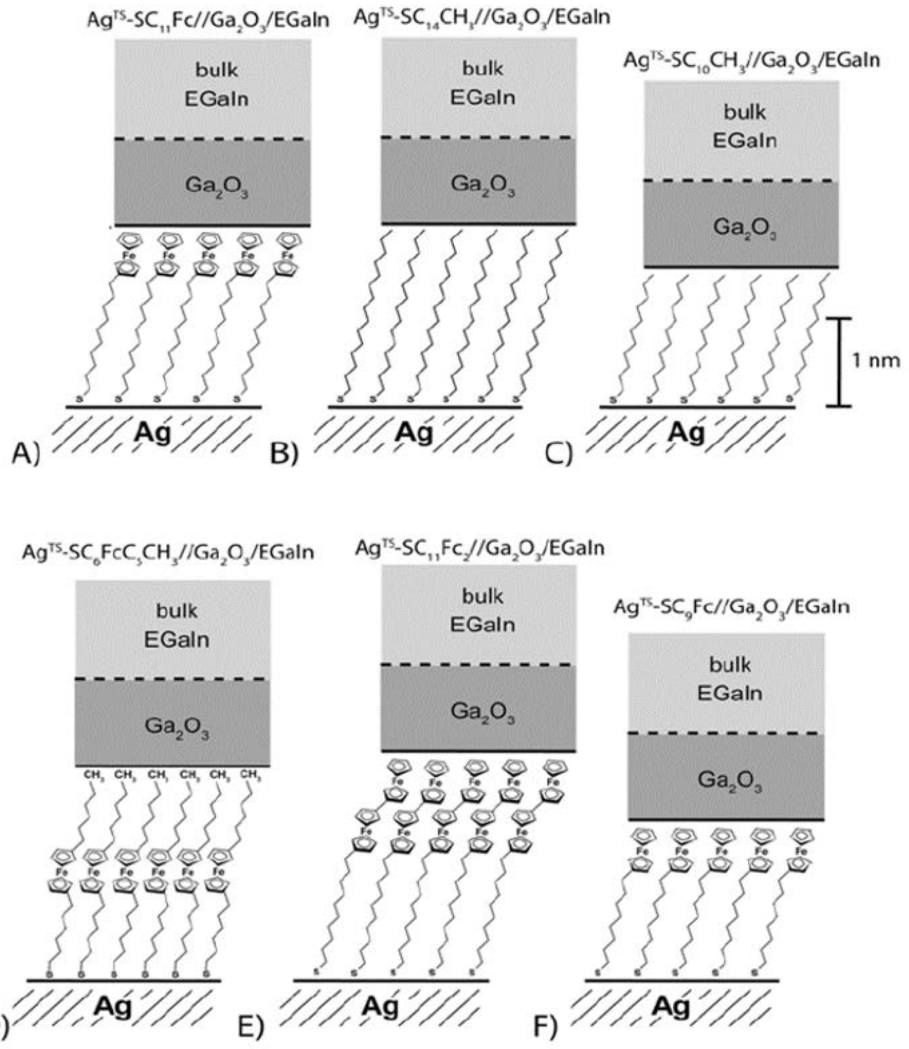

Figure 3.29: Junction Ag^{TS}-$SC_nFc//Ga_2O_3/EGaIn$ analyzed by the group of Nijhuis [213].

In particular, the results reported with the system "Ag^{TS}SC$_{11}$Fc // Ga$_2$O$_3$ / EGaIn" are shown in the Figure 3.30 a) that shows a histogram of all 997 values of |J| collected at -1.0 V on 53 Ag^{TS}-SC$_{11}$Fc//Ga$_2$O$_3$/EGaIn junctions. The Gaussian fit to this histogram gives the log-mean and log-standard deviation for |J(-1 V)|. In the black “average trace”, these log-means determine the data points, while the log-standard deviations determine the error bars (white). The average trace is superimposed on all 997 traces recorded for the Ag^{TS}-SC$_{11}$Fc//Ga$_2$O$_3$/EGaIn junctions. In Figure 3.30 b) the proposed energy level diagrams are shown.

The results were rationalized as follows: at sufficient forward bias (Ga2O3/EGaIn is negatively biased) that is when the Fc HOMO is energetically accessible, the conductive portion of the SAM does not significantly hinder charge transport, and the insulating (CH$_2$)$_n$ portion of the SAM constitutes the sole tunneling barrier presented by the SAM. At reverse bias (Ga2O3/EGaIn is positively biased), the HOMO is inaccessible, and both the conductive and insulating portions of the SAM together (the entire C$_{11}$Fc group) form the barrier to tunneling. Thus, charges encounter a wider tunneling barrier at reverse bias than at forward bias. Since tunneling current decreases exponentially with increasing width of the barrier, a higher current flows at forward bias than at reverse bias, and the junction rectifies.

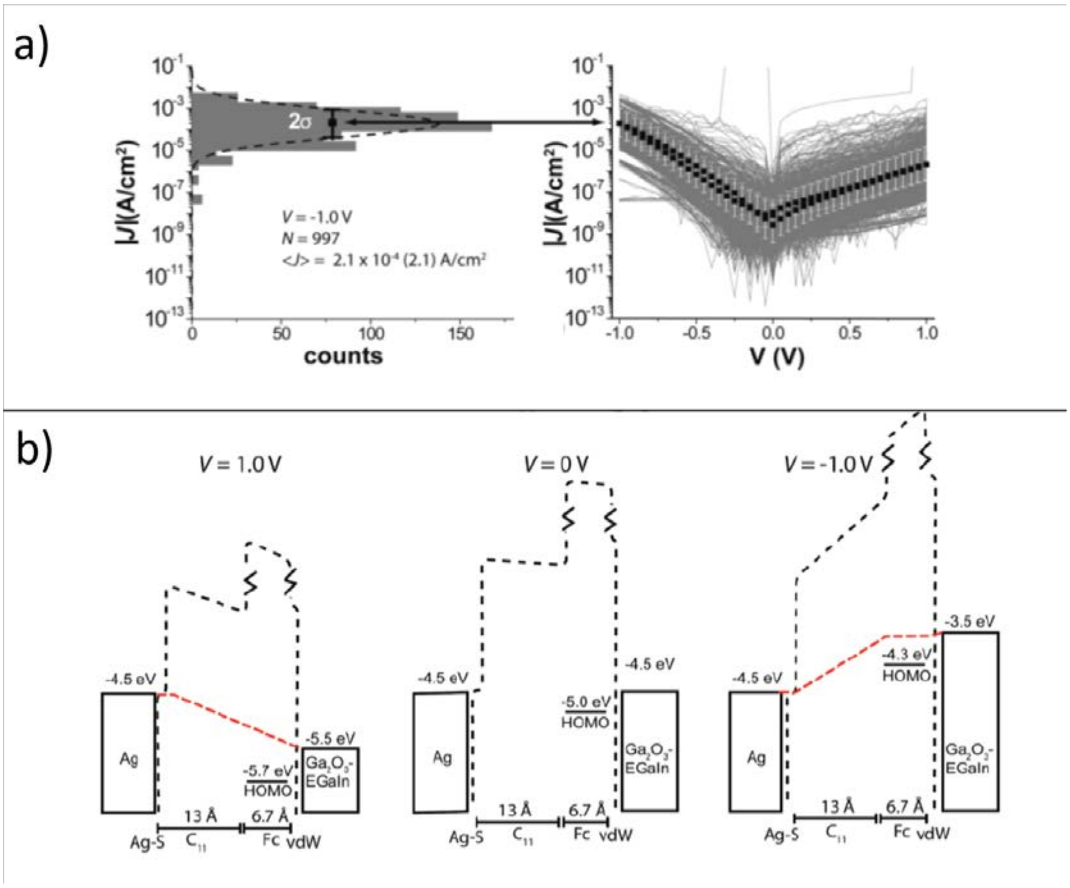

Figure 3.30: a) On the right, the histogram of the values of J measured at V = -1.0 V obtained for Ag^{TS}-$SC_{11}Fc//Ga_2O_3/EGaIn$ junctions, with a Gaussian fit to this histogram giving the log-mean value of J and the log-standard deviation. On the left the average trace of the Ag^{TS}-$SC_{11}Fc//Ga_2O_3/EGaIn$ junctions superimposed over all 997 traces collected on these junctions. b) Schematic representation of the level energy diagram at V= 1, 0 and -1 V [213].

Starting from that knowledge and in collaboration with the group of Prof. Nijhuis, we decided to explore how this theory can be extended to other electroactive molecules to obtain new rectifiers based on a single accessible molecular orbital. So we designed and synthesized a molecule with the same insulating bridge of $SC_{11}Fc$ but modifying the electroactive part by a tetrathiafulvalene unit. Specifically we chose $BTTF_2$ which synthesis and characterization have been already described in Section4.3.

The formation and the characterization of SAMs of $BTTF_2$ on gold (S_{BTTS_2}) is here reported as well as some preliminary results of rectification.

3.6.3 Preparation and characterization of S_{BTTS_2}

The SAM $S_{BTTS_2}$was prepared on a substrate of 50 nm of gold (111) evaporated on glass. As usual, the substrates were firstly washed, sonicating in a series of HPLC pure-grade solvents (dichlorometane, acetone and ethanol), then activated through UV-Ozone cleaner treatment, left in ethanol for 20 minutes and finally immersed in the solution of the molecule of interest (see Table 3.4 for the conditions). The process was carried out under Argon atmosphere and with light exclusion.

After 24h, the substrates were washed with toluene and analyzed by different techniques such us water contact angle, ToF-SIMS and CV, in order to demonstrate the ability of BTTFS$_2$ to self-assemble on gold in the used conditions.

Table 3.4: List of conditions for the formation of SAM S_{BTTS_2}.

Substrate	SAM	Solution	Immersion Time	Temperature
Gold	S_{BTTFS_2}	0,5 mM BTTFS$_2$ in Toluene	24h	3h 45ºC; 21 h R.T.

The CA measurements were carried out depositing 5 μL of ultra-pure water on the functionalized surface obtaining the value of 82,0º ± 1,8º. This value of contact angle agrees with the presence of a phenyl ring on the surface [261].

Furthermore, from the ToF-SIMS analysis the peaks corresponding to the molecule anchored as well as some characteristic fragmentation peaks were observed, as reported in Figure 3.31.

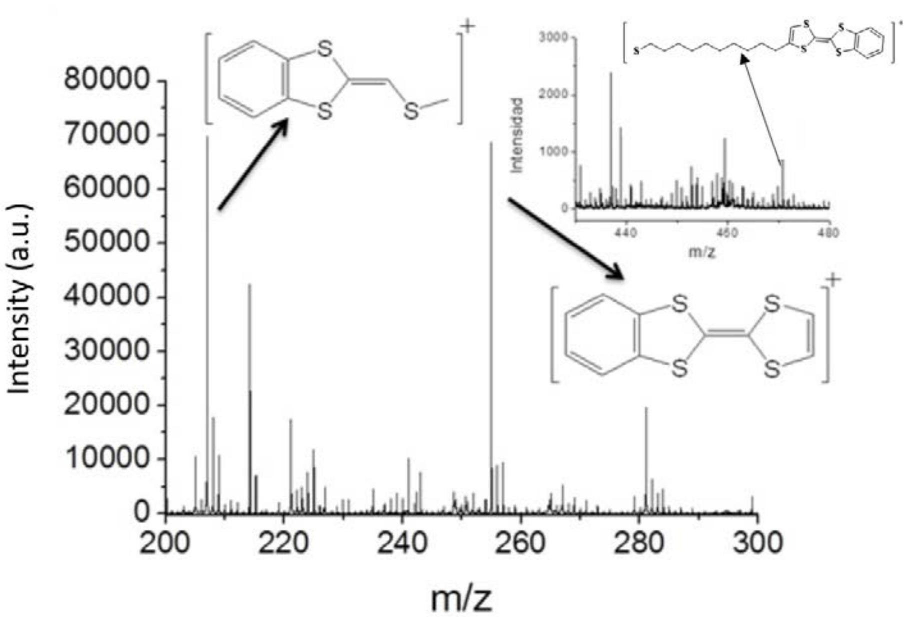

Figure 3.31: ToF-SIMS analysis of S_{BTTS_2}.

Moreover S_{BTTS_2} was characterized by electrochemical techniques. Its electrochemical properties were studied by CV using as electrolyte a 0,1 M solution of $LiClO_4$ in acetonitrile. The first oxidation process to the radical cation was observed at $E^1_{1/2}$ = +0,54 V vs Ag (s) and the formation of the dication was detected at $E^2_{1/2}$ = +0,87 V vs Ag (s), as it can be observed in Figure 3.32 a).

Hence, it can be stated that the formation of the SAM S_{BTTS_2} was successfully achieved.

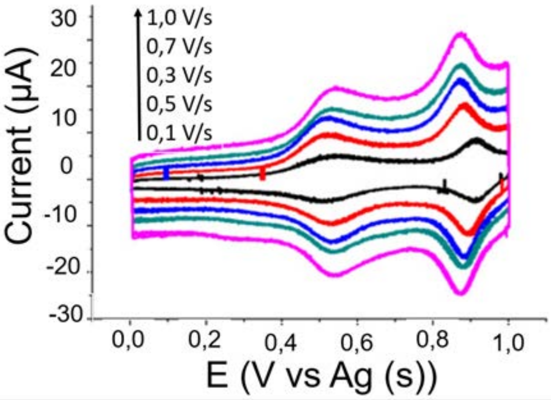

Figure 3.32: CV of S_{BTTS_2} a) 0.1 M solution of $LiClO_4$ in acetonitrile vs Ag (s).

The SAMs for the charge transport measurements were grown on template stripping (TS) surfaces in order to achieve ultra-flat and clean substrates. These surfaces were manufactured following a procedure well described in literature [262, 263, 264]. The fabrication process consists in depositing the metal onto a very flat Si/SiO_2 substrate by evaporation. Then, the metal is transferred on a glass substrate through a mechanical stripping, as better discussed in the experimental section. Hence, once fabricated, the substrates were directly immersed in the solution containing $BTTFS_2$ following the previously mentioned conditions. The SAMs thus obtained were characterized by XPS to achieve information particularly useful in charge transport studies, such as the SAM thickness and the orientation of the molecules on the surface.

Specifically, by the Angle Resolved XPS measurements (ARXPS), shown in Figure 3.33, the SAM thickness was estimated from the Au-S S2p peaks and was found to be 21,3 Å (including Au-S bond = 1,8 Å). The coverage was calculated from the S2p/Au4f peak at normal emission (ϑ = 900) yielding 2,16 x 10^{-10} mol/cm^2 .

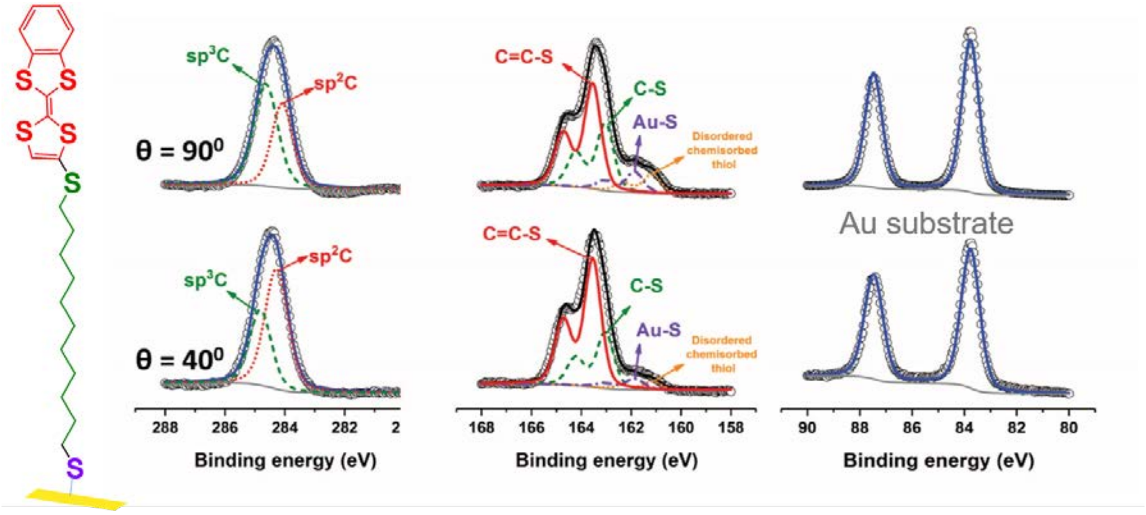

Figure 3.33: ARXPS measurements of Au^{TS} S$_{BTTS_2}$.

Furthermore, from the values of the binding energies for C1s, it is possible to get information on the position of the TTF core on the surface. It can be seen that at normal emission (ϑ = 90°) the contribution of the alkyl part (BE = ~284,8 eV) is higher than that of the TTF moiety (BE = ~284 eV), whereas the situation is reversed for the normal incidence (ϑ = 40°). These results indicate that the TTF moiety is facing upright.

3.6.4 Charge transport through S$_{BTTS_2}$

Since, as previously mentioned, S$_{BTTS_2}$ has been fabricated to investigate the mechanism of charge transport in EGaIn junctions, the diagrams of the energy levels for that SAM were qualitatively analyzed (Figure 3.34). In these diagrams it can be seen how the molecule is bonded to the lower Au electrode thanks to the sulfur atom followed by the aliphatic chain. Finally, the molecule ends with the electroactive part (TTF moiety) that is located next to the Ga_2O_3 / EGaIn electrode. The HOMO level, which is the orbital that can participate in the transport process, is ilustrated between the two electrodes as well as the metal workfunctions at different bias voltage.

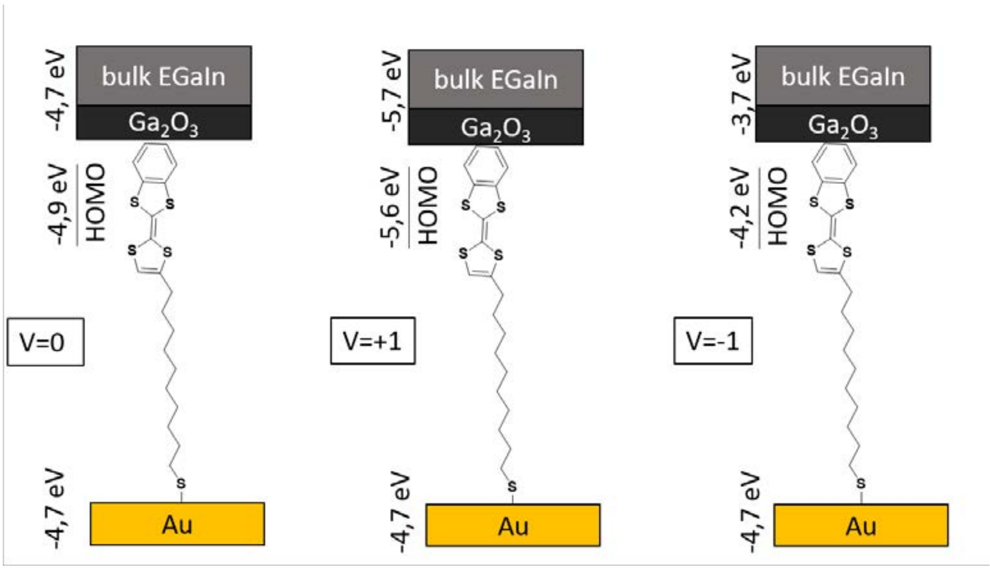

Figure 3.34: Schematic representation of the $Au^{TS}S_{BTTS_2}//Ga_2O_3/EGaIn$ junction and energy levels involved.

The work functions of the two electrodes are reported in the literature, and have values of 5,1 eV in the case of the Au, and 4,3 eV for the Ga_2O_3 / EGaIn electrode. In the initial state the circuit is open (V = 0 V) and the Fermi levels of both electrodes are aligned with an intermediate value of -4,7 eV. The energy of the HOMO of $BTTS_2$was determined by the cyclic voltammetry data previously described (Figure 3.32 a)). Indeed, HOMO (E_{HOMO}) and the LUMO (E_{LUMO}) energies of a molecule can be estimated from its redox potentials versus Fc / Fc $^+$ using the following equations:

$$E_{HOMO} = -E_{OX}^{\frac{1}{2}} vsFc - 4,8eV$$

$$E_{LUMO} = -E_{RED}^{\frac{1}{2}} vsFc - 4,8eV$$

where E_{ox} $^{1/2}$ vs Fc and E_{red} $^{1/2}$ vs Fc are respectively the oxidation and reduction potential of the electroactive species, while 4,8 eV is the energy value of Fc/Fc$^+$ under vacuum.

In this way, the estimated value of the HOMO of $BTTS_2$was calculated to be -4,9 eV at open circuit. When a potential of ± 1 V is applied, the Fermi level of the Ga_2O_3 / EGaIn electrode increases or decreases its initial value moving 1,0 V with respect to the gold level.

According to Nijhuis theory [213], also the levels of the molecular orbitals move along with Fermi level even if just in part, that is 0,7 V. Hence, 0,3 V are lost as potential drop caused by van der Waals forces at the interface SAM //Ga$_2$O$_3$.

As in the case of the Fc SAMs previously discussed, for our system we expected to get high current densities when a negative potential around -1 V is applied to the electrode Ga$_2$O$_3$ / EGaIn, since in this case the HOMO could participate in the transport mechanism because it would be sitting in between the workfunction energy of the two electrodes. However, if the potential applied is positive, the HOMO level would approach the Fermi level of the electrode EGaIn and, therefore, no clear conclusions could a priori be drawn on the possible rectification of the system because of the inaccuracies in the estimation of the orbital energies.

Nevertheless, the transport measurements performed in the system Au^{TS}S$_{BTTS_2}$//Ga$_2$O$_3$/EGaIn showed opposite behavior compared with the system "Ag^{TS}SC$_{11}$Fc // Ga$_2$O$_3$ / EGaIn". In other words, it has a rectifier behavior at positive voltage value (see Figure 3.35). In particular, the results obtained are reported in Figure 3.35 where the the average trace is superimposed on 352 traces recorded while the histograms show all 352 values of |J| collected at +1,5 V and at -1,5V. Several measurements were performed on different SAMs batches, confirming the results.

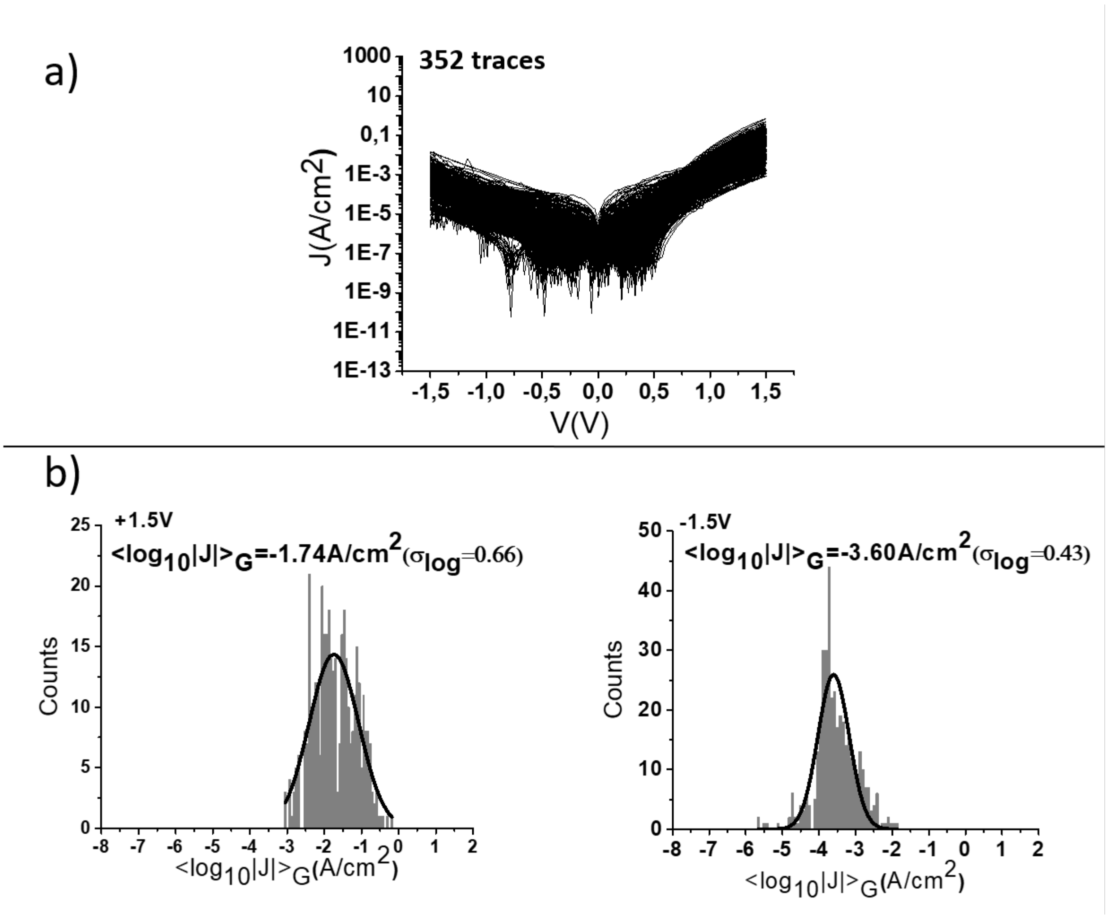

Figure 3.35: a) Average trace of the $Au^{TS}S_{BTTS_2}//Ga_2O_3/EGaIn$ junctions superimposed over all 352 traces collected on these junctions. b) Histogram of the values of J measured at V = ± 1,5 V obtained for $Au^{TS}S_{BTTS_2}//Ga_2O_3/EGaIn$ junctions, with a Gaussian fit to this histogram giving the log-mean value of J.

Currently, other experimental measurements as well as theoretical calculations are underway to find a rationalization for the results achieved. One possible explanation could involve the interactions that take place between the TTF molecules in the well packed S_{BTTS_2} SAM.

3.6.5 Summary

This project arises from the necessity to shed light on the mechanisms of charge transport in SAMs analogous to those already studied in the group of Prof. Nijhuis, through EGaIn junctions. Hence, S_{BTTS_2} was fabricated, characterized and employed in studies of current rectification. The system showed a rectifying behavior at positive bias potential, contradicting the forecasts. Currently, further experiments as well as theoretical calculations are underway in Nijhuis' group, aiming at confirming the experimental evidence already obtained and, mainly, trying to rationalize them. The results could open the way towards the fabrication of new electronic devices with the role of current rectifiers.

4

Polychlorotriphenylmethyl derivatives

In the following chapter polychlorotriphenylmethyl (PTM) derivatives will be introduced as electroactive molecules. Specifically, the PTM radical silane derivative r-PTMsil, was used to functionalize indium tin oxide (ITO) with the aim of realizing a switchability study on a transparent electrode. The electrochemically stimulated conversion of the PTM core between radical ($[PTM]^{\cdot}$) and anion ($[PTM]^{-}$) states was followed by monitoring the magnetic and optic response of the modified ITO electrode, giving rise to a reversible switch stable over more than ten cycles.

Moreover, r-PTMsil, together with the corresponding non electroactive derivative αH-PTMsil, was subsequently integrated in p- and n-type OFET devices, by functionalizing the SiO_2 dielectric. The influence of these two molecules on the device performance was tested. In the case of OFETs functionalized with r-PTMsil, it was not possible to charge this monolayer by the application of an electric pulse as it was anticipated. However, interestingly we observed that the dipole moments of the different SAMs had a clear impact on the device performances. In particular, in fullerene C_{60} -based OFETs the presence of r-PTMsil at the dielectric/semiconductor interface impeded the device to switch on and, when r-PTMsil was integrated in pentacene-based OFETs, the device performances substantially decreased. Contrariwise, when αH-PTMsil was introduced in the pentacene-based OFETs, an enhancement of the device performance was reached, with mobility values improving one order of magnitude.

Finally, in the last part of the chapter the electrochemical characterization of the poly-radical r-PTMpol will be described. This polymer was designed and synthesized with the aim of fabricating a new attractive material for charge storage applications. Because of this, carbon based electrodes modified with r-PTMpol were fabricated and used as working electrodes in cyclic voltammetry measurements. It was found that the diffusion coefficient of lithium ion in polymer r-PTMpol, in a first approximation, has a value comparable to those reported for lithium intercalation. This indicates the good electrochemical behavior of r-PTMpol when it is used as electron active material as well as the viability of this compound in charge storage devices.

4.1 Objectives

The objectives of this chapter can be resumed as follows:

1) Design and synthesis of polychlorotriphenylmethyl (PTM) derivatives αH-PTMsil, r-PTMsil and r-PTMpol, shown in Figure 4.1.

2) Characterization of the SAM $S_{\text{r-PTMsil}}$ and study of its switching behavior using optical and magnetic outputs.

3) Integration of the PTM derivatives in devices:

A) Introduction of αH-PTMsil and r-PTMsil derivatives in p- and n-type OFET devices by the functionalization of the SiO_2 dielectric, and study of their influence on the device performance.

B) Electrochemical characterization of r-PTMpol as a possible new material for charge storage devices.

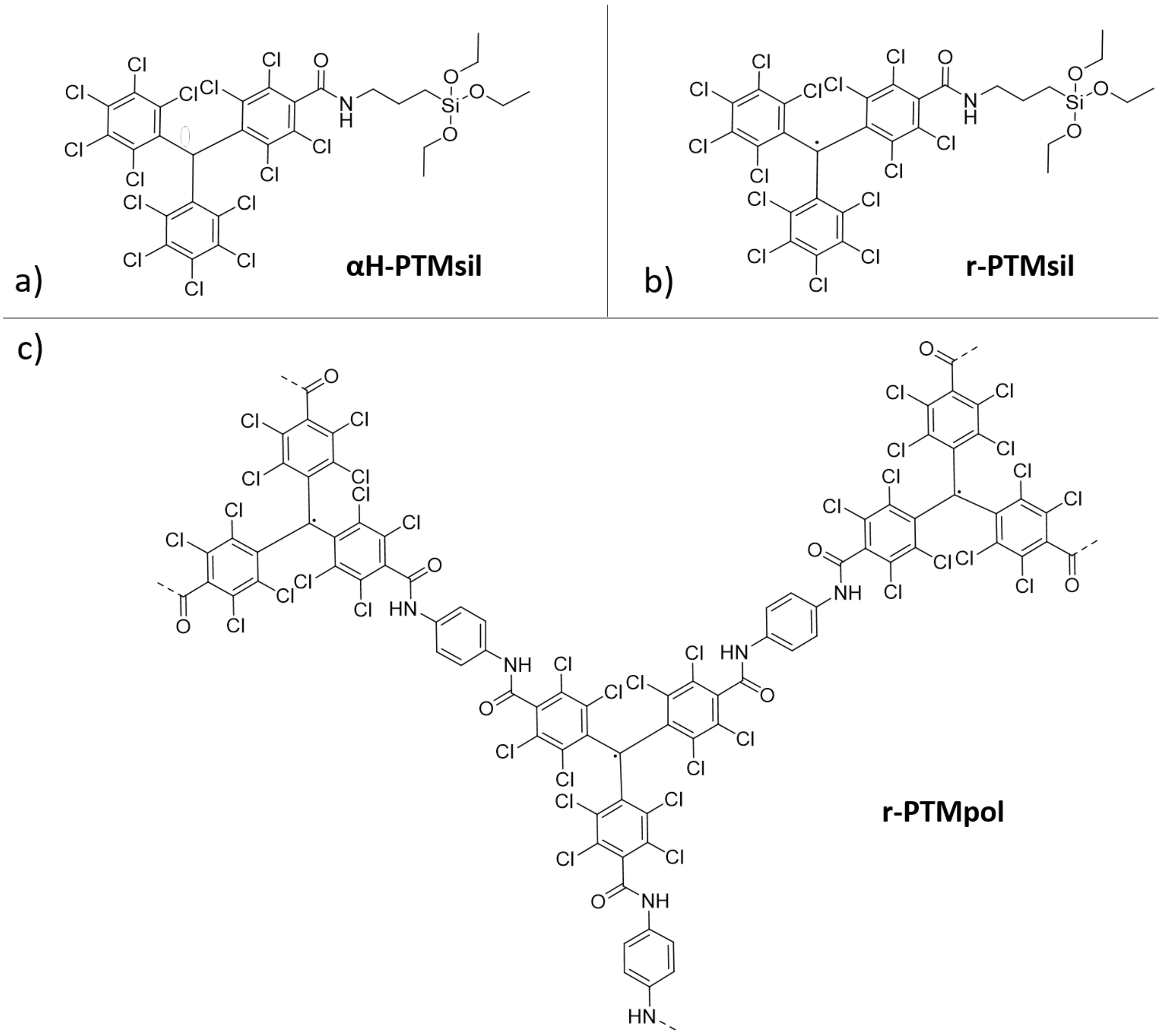

Figure 4.1: Structure of PTM derivatives used.

4.2 Introduction to polychlorotriphenylmethyl radicals

Polychlorotriphenylmethyl (PTM) radicals are stable organic radicals composed by three partially or totally chlorinated benzene rings connected to a central carbon with sp2 hybridization, known as α-carbon. The six bulky chlorine atoms in ortho positions provide steric shielding to the α-carbon, where the spin density is mostly localized, conferring a great chemical and thermal stability to these molecules (Figure 4.2) [265, 266, 267]. This steric hindrance is also responsible for their chirality, due to restricted internal rotations.

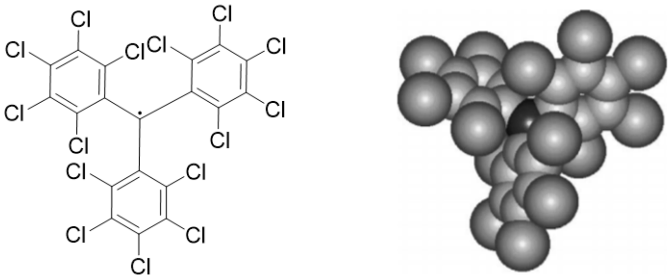

Figure 4.2: Structure of PTM.

In solution, PTM radicals are stable, even under the presence of oxygen and in acid conditions, but solely when they are under light exclusion. Contrariwise, when they are irradiated with light, they lose the ortho chlorine atoms, degenerating in fluorenyl radical species [268]. The light stability of PTM radical increases substantially in solid state.

PTM molecules show a versatile chemistry due to the possibility to functionalize the meta and para positions of the aromatic rings without losing their radical character. The preparation of PTM radical generally starts with the synthesis of the polychlorinated triphenylmethane skeleton having a hydrogen in the α-carbon (αH-PTM). To generate the corresponding radical, the αH-PTM is treated with a strong base first, giving the anion form, and with an oxidant agent then, usually iodine, p-chloranil or silver nitrate (Figure 4.3).

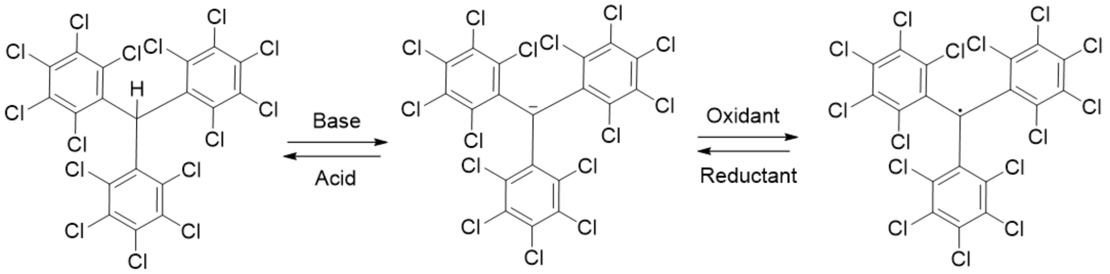

Figure 4.3: Synthesis of PTM radical.

A wide range of PTM derivatives with a large variety of functional groups has been reported[269]. The possibility to design numerous derivatives adapted to concrete functions, makes PTM radicals particularly appealing in the field of materials science.

PTM radicals ($[PTM]^{\cdot}$), are electroactive molecules, their one-electron oxidation gives rise to the PTM cation ($[PTM]^{+}$) while their one-electron reduction produces the PTM anion form ($[PTM]^{-}$). Thanks to their electrochemical behavior, the PTM derivatives can act in donor-acceptor (D-A) systems as donor or acceptor when they are in their anion or radical form, respectively. For these unique characteristics, PTM radical derivatives have been used in dyads to study Intramolecular Electron Transfer (IET) phenomena [270, 271, 272, 273].

The reduction and oxidation processes can be visualized as two reversible redox waves in CV measurements in solution, as reported in Figure 4.4. The conversion of $[PTM]^{\cdot}$ to $[PTM]^{-}$ is of particular interest, since it occurs at very low voltage and it is the base of many studies of electochemical switches in solution [22, 274] as well as on surfaces, through the preparation of SAMs, principally on silicon oxide, indium tin oxide (ITO) and gold [275, 276, 277].

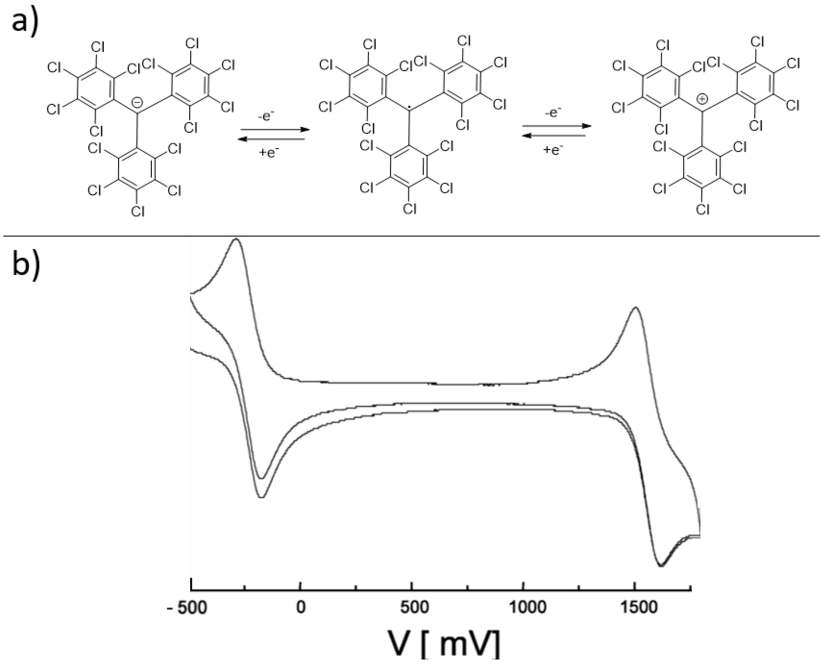

Figure 4.4: a) Reversible reduction and oxidation process of PTM. b) CV measurements of PTM radical in solution vs. $Ag/AgNO_3$. A platinum wire was used as counter electrode and a solution of 0.1 M tetrabutyl ammonium hexafluorophospate ($TBAPF_6$) in dichloromethane as electrolyte.

In these PTM-based switches, magnetic and optical output mechanisms have been used as read-out of the system, since the two redox species (i.e., $[PTM]^{\cdot}$and $[PTM]^{-}$), are characterized by different magnetic and optical properties. In particular $[PTM]^{\cdot}$ is paramagnetic and, if investigated by Electron Paramagnetic Resonance (EPR), gives a single and narrow (less than 1 Gauss) line centered at a g value very close to the value of the free electron (g = 2.0023) due to the low spin orbit interaction [267]. Apart from the central line, the EPR spectrum shows a small equidistant pair of lines on both sides of the main line as well as a more separated and broad doublet. These signals correspond to the coupling of the free electron with the ^{13}C nuclei (I = 1/2, natural abundance 1 %) of the triphenylmethyl skeleton [278]. Contrariwise, the [PPM]$^-$ is diamagnetic and do not produce any EPR response.

Regarding the optical response, both PTM redox species give a different shape in UV/visible absorption spectra. PTM radicals show a very characteristic absorption at 385 nm, while the most significant absorption band of the anion appears at 515 nm. Furthermore, contrary to the PTM radical, which is fluorescent in the red region (λ_{em}= 650 nm), the corresponding PTM anion is a non-fluorescent species.

4.3 Design and synthesis of the PTM derivatives αH-PTMsil, r-PTMsil and r-PTMpol

αH-PTMsil and r-PTMsil have been designed having a trietoxysilane as terminal group that was introduced to the PTM skeleton through the formation of an amide bond. The presence of this anchoring group allows the covalent fuctionalization of ITO and SiO_2 substrates.

The synthesis of both PTM derivatives requires the preparation of the derivative **9**, already described in literature [265]. The reported procedure involves the use of drastic acidic conditions (fuming sulfuric acid) and long reaction times (~90 h). Nevertheless, we proposed an alternative methodology for the preparation of **9** Figure 4.5, avoiding the use of strong acidic conditions and making the synthetic pathway shorter than the reported procedure.

As it is shown in Figure 4.5, two subsequent Friedel-Craft reactions were performed to obtain compound **7** and **8**, as fully described in literature [279]. Then, the carboxylic acid derivative **9** was obtained by a direct carbonation of the organo-lithium intermediate generated adding tetramethylethylenediamine (TMEDA) and n-butyl lithium (n-BuLi) to a solution of **8** in tetrahydrofuran (THF). The reaction was performed bubbling carbon dioxide in gas phase to the solution, in strictly dry conditions, under argon atmosphere and at low temperature (-78°C), in order to ensure the persistence of the organo-lithium intermediate. The mixture of reaction was acidified with HCl 1 M, and the crude was purified by column chromatography. Thereby, the PTM derivative **9** was obtained with 40% yield. The drawback of this new protocol of reaction is the production of unwanted secondary compounds due to a parasite reaction of halogen-metal exchange, that occurs when organo-lithium compounds are used in presence of aryl halides and consists in the removal of halogen atoms from the benzyl ring. For this reason a further purification step is required.

At this point, in order to obtain the αH-PTMsil, **9** was first converted to the acid chloride **10** by heating it in tionyl chloride at reflux temperature for 24 h [280]. Subsequently compound **10** was finally coupled with (3-aminopropyl)triethoxysilane (APTES), in presence of triethylammine, giving αH-PTMsil with high yield (83%).

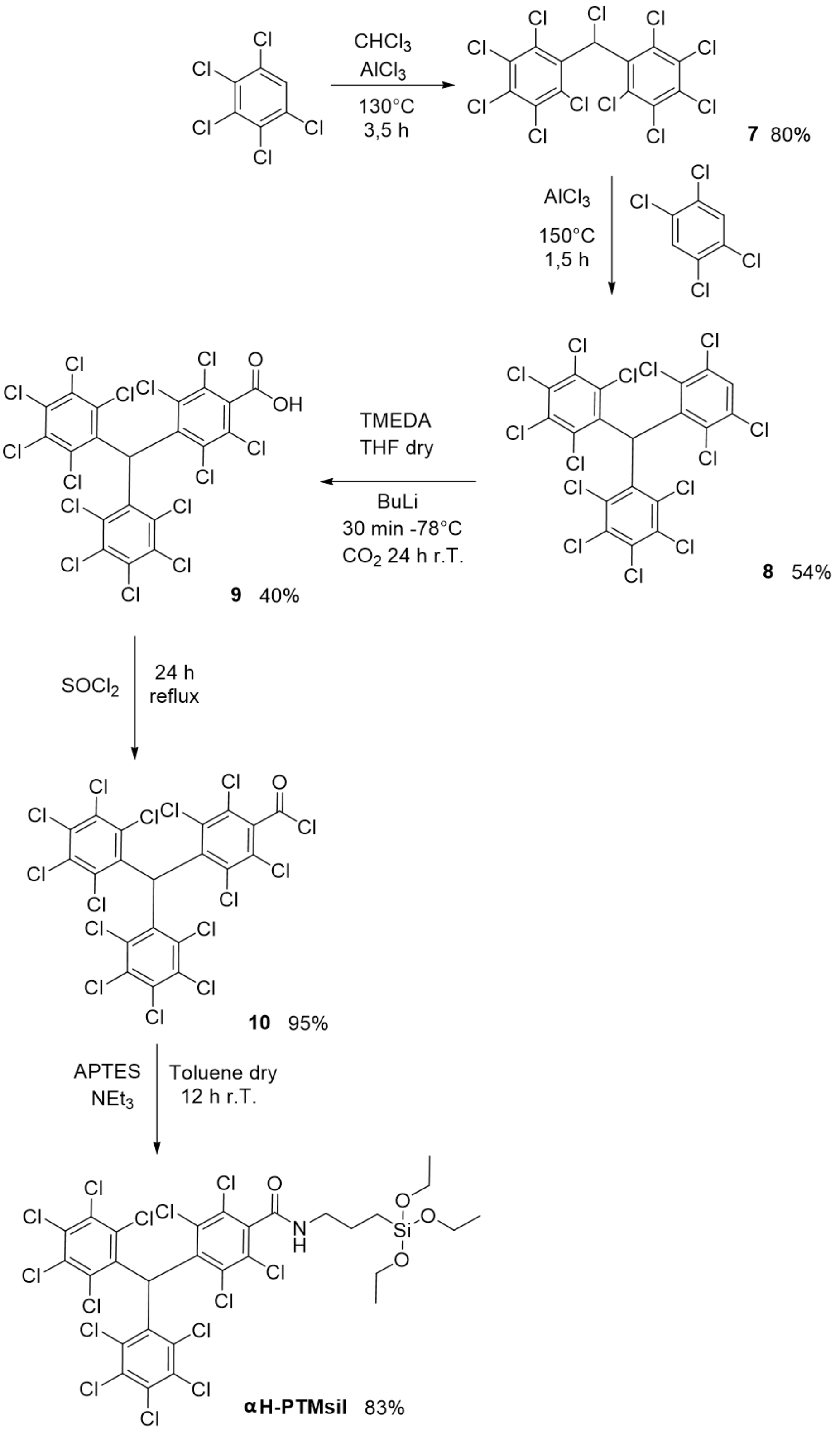

Figure 4.5: Synthetic pathway of αH-PTMsil.

On the other hand, to achieve r-PTMsil (see Figure 4.6), compound **9** was deprotonated in the α position, using KOH. The corresponding PTM anion thus generated was subsequently oxidized with $AgNO_3$ giving the radical derivative **11**. Furthermore, the reactions of acylation and amidation done to obtain αH-PTMsil were performed again on **11** and **12** [281], respectively, giving r-PTMsil with 51,6 % yield.

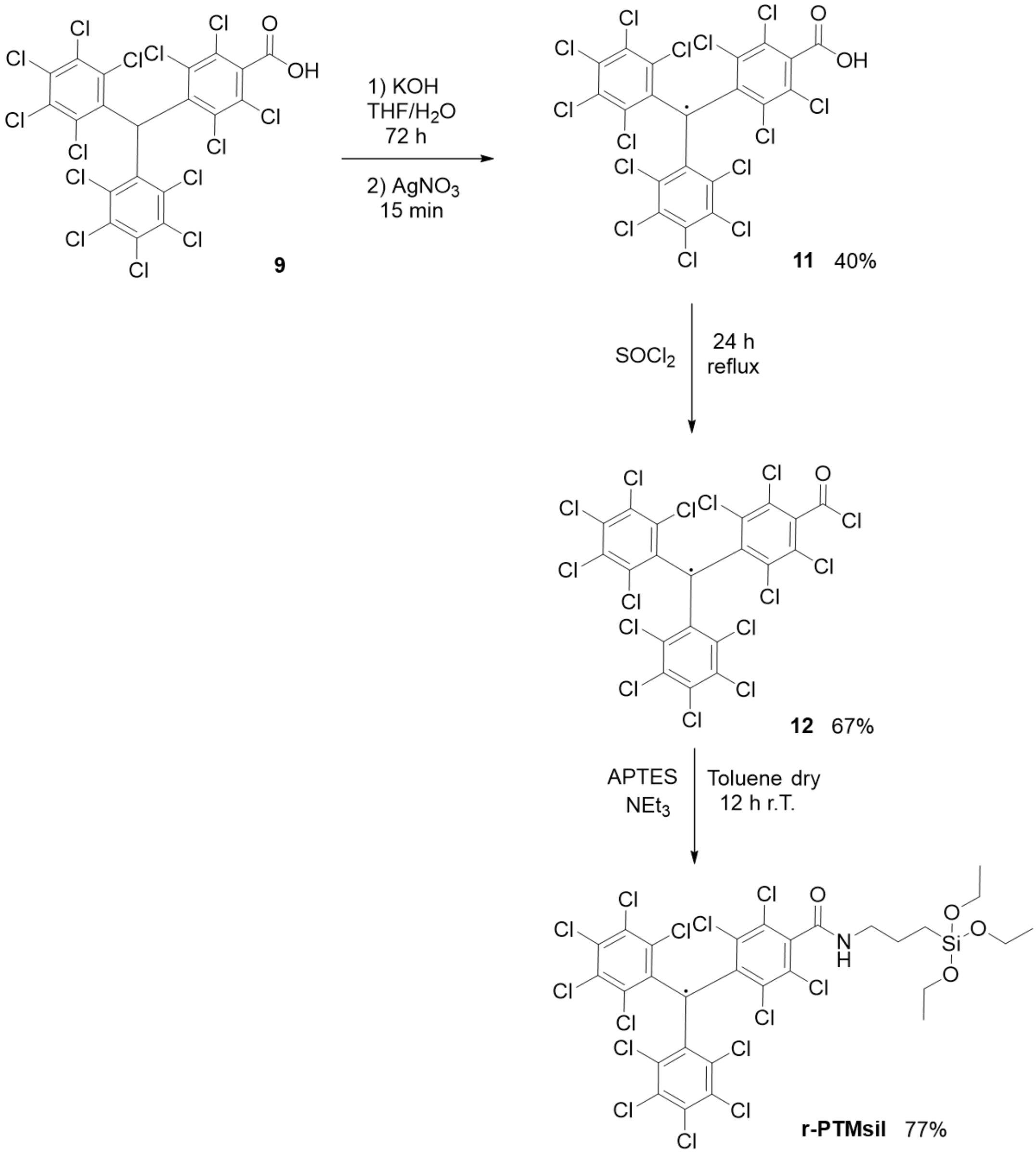

Figure 4.6: Synthetic pathway of r-PTMsil.

αH-PTMsil was characterized as usual by NMR, IR spectroscopy and mass spectrometry. The characterization of r-PTMsil was furthermore carried out using EPR spectroscopy, in order to have evidence on the radical behavior of this molecule, as reported in the experimental section.

Moreover, the electrochemical properties r-PTMsil were studied by CV measurements in solution, using tetrabutylammonium hexafluorophosphate ($TBAPF_6$) 0,02 M in acetonitrile (ACN) as electrolyte, a silver wire and two platinium wires as reference, counter and working electrode, respectively (Figure 4.7). The reversible redox wave observed at $E_{1/2}$= -0,01 V is ascribed to the conversion of the PTM radical moiety to the anion $[PTM]^-$.

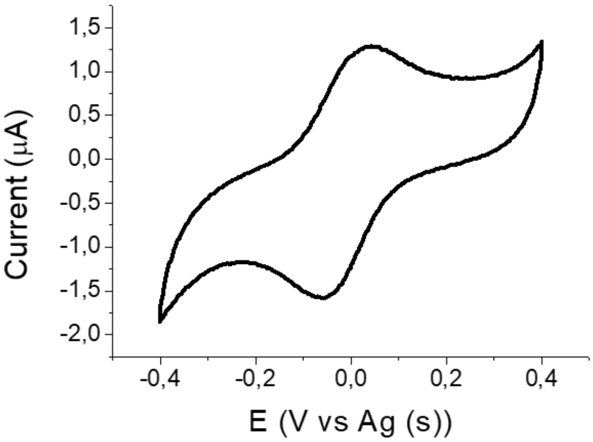

Figure 4.7: CV of r-PTMsil. $TBAPF_6$ 0,02 M in ACN was used as electrolyte, a silver wire and two platinum wires were used as reference, counter and working electrode, respectively. The scan rate was 0,5 Vs^{-1}.

Apart from αH-PTMsil and polyradical r-PTMsil, the other PTM derivative here synthesized was the polymer r-PTMpol. The synthesis of r-PTMpol was conceived to provide a new material with high charge storage properties, as will be better discussed in Section4.6. In order to reach this purpose, the monomer precursor **17** was designed having three acyl chloride functional groups in para-position. It was assumed that the high reactivity of this group could promote the reaction with *p*-phenylenediamine, giving rise to a bi-dimensional poly-radical polymer (Figure 4.1 c)).

The synthesis of **17** is reported in Figure 4.8 and was achieved as follows. Firstly, a Friedel-Craft reaction of tetrachlorobenzene with chloroform in presence of $AlCl_3$ was performed, giving **13** with 25% yield [279]. To a solution of **13** in dry THF at low temperature TMEDA was added and then n-BuLi, generating the organo-lithium intermediate. The solution was then quenched with ethyl chloroformate and compound **14** was thus obtained with 90% yield [282]. Then, **14** was converted to the radical derivative **15**. The deprotonation of the hydrogen in α position was achieved using tetrabutylammonium hydroxide (Bu_4NOH) and the PTM anion thus generated was subsequently oxidized in presence of silver nitrate giving the corresponding radical derivative (81% yield). **15** was then hydrolyzed in acidic conditions using H_2SO_4 at 100°C for 24 h giving **16** that was, in turn, dissolved and heated in thionyl chloride for 24 h providing **17** (90% yield). In this case, it was not possible to conduct a direct carbonation using CO_2 (g), as described for **9**, due to problems of purification of the crude mixture of reaction thus obtained. All the compounds synthesized were purified by column cromatography and characterized by NMR spectroscopy (non radical compound), mass spectrometry, IR and EPR spectroscopy (radical compounds).

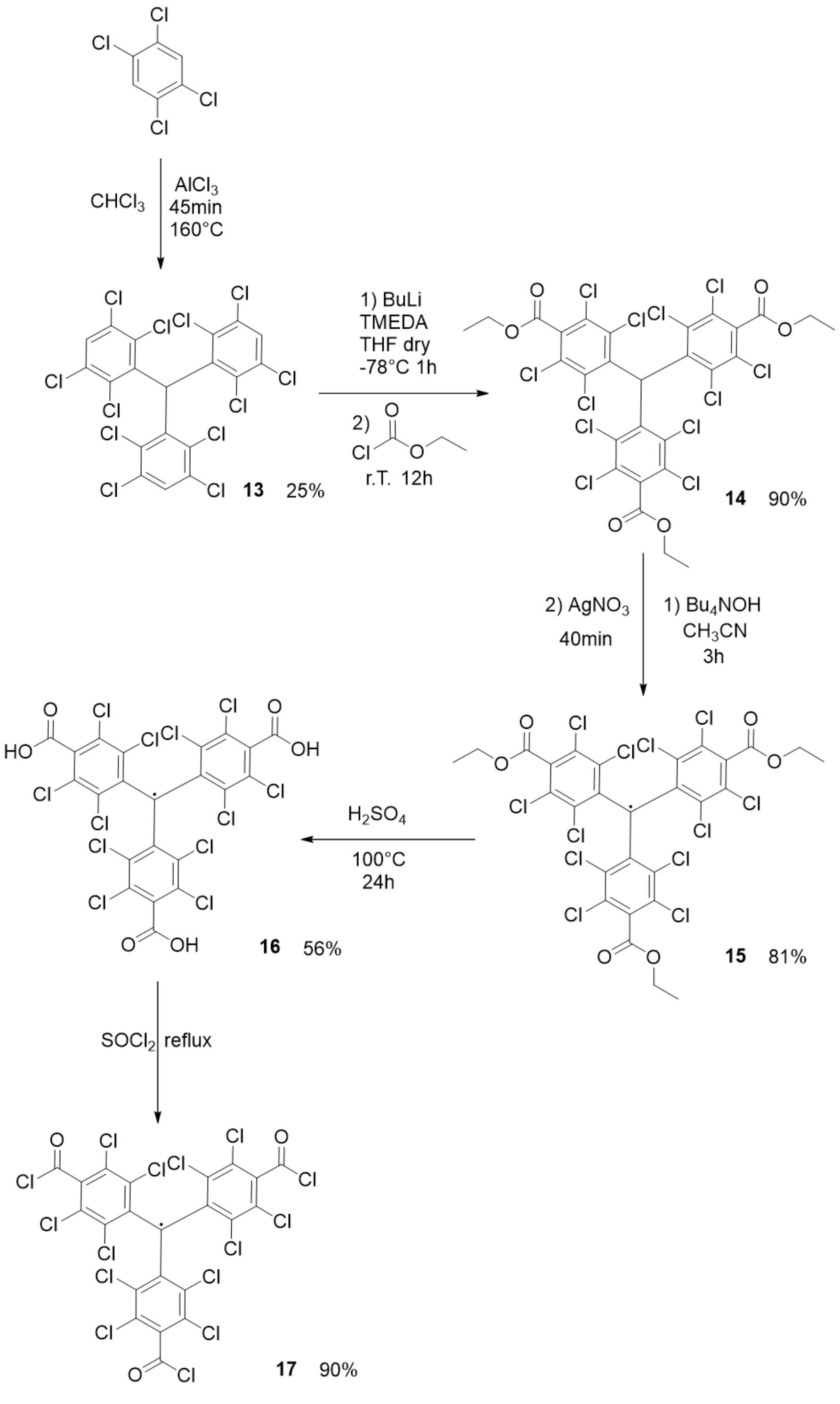

Figure 4.8: Synthetic pathway of **17**.

In order to generate the polymer r-PTMpol, **17** was reacted with *p*-phenylenediamine in presence Et_3N in dry THF. This mixture was refluxed for 3 days under argon with light exclusion (see Figure 4.9). The precipitated was isolated by filtration, washed with excess of THF and dried under vacuum. A dark reddish/brown very insoluble solid was obtained and identified as r-PTMpol.

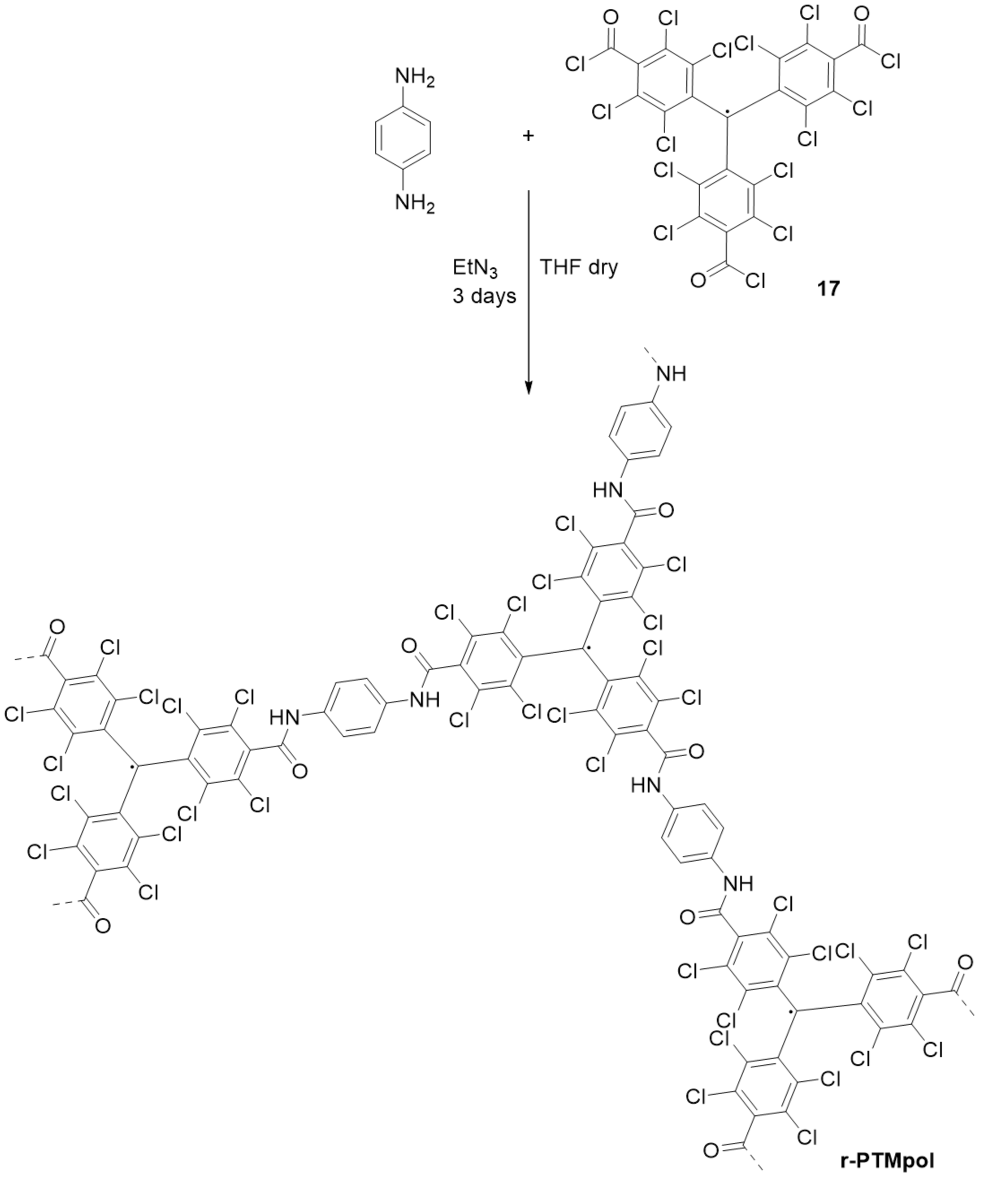

Figure 4.9: Synthetic pathway of r-PTMpol.

This compound was characterized by IR, X-ray, UV-Vis and EPR. In particular, the IR spectrum showed a new peak at 1675 cm^{-1} corresponding to a new carbonyl group, since the peak related to the COCl stretching at 1788 cm^{-1}, visible in the precursor **17**, disappeared. The peak at 1675 cm^{-1} as well as the one around 3381 cm^{-1}, related to the N-H stretching, clearly confirmed the formation of an amide bond, and so the reaction success (see Figure 4.10).

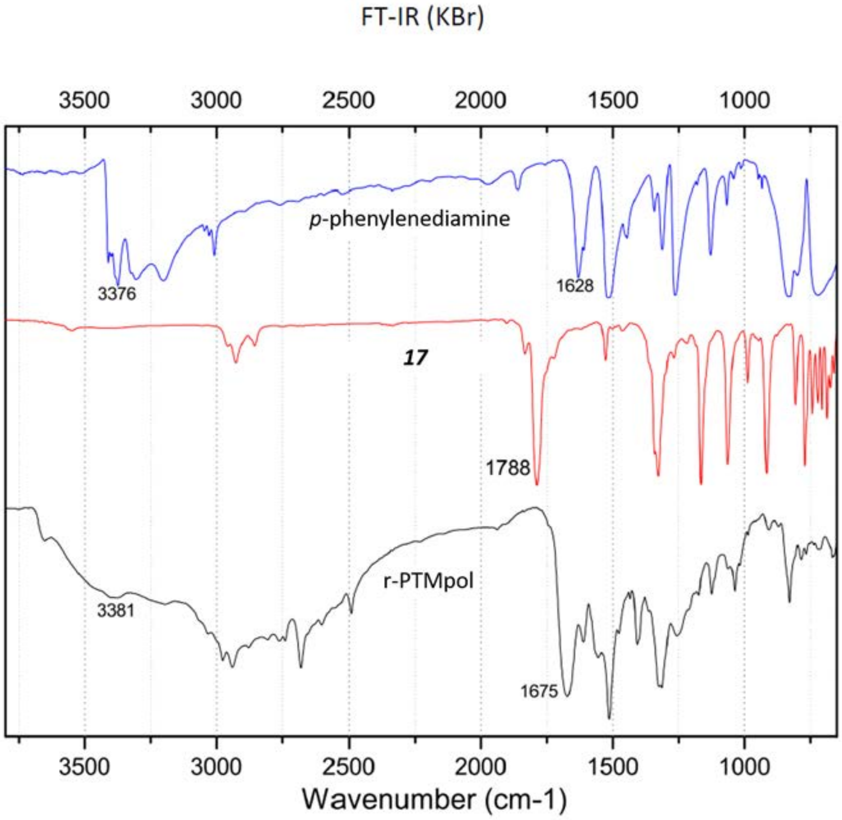

Figure 4.10: Fourier Transform Infrared Spectroscopy measurements of *p*-phenylenediamine (blue line), derivative **17**(red line) and r-PTMpol (black line).

In addition, UV-Vis and EPR confirmed that the radical character was preserved during the polymerization, observing the typical PTM radical absorbance band at 386 nm (Figure 4.11 a)) and the typical EPR signal for PTM radical derivatives, with g value of 2,002 (Figure 4.11 b)) .

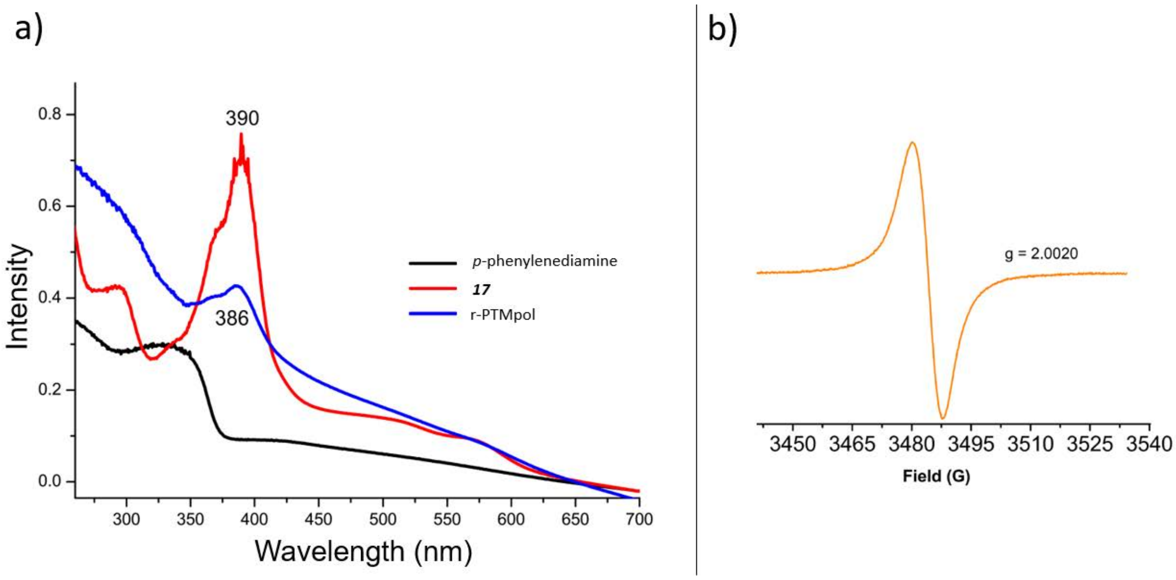

Figure 4.11: a) UV-Vis spectra in solid state of *p*-phenylenediamine (black line), derivative **17** (red line) and r-PTMpol (blue line). b) EPR spectrum of r-PTMpol.

4.4 Switches on ITO surfaces based on $S_{r\text{-}PTMsil}$

In order to carry out the formation of $S_{r\text{-}PTMsil}$ SAMs on ITO, the surfaces were cleaned by degreasing in ultrasonic baths of different solvents (dichloromethane, acetone and ethanol). The substrates were then immersed in a solution of piranha at 80°C for 30 minutes, to generate a homogeneous layer of OH active sites on the ITO surfaces. Then, they were rinsed with ultra-pure water, dried under N_2 flow and immediately immersed in the solution of r-PTMsil following the procedure reported in Table 4.1. Afterwards, the modified surfaces were rinsed thoroughly with clean toluene, in order to remove the physisorbed material, giving rise to the SAM $S_{r\text{-}PTMsil}$.

Table 4.1: List of conditions for $S_{r\text{-}PTMsil}$ formation.

Substrate	**SAM**	**Solution**	**Immersion Time**
ITO	$S_{r\text{-}PTMsil}$	1 mM of r-PTMsil in dry toluene	12 h

$S_{r\text{-}PTMsil}$ was characterized by cyclic voltammetry (CV). The functionalized substrate was used as working electrode, while a platinum wire and a Ag wire were used as counter and reference electrodes, respectively. A 0,02 M solution of $TBAPF_6$ in acetonitrile was employed as electrolyte. A reversible redox wave was observed at $E_{1/2}$ = -0,12 V which corresponds to the reduction of the radical to the anion form.

Furthermore, the SAM stability was tested during repeated electrochemical cycling. In the CV the current intensity did not decrease after 10 cycles, confirming a great SAM stability (Figure 4.12).

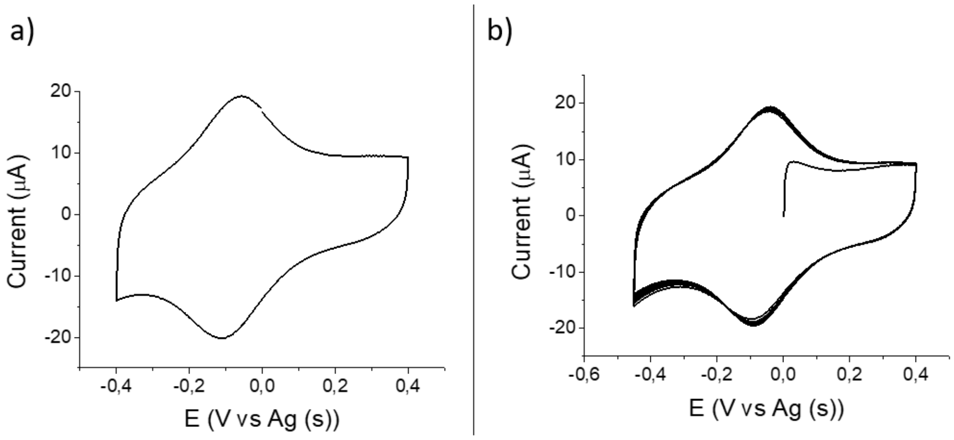

Figure 4.12: CV of $S_{r\text{-}PTMsil}$. The functionalized surface was used as working electrode, $TBAPF_6$ 0,02 M in ACN was used as electrolyte, and a silver wire was used as reference electrode. The scan rate was 0,5 Vs^{-1}. b) The CV measurement was repeated for 10 cycles.

Finally, the CV performed at different scan rates showed the linear dependence with the current, proving the surface confinement of the PTM molecules (Figure 4.13).

The SAM coverage was calculated from the I_{pa} yielding a coverage of $5 \cdot 10^{-11}$ mol/cm^2.

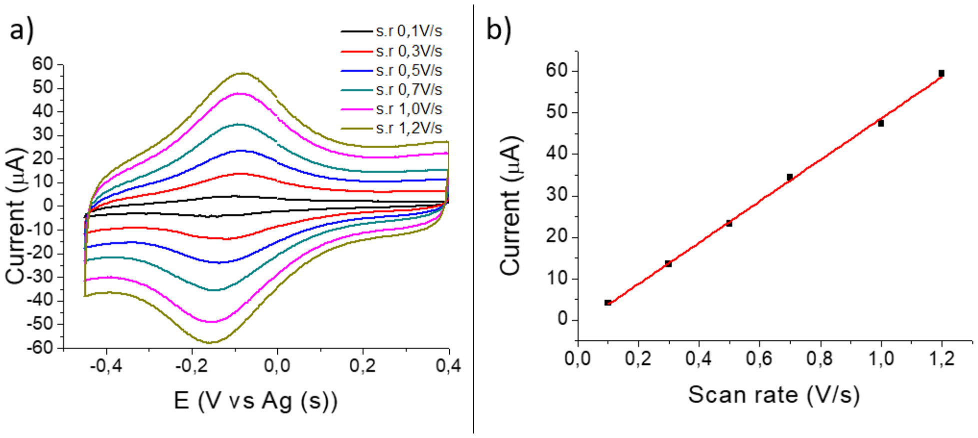

Figure 4.13: a) CV of $S_{r\text{-}PTMsil}$ at different scan rates (s.r.). The functionalized surface was used as working electrode, $TBAPF_6$ 0,02 M in ACN was used as electrolyte, and a silver wire was used as reference electrode. b) Linear relationship of the current peak vs. the scan rate.

Further optical and magnetic characterization were performed to confirm the SAM formation. The UV-Vis absorbance of $S_{r\text{-}PTMsil}$ showed a band at 371 nm comparable with the absorbance band of the r-PTMsil in solution (Figure 4.14).

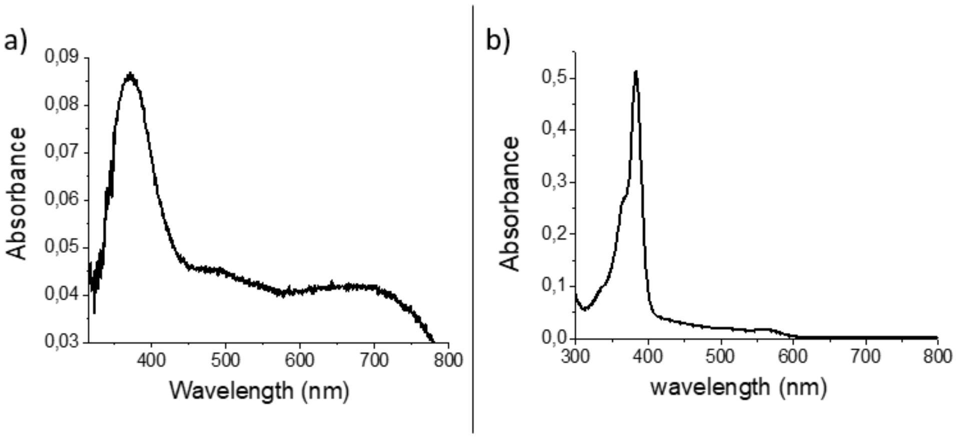

Figure 4.14: UV-Vis absorption spectrum of a) of $S_{r\text{-PTMsil}}$ and b) r-PTMsil in dichloromethane.

Further, the EPR spectra of $S_{r\text{-PTMsil}}$ exhibited the typical signal of the confined PTM radical (g factor = 2.0030), comparable with the EPR response of r-PTMsil in solution (Figure 4.15) . As expected for surface immobilized PTMs [277], the EPR spectra of $S_{r\text{-PTMsil}}$ has a larger linewidth than in solution.

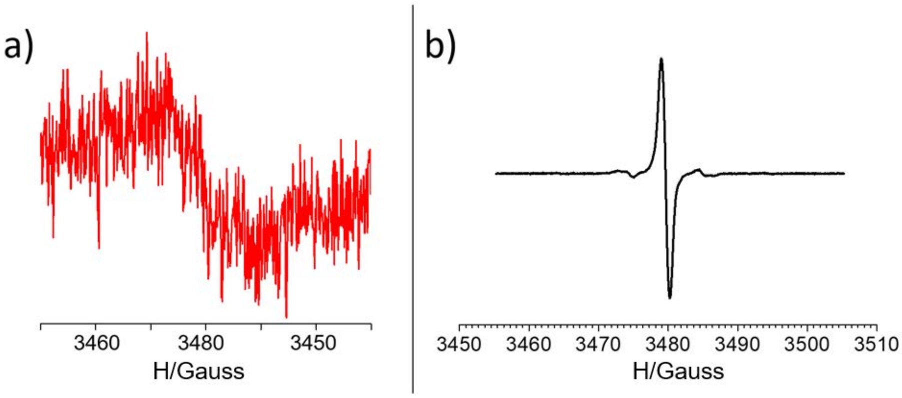

Figure 4.15: EPR measurement of a) $S_{r\text{-PTMsil}}$ and b) r-PTMsil in dichloromethane.

4.4.1 Switchability study of $S_{r\text{-PTMsil}}$

The electrochemical switch of $S_{r\text{-PTMsil}}$ was fully investigated in order to realize a bi-state molecular switch on a transparent surface that could find application in the field of memory devices. Not least, the acquirement of a full knowledge of the r-PTMsil behavior on surface was required to the subsequent implementation of that molecule in electronics devices, as exposed in section Section4.5.

In order to monitor in situ the optical absorption properties as read-out mechanism of the electrochemical switch of $S_{r\text{-PTMsil}}$, an electrochemical cell was designed to fit the sample in UV-Vis-NIR holder. Hence, a standard 2 mm pathway quartz cuvette was fixed inside the UV-Vis-NIR spectrophotometer and filled with a solution of 0,02 M of $TBAPF_6$ in acetonitrile. All the electrodes were placed inside the cuvette with the functionalized ITO substrate fully fitting the optical pathway. The potentiostat was connected to the electrodes in the cuvette located inside the spectrophotometer and a voltage pulse of -0,4 V was applied to $S_{r\text{-}PTMsil}$ for 200 seconds, in order to form the corresponding anionic species. The absorption spectrum was then registered and a new voltage pulse of +0,4V was applied to recover the radical form. Both redox states of the SAM were identified in the UV-Vis spectra registered before and after the voltage application, since the two forms exhibit distinct absorption bands at 371 nm for the radical and 515 nm for the anion (Figure 4.16). It should be noticed that the broad absorption band around 480 nm was not originated from the radical nor from the anion but it came from the ITO functionalization [283]. Thus, there is a lack of a proper blank to be used as reference in the absorbance measurement of functionalized ITO substrates, because the latter is structurally modified upon covalent functionalization. Since the ITO absorption band is partially overlapped with the anion one, the switching was monitored following the absorption band at 371 nm (Figure 4.16 b)). After nine cycles a decrease in the signal intensity was observed, but the ON/OFF ratio was still significant, demonstrating that the optical read-out is completely viable for this system.

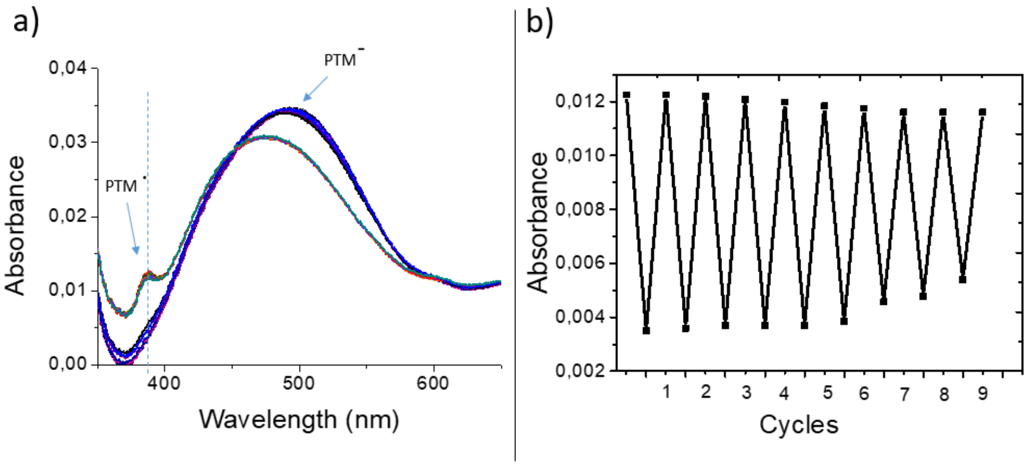

Figure 4.16: Electrochemical induced switch of $S_{r\text{-}PTMsil}$ monitored by UV-Vis absorption spectroscopy. b) Nine cycles of the redox switch monitored following the absorption band at λ = 371 nm.

As already mentioned, the radical derivative is paramagnetic (S = 1/2), while the anion is a diamagnetic species (S = 0). For this reason the electrochemical switch was additionaly monitored employing the magnetic output measured by EPR. This time the electrochemical switch of $S_{r\text{-}PTMsil}$ was performed ex situ in a conventional electrochemical cell, applying a potential pulse of +0,4 V or -0,4 V for 200 seconds, depending on the species we wanted to generate. The switching in situ was not possible due to the problems of molecule desorption when a magnetic field is applied in presence of an electrolyte solution. This problem was already observed in our group with similar systems [283]. Hence, for each reduction and oxidation steps the functionalized surface was extracted from the electrolyte solution and immediately measured in the EPR in air. We observed that the EPR signal corresponding to the oxidized state of the SAM practically disappeared upon reduction to the anionic form, as expected. A residual EPR signal (g factor = 2,0013) from the ITO/glass substrate was seen, as already observed in our group with similar systems on ITO substrates. One switching cycle is shown in Figure 4.17 confirming that also the magnetic characteristics of $S_{r\text{-}PTMsil}$ represent a suitable read-out tool to determine the redox state of this system.

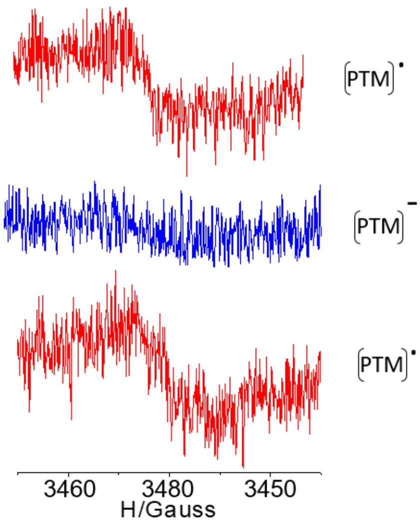

Figure 4.17: Electrchemical induced switch of $S_{r\text{-}PTMsil}$ monitored by EPR measurements.

4.4.2 Summary

The new PTM derivative r-PTMsil was used to functionalize a transparent and conductive ITO surface giving rise to a bi-state system whose switch was monitored through optical and magnetic outputs.

The electrochemical conversion between the radical and the anion species in $S_{r\text{-}PTMsil}$ occurs at very low voltage (-0,12 V vs. Ag (s)). Each state of the switch exhibits different magnetic and optical properties, hence the electrochemical switch was monitored following the changes in UV-Vis and EPR spectra. $S_{r\text{-}PTMsil}$ in its radical form has spin S = 1/2 and shows an EPR signal and an absorbance band at 371 nm, while the anionic state is diamagnetic (S = 0, no EPR signal) and presents an absorbance band at 515 nm. This study demonstrates that r-PTMsil was able to form a robust SAM on ITO surfaces and, furthermore, it gives a proof of concept of the possibility to use this system as memory device.

4.5 Integration of r-PTMsil and αH-PTMsil in OFETs by functionalizing the dielectric[1]

4.5.1 Functionalization of the dielectric in organic field-effect transistors

Organic field-effect transistors (OFETs) are extremely sensitive to the interfaces, such as the gate dielectric/organic semiconductor interface [284].

Charge transport is dominated by the interplay between semiconductor and gate dielectric [285]. The interactions at the interface determine the polarity and mobility of the charge carriers and control the operational stability and the threshold voltage (V_{th}) [286, 287, 288, 289]. The surface chemistry of the gate dielectric is also crucial in determining the molecular order and the thin film morphology of the organic semiconductor (OSC). Therefore, when the OCS is deposited on the dielectric, phenomena such as nucleation, growth, dewetting, ripening, and recrystallization occur at the interface between them. Hence, the organic molecules experience energy barriers principally associated with diffusion and aggregation that are affected by the dielectric surface tension and roughness.

In light of this, the modification of the gate dielectric is a powerful option to affect the OFET performance.

SAMs provide an attractive possibility for dielectric modification. Despite their minuscule thickness, SAMs not only provide a transitional layer between inorganic oxide and organic semiconductor but can function as a low voltage dielectric if properly designed [290].

Moreover, the SAM formation affects the surface tension and the roughness of the dielectric. Hence, it has a crucial role in the deposition of the OSC, influencing the mechanism of growth of the semicondutor on it [291, 292]. Another important parameter that can be modified by the presence of a SAM on the dielectric is the orientation of the different crystalline facets of the OSC during the nucleation phase

---

[1] This work was done in collaboration with Dr. Lijia Chen and Dr. Sergi Riera.

[293]. Molecular orientation with respect to the channel is crucial, as charge mobility is usually anisotropic in π-conjugated materials. Lastly, also the critical size and the dimensionality of nuclei could change depending on the SAMs presence.

Furthermore, the SAM formation may also reduce or modify surface reactivity of the dielectric/organic interface improving the device stability [288]. This minimizes the bias stress, which results in the V_{th} shift upon repeated OFET operations with the decay of the source–drain current.

Fukuda et al. evaluated the effect of the chain length of alkyl-SAMs on the SiO_2 dielectric on the FET device performance. It was found that alkyl-chains of mid-length ~$(CH_2)_{12}$ facilitate the highest mobility in pentacene based devices [294]. This was attributed to the disordered nature of mid-length alkyl chain SAMs promoting a smooth liquid like surface for semiconductor growth. Additionally, the relationship between SAM structure and electronic performance of various commonly used organic semiconductors was also investigated by Kobayashy et al. They stated that the ordering of SAMs molecules with molecular dipoles produces a built in electric field on the OFET, which is superimposed to the externally applied gate field. The experimentally observed shift of V_{th} could be attributed to this additional local field created by the SAMs [285]. The OFET characteristics/SAM dipole moment relationship was also investigated by Takahashi and Park [295]. They agreed that the aligned dipoles between the gate insulator and the organic semiconductor thin film effectively added to the field induced by the gate voltage, shifting the gate voltage dependence of the transistor characteristics [296]. Halik and his group investigated a series of thin-film transistor devices using pure and mixed SAMs in hybrid AlO_x/ SAM dielectrics OFETs. They compared molecules with similar or different dipole moments in order to evaluate the contribution of the dipole moment to the device performance. Furthermore, one of the molecules used for the SAMs was a derivative of the fullerene C_{60}, known to have strong acceptor properties and reversible redox behavior. By dilution of C_{60} in mixed SAMs with non redox active molecules, they also reached to observe the charging of the fullerenes during the device operation that was reflected on a rising anticlockwise hysteresis in the transfer characteristics of the devices with increasing fullerene moiety in the SAM (Figure 4.18) [297].

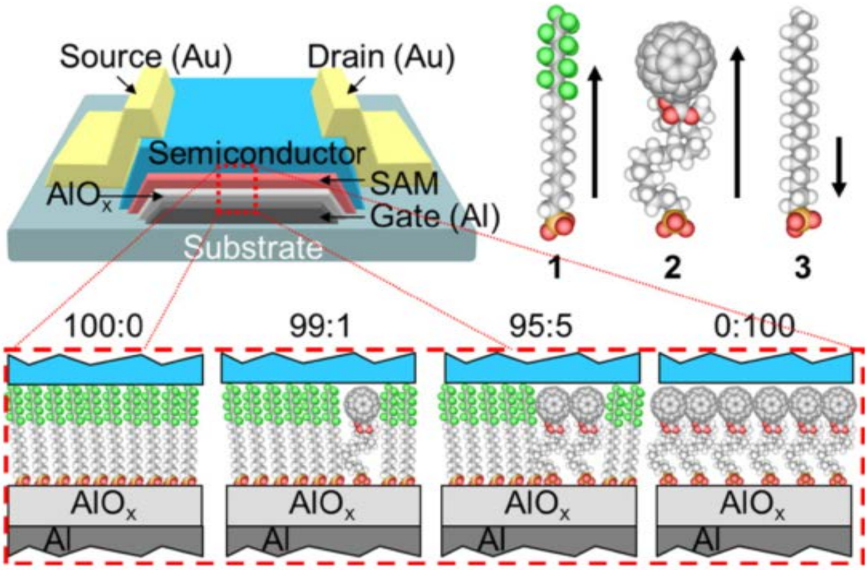

Figure 4.18: Schematic cross-section of a fully patterned bottom- gate top-contact transistor with AlO$_x$/SAM hybrid dielectrics (top-left). Chemical structure of SAM-forming molecules and direction of the molecular dipole component perpendicular to the surface (top-right, arrow heads show negative ends of the dipoles). Schematic sketch of pure and mixed SAM hybrid dielectrics composed of 2 and 3 [297].

The possibility to charge the C_{60} moieties was further exploited in OFETs devices by realizing an electrically programmable self-assembled molecular gate dielectric layer that could be reversibly charged and discharged. These devices showed to retain their digital states even when the supply voltage was removed, providing a non-volatile memory [298].

Since the interfacial modifications can have profound effects on the device performance, we aimed to systematically investigate the effect of r-PTMsil on SiO_2 dielectric in OFETs. Since r-PTMsil is electrochemically bi-stable, we were interested in testing if it is possible to induce the electrochemical switch of the molecule, once it is integrated into the OFET. The sensing of the two redox states could give rise to a memory device. Furthermore, using the structurally similar non electroactive derivative αH-PTMsil, we planned to perform a systematic comparison to understand how the presence of the two SAMs with almost identical molecular structure but different electronic structure could affect the device performances.

4.5.2 Design and fabrication of the OFETs devices

SAMs of r-PTMsil, as well as SAMs of αH-PTMsil, were grown on the SiO_2 substrates. These two molecules are structurally similar but substantially differ in their electronic properties. In fact, the radical character of r-PTMsil is responsible for its electroactive behavior (as already described in Section4.4). Contrariwise, αH-PTMsil is a non electroactive species. As a reference also SAMs of hexamethyldisilazane (HMDS) on the SiO_2 were prepared. These SAMs are commonly used in OFETs to passivate the polar groups of the SiO_2 dielectric that cause charge trapping. Furthermore, since HMDS SAMs also provide a more hydrophobic surface, they also can have an impact on the organic semiconductor thin film morphology.

The devices so differently functionalized were structurally and electrically characterized and the results obtained were compared with those from devices without any dielectric functionalization (i.e. bare SiO_2).

Specifically, the OFETs were fabricated in the bottom-gate, bottom-contact architecture on silicon substrates with a SAM/SiO_2 gate dielectric with gold source and drain electrodes. The electrodes layout was photolithographically patterned on the SiO_2 layer by means of a micro-writer, while the gold (40 nm) was deposited by thermal evaporation (system Auto 306 from Boc Edwards) using chromium (5 nm) as adhesive layer. Before proceeding to the deposition of the organic semiconductor (OSC), the specific SAM was grown on the dielectric, through chemisorption at solid-liquid interface, as explained later. Finally, a thin film of OSC was grown on the SAM. Specifically two OCS were chosen: 1) pentacene (P5, p-type semiconductor) and 2) fullerene C_{60} (n-type semiconductor). Films of P5 and C_{60} (50 nm thick) were fabricated by high-vaccumm deposition (10^{-7} mbar), with a growth rate of 0,2 Å/s keeping the substrate temperature constant at 60°C for P5 and at 25°C for C_{60}. The optimization of the OSC thickness was done calculating the mobility of the bare dielectric devices as function of the semiconductor thickness. The device geometry is schematically represented in Figure 4.19.

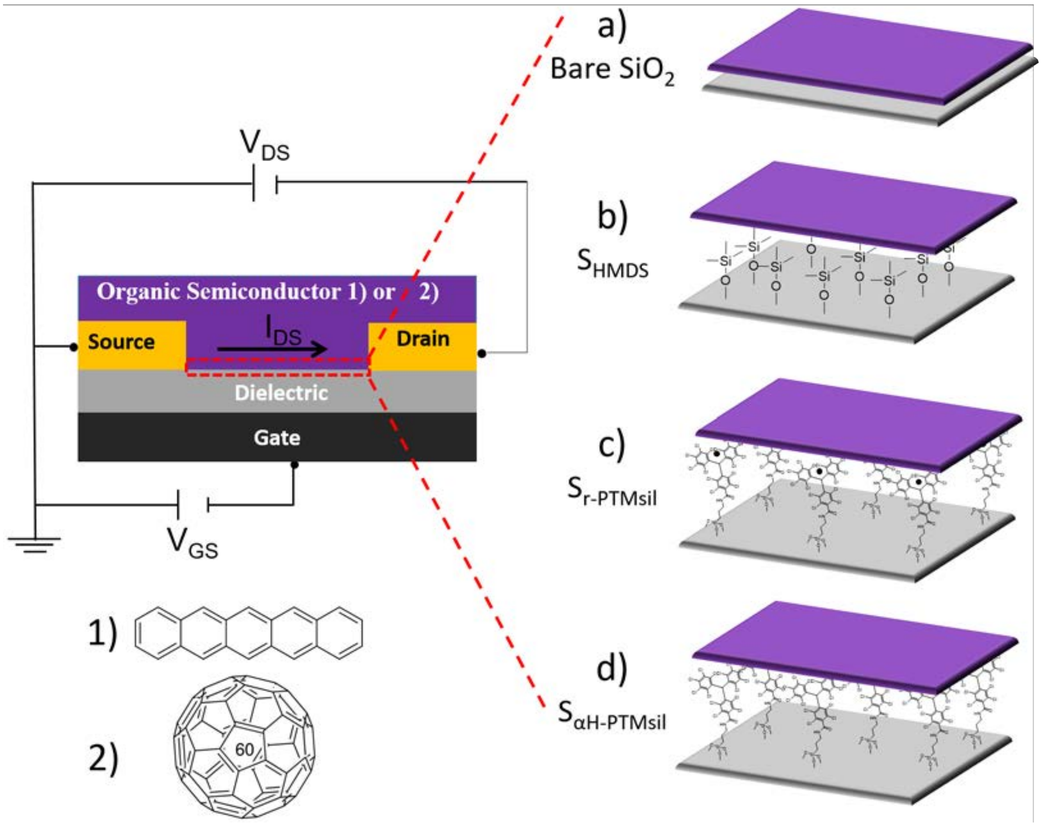

Figure 4.19: Schematic representation of the OFET geometry used and of the different dielectric/semiconductor interfaces. Structure of the semiconductor used: 1) pentacene, 2) fullerene C_{60}.

Before proceeding with the SAMs formation, the substrates where washed with ethanol and isopropanol HPLC pure grade. They were subsequently activated by exposure in a UV/ozone chamber for 20 minutes and, then, immediately immersed in the solution of interest following the conditions reported in Table 4.2. The substrates were left under inert atmosphere and light exclusion and, finally, they were rinsed with dry toluene and dried under nitrogen flow.

Table 4.2: List of conditions used for the dielectric funtionalization.

Substrate	SAM	Solution	Immersion Time
SiO_2	$S_{r\text{-PTMsil}}$	1 mM of r-PTMsil in dry toluene	12 h
SiO_2	$S_{\alpha H\text{-PTMsil}}$	1 mM of aH-PTMsil in dry toluene	12 h
SiO_2	S_{HMDS}	1 mM of HMDS in dry toluene	4 h

The so treated substrates were macroscopically characterized by contact angle (CA), providing the values of 79°, 94° and 102° for S_{HMDS}, $S_{r\text{-PTMsil}}$ and $S_{\alpha H\text{-PTMsil}}$, respectively

(Figure 4.20). As expected, these values were higher than the CA of a non functionalized SiO_2 surface (58°) in agreement with the more hydrophobic character of these molecules. Hence, CA characterization qualitatively proved the successful surface functionalization. Moreover, they provided information about an important parameter, such as hydrophilicity, that could influence the thin film growth of the OSC and the resulting thin film morphology and structure.

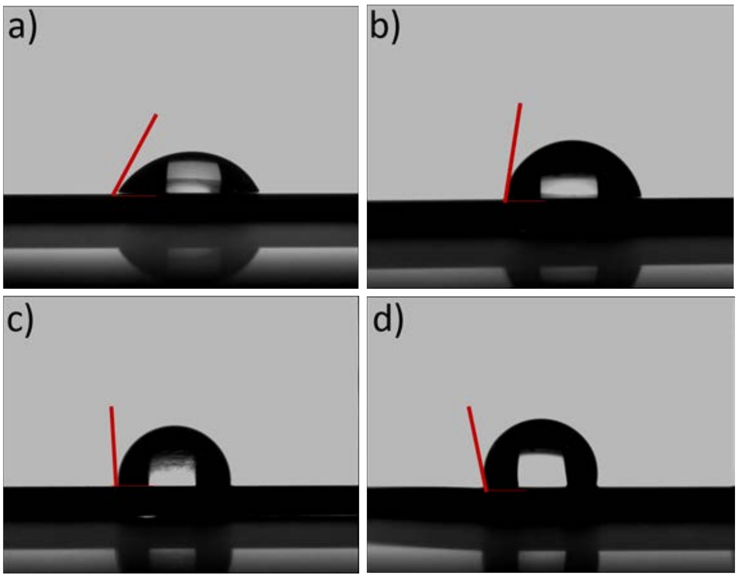

Figure 4.20: Contact angle measurements of a) bare SiO_2, b) S_{HMDS}, c) $S_{r\text{-}PTMsil}$ and d) $S_{\alpha H\text{-}PTMsil}$.

Once the functionalization was achieved, the deposition of the semiconductor was carried out, as already described, and the effect of the different SAMs on the OSCs growth was assessed at first by a topographic analysis. The AFM images of the pentacene deposited on the different SAMs showed, at a first visual inspection, a homogeneous film of the OSC. Moreover, the grains appeared very similar in size for all four kinds of surfaces (see Figure 4.21). The Root Mean Squared (RMS) Roughness, that is the standard deviation of the surface height-values for the sample area, was found to be 20,1 nm, 14,2 nm, 12,4 nm, 11,4 nm for the p-type OFETs without any functionalization and functionalized with HMDS, r-PTMsil and αH-PTMsil, respectively (i.e. Bare SiO_2 /P5, S_{HMDS} /P5, $S_{r\text{-}PTMsil}$ /P5 and $S_{\alpha H\text{-}PTMsil}$ /P5). Hence, pentacene films were smoother when the dielectric was functionalized, being even smoother with $S_{r\text{-}PTMsil}$ and $S_{\alpha H\text{-}PTMsil}$. From this, a correlation was deduced between SiO_2 surface tension and smoothness of pentacene films: by increasing the hydrophobic character of the SiO_2 surfaces, the roughness of the evaporated pentacene film improved.

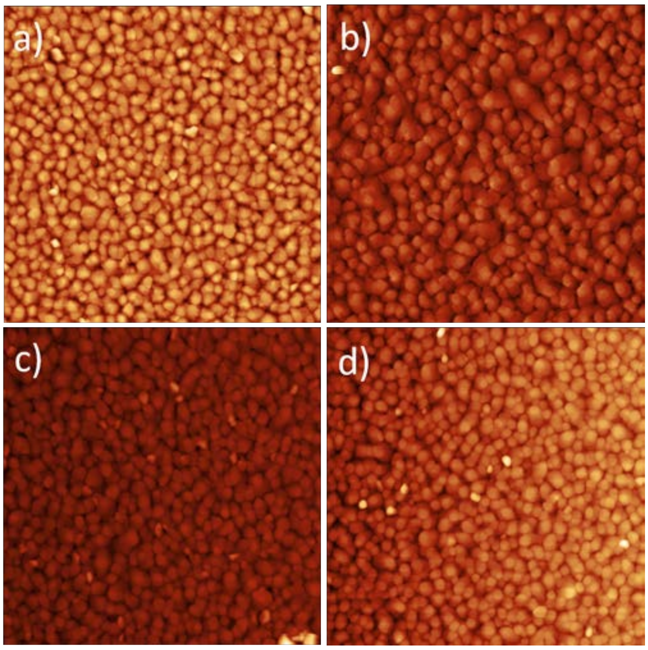

Figure 4.21: AFM images (5x5 μm^2) of a) Bare SiO_2 /P5, b) S_{HMDS} /P5, c) $S_{r\text{-}PTMsil}$ /P5 and d) $S_{\alpha H\text{-}PTMsil}$ /P5.

By XRD analysis, the high crystallinity of the semiconductor was certified without any significant difference among the various devices (Figure 4.22). This data confirm that the pentacene crystal phase is not altered by the surface functionalization. Moreover, the XRD spectra displayed multiple peaks with a good signal-to-noise ratio. According to literature, the interplanar spacing from the peaks suggested that the long axes of pentacene molecules was almost perpendicularly aligned to the surface forming a layered structure and the crystal structure is in agreement with the triclinic polymorrph of pentacene [299, 300].

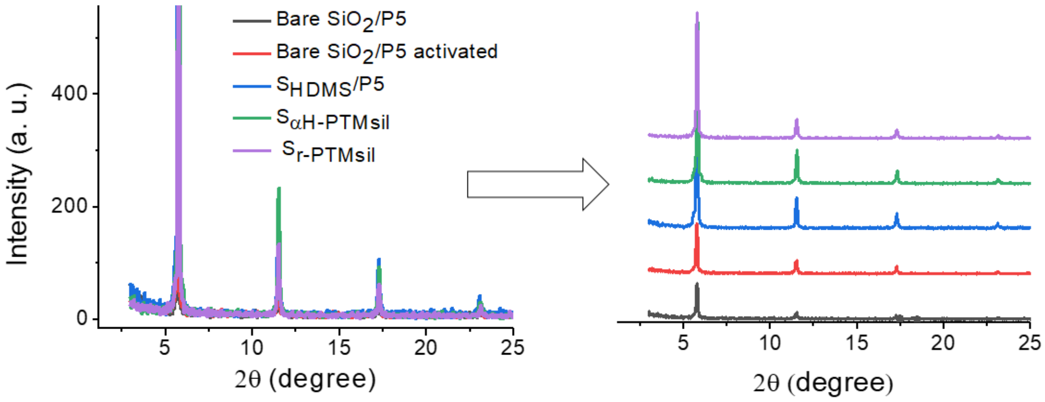

Figure 4.22: XRD analysis of the pentacene thin film on bare SiO_2 and on the differently functionalized SiO_2 surfaces.

AFM and XRD measurements were performed also in the case of C_{60}. AFM images showed a less compact film, compared to the pentacene one, and, as previously observed with the pentacene film, no difference in the topography were detected at a visual inspection among all the different substrates used (i.e. bare SiO_2 and SiO_2 functionalized with HMDS, r-PTMsil or αH-PTMsil molecules, see Figure 4.23).

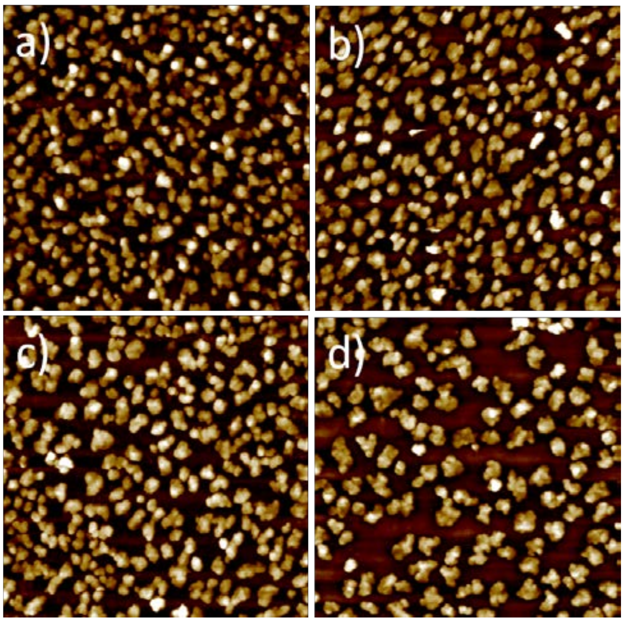

Figure 4.23: AFM images (5x5 μm^2) of C_{60} evaporated on a) bare SiO_2 b) S_{HMDS} , c) $S_{r\text{-}PTMsil}$ and d) $S_{\alpha H\text{-}PTMsil}$.

Furthermore, the film crystallinity was investigated by XRD measurements (Figure 4.24) but, unfortunately, we got a signal only when the C_{60} film was evaporated on SiO_2 substrates modified with $S_{\alpha H\text{-}PTMsil}$. In this case, a (111) reflection characteristic of C_{60} thin films can be noted, according to the literature [301].

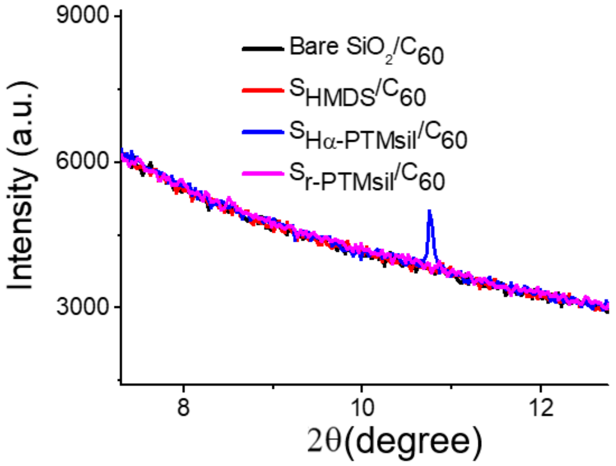

Figure 4.24: XRD analysis of the C_{60} grown on the different SAMs and on bare SiO_2.

4.5.3 SAMs influence on the electric characteristics of the OFET devices

The electric characteristics of the OFETs were measured under nitrogen ambient conditions in a glove box at room temperature, using a dual channel SMU 2612 from Keithley.

For the p-type OFETs (pentacene as semiconductor) functionalized with HMDS, αH-PTMsil and r-PTMsil and without any functionalization (i.e. S_{HMDS} /P5, $S_{\alpha H\text{-}PTMsil}$ /P5, $S_{r\text{-}PTMsil}$ /P5 and Bare SiO_2 /P5, respectively) the transfer characteristics (I_{DS} vs. V_{GS}) were recorded. In Figure 4.25, the source-drain current (I_{DS}) in a logarithmic and linear scale is shown against the gate voltage V_{GS} at a constant source-drain voltage V_{SD} = -40 V with a sweeping speed of 0,1 V/s. Carrier mobility (μ) and on voltage (V_{on}) parameters were extracted from these measurements, and were deeply analyzed.

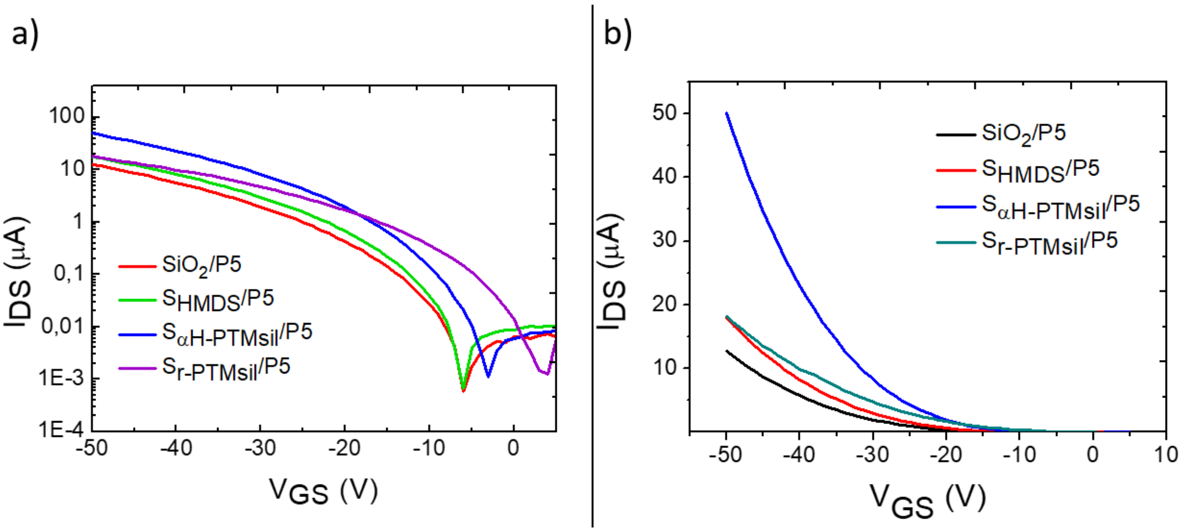

Figure 4.25: a) Lin-lin and b) log-lin transfer characteristics of pentacene OFETs with and without dielectric functionalization.

In Figure 4.26 the calculated on voltage values are reported for each system. The passivation of the dielectric with S_{HMDS} had an almost negligible effect on the V_{on} while, it moved towards more positive values when αH-PTMsil and r-PTMsil were at the dielectric/semiconductor interface. Noteworthy, in the case of r-PTMsil a remarkable shift towards positive values of ~2 V was observed. This means that it is easy to switch on the devices with $S_{r\text{-}PTMsil}$ /P5, which could be due to the additional electrical field created by the dipolar r-PTMsil SAM-molecules, whose negative end is directed towards the semiconductor. According to literature, it is assumed that this additional field adds to the applied gate field, and hence a lower external voltage is required to switch on the device. Previous calculations were done on similar systems, where the dipole moment of PTM radical derivatives was found to be remarkably higher (in absolute value) than the dipole moment of the corresponding αH-derivatives (unpublished data from our group). In accordance to this, we expect the same for r-PTMsil and αH-PTMsil molecules. This could justify the similar V_{on} tendency to move towards more positive values in the case of $S_{\alpha H\text{-}PTMsil}$ /P5 and $S_{r\text{-}PTMsil}$ /P5 compared to S_{HMDS} /P5 and SiO_2 /P5 based devices, as well as the high difference in value between the V_{on} of $S_{\alpha H\text{-}PTMsil}$ /P5 and $S_{r\text{-}PTMsil}$ /P5 . Currently, calculations are being performed on the dipole moments of these SAMs.

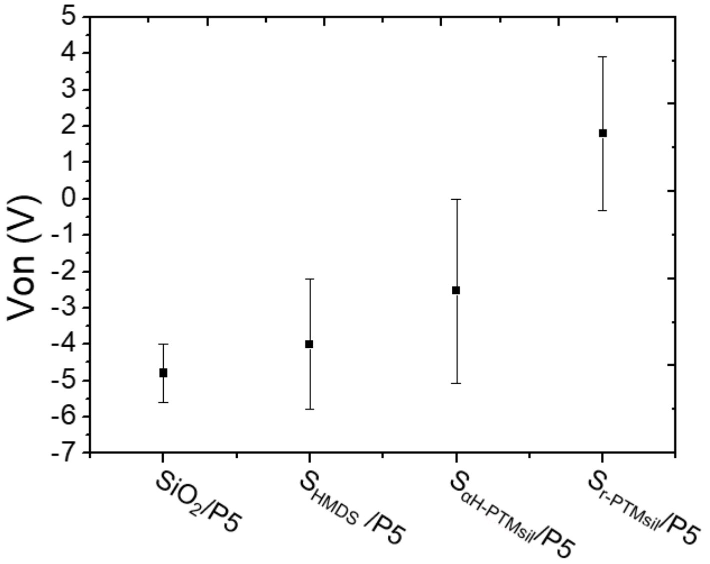

Figure 4.26: V_{on} values of SiO_2 /P5, S_{HMDS} /P5, $S_{\alpha H\text{-}PTMsil}$ /P5 and $S_{r\text{-}PTMsil}$ /P5 based devices.

The carrier mobility (μ) values are reported in Figure 4.27. As it it possible to see from the plot, an improvement was observed passing from Bare SiO_2 /P5 devices to S_{HMDS}/P5 OFETs. The mobility further increased when the dielectric was functionalized with αH-PTMsil. This was in accordance to the enhancement of the surface hydrophobicity passing from a bare SiO_2 to a dielectric modified with HMDS and αH-PTMsil which, as already seen, gave rise to a smoother pentacene film. Surprisingly, the same tendency was not followed by $S_{r\text{-}PTMsil}$/P5 based devices, where a drastic decline of the carrier mobility was observed compared to the case of the non-radical PTM molecules.

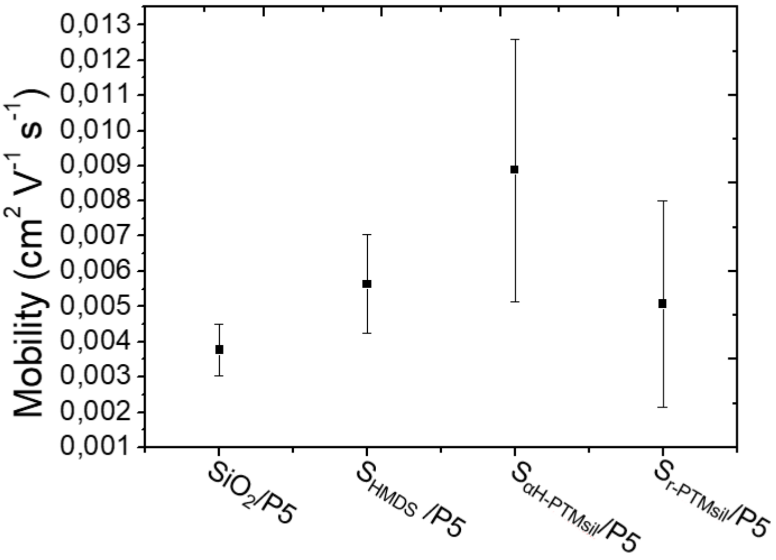

Figure 4.27: Mobility values of SiO_2 /P5, S_{HMDS} /P5, $S_{\alpha H\text{-}PTMsil}$ /P5 and $S_{r\text{-}PTMsil}$ /P5 based devices.

The unexpected low mobilities of $S_{r\text{-PTMsil}}$/P5 OFETs could be due to the charge trapping which could take place when the radical derivatives are at the dielectric/semiconductor interface. Calculations of the subthreshold swing (SS), which can be directly associated to charge trapping density were realized and were in agreement with this hypothesis. Indeed, the highest values of SS were obtained in the case of $S_{r\text{-PTMsil}}$/P5 devices, as reported in Figure 4.28.

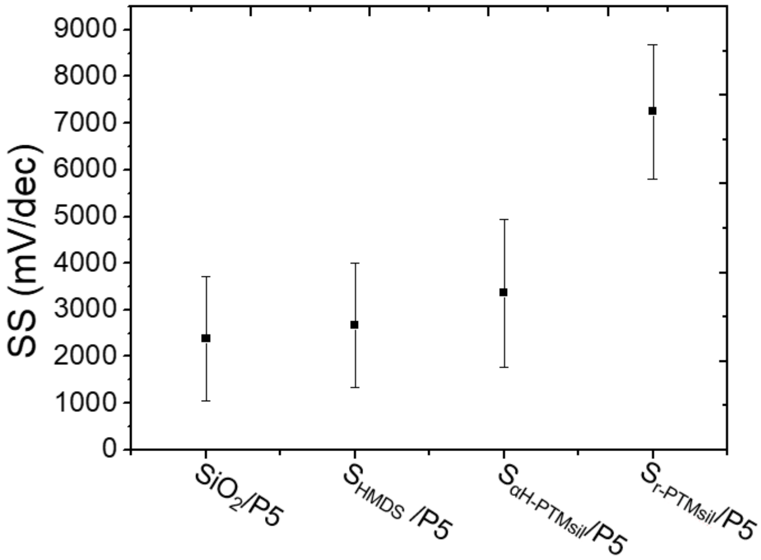

Figure 4.28: SS values of SiO_2 /P5, S_{HMDS} /P5, $S_{\alpha H\text{-PTMsil}}$ /P5 and $S_{r\text{-PTMsil}}$ /P5 based devices.

The output characteristics (I_{DS} vs. V_{DS}) of all the devices were recorded at different gate voltage, as reported in Figure 4.29.

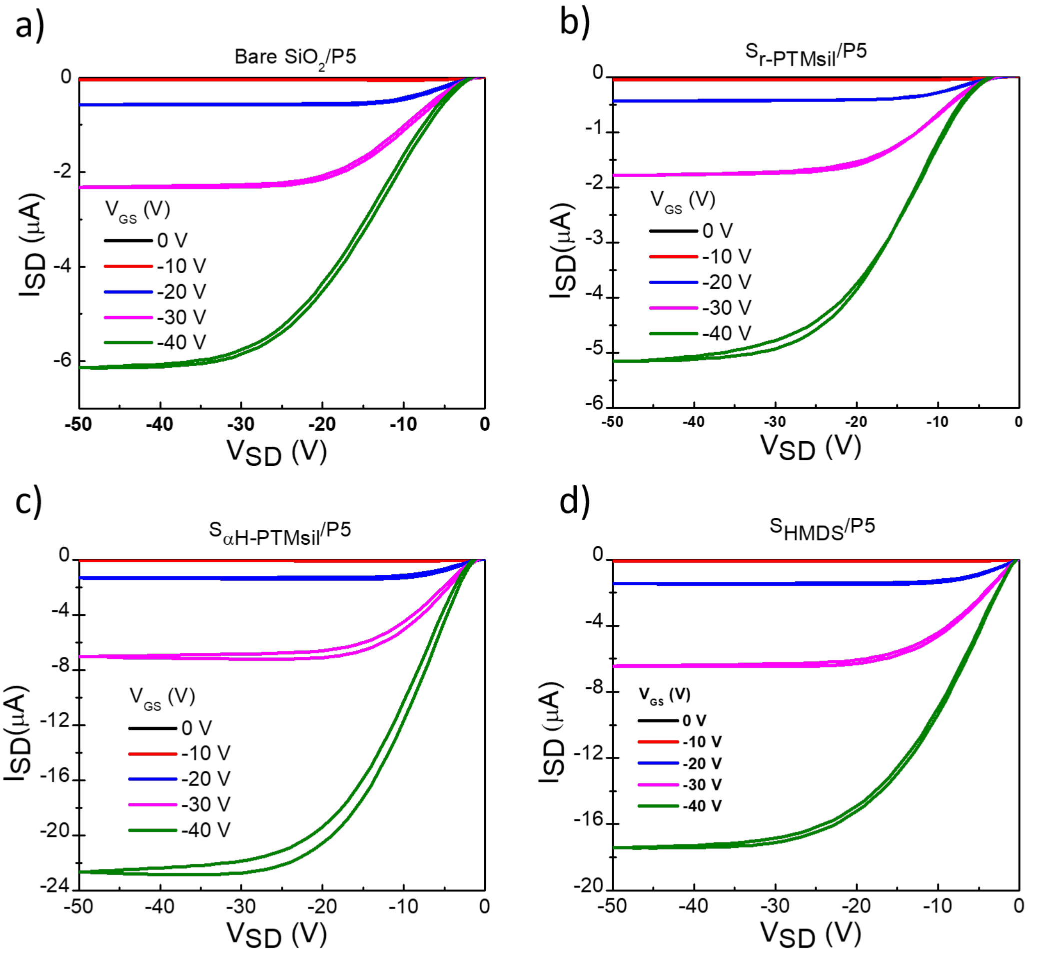

Figure 4.29: Output characteristics of the pentacene OFETs with and without dielectric functionalization.

The contact resistance, responsible for the nonlinear increase of the I_{SD} current in the output characteristics at low V_{SD}, decreased passing from bare SiO_2/P5 to $S_{\alpha H\text{-}PTMsil}$ /P5 or S_{HMDS}/P5 devices, whereas $S_{r\text{-}PTMsil}$ /P5 based devices showed a very similar behavior to the bare SiO_2/P5 OFETs. The less efficient charge injection in $S_{r\text{-}PTMsil}$ /P5 based OFETs suggests that the different functionalization of the dielectric could have an impact also on the electrode-semiconductor interface in terms of contact resistance. The higher contact resistence found in the devices with $S_{r\text{-}PTMsil}$ might also be related with the lower mobility found in these devices and the charges density of traps. Nevertheless, calculations are currently in progress to clarify better these observations.

The OFET devices are said to show hysteresis when I_{DS} depends on the sweep direction of V_{GS} [302]. The hysteresis depends on multiple factors, among all the possibility of the polarization of the gate dielectric. We investigated the device hysteresis by performing voltage sweeps at different speed, noting that in our case the hysteresis was not dependent on the SAM which was at dielectric/semiconductor interface. This indicates that no charges were accumulating as it could be anticipated with the electroactive PTM radical SAM and as reported in literature in the case of C_{60} SAMs at the dielectric AlO_x/semiconductor interface [297].

To additionally investigate if the modulation of the r-PTMsil charge could be controlled in our OFET configuration, so to use our system as memory device, further tests were performed. A pulse of +40 V or -40 V was applied between the gate and the source electrodes for ten seconds and the transfer characteristics of the device were registered after each pulse application. The measurement was repeated four times, each time switching from a negative (-40 V) to a positive (+40) pulse. The same experiment was carried out on all the functionalized devices. Hence, a shift in the V_{th} was expected in $S_{r\text{-}PTMsil}$ /P5 device as an effect of the molecular switch of the PTM radical derivative to the PTM anion, supposing that the switch could be promoted in the used conditions. Unfortunately no clear changes were observed between $S_{r\text{-}PTMsil}$ /P5 and the other devices, proving that the polarization effects at which the molecules are exposed were not sufficient to promote the radical/anion switch of the PTM radical derivative. This could be attributed to the low number of π-π interactions present along the PTM SAM that avoids the formation of a conductive path where the charges could flow, after injection, from the electrodes.

The same systematic study was conducted on the n-type devices, namely when fullerene C_{60} is used as the OSC. The transfer characteristics in lin-lin as well as in log-lin scale of the four different devices (i.e., Bare SiO_2 /C_{60}, S_{HMDS} /C_{60}, $S_{r\text{-}PTMsil}$ /C_{60} and $S_{\alpha H\text{-}PTMsil}$/$C_{60}$) are reported in Figure 4.30, while the parameters extracted are listed in Table 4.3.

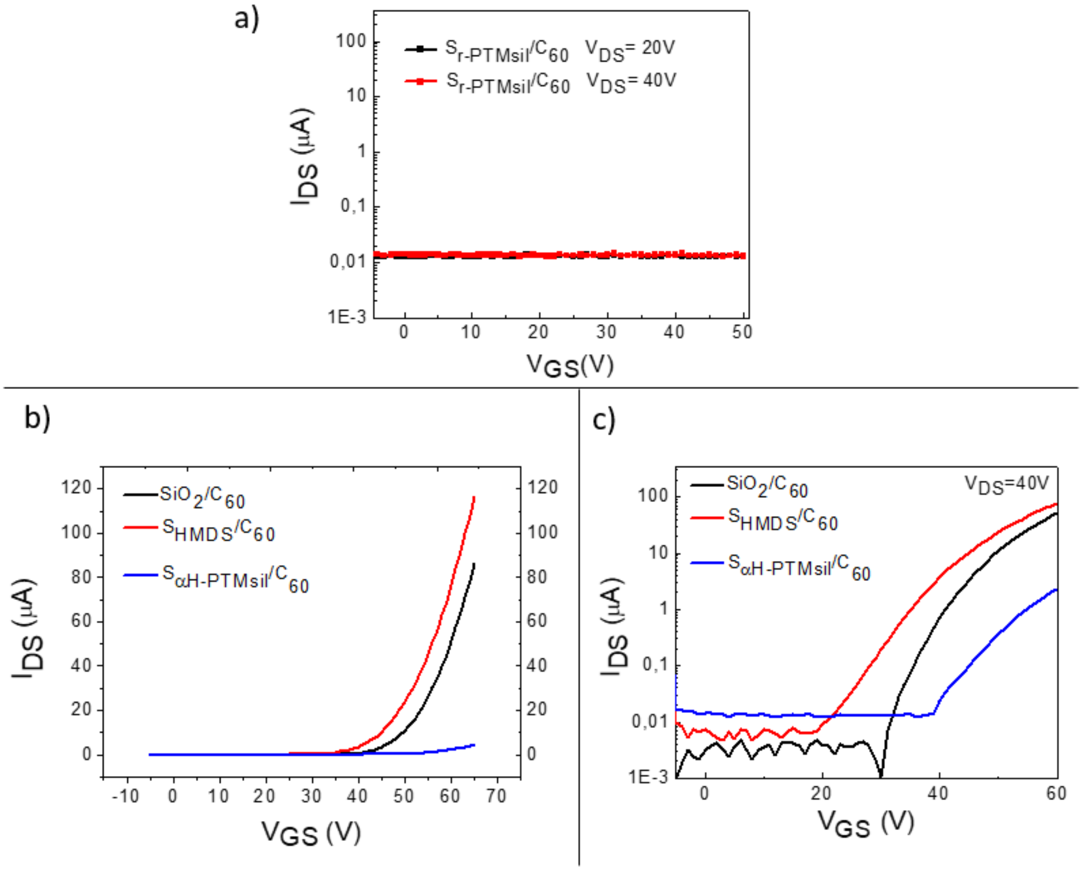

Figure 4.30: a) Log-lin transfer characteristics of $S_{r\text{-}PTMsil}$ /C_{60} at V_{DS} of 20 V (black line) and 40 V (red line). b) Lin-lin and c) log-lin transfer characteristics of the SiO_2 /C_{60}, S_{HMDS} /C_{60} and $S_{\alpha H\text{-}PTMsil}$/$C_{60}$ based OFETs.

Table 4.3: n-type OFETs electrical characteristics.

Device	V_{on} (V)	Mobility ($cm^2V^{-1}s^{-1}$)
Bare SiO_2/C_{60}	28,7	$4{,}42x10^{-2}$
S_{HMDS}/C_{60}	21,2	$4{,}74x10^{-2}$
$S_{\alpha H\text{-}PTMsil}$/$C_{60}$	36,7	$9{,}5x10^{-3}$
$S_{r\text{-}PTMsil}$/C_{60}	-	-

Importantly, in this case the device with the PTM radical SAM ($S_{r\text{-}PTMsil}$ /C_{60}) did not switch on, that is no current could be measured. In contrast, $S_{\alpha H\text{-}PTMsil}$/$C_{60}$ and S_{HMDS}/C_{60} devices presented a V_{on}~37 V and ~21 V, respectively. In general, it can be stated that the dielectric passivation with S_{HMDS} SAM had a positive effect on the V_{on} of the devices reducing the value from ~29 V (in the case of bare SiO_2/C_{60}) to ~21 V. On the contrary, a shift towards more positive V_{on} values was registered passing from the bare

SiO_2/C_{60} to the functionalized $S_{\alpha H\text{-}PTMsil}/C_{60}$ based OFETs. These effects are in line with the results previously discussed for the p-type semiconductor, since they could be rationalized considering the dipolar moment of the molecules used. Nevertheless, contrary to the previous case, here the additional electrical field of the dipolar moment of αH-PTMsil SAM-molecules reduces the applied gate field making the devices harder to be switched on. The extreme case is represented by the $S_{r\text{-}PTMsil}$ /C_{60} based devices where the electrical polarity of the system had even stronger effect incompatible with the devices operation.

Analyzing the carrier mobility reported in Table 4.3, it can been seen that , accordingly to the electrical effects already proposed, the performance of the devices decreased when $S_{\alpha H\text{-}PTMsil}/C_{60}$ or $S_{r\text{-}PTMsil}/C_{60}$were used (in the last case, the devices did not work at all). Contrarily, the charge mobility remains almost unaltered between devices with unfunctionalized dieletric ($4{,}42 \cdot 10^{-2}$ $cm^2V^{-1}s^{-1}$) and S_{HMDS}/C_{60} based OFETs, which showed values of $4{,}74 \cdot 10^{-2}$ $cm^2V^{-1}s^{-1}$.

All the results obtained can be rationalized as follows: the OSC film seems to be not influenced by the different molecules at the dielectric/OSC interface, as deduced from AFM and XDR measurements. However, it cannot be completely rule out the presence of different molecular arrangement in the first OSC monolayer in contact with the substrate. A clear impact of the molecules on the p- and n-type OFETs characteristics is observed, possibly due to the different contribution of the dipole moment of the molecules used for the dielectric functionalization. Specifically, $S_{r\text{-}PTMsil}$ and $S_{\alpha H\text{-}PTMsil}$ have dipole moments which, more or less strongly, enhanced or reduced the gate field in the p- and n- type OFETs respectively. Specifically, $S_{r\text{-}PTMsil}$ had a particulary strong influence on the V_{on} of p-type based OFETs, which was found to be more positive compared to the values showed by the other bare or functionalized devices. Furthermore, in pentacene-based OFETs an enhancement of the mobility was observed when $S_{\alpha H\text{-}PTMsil}$ was used at the dielectric/semiconductor interface, attributable to the better charge injection as well as to the more favorable hidrophobic character of $S_{\alpha H\text{-}PTMsil}$.

Regarding n-type OFETs where C_{60} was used as semiconductor, both αH-PTMsil and r-PTMsil molecules decreased the device performances. The presence of $S_{r\text{-}PTMsil}$ at the dielectric/semiconductor interface, impede the device to switch on, while using $S_{\alpha H\text{-}PTMsil}$ larger V_{on} and lower mobility were obtained.

Further theoretical calculations are underway to establish the component of the dipole moment of αH-PTMsil and r-PTMsil along the molecular axis to provide a definitive proof of the dipole moment contribution.

4.5.4 Summary

r-PTMsil and αH-PTMsil were introduced in C_{60} and pentacene based OFET devices by functionalizing the SiO_2 dielectric. A comparative study was carried out between devices containing the two molecules at dielectric/semiconductor interface, in order to verify how the different electrical properties of these compounds affect the devices characteristics. Furthermore, we were investigating if the conversion between r-PTMsil to the anionic form could be realized once the molecule is integrated into the device. Even if the switch of r-PTMsil was not appreciated, interesting results were obtained. It was clearly demonstrated that in case of n-type OFET (i.e., C_{60}) both molecules have a negative effect on the device performances. The extreme case is represented by r-PTMsil that impedes the devices to switch on. Contrariwise, r-PTMsil and αH-PTMsil have positive influences on p-type (i.e., pentacene) OFETs performances, where an enhancement of the device mobility is obtained in presence of αH-PTMsil and a shift of the V_{on} towards more positive values is registered with r-PTMsil. The phenomena observed were attributed to the dipole moment of the SAMs grown on the dielectric, but further theoretical analysis is required to confirm it.

4.6 r-PTMpol as charge storage system [2]

There is an ever-increasing demand for smart energy storage devices justified by the ever more looming presence of electric vehicles in the market and large-scale power grids that must deliver high energy and high power along with a longer cycle life. It is also simultaneously essential to develop an eco-friendly and cleaner energy storage system for sustainable future use. To date, electroactive organic molecules are imposing themselves as a possible eco-friendly alternative to the heavily toxic and expensive inorganic insertion electrodes used nowadays.

In this sense, a particular interest must be dedicated to organic radicals. The pioneering work of Oyaizu and Nishide demonstrated the use of organic radicals for charge storage applications [303]. Nevertheless, most of the research on organic radical charge storage materials used 2,2,6,6- tetramethylpiperidine-N-oxyl (TEMPO) – based linear or branched polymers as the electroactive material, where the polymers comprised flexible alkyl chains and TEMPO radicals were attached as pendants [304].

Recent advancements in nanotechnology have resulted in the development of new

---

[2] This work was performed in collaboration with Dr. Ajayakumar Murugan, Dr. Elena Marchante and Dr. Dino Tonti.

materials and a greater fundamental understanding of their properties. Those advancements are currently enabling new types of hybrid energy-storage devices that exhibit characteristics of batteries and electrochemical capacitors. Some of these new designs utilize polymer electrodes or polymer electrolytes and also some unique combinations as cell components have been proposed [305]. For instance, a conceptually novel all-organic sodium hybrid capacitors was rationally designed by replacing the conventional electrodes with clean, green, and metal free organic molecules to host ions [306]. Polymer organic radical gel materials were also found to support fast bulk-redox charge storage for surface double layer ion exchange at carbon electrodes [307].

Towards high performing charge storage materials based on organic radicals, the investigation of how varying the polymer backbone and/or the radical entity is of great interest. Moreover, there are no reports of 2D-radical materials for charge-discharge applications. In light of this, we synthesized the novel radical polymer (r-PTMpol) with rigid polymeric backbone where the backbone was constructed with carbon centred radicals, i.e., PTM$^{\cdot}$ units, as described in Section4.3. Moreover, in the following section we reported the preliminary electrochemical study performed on this novel material, with the aim of demonstrating the potential of this polymer as a new class of charge storage systems.

4.6.1 Electrochemical characterization of r-PTMpol

In order to electrochemically characterize r-PTMpol and evaluate its potential as charge storage material, it was deposited on an aluminum foil during a process of electrode slurry fabrication. This is the conventional process for the electrode manufacturing in charge storage devices, and consists in depositing, by casting on the electrode, a dispersion of the active material mixed with a high conductive material (often carbon) and an inert polymer, useful to enhance the mechanical stability of the active material on the electrode. In our case 2 mg of active material were thoroughly mixed by grinding together with 1 mg of carbon black (CSP) and 0,5 mg of polyvinylidene fluoride (PVDF). 300 mL of 1-metil-2-pirrolidone (NMP) were used as solvent. Finally, 150 mL of the dispersion were casted on aluminum foil and the solvent was left evaporating overnight heating up to 40°C under vacuum. Figure 4.31 shows the fabricated electrodes.

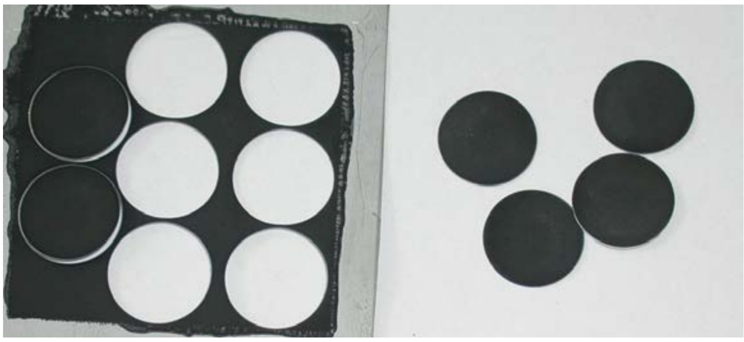

Figure 4.31: Illustration of the working electrode (11 mm diameter) fabricated by slurry manufacturing.

A home made specific electrochemical cell was used to perform the electrochemical characterization. This cell was designed in our group by Elena Marchante and consists of three teflon pieces that permit to hold the modified working electrode (WE) exposing a specific active area to the electrolyte solution (0,125 cm^2). The three pieces are sandwiched and fixed together by four screws. The setup permits to incorporate the counter (CE) and the reference electrodes (RE) through the upper part of the cell, in a perpendicular orientation with respect to the WE. Furthermore, the cell is provided with an electrolyte container located in the center, that can be sealed off with an adapter in order to isolate the system from the external environment and from light (Figure 4.32).

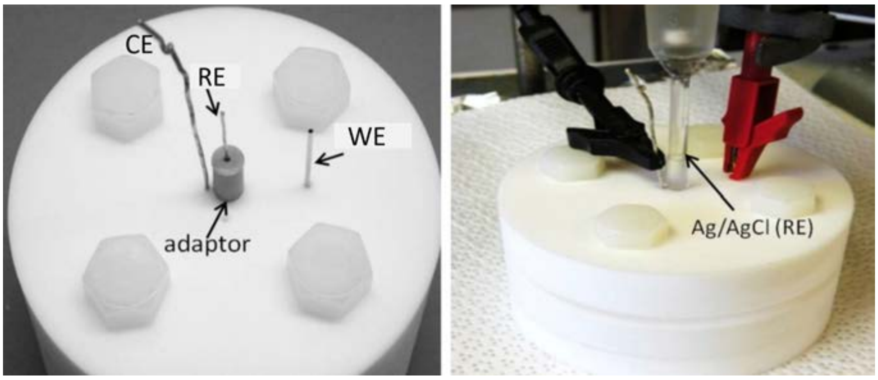

Figure 4.32: Electrochemical cell used for the cyclic voltammetry measurements.

First of all, we started characterizing the precursor of the PTM polymer, the PTM radical derivative **17**, in order to see if the conditions used for the electrode preparation were compatible with PTM derivatives, so as to have a reference for our system. Cyclic voltammetry measurements were performed using the aluminum foil covered by **17**/CSP/PVDF based pellet as WE, while a platinum and a silver wire were used as CE and RE, respectively. A solution of tetrabutylammonium hexafluorophosphate (TBAPF$_6$) in acetonitrile was selected as electrolyte. Figure 4.33 a) shows the CV response at three different scan rates (i.e. 10, 20 and 50 mV/s). The reversible redox wave observed at $E_{1/2}$= 0,03 V (at scan rate of 0,02 V/s) is ascribed to the conversion of the PTM radical moiety to the corresponding anion.

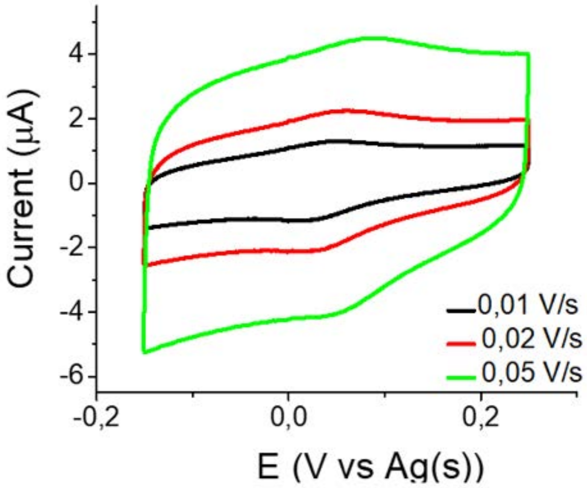

Figure 4.33: CV of monomer **17** at different scan rates. $TBAPF_6$ 0,02 M in ACN was used as electrolyte, a silver and a platinum wires were used as reference and counter electrode, respectively.

The CV measurements of r-PTMpol were performed using the same conditions mentioned above for **17**. Unfortunately, no clear peaks that could be associated to the redox process of the molecule were observed (Figure 4.34 a)), possibly due to the lack of an appropriate counter ion for the stabilization of the negative charges produced as a consequence of the reduction process.

Hence, another salt, namely lithium tetrafluoroborate ($LiBF_4$), was used as electrolyte. $LiBF_4$ was chosen since it is a standard salt for charge storage measurements and the smaller size of the cations could favour the intercalation and therefore the anions stabilization. In our case, the best result was obtained using a 0,02 M solution of $LiBF_4$ in acetonitrile. Importantly the electrolytic solution was dried on molecular sieves in order to reduce the amount of water in there that could affect the electrochemical process. In these new conditions the CV of r-PTMpol showed a cathodic peak at -0,25 V and an anodic one at 0,18 V at 0,02 V/s. A remarkable peak-peak separation was observed, indicative of a slow redox reaction.

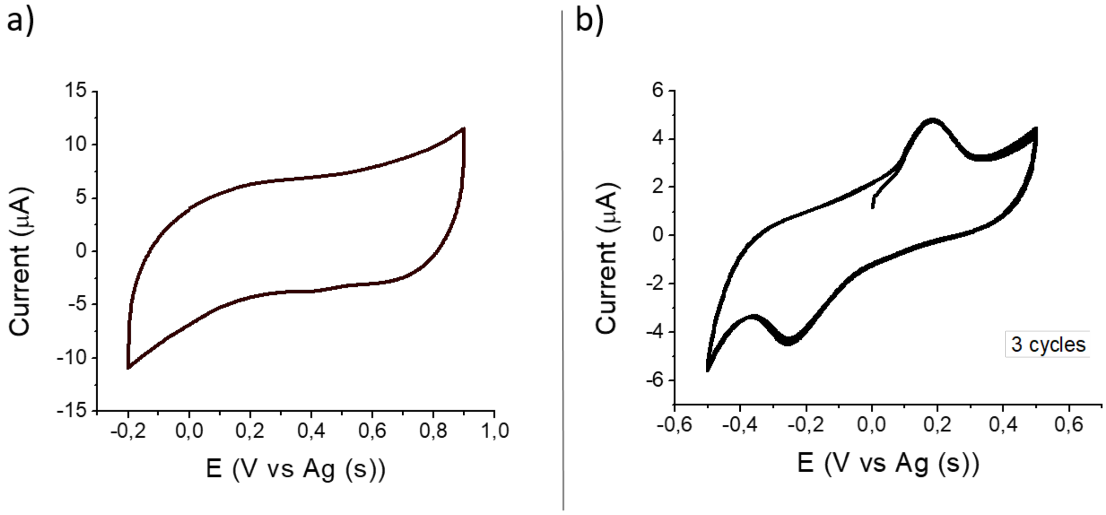

Figure 4.34: CV of r-PTMpol at scan rate of 0,02 V/s. a) TBAPF$_6$ and b) LiBF$_4$ 0,02 M in ACN were used as electrolyte and a silver and a platinum wires were used as reference and counter electrode, respectively.

Moreover, through the dependence between the current density and the square root of the scan rate, it is possible to have information about the diffusion coefficient, accordingly to the Randles-Sevcik equation (see 4.1)

$$I_P = 2,69 \cdot 10^{-5} n^{\frac{3}{2}} D^{\frac{1}{2}} v C \tag{4.1}$$

where I_p is the current maximum, n is the number of electrons transferred in the redox event, D is diffusion coefficient in cm^2·s^{-1}, C is the concentration expressed in mol·cm^3 and v is the scan rate in V·s^{-1}.

From this equation, D can be extracted as follows:

$$D = \left(\frac{m}{2,69 \cdot 10^{-5} n^{\frac{3}{2}} C} \right)^2 \tag{4.2}$$

where m is the slope line obtained plotting the current density vs. $\sqrt{v}$ (see Figure 4.35).

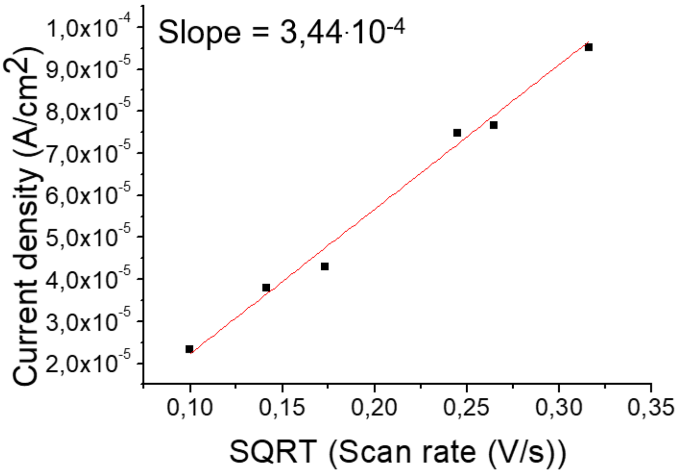

Figure 4.35: Current density vs. $\sqrt{v}$ dependence of r-PTMpol.

In this first approximation, the diffusion coefficient was found to be ~ $1{,}6 \cdot 10^{-8}$ $cm^2 \cdot s^{-1}$. This value is in agreement with the data reported in literature for lithium intercalation [308] and encourages further investigations in this sense. Even if further experiments are underway, in a first analysis the r-PTMpol can be considered a promising material for charge storage devices. Further evidences in this sense must be provided by specific charge-discharge measurements which are currently running.

4.6.2 Summary

r-PTMpol is a polymeric poly-radical PTM derivative that was designed and synthesized to be texted as a new material for charge storage applications. This molecule was deposited on aluminum working electrodes through a process of slurry fabrication. Preliminary cyclic voltammetry experiment were carried out on the polymer as well as on the momomeric precursor (derivative **17**). After optimizing the conditions, it was found that when using the polymer r-PTMpol as active material, the diffusion coefficient for lithium ions points towards ion intercalation, which is promising for efficiently charging the material. This preliminary results lay the foundation for a deeply investigation for proving the practicability of this material in charge storage devices.

5

Experimental methodologies

5.1 Synthesis of the molecules used

Synthesis of 1

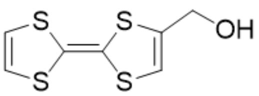

$NaBH_4$ (89 mg, 2,4 mmol) was added to a solution of the commercial available 2-formyltetrathiafulvalene (500 mg, 2,1 mmol) in 20 mL of MeOH. The solution was stirred for 30 minutes under inert atmosphere. Finally, CH_2Cl_2 was added and the mixture thus obtained was washed with brine first and then with water. The isolated organic phase was dried with $MgSO_4$ and the solvent was evaporated under reduced pressure. A yellow solid was obtained and purified by column chromatography (silica gel) using CH_2Cl_2 as eluent. Finally, compound **1** was obtained in 96% yield [211].

IR: (ν/cm^{-1}): 3290; 3057; 2925; 2857; 1542; 1456; 1114; 109; 1016; 793; 767; 648; 628.

^{1}H NMR (250 MHz CD_2Cl_2), δ (ppm): 6,35 (s 2H); 6,24 (s, 1H); 4,37 (s, 2H); 1,96 (s, 1H).

^{13}C NMR (400 MHz CD_2Cl_2), δ (ppm): 137,43; 119,54; 119,47; 115,50; 111,50; 109,86; 60,96.

LDI-TOF (m/z): calculated Mol. Wt $C_7H_6OS_4$: 234,3; experimental (in positive mode): 233,9 [M].

Synthesis of TTFS$_2$

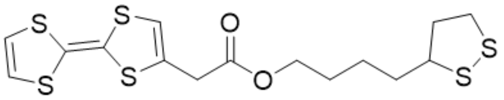

290 mg (1,23 mmol) of compound **1** and 305 mg (1,5 mmol) of thioctic acid were dissolved in 40 mL of CH_2Cl_2 previously treated with basic alumina. The solution was kept under inert atmosphere and was stirred at 0ºC during 15 minutes. Then, 379 mg (1,8 mmol) of N,N'-dicicloesilcarbodiimmide (DCC) and 45 mg (0,4 mmol) of 4-dimethylaminopyridine (DMAP) dissolved in 10 mL of CH_2Cl_2 were added, and the resulting solution was left under stirring for 15 minutes more at 0º C. The reaction mixture was kept 24 h under stirring at room temperature. Finally, the solution was washed with water, the organic layer was isolated, dried with $MgSO_4$ and evaporated under reduced pressure. The crude of reaction was purified by column chromatography silica gel, using CH_2Cl_2 as eluent and the final compound **2** was obtained as a yellow powder with 90% yield [212].

IR: (ν/cm^{-1}): 3062; 2925; 2824; 1728; 1578; 1518; 1456; 1389; 1151; 1125; 661; 570.

^{1}H NMR (400 MHz, CD_2Cl_2), δ (ppm): 6,36(s, 1H); 6,35 (s, 2H); 4,81 (s, 2H) 3,60-3,54 (m, 1H); 3,20-3,07 (m, 2H); 2,49-2,41 (m, 1H); 2,36 (t, J = 7,3 Hz, 2H); 1,94-1,86 (m, 1H) 1,74-1,61 (m, 4H); 1,51- 1,41 (m 2H).

^{13}C NMR (500 MHz CD_2Cl_2), δ (ppm): 172,81; 131,41; 119,19; 119,16; 119,08; 111,55; 109,05; 60,58; 56,38; 40,23; 38,55; 34,56; 33,73; 28,65; 24,60.

LDI-TOF (m/z): calculated Mol. Wt. $C_{15}H_{18}0_2S_8$: 422,6; experimental (in positive mode): 421,9 [M].

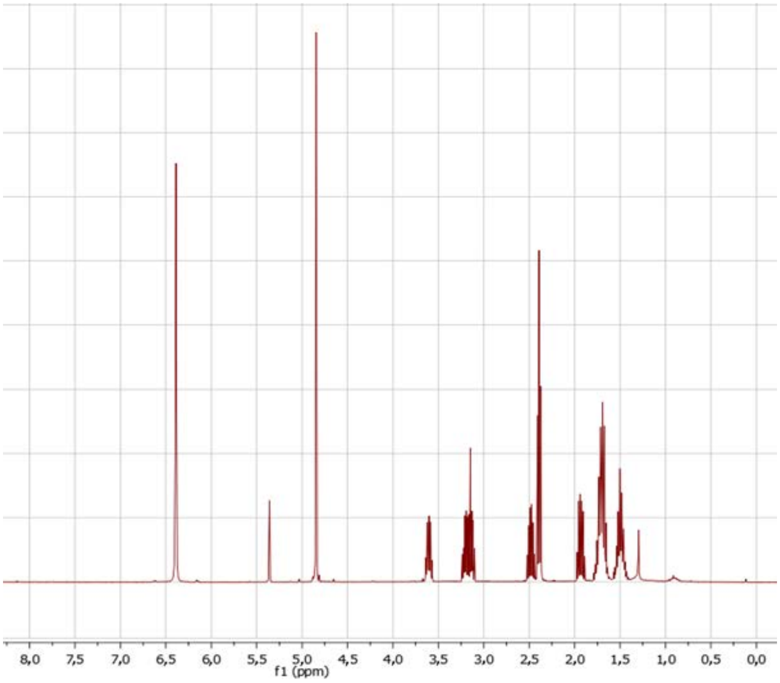

Figure 5.1: ^{1}H NMR (400 MHz, CD_2Cl_2) of $TTFS_2$.

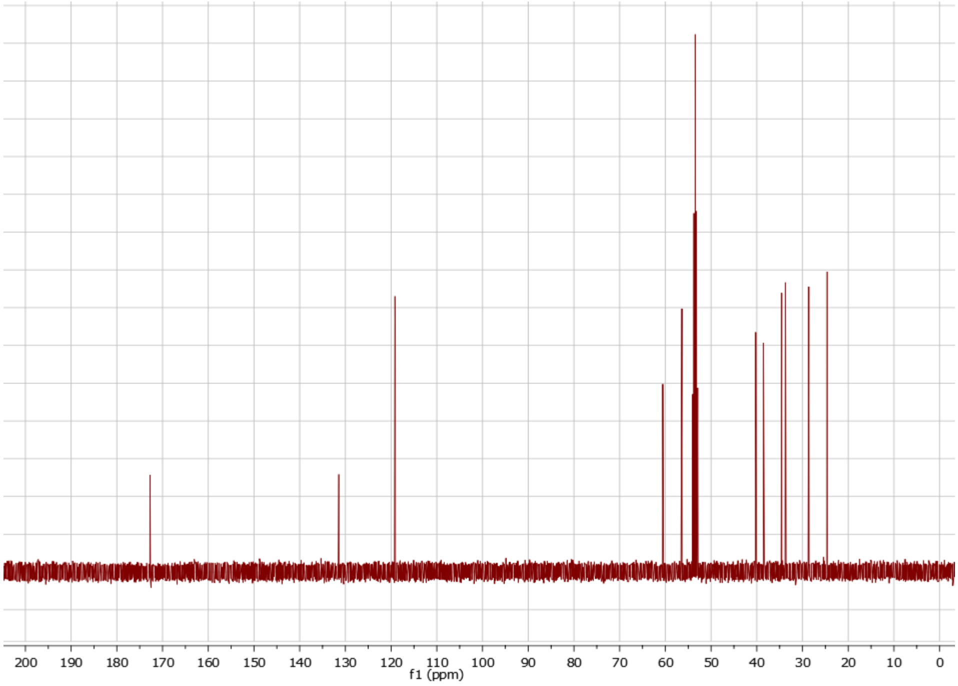

Figure 5.2: ^{13}C NMR (500 MHz, CD_2Cl_2) of $TTFS_2$.

Synthesis of AQSi

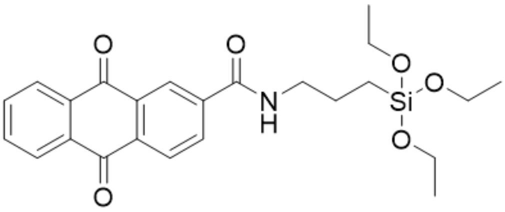

300 mg of anthraquinone-2-carboxylic acid (1,2 mmol) were dissolved in 5 mL of $SOCl_2$ under inert atmosphere and the mixture was stirred overnight at reflux temperature. The excess of $SOCl_2$ was then removed by flowing nitrogen. The solid thus obtained was subsequently dissolved in 20 mL of dry toluene. APTES and NEt_3 (1,3 mmol each) were then added. The mixture was stirred for 3 h. After that, the solvent was removed under vacuum and the solid obtained was dissolved in chloroform. Successive precipitations and filtrations in an ether/hexane mixture were carried out to remove tri-ethyl ammonium chloride. AQSi was obtained in a 70% yield [99].

^{1}H NMR (400 MHz, $CDCl_3$), δ (ppm): 8,59 (bs, 1H); 8,39 (d; J = 8,1 Hz, 1H); 8,35 – 8,32 (m, 2H); 8,30 (dd, J = 8,1; 1,4 Hz, 1H); 7.83 (m, 2H); 6.88 (m, 1H); 3.85 (q, J = 7,0 Hz, 6H); 3.54 (q, J = 6,5 Hz, 2H); 1,86 – 1,78 (m, 2H); 1,23 (t, J = 7,0 Hz, 9H); 0,77 – 0,72 (m, 2H).

13C NMR (400 MHz, $CDCl_3$), δ (ppm): 182,51; 165,52; 139,90-124,48; 58,59; 42,49; 22,80; 18,29; 7,96.

IR-ATR υ (cm^{-1}): 3289; 2977; 2919; 2878; 1678; 1644; 1592; 1545; 1389; 1331; 1267; 1162; 1069; 960; 925; 774; 693.

LDI-TOF (m/z): calculated Mol. Wt. $C_{24}H_{29}NO_6Si$: 455,58; experimental (in negative mode): 455,02 [M].

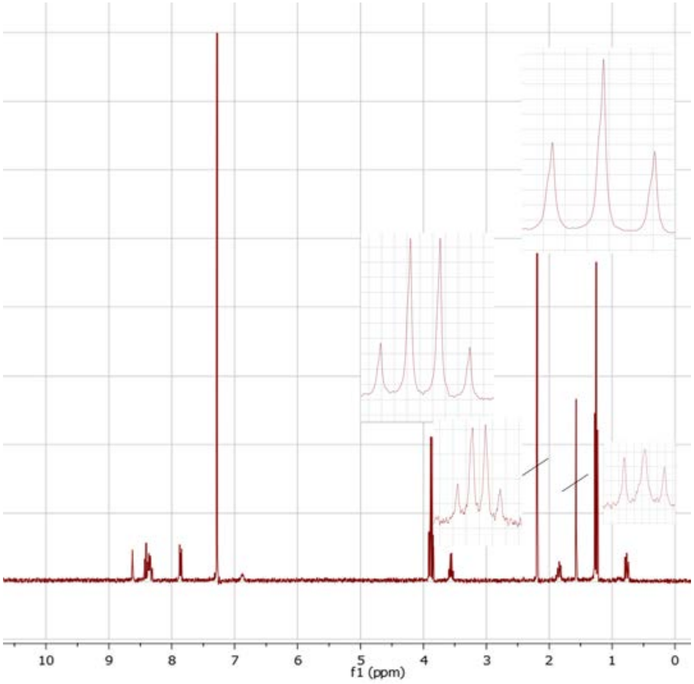

Figure 5.3: ^1H NMR (400 MHz, $CDCl_3$) of AQSi.

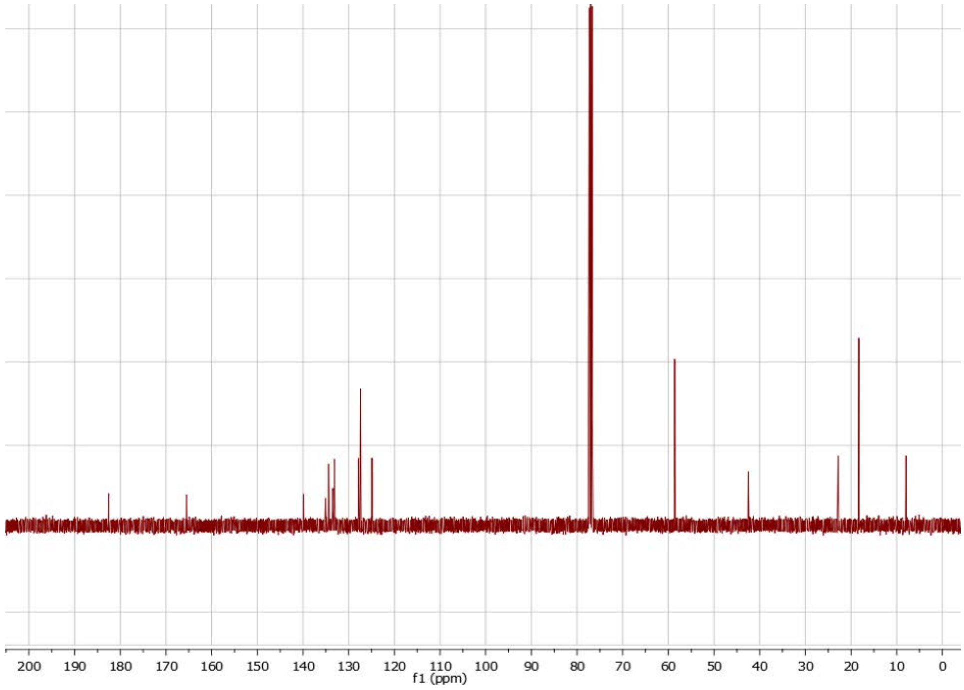

Figure 5.4: ^{13}C NMR (400 MHz, $CDCl_3$) of AQSi

Synthesis of AQS_2

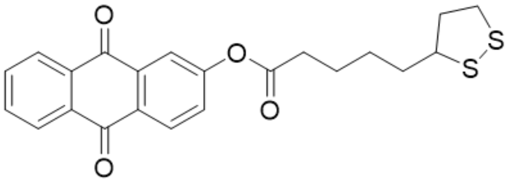

2-hydroxyanthracene-9,10-dione (205 mg 0,9 mmol) was dissolved in dry dichloromethane (60 ml) and 0,2 ml (1,5 mmol) of NEt_3 were then added dropwise. The mixture was stirred at 0°C for 15 min under Ar atmosphere. After the addition of lipoic acid chloride (272 mg, 1,2 mmol), dissolved in dry CH_2Cl_2 (4 mL), the mixture was stirred overnight at room temperature and the residue purified by a chromatography column (silica gel, CH_2Cl_2) giving the compound AQS_2 (158 mg, 47%) as a yellow powder [102].

^{1}H NMR (600 MHz, CD_2Cl_2), δ (ppm): 8,29-8,22 (m, 3H); 7,94 (d, 1H, J=6 Hz); 7,79-7,77 (m, 2H,); 7,51- 7,49 (m, 1H, Ar-H); 3,62-3,59 (m, 1H); 3,18-3,10 (m, 2H); 2,64 (t, 2H, J = 6 Hz); 2,40- 2,34 (m, 1H); 1,94-1,90 (m, 1 H); 1,81-1,70 (m, 4H); 1,59-1,43 (m, 2H).

^{13}C NMR (250 MHz, CD_2Cl_2), δ (ppm): 182,52; 182,24; 171,57; 155,73; 135,48-120,25; 56,72; 40,64; 38,94; 34,96; 34,40; 29,02; 24,85.

IR-ATR ʋ (cm^{-1}): 2913; 2855; 1753; 1661; 1580; 1458; 1417; 1383; 1348; 1284; 1197; 1145; 1116; 931; 855; 710; 664.

LDI-TOF (m/z): calculated Mol. Wt. $C_{22}H_{20}O_4S_2$: 412,5; experimental (in negative mode): 411,9 [M]; 222,98 [M- $C_8H_{13}OS_2$].

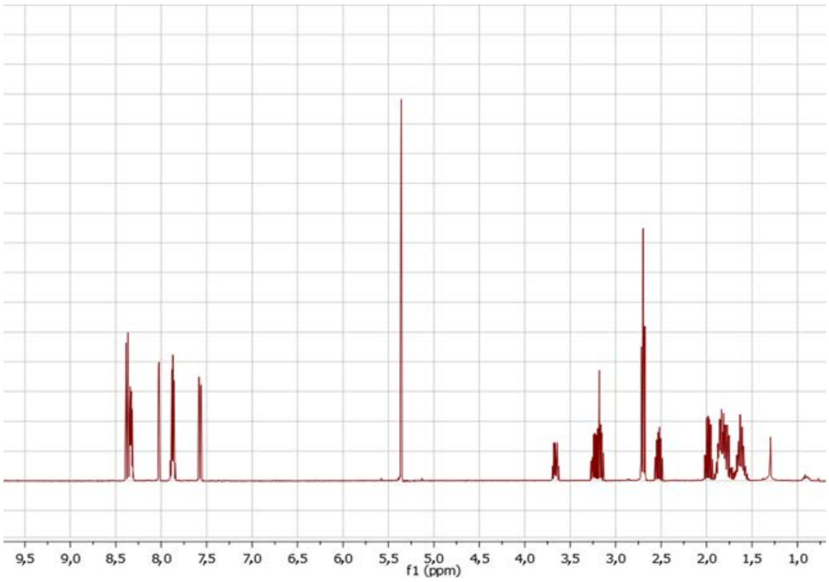

Figure 5.5: ^1H NMR (600 MHz, CD_2Cl_2) of AQS_2.

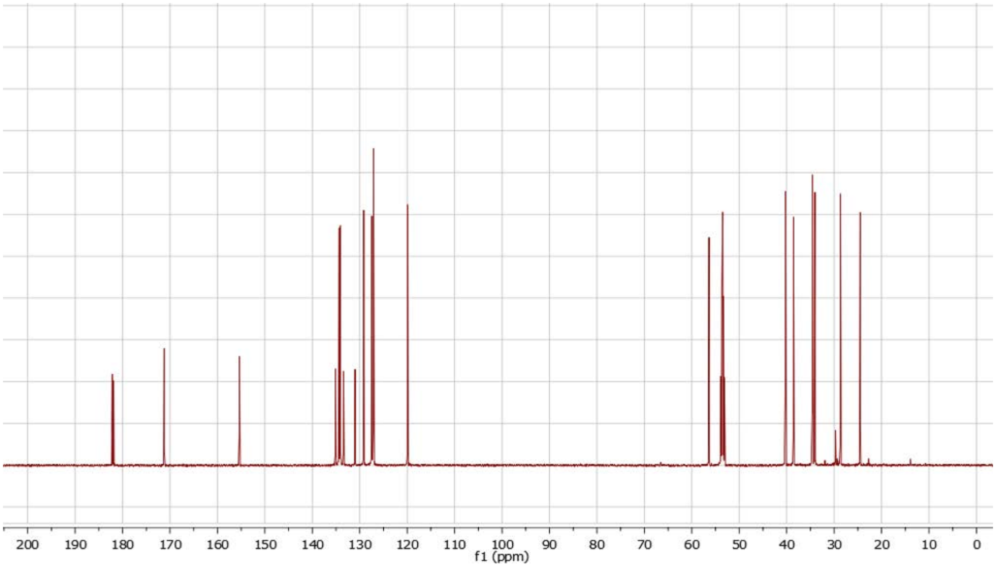

Figure 5.6: ^1H NMR (250 MHz, CD_2Cl_2) of AQS_2.

Synthesis of 2

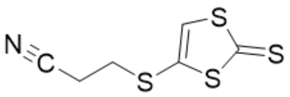

Bis (tetra-n-butylammonium) bis (1,3-dithiole-2-thione-4,5-dithiolato) zinc complex (5 g, 5,3 mmol) and piridinium chloride (2,39 g, 20,7 mmol) were dissolved in distilled acetonitrile (100 mL). The solution was heated at 70 °C and 3-bromopropionitrile (1,8 mL, 22,7 mmol) was added. The solution was stirred during 2 h. Then, the resulting suspension was cooled down to room temperature and filtered under vacuum. The solvent was evaporated and the solid thus obtained was dissolved in dichloromethane. The organic layer was washed with water three times and dried with $MgSO_4$. The compound was concentrated under reduced pressure and subsequently purified through column chromatography (silica gel, CH_2Cl_2). Compound **2** was thus obtained with 60% yield [214].

IR-ATR υ (cm^{-1}): 3035; 2960; 2902; 2235; 1690; 1632; 1406; 1319; 1278; 1180; 924; 862; 768; 710; 583; 542.

^1H NMR ($CDCl_3$), δ (ppm) : 2,76-2,82 (t, 2H, J = 6 Hz), 3,12-3,19 (t, 2H, J 6 Hz), 7,18 (s, 1H).

^{13}C NMR ($CDCl_3$), δ (ppm): 18,63; 31,74; 117,01; 132,62; 135,01; 213,72.

Synthesis of 3

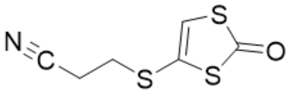

To a solution of **2** (0,5 g, 2,3 mmol) in 60 mL of dichloromethane, AcOH (20 mL) and $Hg(OAC)_2$ (2,2 g, 6,9 mmol) were added. The mixture was stirred at room temperature for 1 h and then filtered on celite. The organic layers were washed with $NaHCO_3$ first and water after, dried under $MgSO_4$ and evaporated under reduced pressure. Column chromatography (silica gel, hexane/CH_2Cl_2 4/6) was performed to purify the compound, which was obtained with 80% yield [**?**].

IR-ATR υ (cm^{-1}): 3088; 2925; 2826; 2247; 1736; 1685; 1621; 1418; 1290; 1122; 937; 838; 745; 658; 438.

^1H NMR(400 MHz, CD_2Cl_2), δ (ppm): 7,09 (s, 1H); 3,02 (t, 2H, J = 6,9 Hz); 2,71 (t, 2H, J = 6,9 Hz).

^{13}C NMR(400 MHz, CD_2Cl_2), δ (ppm): 192,01; 126,10; 123,40; 117,83; 31,84; 18,90.

Synthesis of 4

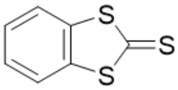

A mixture of 1,3-benzodithiolylium tetrafluoroborate (2,5 g, 10,4 mmol) and elemental sulfur (0,5 g, 15,6 mmol) were dissolved in anhydrous pyridine (17 mL). The mixture was refluxed during 5 h. $CHCl_3$ was then added and the organic phase was washed first with water and then with a solution of HCl 1 M. The crude of reaction was subjected to column chromatography, silica gel (CH_2Cl_2/Hex 1/1). Compound **4** was obtained with 51% yield [216].

^{1}H NMR(400 MHz, CD_2Cl_2), δ (ppm): 7,52 (dd, 2H, J = 6,0); 7,41 (dd, 2H, J = 6,0).

^{13}C NMR(400 MHz, CD_2Cl_2), δ (ppm): 212,77; 141,40; 127,79; 122,18.

LDI-TOF (m/z): calculated Mol. Wt. $C_7H_4S_3$: 184,3; experimental (in negative mode): 183,9 [M].

Synthesis of 5

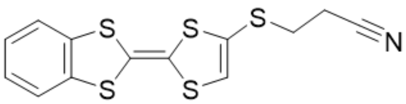

Compound **3** (150 mg, 8,1 mmol) and **4** (182 mg, 8,9 mmol) where heated to reflux temperature in dry $P(OMe)_3$ (6 mL) for 4 h under inert atmosphere. The solvent was removed by bubbling nitrogen and the crude of reaction was purified by column chromatography (silica gel, hexane/dichloromethane 3/7). Compound **5** was thus obtained with 79% yield.

^{1}H NMR (400 MHz, CD_2Cl_2), δ (ppm): 7,32-7,25 (m, 2H); 7,15 (dd, 2H, J = 6,9); 6,61 (s, 1H); 2,99 (t, 2H, J = 7); 2,70 (t, 2H, J = 7).

^{13}C NMR (350 MHz, CD_2Cl_2), δ (ppm): 136,82; 126,63; 126,50; 124,32; 122,46; 122,30; 118,01; 113,04; 110,60; 31,25; 18,93.

IR: (ν, cm^{-1}): 3074; 2923; 2850; 2248; 1878; 1569; 1505; 1425; 1312; 1286; 1260; 1226; 1179; 1123; 1031; 992; 970; 929; 811.

LDI-TOF (m/z): calculated Mol. Wt. $C_{13}H_9NS_5$: 338,54 ; experimental (in positive mode): 338,94 [M] .

Synthesis of 6

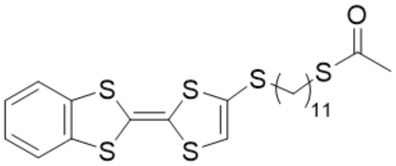

To a solution of **5** (120 mg, 0,35 mmol) in dry DMF (6 mL) a solution of CsOH (65 mg, 0,39 mmol) in anhydrous MeOH (3 mL) was added, dropwise under inert atmosphere. The solution was stirred for 1 h and then (11-bromoundecyl) thioacetate (0,27 mL, 0,44 mmol) was added and the mixture was left stirring overnight at room temperature. The solvent was evaporated under reduced pressure and the residue was dissolved in CH_2Cl_2. The organic layer was washed with water (x4), dried with $MgSO_4$, filtered and evaporated. The crude was purified by column chromatography (silica gel, hexane/dichloromethane 3/7). Compound **6** was obtained with 55% yield.

^{1}H NMR(400 MHz, CD_2Cl_2), δ (ppm): 7,28 (dd, J= 6,03; 3,1 Hz, 2H); 7,15 (dd, J= 5,9; 3,3 Hz, 2H); 6,39 (s, 1H); 2,85 (t, J= 7,4 Hz, 2H); 2,77 (t, J= 7,4 Hz, 2H); 1,66-1,58 (m, 3H); 1,41-1,28 (m, 15H).

^{13}C NMR(150 MHz, CD_2Cl_2), δ (ppm): 196,10; 137,10; 137,03; 127,79; 126,50; 126,38; 122,40; 122,36; 122,31; 122,28; 122,24; 122,22; 121,98; 114,28; 108,85; 36,38; 30,83; 29,96; 29,90; 29,87; 29,83; 29,50; 29,47; 29,44; 29,23; 29,20; 28,72.

IR (ν, cm^{-1}) 3080; 2917; 2850; 1673; 1467; 1445; 1427; 1348; 1281; 1260; 1228; 1137; 1114; 1028; 1000; 937; 811.

LDI-TOF (m/z):calculated Mol. Wt. $C_{23}H_{30}OS_6$: 514,87 ; experimental (in positive mode): 514,08 [M].

Synthesis of $BTTFS_2$

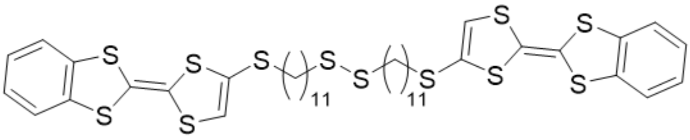

To a solution of **6** (100 mg, 0,19 mmol) in a mixture of dry THF (5 mL) and MeOH (5 mL), a solution of MeONa (29 mg, 0,54 mmol) in MeOH (2 mL) is added under inert atmosphere. The mixture of reaction was stirred at room temperature for 20 h. Then 20 mL of a NH_4Cl 0,1 M were added. The solution was concentrated under reduced pressure and the crude of reaction was dissolved in CH_2Cl_2, washed with water (x6), dried with $MgSO_4$, filtered and evaporated. $BTTFS_2$ was obtained as an orange powder with 54% yield.

^{1}H NMR(360 MHz, CD_2Cl_2), δ (ppm): 7,30-7,25 (m, 4H); 7,15-7,16 (M, 4H); 6,39 (s, 2H); 2,27 (t, J=7,4 Hz, 4H); 2,68 (t, J=7,4 Hz, 4H) ; 1,68-1,59 (m, 6H); 1,68-1,27 (m, 30H).

^{13}C NMR(600 MHz, CD_2Cl_2), δ (ppm): 137,10; 137,03; 122,79; 126,4; 122,33; 122,3; 122; 39,58; 36,39; 29,9; 29,87; 29,84; 29,61; 29,45; 28,89; 28,72.

HRMS // ESI$^+$ (m/z) in $CHCl_3$/MeOH: calculated: 965,0766 [M+Na]$^+$; experimental: 965,0752 [M+Na].$^+$

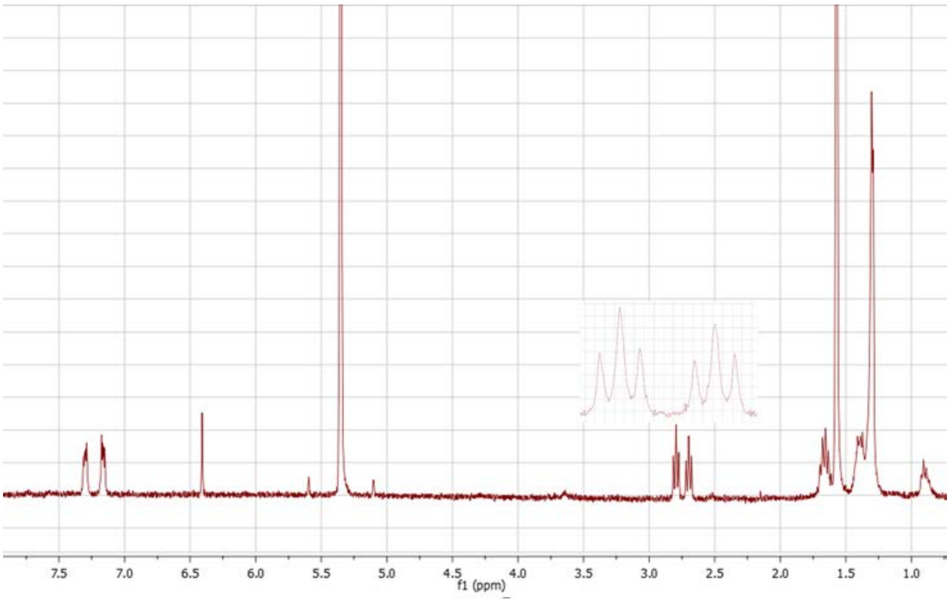

Figure 5.7: ^{1}H NMR (360 MHz, CD_2Cl_2) of $BTTFS_2$.

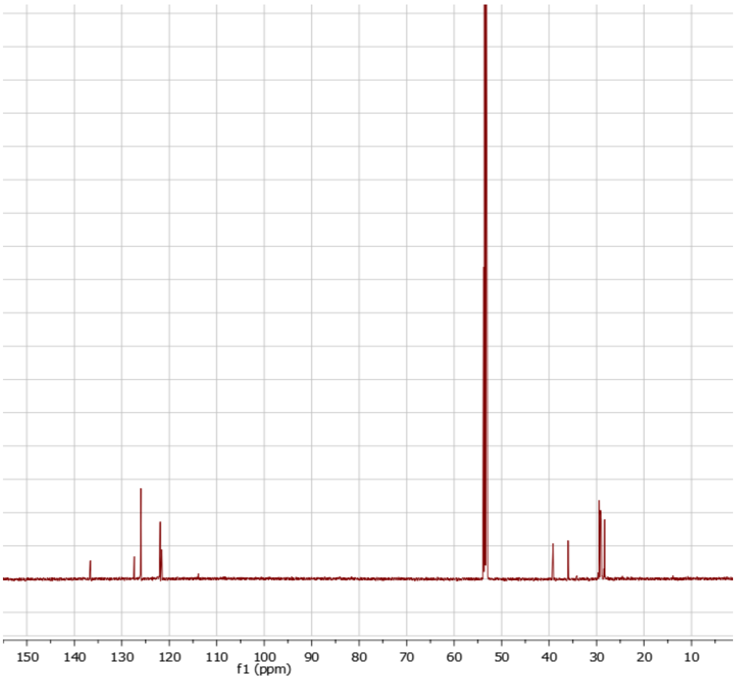

Figure 5.8: ^{13}C NMR(150 MHz, CD_2Cl_2) of $BTTFS_2$.

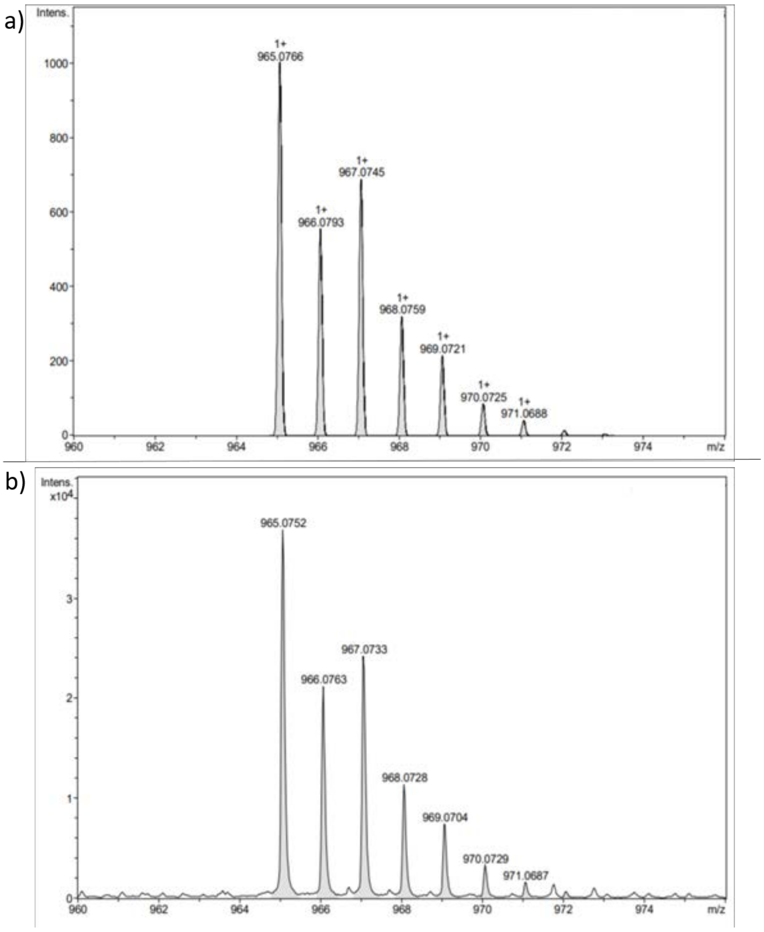

Figure 5.9: HRMS // ESI$^+$ (m/z) of $BTTFS_2$ a) theoretical and b) experimental.

Synthesis of 7

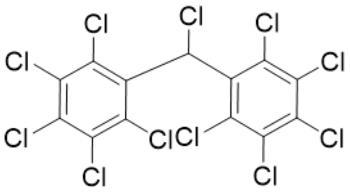

A mixture of 1,2,3,4,5-pentachlorobenzene (10 g, 39,9 mmol), chloroform (1,6 mL, 19,9 mmol) and aluminum chloride (2,6 g, 19,5 mmol) was heated at 130°C for 3,5 hours in a glass pressure vessel. The mixture was cooled down, poured into ice and HCl 1N and extracted with chloroform. The organic layer was washed with water, dried with sodium sulfate and evaporated. The product was recrystallized from chloroform obtaining compound **7** as a white powder (80 % yield) [309].

^{1}H NMR (200MHz, $CDCl_3$), δ (ppm):7,12 (s 1H, αH)

LDI-TOF (m/z): calculated Mol. Wt. $C_{13}HCl_{11}$: 547,13 ; experimental (in negative mode): 545,6 [M-1]

Synthesis of 8

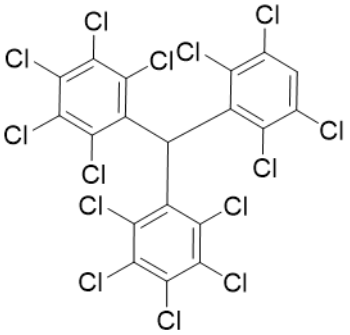

A mixture of **7** (4,2 g, 7,8 mmol), 1,2,4,5tetrachlorobenzene (3,3 g, 15,7 mmol) and aluminum chloride (1 g, 7,8 mmol) was heated at 150°C for 1,5 hours in a glass pressure vessel. The mixture was cooled down, poured into ice and HCl 1 N and extracted with chloroform. The dark solid thus obtained was purified by digestion with pentane and then by column chromatography (silica gel, hexane). A white powder with 54 % yield was finally recovered [309].

^{1}H NMR (200MHz, CDCl$_3$), δ (ppm): 7,66 ppm (s 1H); 6,98 (s 1H).

LDI-TOF (m/z): calculated Mol. Wt. $C_{19}H_2Cl_{14}$:726,56; experimental (in negative mode): 725,3 [M-1], 690,3 [M-35].

Synthesis of 9

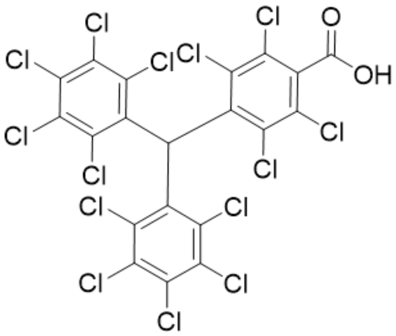

Compound **8** (1,29 g, 1,77 mmol) and Tetramethylethylenediamine (TMEDA) (0,29 mL, 1,95 mmol) were dissolved in 50 mL of dry THF under a slight flux of argon at -78°C. To the mixture n-butillitium 1,6 M in hexane (1,22 mL, 1,95 mmol) was added. The reaction was kept at low temperature for 30 minutes. Then, an excess of CO_2 gas was added bubbling the solution during 15 minutes. Then, the CO_2 flow was stopped and the mixture of reaction was stirred under CO_2 atmosphere overnight. The solvent was evaporated at reduced pressure and the product dissolved in ethyl ether and washed with acid water (pH~ 3) three times. Finally the organic phase was dried with anhydrous magnesium sulphate and the solvent was evaporated at reduced pressure. The crude of reaction was purified by column chromatography (silica gel, ethyl ether/dichloromethane 2/8. The white powder obtained was further washed with acidic water and dried again. Compound **9** was obtained with 40% yield.

^{1}H NMR (400MHz, CDCl$_3$), δ (ppm): 7,0 (s, 1H).

^{13}C NMR (600MHz, CDCl$_3$), δ (ppm): 163,71; 137,23; 137,13; 135,01; 135,13; 134,01; 134,12; 133,82; 133,65; 133,46; 133,45; 133,01; 132,40; 132,35; 128,80; 127,93; 56,50.

IR-ATR υ (cm^{-1}): 3435; 1716; 1555; 1408; 1369; 1330; 1296; 1231; 1185; 1097; 902; 854; 809; 752; 657; 649; 615.

LDI-TOF (m/z): calculated Mol. Wt. $C_{20}H_2Cl_{14}O_2$: 770,57; experimental (in negative mode): 769,3 [M-1], 725,3 [M-COOH].

Synthesis of 10

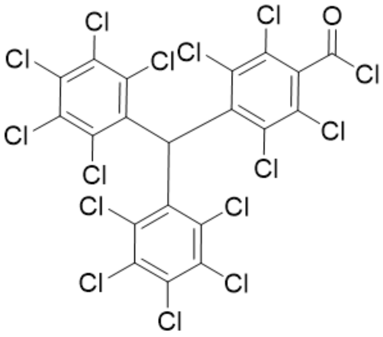

A solution of **9** in thionyl chloride (150 mg, 0,19 mmol in 3 mL) was refluxed for 24 h . The excess of $SOCl_2$ was removed bubbling argon and the resulting solid was purified by column chromatography (silica gel, $CHCl_3$). Compound **10** was thus obtained with 95% yield [280].

^{1}H NMR (400MHz, $CDCl_3$), δ (ppm): 7,01 (s; 1H).

IR-ATR υ (cm^{-1}): 2921; 1778; 1543; 1465; 1409; 1358; 1296; 1239; 1215; 935; 864; 811.

LDI-TOF (m/z): calculated Mol. Wt. $C_{20}HCl_{15}O$: 789,02; experimental (in negative mode): 788,3 [M-1], 753,3 [M-Cl].

Synthesis of αH-PTMsil

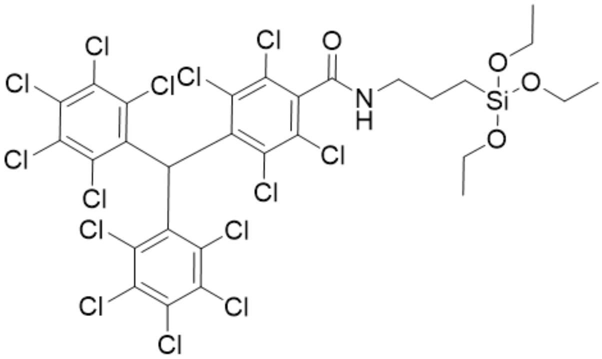

Compound **10** (50 mg, 0,06 mmol) was dissolved in dry toluene (10 mL) under a slight flux of argon. Then triethylammine (8,8 μL, 0,06 mmol) and APTES (14,8 μL, 0,06 mmol) were added consecutively. The mixture was stirred overnight at room temperature and under argon atmosphere. Successive precipitation of triethyl ammonium chloride were achieved in chloroform/hexane mixture. The solvent was evaporated at reduced pressure and αH-PTMsil was obtained as a white powder in 83 % yield.

^{1}H NMR (400 MHz, CDCl$_3$), δ (ppm): 6,99 (s, 1H); 6,30 (t, 1H); 3,81 (q, 6H, J = 7,0 Hz); 3,49 (t, 2H); 1,81 (dd, 2H); 1,21 (t, 9H); 0,74 (t, 2H).

^{13}C NMR (600 MHz, CDCl$_3$), δ (ppm): 163,10; 138,57; 138,10; 136,27; 136,31; 136,18; 135,16; 134,10, 134,08; 134, 01; 133,99; 133,75; 133,69; 132,79; 132,74; 132,69; 131,20; 130,19; 58,73; 56,59; 42,46; 22,54; 18,42; 8,08.

IR-ATR υ (cm^{-1}): 3238; 2919; 2850; 1638; 1568; 1452; 1371; 1336; 1296; 1110; 1069; 948; 873; 786.

LDI-TOF (m/z): calculated Mol. Wt. $C_{29}H_{23}Cl_{14}NO_4Si$: 973,92; experimental (in negative mode): 972,1 [M-1H]; 902,1 [M-2Cl].

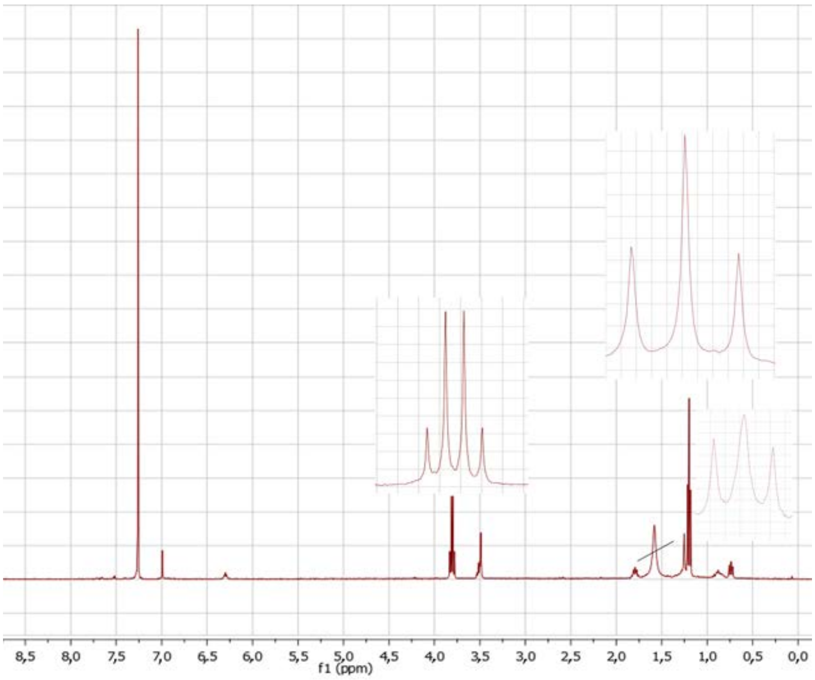

Figure 5.10: ^{1}H NMR (400 MHz, CDCl$_3$) of αH-PTMsil.

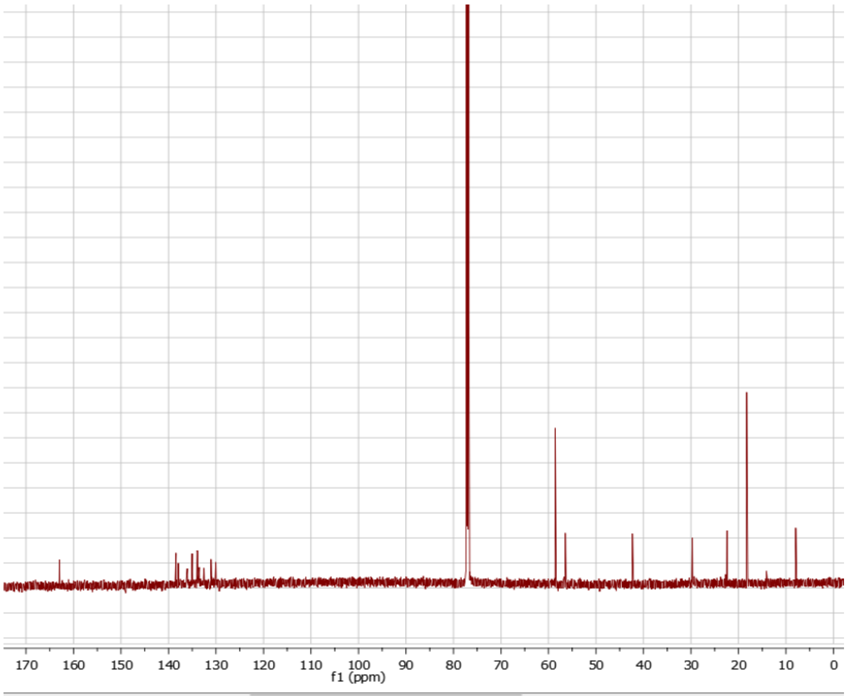

Figure 5.11: ^{13}C NMR (600 MHz, $CDCl_3$) of αH-PTMsil.

Synthesis of 11

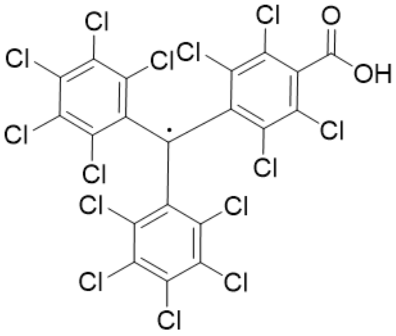

The PTM carboxylic acid derivative **9** (119 mg, 0,15 mmol) was dissolved in a mixture of water and THF previously degassed under argon atmosphere and light exclusion. Then 100 mg (1,80 mmol) of KOH were added and the mixture was stirred for 72 hours. $AgNO_3$ (367 mg, 2,16 mmol) was then added to the solution. After stirring 15 minutes the reaction mixture was filtered through silica gel using chloroform. The solvent was evaporated and the compound was dissolved in chloroform/methanol mixture (1/1). The solution was stirred overnight in presence of amberlite ir 120, then the amberlite was removed by filtration and the solvent eliminated under reduced pressure affording compound **11** as a red solid (40% yield).

LDI-TOF (m/z): calculated Mol. Wt. $(C_{20}HCl_{14}O_2)^{\bullet}$: 769,5; experimental (in negative mode): 768,7 [M]; 698,7 [M-2Cl].

IR-ATR υ (cm^{-1}): 3455; 1713; 1563; 1441; 1372; 1337; 1296; 1239; 1215; 935; 864; 811.

EPR in CH_2Cl_2: g = 2,0026 ΔH_{pp}= 1,1 G; $a_{^{13}C_{\alpha}}$ = 29,5 G; $a_{^{13}C_{o,b}}$ =10; 12,2 G.

Synthesis of 12

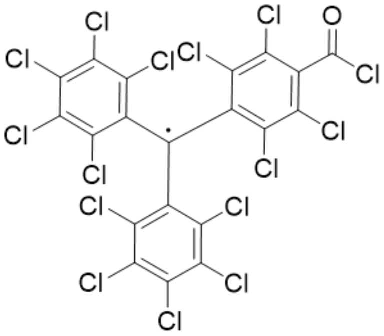

A solution of **11** (120 mg, 0,15 mmol) in thionyl chloride (3 mL) was refluxed for 24 h under argon atmosphere and light exclusion. The excess of $SOCl_2$ was evaporated fluxing argon and the crude of reaction was purified by column chromatography (silica gel, $CHCl_3$). Radical **12** was obtained as a red powder with 67% yield [281].

LDI-TOF (m/z): calculated Mol. Wt. $(C_{20}Cl_{15}O)^{\bullet}$: 788,01; experimental (in negative mode): 788,63[M].

IR-ATR υ (cm^{-1}): 2974; 2841; 1780; 1695; 1532; 1503; 1458; 1408; 1331; 1257; 1331; 1257; 1159; 1049; 1019; 943; 922; 861; 811; 758; 734; 708.

EPR in CH_2Cl_2: g = 2,0026 ΔH_{pp}= 1,3 G; $a_{^{13}C_{\alpha}}$ = 29,5 G; $a_{^{13}C_{o,b}}$ =10; 12,2 G.

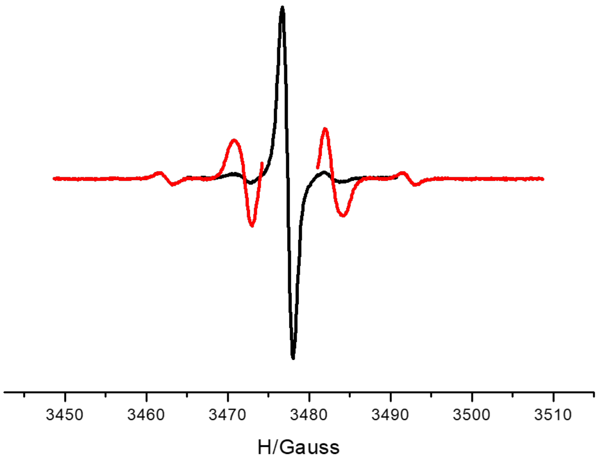

Figure 5.12: EPR spectra of **12** in CH_2Cl_2

Synthesis of r-PTMsil

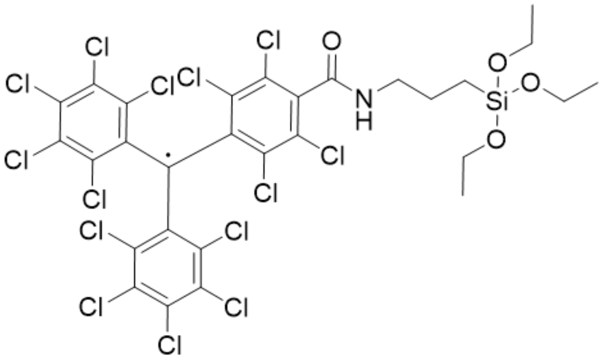

Radical **12** (24 mg, 0,03 mmol) was dissolved in fresh distilled toluene (10 mL), under a slight flux of argon and light protection. Then triethilammine (4,2 µL, 0,03 mmol) and APTES (7 µL, 0,03 mmol) were added consecutively. The mixture was stirred overnight at room temperature and under argon atmosphere. The solvent was evaporated under reduced pressure and the resulting solid was dissolved in chloroform. Hexane was added to precipitate triethyl ammonium chloride and the product was filtrated. The evaporation of the solvent yielded PTMsil rad (77%).

LDI-TOF (m/z): calculated Mol. Wt. $(C_{29}H_{22}Cl_{14}NO_4Si)^{\bullet}$: 972,9; experimental (in negative mode): 902,2 [M-2Cl].

IR-ATR υ (cm^{-1}): 3200; 2919; 2850; 1651; 1558; 1461; 1335; 1225; 1165; 1099; 1072; 940; 792; 696.

EPR in toluene: $g = 2{,}0028$ ΔH_{pp}= 1,26 G; $a_{13_{C_\alpha}}$ = 29,5 G; $a_{13_{C_{o,b}}}$ =10; 12,2 G.

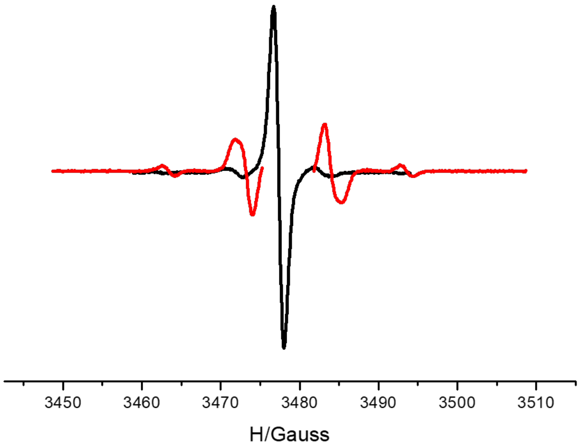

Figure 5.13: EPR spectra of **r – PTMsil** in toluene.

Synthesis of 13

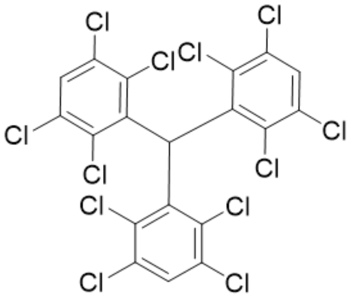

To 1,2,4,5 tetrachlorobenzene (5 g, 23 mmol) $AlCl_3$ (0,36 g, 2,7 mmol) and chloroform (20 mL, 2,5 mmol) was added. The mixture was heated at 160°C for 45 minutes in a glass pressure vessel. The black viscous reaction crude was poured into HCl 1M/ice and was extracted with chloroform. The organic layer was washed with water (x3), dried with dry $MgSO_4$, filtered and concentrated. The excess of 1,2,4,5 tetrachlorobenzene was removed by digestion with pentane. Further purification by column chromatography on silica gel (eluent: hexane) was required. Compound **13** was obtained with 25% yield [279].

LDI-TOF (m/z): calculated Mol. Wt. $C_{19}H_4Cl_{12}$:657,67; experimental (in negative mode): 656,44 [M-1], 584,53 [M-2Cl].

1H NMR (200 MHz, CDCl3), δ (ppm): 6,98,1 (s, 1H); 7,65 (s, 3H).

Synthesis of 14

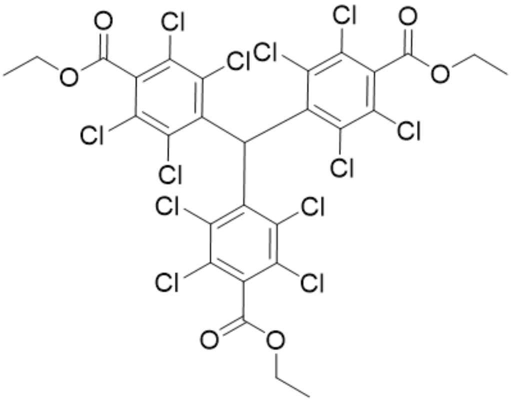

Compound **13** (300 mg, 0,45 mmol) and TMEDA (0,22 mL, 1,50 mmol) were dissolved in dry THF (30 mL) under inert atmosphere. the mixture of reaction was cooled at -78°C and 0,98 mL of a solution 1,6 M of n-butyllithium in hexane were then added. The mixture was stirred at low temperature for 1 h. The reaction was quenched with ethyl chloroformate and the mixture was allowed to reach room temperature overnight. The solvent was evaporated and the residue was dissolved in dichloromethane. The organic phase was washed with water, dried with sodium sulphate, filtrated and evaporated. The reaction crude was purified by column chromatography (silica gel, hexane/AcOEt 12/1) obtaining **14** with 90% yield [282].

^{1}H NMR (400 MHz, $CDCl_3$), δ (ppm): 7,01 (s; 1H); 4,49 (q, 6H, J = 7,1); 1,43 (t, 9H, J = 7,1).

^{13}C NMR (400 MHz, CD_2Cl_2), δ (ppm): 163,44; 138,85; 136,03; 135,41; 134,44; 130,85; 129,86; 63,56; 56,75; 14,20.

LDI-TOF (m/z): calculated Mol. Wt. $C_{28}H_{16}Cl_{12}O_6$: 873,86; experimental (in negative mode): 872,42 [M-1], 800,54 [M-COOEt].

IR υ (cm^{-1}) 2927; 2856; 1737; 1557; 1557; 1439; 1373; 1261; 1221; 1205; 1115; 1016; 857; 832; 752; 649.

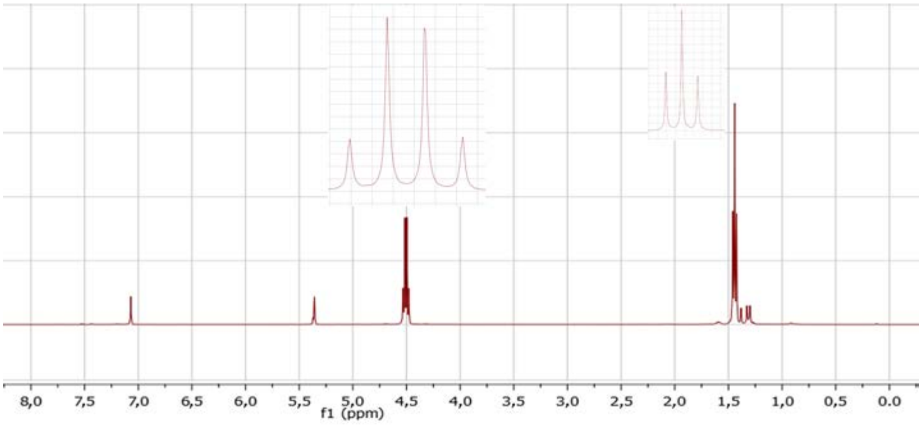

Figure 5.14: ^{1}H NMR (400 MHz, $CDCl_3$) of **14**.

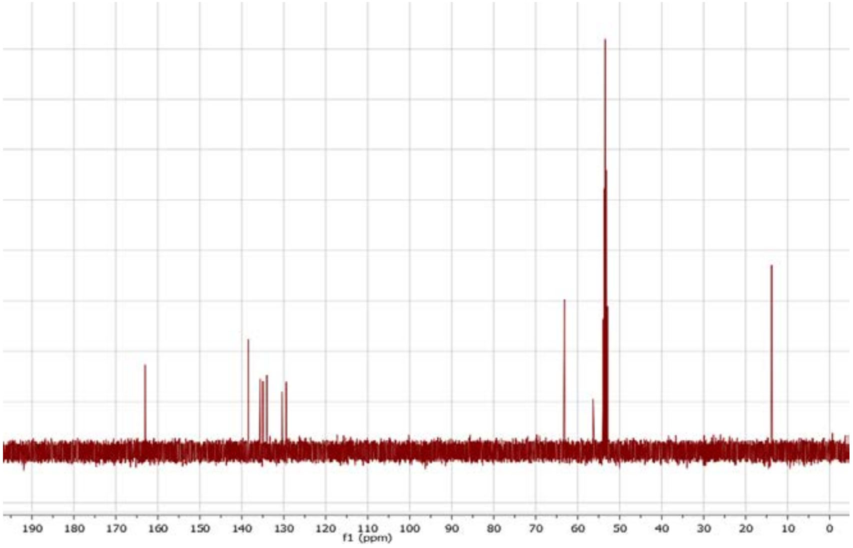

Figure 5.15: ^{13}C NMR (400 MHz, $CDCl_3$) of **14**.

Synthesis of 15

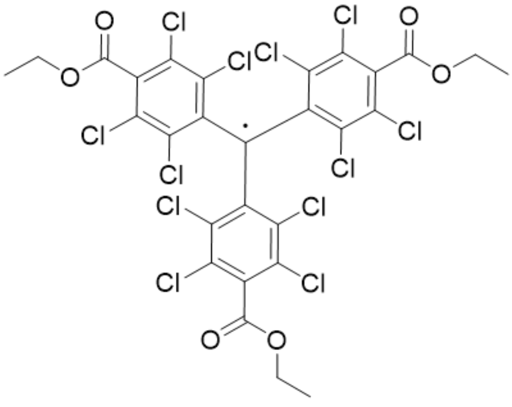

To a solution of **14** (180 mg, 0,21 mmol) in CH_3CN, 0,2 mL of a solution 1 M of Bu_4NOH in MeOH were added and the mixture was stirred at room temperature for 3 h under light exclusion. Then, $AgNO_3$ (0,49 g, 2,88 mmol) was added. The mixture was stirred for 40 min, then it was filtered on silica gel eluting with chloroform. The solvent was evaporated and **15** was obtained as red solid (81% yield) [282].

IR υ (cm^{-1}) 2983; 1741; 1552; 1462; 1369; 1336;1298; 1257;1222; 1202; 1112; 1017; 861; 795; 656.

LDI-TOF (m/z): calculated Mol. Wt. $(C_{28}H_{15}Cl_{12}O_6)^{\bullet}$: 872,7; experimental (in negative mode): 872,6 [M]; 800,6 [M-COOEt].

EPR in CH_2Cl_2: g = 2,0021 ΔH_{pp}= 0,44 G; $a_{^{13}C_{\alpha}}$ = 29,5 G; $a_{^{13}C_{o,b}}$ =10; 12,2 G.

Synthesis of 16

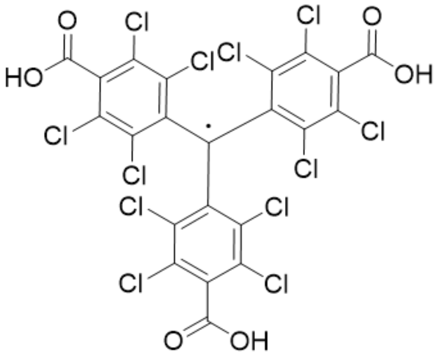

A mixture of **15** (150 mmol) and concentrated H_2SO_4 (20 mL) was stirred at 100°C for 48 h and under light exclusion. The mixture of reaction was cooled down and poured onto ice. The crude was extracted with ethyl ether and washed with a saturated solution of Na_2CO_3. The aqueous phase was acidified with HCl 12 M and extracted with ether. The organic layer was dried with $MgSO_4$, filtered and concentrated, giving compound 16 as a red powder (56% yield).

IRυ (cm^{-1}) 3000; 1720; 1554; 1404; 1333; 1299; 1226; 1204; 1100; 1121; 1056; 866; 824; 784; 716; 692.

LDI-TOF (m/z): calculated Mol. Wt. $(C_{22}H_3Cl_{12}O_6)^{\bullet}$: 788,69; experimental (in negative mode): 788,6 [M].

EPR in CH_2Cl_2/ EtOH: g = 2,0025 ΔH_{pp}= 0,38 G; $a_{^{13}C_{\alpha}}$ = 29,5 G; $a_{^{13}C_{o,b}}$ =10; 12,2 G.

Synthesis of 17

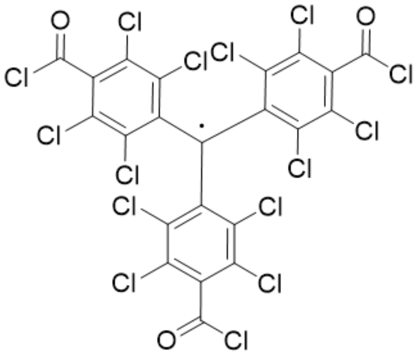

A mixture of **16** (100 mmol) and $SOCl_2$ (7 mL) was stired at reflux temperature for 48 h under light exclusion. The excess of $SOCl_2$ was then removed fluxing nitrogen, and the crude of reaction was dissolved in chloroform and purified by chromatography on silica gel (eluent: chloroform). **17** was obtainedas a red solid with 90% yield.

IRυ (cm^{-1}) 1782; 1533; 1502; 1454; 1336; 1321; 1298; 1262; 1146; 1049; 1021; 931; 862; 808; 762; 708.

LDI-TOF (m/z): calculated Mol. Wt. $(C_{22}H_{15}Cl_{15}O_3)^{\bullet}$: 844,03; experimental (in negative mode): 844,2 [M]; 772,3 [M-2Cl].

EPR in CH_2Cl_2: g = 2,0020 ΔH_{pp}= 1,2 G; $a_{13_{C_\alpha}}$ = 29,5 G; $a_{13_{C_{o,b}}}$ =10; 12,2 G.

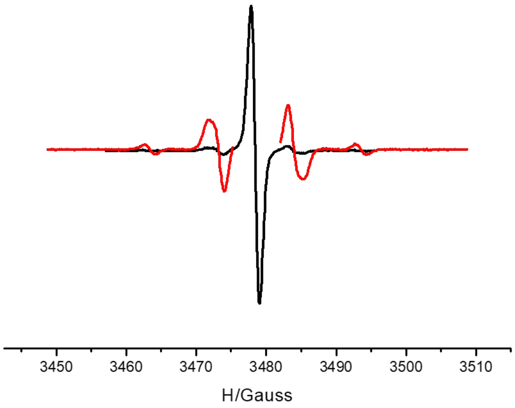

Figure 5.16: EPR spectra of **14** in CH_2Cl_2

5.2 Reagents, solvents and substrates

Reagents and solvents

F-β-CD and β-CD were purchased, respectively, from Cyclolab and Chemika. N-decanethiol ($C_{10}SH$), 11-(ferrocenyl) undecanethiol (FcC_{11}) and 6-(ferrocenyl) hexanethiol (FcC_6) were purchased from Sigma-Aldrich and used without further purification, as well as lithium perchlorate ($LiClO_4$), tetrabutylammonium hexafluorophosphate ($TBAPF_6$) and lithium tetrafluoroborate ($LiBF_4$). All the other reagents employed for synthesis were purchased from Sigma-Aldrich or abcr GmbH and used as received. Silica gel used in column chromatography was Silica gel 60 A RS from Carlo Erba. The solvents used for the synthetic work were synthesis grade and commercially available in Scharlab. For the synthesis of TTF derivatives, CH_2Cl_2 was always filtrated on basic activated aluminum oxide from Sigma Aldrich. THF and toluene were distilled in presence of sodium metal and benzophenone in order to remove traces of water. All the solvents used for the SAMs preparation and characterization were HPLC pure grade and were supplied by Teknokroma. Pentacene and Fullerene C_{60} employed as semiconductors were purchased from Osilla.

Substrates for SAMs formation and devices

Commercial substrates of 50 nm of polycristallyne gold evaporated on glass adhesive layer provided by Phasis were used as platform for the preparation of the mono-component $S_{FcC_{11}dil}$.

Commercial substrates of 70 nm of ITO on glass from Delta Technologies, were used as platform for the preparation of the mono-component S_{AQSi} and $S_{r\text{-}PTMsil}$.

Glass substrates with a 50 nm thick gold layer and refractive index of 1,5168 (Xantec SC AU, Xantec bioanalytics, Kevelaer-Kervenheim, Germany) were used as platforms for the fabrication of S_{AQS2} when used in SPR measurements.

Gold (111) substrates consisting of 300 nm Au on mica were purchased from Georg Albert PVD-Beschichtungen and were used for the preparation of S_{TTFS_2}.

Commercial silicon substrate from Fraunhofer and from Si-mat were used for the preparation of the FETs.

5.3 Procedures and apparatus

5.3.1 Fabrication of patterned ITO//gold substrates

Patterned surfaces with ITO//gold regions were realized by gold evaporation on ITO-coated glass substrates using a metallic mask with 3 cm width stripe design. 15 nm of Cr and 75 nm of gold were deposited through thermal evaporation using the system Auto 306 from Boc Edwards.

5.3.2 Fabrication of planar electrodes on ITO substrates

All the electrode were fabricated through a photolithographic process followed by an acidic etching.

The photolitographic protocol was carried out in a 10000 class cleanroom.

ITO-coated glass slides (70 nm of ITO on glass) were rinsed with HPLC pure grade acetone and isopropanol, and dried with a nitrogen stream. Positive S1813 photoresist was spin-coated with speed = 4000 rpm and spinning acceleration = 5700 rpm/s. After the deposition the substrates were annealed on a hot-plate at 100 °C for 60 s. The electrode pattern, designed using computer aided design (CAD), were applied to the photoresist film using a laser-assisted writer (Durham magneto-optics, λ = 405 nm). The exposed resist was then washed away by the developer solution first (MF319 developer for 60 s) and then by ultrapure water, leaving windows of the bare underlying material. an acidic etching with HCl 32% v/v for 10 min of the uncoated ITO was performed to define the designed electrodes. The resist was finally removed by rinsing with acetone and isopropanol.

5.3.3 Fabrication of ultra flat electrodes for EGaIn measurements

Ultraflat Au surfaces were prepared by a template-stripping (TS) procedure [213]. A layer of 500 nm of gold was deposited by electron-beam (e-beam) evaporation at $2\text{-}3 \cdot 10^{-6}$ Torr at a rate of 8-10 Å/s on silicon wafers with their native SiO_2 layer present. Ultra clean glass slides (typically 1 cm^2 and 500 μm thick), which were cleaned by washing with EtOH, and subsequent exposure to oxygen plasma for 30 min, were glued at the Au-surface using a thermal adhesive epoxy. The thermal adhesive was cured by heating in an oven at 80°C during 18 h. The glass substrates were then cleaved off the Si-wafer, giving rise to ultra flat gold substrates on glass.

5.3.4 Preparation of self-assembled monolayers (SAMs)

General protocol

All the glassware used for the SAMs preparation was firstly cleaned by immersion in a milliQ water solution of Hellmanex (2% v/v) for 3 h. Afterwards the substrates were washed several times with milliQ water, and finally dried under a nitrogen flow. The substrates employed for the SAMs formation were washed with a series of solvents with increasing polarity (dichloromethane, acetone and ethanol) and dried under nitrogen flow. Then the substrates were exposed in a UV/ozone chamber for 25 minutes. Finally the surfaces were immersed in the solution of the target molecule. The SAM formation was always carried out under light exclusion and nitrogen atmosphere.

Preparation of $S_{FcC_{11}dil}$

The substrates (50 nm of polycristallyne gold evaporated on glass) were immersed in a solution 2 mM of 11-(ferrocenyl) undecanethiol / n-decanethiol $FcC_{11}/C_{10}SH$ 1/9 in ethanol for 18 h at ambient temperature (25 ∓ 3°C). The samples were then removed from the solution, rinsed several times with ethanol and, finally, dried under nitrogen flow.

Preparation of S_{AQSi}

The activated substrates (70 nm of ITO on glass) were immersed in a solution 0,5 mM of AQSi in toluene for 4 h at ambient temperature (25 ∓ 3°C). The samples were then rinsed several times with toluene and, finally, dried under nitrogen flow.

Preparation of S_{AQS_2}

Freshly cleaned gold /glass substrates were immersed in a 0,5 mM solution of AQS_2 in THF for 40 h at ambient temperature (25 ∓ 3°C). After that, the samples were rinsed with a large amount of THF and dried with nitrogen flow.

Preparation of $S_{AQSi//FcC_{11}dil}$

The freshly cleaned and activated ITO//gold patterned substrates were immersed in a 0,5 mM solution of AQSi in toluene at room temperature (25 ∓ 3°C), during 4 h. Then, the substrates were rinsed with toluene to eliminate the phisisorbed molecules, dried under a nitrogen flow and immersed in a 2 mM solution of $FcC_{11}/C_{10}SH$ (1/9) in ethanol for 18 h. Finally, the modified surfaces were rinsed with ethanol and dried with nitrogen.

Preparation of S_{TTFS_2}

Freshly cleaned gold (111)/mica substrates were immersed in 1 mM solution of $TTFS_2$ in THF for 72 h at ambient temperature (25 ∓ 3°C). Later, the samples were rinsed with a large amount of THF and dried with a nitrogen flow.

Preparation of S_{BTTFS_2}

Cleaned substrates (50 nm of gold (111) evaporated on glass) were immersed in 0,5 mM solution of $BTTFS_2$ in toluene for 24 h. During the first 3h the solution was heated up to 45ºC, while the remaining 21 h the solution was kept at room temperature (25 ∓ 3°C). The substrates were then removed from the solution, rinsed several times with toluene and dried under a nitrogen flow.

Preparation of $S_{r\text{-}PTMsil}$

The ITO/glass substrates were immersed in a solution 1 mM of r-PTMsil in dry toluene for 12 h at ambient temperature (25 ∓ 3°C). The samples were then rinsed several times with dry toluene and dried under a nitrogen flow.

5.3.5 Procedure for FET Fabrication

Fabrication of MoS_2 based FET devices

Device Fabrication: Monolayer MoS_2 flakes were mechanically exfoliated from commercially available molybdenite crystals (Furuchi, Japan) on thermally oxidized heavily n-doped silicon substrates (ρ Si ≈ 0.001 Ω·cm, tox = 290 nm) on which back-gated FETs were fabricated by means of e-beam lithography with a double-layer of polymethyl methacrylate, thermal evaporation of Au (85 nm) and lift-off in warm acetone (≈50 °C). The devices were annealed at 140 °C for ≈15 h inside a high-vacuum chamber ($\approx 5 \cdot 10^{-8}$ mbar). The FETs were no longer exposed to air after annealing.

Ion Bombardment: Ar-ion bombardment of monolayer MoS_2 FETs was performed by means of a Thermo Fischer EX06 ion gun with acceleration voltage of 500 V. The angle between the ion beam and the substrate surface normal was ≈58°. To avoid shadow effects due to the metal contact thickness, the FETs were oriented with their channel-width direction parallel to the projection of the ion beam on the sample surface. The ion-beam (I ≈ 210 nA) was uniformly raster-scanned over a rectangular area of $\approx 8 \cdot 4$ mm^2.

Fabrication of OFET devices

OFET devices were fabricated in the bottom-gate, bottom-contact architecture on silicon substrates with gold source and drain electrodes. The electrodes layout was photolithographically patterned in the SiO_2 layer by means of a micro-writer, while the gold (40 nm) was deposited by thermal evaporation (system Auto 306 from Boc Edwards) using chromium (5 nm) as adhesive layer. The deposition of the organic semiconductor was carried out by thermal evaporation. Specifically, 1) pentacene (P5, p-type semiconductor) was deposited by high-vaccumm deposition (10^{-7} mbar), with a growth rate of 0,2 Å/s keeping the substrate temperature constant at 60°C and 2) fullerene C_{60} (n-type semiconductor) films were fabricated by high-vaccumm deposition (10^{-7} mbar), with a growth rate of 0,2 Å/s keeping the substrate temperature constant at 25°C.

Fabrication of EGOFET devices

The EGOFETs devices were fabricated on a silicon substrate with gold source and drain electrodes. The electrodes layout was photolithographically patterned by means of a micro-writer, while the 40 nm of gold were deposited by thermal evaporation (system Auto 306 from Boc Edwards) using 5 nm of chromium as adhesive layer. The semiconductor 2,8-difluoro-5,11-bis (triethylsilylethynyl) anthradithiophene (diF-TES-ADT) with a mixture of polystyrene (Mw = 10000 g · mol^{-1}) in a ratio 4:1 was dissolved in chlorobenzene and was deposited through the Bar-Assisted Meniscus Shearing (BAMS) technique [241]. The blend deposition was realized at ambient conditions. A smooth cylindrical bar was positionated ~300 μm above the cleaned Si/SiO_2 substrate with the prefabricated gold electrodes, which was heated at 105°C. About 20 μm of the blend solution were deposited between the bar and the substrate forming a confined meniscus. Immediately, the solution was sheared at a speed of ~1 cm/s. As the bar moved, the meniscus was displaced and by evaporation-induced self-assembly a thin crystalline film was formed.

5.3.6 Spectroscopy and spectrometry techniques

Fourier Transform Infrared Spectroscopy (FT-IR) measurements

The IR spectra were performed by using the Spectrum One FT-IR Spectrometer from Perkin Elmer with the universal ATR Polarization accessory.

X-ray Photoelectron Spectroscopy (XPS) measurements

X-ray photoelectron spectroscopy measurements were done with a Phoibos 150 analyzer (SPECS GmbH, Berlin, Germany) in conditions of ultra-high vacuum (base pressure $5 \cdot 10^{-10}$ mbar) with a monochromatic aluminium Kalpha X-ray source (1486,74 eV). The energy resolution measured by the FWHM of the Ag 3d5/2 peak for a sputtered silver foil was 0,6 eV. The spot size was 3,5 mm by 0,5 mm.

UV-Vis spectroscopy measurements

Absorption spectra were acquired on Varian Cary 5000 UV-Vis-NIR spectrometer (Agilent Technologies). Spectra of samples in solution were acquired by placing the samples in a quartz cell with 1 cm path length.

Spectra of SAMs were acquired using a solid sample holder.

UV-Vis spectroelectrochemistry measurements of SAMs

To optically characterize the fabricated SAMs while performing electrochemical measurements, surface electrochemistry was carried out inside the Cary 5000 UV-Vis-NIR spectrometer, using a 2 mm pathway UV-Vis cuvette as electrochemical cell. All the electrodes were placed inside the quartz cell and connected to the potentiostat/galvanostat 263a (EG&G Princeton Applied Research). The SAM substrate was used as working electrode, while platinum and silver wires were used as counter and quasi-reference electrodes. The cuvette was filled with degassed electrolyte solution of 20 mM $TBAPF_6$ in acetonitrile. The SAM absorbance was measured versus a bare ITO substrate immersed in the same electrolyte, used as reference.

Surface Plasmon Resonance spectroscopy (SPR) measurements

SPR was carried out on a spectrometer SR7000DC (Reichert, Buffalo, USA). SPR substrates (1,44 $cm^2 \cdot$ 0,3 mm) consist of glass with a 50 nm thick gold layer and have a refractive index of 1,5168 (Xantec SC AU, Xantec bioanalytics, Kevelaer-Kervenheim, Germany).

Time-of-Fligth Secondary Ion Mass Spectrometry (ToF-SIMS) measurements

Time of flight secondary ions mass spectrometry measurements were performed with a TOF-SIMS5 using the following specific conditions of analysis: primary gun energy of 25 KV; extractor energy of 10 KV; an emission current 1,00 μA; employing Bi^{3+} with an intensity of the primary ions of 0,26 pA. The experiments were performed under vacuum at 2,3 10^{-9} mbar. The spot size was 250·250 µm with a resolution of 128·128 pixels, collecting above of $1\cdot 10^{12}$ of ionic intensity per spectrum.

Laser Desorption/ionization (LDI) mass spectrometry

LDI analysis were performed using an advanced MALDI-TOF/TOF mass spectrometer with 2kHz speed in TOF mode from Bruker. The samples were deposited from solution on a MTP 384 target plate ground steel TF from Bruker.

Raman and Photoluminescence Spectroscopy

Raman and PL spectra were acquired at room temperature with a Renishaw InVia spectrometer equipped with a 532 nm laser. The measurements were carried out in air using a 100× lens objective (numerical aperture NA = 0,85) providing a beam spot size of ≈700 nm. The excitation power was kept below 1 mW to avoid local heating damage effects. For Raman (PL) measurements, the wavenumber (energy) resolution was ≈1,25 cm^{-1} (≈1 meV). The Si band at 520,3 cm^{-1} was used for normalization.

5.3.7 Electrochemical techniques and FETs characterization

Cyclic Voltammetry (CV) measurements

The measurements of cyclic voltammetry (CV) were carried out using a potentiostat/galvanostat 263a (EG&G Princeton Applied Research). A conventional three-electrode setup was used. For the SAM characterization, the modified substrates were used as the working electrode (WE), while a platinum and a silver wires (0,5 mm of diameter each one) were used as counter (CE) and quasi-reference electrodes (RE), respectively. For the CV of the molecules in solution two platinum and a silver wires (0,5 mm of diameter each one) were used as counter (CE) and working (WE) and quasi-reference electrodes (RE), respectively.

Electrochemical Impedance Spectroscopy (EIS) measurements

The impedance experiments were performed usiong a Biol-Logic VMP3 potentiostat and a Novocontrol Alpha-AN impedance analyzer equipped with a potentiostat POT/GAL 30V/2A electrochemical interface. The EIS measurements were obtained at four different DC potentials, and were superimposed on a sinusoidal potential modulation of ±5 mV (Vrms). The resulting current was recorded over a frequency domain of 200 KHz to 500 mHz. Ninety points, equally spaced on a logarithmic scale, were acquired per decade increment in frequency. All experiments were performed at room temperature and under environmental conditions.

The AC impedance switching measurements were recorded at 1Hz using a Novocontrol Alpha-AN impedance analyzer equipped with a potentiostat POT/GAL 30V/2A electrochemical interface. A low AC voltage of 5 mV was superimposed at different applied DC bias. These cycling experiments were performed by pre-biasing the sample at the corresponding DC voltage for each state, during 5 seconds.

Field effect transistor electrical measurements

EGOFET electrical measurements were acquired at ambient conditions using an Agilent 5100A and Easy Expert software. The samples were connected with a SÜSS probe station.

OFET electrical measurements were performed using a dual channel SMU 2612 from Keithley under inert atmosphere (N_2-filled glovebox). The samples were connected with a SÜSS probe station.

MoS_2 based FETs were electrically characterized only under inert atmosphere (N_2-filled glovebox). Electrical measurements were carried out at room temperature with source-measurement units from Keithley (model 2636A).

5.3.8 Other techniques

Nuclear Magnetic Resonance (NMR)

The ^{1}H-NMR and ^{13}C-NMR spectra were registered on Bruker Avance (III 400 SB, DRX 250, DPX360, 500 and 600 MHz) spectrometer and calibrated using residual undeuterated dichloromethane ($\delta(^1H)$ = 5,32 ppm; $\delta(^{13}C)$ = 53,84 ppm) and residual undeuterated chloroform ($\delta(^1H)$ = 7,26 ppm; $\delta(^{13}C)$ = 77,00 ppm) as internal references. The data analysis was carried out with MestReNova software (MestReLab Research S. L.). The following abbreviations were used to designate multiplicities: br = broad signal, s = singlet, d = doublet, m = multiplet, dd = double doublet.

Contact Angle measurement

The static contact angle measurements were done using Drop Shape Analyzer DSA 100 from KRÜSS. The DSA100 is equipped with a software for measuring the contact angle and the surface tension of a liquid. 5 or 3 µL droplets were deposited on the modified surfaces keeping high reproducibility between the replicas due to the automatic dispenser.

Atomic Force Microscopy (AFM) images

AFM images were obtained working with a 5100 SPM system from Agilent technologies in tapping mode and the images were analyzed using Gwyddion 2,47 software.

Confocal microscopy measurement

Fluorescence measurements were done using a Leica SP5 confocal microscope with HCX PL APO CS 10,0·0,40 DRY UV objective and emission bandwindth of 500-571 nm. The images were analyzed using the software Leica LAS AF Lite.

Electron Paramagnetic Resonance (EPR)

EPR spectra were registered at room temperature on a Bruker ESP 300 E spectrometer provided with a rectangular cavity T102 working with a X band (9,5 GHz). Precautions to avoid undesirable spectral distortion and line broadenings, such as those arising from microwave power saturation and magnetic field over modulation, were taken into account to improve sensitivity. The ITO/glass substrates were placed parallel to the field.

UV/Ozone cleaner

JetLight UVO-Cleaner 42 was used to clean the substrates before the preparation of SAMs or OFET devices. This process is highly effective in removing organic contaminants.

Glovebox

Glove box GP (Concept)-II-P from JACOMEX, with electrical measurement system and an organic evaporator inside was used to make processes under restrictive atmosphere to oxygen and water in an environment of nitrogen.

6

General conclusions

In this thesis work we exposed the results obtained by performing a multidisciplinary study on the switching behavior of redox active molecules anchored on surface and introduced in devices, taking a step towards the achievement of the molecular-level control in electronic devices.

In particular, by investigating four different families of redox active molecules (i.e. anthraquinone (AQ), ferrocene (Fc), tetrathiafulvalene (TTF) and polychlorotriphenylmethyl (PTM) radical derivatives) we concluded that:

1. Organic synthesis is a powerful tool for the realizarion of new materials with high potential in the field of charge storage. Polyradical PTM polymers can be synthesized starting from high reactive PTM derivatives, and could have a key role in the enhancement of the charge storage properties of single PTM molecules.

2. Organic synthesis is a relatively easy tool to supply functionalizations suitable for the surface confinement of the electroactive molecules studied.

3. SAMs of these electroactive molecules on gold and ITO surfaces provide robust and reproducible confined molecular systems fully suitable to study the molecular redox behavior as well as the charge transport properties on surface.

4. SAMs of TTF derivatives on gold employed in EGaIn junctions showed a rectifying behavior that could open the way towards the fabrication of new electronic devices with the role of current rectifiers.

5. Multi-state molecular switches can be achieved by fabricating bi-component electroactive SAMs of both, an electron-donor and an electron aceptor molecule. Remarkably, using Fc and AQ derivatives with functionalization able to graft selectively to gold and ITO, respectively, and employing a patterned ITO//gold substrate as SAMs platform, we obtained a three state switch with locally confined surface properties.

6. The formation of supramolecular interactions on surfaces, such as host-guest complexes, can be tuned by using electroactive SAMs. For instance, the interaction between β-cyclodextrin and SAMs of AQ and Fc on patterned ITO//gold substrates was modulated by changing the redox state of the confined molecules and was used as

read-out of the molecular switch.

7. Electrochemical impedance spectroscopy can be successfully implemented to characterize molecular switches based on electroactive SAMs. Specifically we achieved multi-state molecular switches based on mono-component SAMs of TTF derivatives on gold, by using the capacitance output of the system at defined DC applied potential. Thus, the states of an electrochemical molecular switch can be fixed at different oxidation (or reduction) degrees of the SAM as long as the output response is distinct and constant.

8. SAMs of electroactive molecules on specifically designed ITO electrodes could be used to modify the surface tension giving rise to a micro-electromechanical system (MEMS). Specifically, SAMs of AQ derivatives on properly designed planar ITO electrodes were introduced in microfluidics chips and the redox activity of the AQ moiety was exploited to perform some of the digital microfluidic operations, such as water splitting and merging. The low voltage operation is an important figure of merit of the system.

9. Specifically designed redox molecules can be introduced in field effect transistors by functionalizing a) the gate electrode, b) the dielectric, c) the active channel.

a) The redox state of TTF derivatives anchored on the gate of an EGOFET device was proved to have strong influence on the device response. The additional charges onto the electrode surface, due to the TTF oxidation, strongly influence the doble layer organization in the electrolyte/gate interface and, as a consequence, the capacitive coupling between the gate and the semiconductor.

b) The dipolar moment of SAMs based on PTM radical derivatives and introduced at dielectric/semiconductor interface of p- and n-type OFETs demonstrated to have a remarkable effect on the device performance, by enhancing or reducing the gate electric field, respectively.

c) MoS_2 based FETs can be functionalized by recovering the sulfur vacancies in the MOS_2 active channel using thiolated Fc derivatives. The electrochemical switch of the Fc moiety can be exploited as a proof of the molecular functionalization.

In general, it can be concluded that the knowledge produced by the studies realized in this doctoral thesis constitutes an important resource in the field of organic electronics for the development of molecular based devices.

Bibliography

[1] R. P. Feynman. There's plenty of room at the bottom. *Eng. Sci.*, 23:22–36, 1960.

[2] S. A. Edwards. *Final Thoughts on The Destination, in The Nanotech Pioneers: Where Are They Taking Us?* Wiley-VCH Verlag GmbH & Co. KGaA, Weinheim, Germany, 2007 edition, 2006.

[3] S. E. Thompson and S. Parthasarathy. Moore's law: the future of Si microelectronics Status of Moore's law. *Mater. Today*, 9:20–25, 2006.

[4] J. M. Lehn. Toward complex matter: supramolecular chemistry and self-organization. *Proc. Natl. Acad. Sci. USA*, 99:4763–8, 2002.

[5] T. R. Kelly, M. C. Bowyer, K. V. Bhaskar, D. Bebbington, A. Garcia, F. Lang, M. H. Kim, and M. P. Jette. A Molecular Brake. *J. Am. Chem. Soc.*, 116:3657–3658, 1994.

[6] H. Hu, M. Zhu, X. Meng, Z. Zhang, K. Wei, and Q. Guo. Optical switching and fluorescence modulation properties of photochromic dithienylethene derivatives. *J. Photochem. Photobiol., A*, 189:307–313, 2007.

[7] N. Zheludev. Single nanoparticle as photonic switch and optical memory element. *J. Opt. A: Pure Appl. Opt.*, 8:S1–S8, 2006.

[8] R. Klajn. Spiropyran-based dynamic materials. *Chem. Soc. Rev.*, 43:148–184, 2014.

[9] T. Ikeda and O. Tsutsumi. Optical Switching and Image Storage by Means of Azobenzene Liquid-Crystal Films. *Science*, 268:1873–1875, 1995.

[10] J. Zheng, J. Li, Y. Jiang, J. Jin, K. Wang, R. Yang, and W. Tan. Design of aptamer-based sensing platform using triple-helix molecular switch. *Anal. Chem.*, 83:6586–6592, 2011.

[11] R. Bashir. *Handbook of Nanoscience, Engineering, & Technology.* CRC Press, 2007 edition, 2003.

[12] Alexis Goulet-Hanssens and Christopher J. Barrett. Photo-control of biological systems with azobenzene polymers. *J. Polym. Sci., Part A: Polym. Chem.*, 51:3058–3070, 2013.

[13] J. R. Kumita, O. S. Smart, and G. A. Woolley. Photo-control of helix content in a short peptide. *Proc. Natl. Acad. Sci. USA*, 97:3803–3808, 2000.

[14] Zhongdu Liu. Solid State Electrical Switch. EP20000303208, 2003.

[15] D. A. Leigh, J. K. Y. Wong, F. Dehez, and F. Zerbetto. Unidirectional rotation in a mechanically interlocked molecular rotor. *Nature*, 424:174–179, 2003.

[16] D. A. Leigh, V. Marcos, T. Nalbantoglu, I. J. Vitorica-Yrezabal, F. T. Yasar, and X. Zhu. Pyridyl-Acyl Hydrazone Rotaxanes and Molecular Shuttles. *J. Am. Chem. Soc.*, 139:7104–7109, may 2017.

[17] W. R. Browne and B. L. Feringa. Making molecular machines work. *Nat. Nanotechnol.*, 1:25–35, 2006.

[18] M. R Panman, C. N. Van Dijk, A. Huerta-Viga, H. J. Sanders, B. H. Bakker, D. A. Leigh, A. M. Brouwer, W. J. Buma, and S. Woutersen. Transient two-dimensional vibrational spectroscopy of an operating molecular machine. *Nat. Commun.*, 8:1–8, 2017.

[19] J.-C Olsen, A.C. Fahrenbach, A Trabolsi, D.C. Friedman, S.K. Dey, C.M. Gothard, A.K. Shveyd, T.B. Gasa, J.M. Spruell, M.A. Olson, C Wang, H.-P Jacquot De Rouville, Y.Y. Botros, and J.F. Stoddart. A neutral redox-switchable [2]rotaxane. *Org. Biomol. Chem.*, 9:7126–7133, 2011.

[20] H. R. Tseng, S. A. Vignon, P. C. Celestre, J. Perkins, J. O. Jeppesen, A. Di Fabio, R. Ballardini, M. T. Gandolfi, M. Venturi, V. Balzani, and J. F. Stoddart. Redox-Controllable Amphiphilic [2]Rotaxanes. *Chem.-Eur. J.*, 10:155–172, 2004.

[21] W. Q. Deng, A. H. Flood, J. F. Stoddart, and W. A. Goddard. An electrochemical color-switchable RGB dye: Tristable [2]catenane. *J. Am. Chem. Soc.*, 127:15994–15995, 2005.

[22] Carlos Franco, Marta Mas-Torrent, Antonio Caballero, Arturo Espinosa, Pedro Molina, Jaume Veciana, and Concepció Rovira. Pyrene-Based Dyad and Triad Leading to a Reversible Chemical and Redox Optical and Magnetic Switch. *Chem. -Eur.J.*, 21:5504–5509, 2015.

[23] S. H. Hsiao and J. S. Han. Solution-processable transmissive-to-green switching electrochromic polyamides bearing 2,7-bis(diphenylamino)naphthalene units. *J. Polym. Sci. A*, 55:1409–1421, 2017.

[24] T. Xu, E. C. Walter, A. Agrawal, C. Bohn, J. Velmurugan, W. Zhu, H. J. Lezec, and A. A. Talin. High-contrast and fast electrochromic switching enabled by plasmonics. *Nat. Commun.*, 7:1–6, 2016.

[25] D. Posadas and M. Florit. The redox switching of electroactive polymers. *J. Phys. Chem. B*, 108:15470–15476, 2004.

[26] O. Kim, T. Joo Shin, and M. J. Park. Fast low-voltage electroactive actuators using nanostructured polymer electrolytes. *Nat. Commun.*, 4:1–9, 2013.

[27] P. M. Mendes. Stimuli-responsive surfaces for bio-applications. *Chem. Soc. Rev.*, 37:2512, 2008.

[28] A. Ulman. Formation and Structure of Self-Assembled Monolayers. *Chem.Rev.*, 96:1533–1554, 1996.

[29] J. C. Love, L. A. Estroff, J. K. Kriebel, R. G. Nuzzo, and G. M. Whitesides. *Self-assembled monolayers of thiolates on metals as a form of nanotechnology*, volume 105. 2005.

[30] E. Lörtscher. Wiring molecules into circuits *Nat Nanotechnol.*, 8:381-384, 2013.

[31] M. Kawasaki, T. Sato, T. Tanaka, and K. Takao. Rapid self-assembly of alkanethiol monolayers on sputter-grown Au(111). *Langmuir*, 16:1719–1728, 2000.

[32] F. Bensebaa, R. Voicu, L. Huron, T. H. Ellis, and E. Kruus. Kinetics of Formation of Long-Chain n -Alkanethiolate Monolayers on Polycrystalline Gold. *Langmuir*, 13:5335–5340, 1997.

[33] C. D. Bain, E. B. Troughton, Y. Tai Tao, J. Evall, G. M. Whitesides, and R. G. Nuzzo. Formation of Monolayer Films by the Spontaneous Assembly of Organic Thiols from Solution onto Gold. *J. Am. Chem. Soc.*, 111:321–335, 1989.

[34] C. Love, D. B Wolfe, R. Haasch, M. L. Chabinyc, K. E Paul, G. M Whitesides, and R. G Nuzzo. Formation and structure of self-assembled monolayers of alkanethiolates on palladium. *J. Am. Chem. Soc.*, 125:2597–2609, 2003.

[35] C. P. Collier, G. Mattersteig, E. W. Wong, Y. Luo, K. Beverly, J. Sampaio, F. M. Raymo, J. F. Stoddart, and J. R. Heath. A [2]catenane-based solid state electronically reconfigurable switch. *Science*, 289:1172–1175, 2000.

[36] R. Lloyd Carroll and Christopher B. Gorman. The genesis of molecular electronics, 2002.

[37] H.B. Akkerman, P.W.M. Blom, D.M. de Leeuw, and B. de Boer. Towards molecular electronics with large-area molecular junctions. *Nature*, 441:69–72, 2006.

[38] S. Zhang, C.M. Cardona, and L. Echegoyen. Ion recognition properties of self-assembled monolayers (SAMs). *Chem. Commun.*, 43:4461, 2006.

[39] A. L. Eckermann, D. J. Feld, J. A. Shaw, and T. J. Meade. Electrochemistry of redox-active self-assembled monolayers. *Coord. Chem. Rev.*, 254:1769–1802, 2010.

[40] C. E. D. CHIDSEY. Free Energy and Temperature Dependence of Electron Transfer at the Metal-Electrolyte Interface. *Science*, 251:919–922, 1991.

[41] Woon Seok Yeo and Milan Mrksich. Electroactive self-assembled monolayers that permit orthogonal control over the adhesion of cells to patterned substrates. *Langmuir*, 22:10816–10820, 2006.

[42] Koon-Gee Neoh Bin Zhang, Yu Chen and En-Tang Kang. *Electrical Memory Materials and Devices.* RSC, 2015.

[43] A. D. Shukla, A. Das, and M. E. Van Der Boom. Electrochemical addressing of the optical properties of a monolayer on a transparent conducting substrate. *Angew. Chem. Int. Ed.*, 44:3237–3240, 2005.

[44] S. Sortino, S. Petralia, S. Conoci, and S. Di Bella. Novel Self-Assembled Monolayers as Redox Molecular Switches. *J. Am. Chem. Soc.*, 125:1122, 2003.

[45] J. S. Lindsey and D. F. Bocian. Molecules for charge-based information storage. *Acc. Chem. Res.*, 44:638–650, 2011.

[46] N. Crivillers, Y. Takano, Y. Matsumoto, J. Casado-Montenegro, M. Mas-Torrent, C. Rovira, T. Akasaka, and J. Veciana. Electrochemical and magnetic properties of a surface-grafted novel endohedral metallofullerene derivative. *Chem.Commun.*, 49:8145, 2013.

[47] C. Simão, M. Mas-Torrent, J. Casado-Montenegro, F. Otón, J. Veciana, and C. Rovira. A three-state surface-confined molecular switch with multiple channel outputs. *J. Am. Chem. Soc.*, 133:13256–13259, 2011.

[48] N. Crivillers, M. Mas-Torrent, J. Vidal-Gancedo, J. Veciana, and C. Rovira. Self-assembled monolayers of electroactive polychlorotriphenylmethyl radicals on Au(111). *J. Am. Chem. Soc.*, 130:5499–5506, 2008.

[49] I. Alcón, M. Gonidec, M. R. Ajayakumar, M. Mas-Torrent, and J. Veciana. A surface confined yttrium(iii) bis-phthalocyaninato complex: a colourful switch controlled by electrons. *Chem. Sci.*, 7:4940–4944, 2016.

[50] E. Marchante, N. Crivillers, M. Buhl, J. Veciana, and M. Mas-Torrent. An Electrically Driven and Readable Molecular Monolayer Switch Based on a Solid Electrolyte. *Angew. Chem. Int. Ed.*, 55:368–372, 2016.

[51] J. F. Rusling and S. L. Suib. Characterizing Materials with Cyclic Voltammetry, 1994.

[52] D. H. Evans, K. M. O'Connell, R. A. Petersen, and M. J. Kelly. Cyclic Voltammetry. *J. Chem. Educ.*, 60:290–293, 1983.

[53] P. T Kissinger and W. R. Heineman. Cyclic voltammetry. *J. Chem. Educ.*, 60:9242–9245, 1983.

[54] J. R. Macdonald and W. B. Johnson. Fundamentals of Impedance Spectroscopy. In *Impedance Spectroscopy: Theory, Experiment, and Applications*. John Wiley & Sons, Inc., Hoboken, NJ, USA, 2005.

[55] L. V. S. Philippe, G. W. Walter, and S. B. Lyon. Investigating Localized Degradation of Organic Coatings. *J. Electrochem. Soc.*, 150:B111, 2003.

[56] J. R. Macdonald. Impedance spectroscopy and its use in analyzing the steady-state AC response of solid and liquid electrolytes. *J. Electroanal. Chem.*, 223:25–50, 1987.

[57] Paulo R. Bueno, F. Fabregat-Santiago, and Jason J. Davis. Analytical chemistry. *Anal. Chem*, 85:411–417, 2013.

[58] S. Casalini, T. Cramer, F. Leonardi, M. Cavallini, and F. Biscarini. *Low-Dimensionality Effects in Organic Field Effect Transistors, in Organic Nanomaterials: Synthesis, Characterization, and Device Applications.* ohn Wiley & Sons, Inc., Hoboken, NJ, USA., 2013.

[59] Y. Caro, L. Anamale, M. Fouillaud, P. Laurent, T. Petit, and L. Dufosse. Natural hydroxyanthraquinoid pigments as potent food grade colorants: an overview. *Nat. Prod. Bioprospect.*, 2:174–193, 2012.

[60] E. A. Rodgers-Vieira, Z. Zhang, A. C. Adrion, A. Gold, and M. D. Aitken. Identification of anthraquinone-degrading bacteria in soil contaminated with polycyclic aromatic hydrocarbons. *Appl. Environ. Microbiol.*, 81:3775–3781, 2015.

[61] N. N. Gessler, A. S. Egorova, and T. A. Belozerskaya. Fungal anthraquinones. *Appl. Biochem. Microbiol.*, 49:85–99, 2013.

[62] M. Y. Okamura and G. Feher. Proton transfer in reaction centers from photosynthetic bacteria. *Annu. Rev. Biochem.*, 61:861–896, 1992.

[63] B. L. Trumpower. The Protonmotive Q Cycle energy transduction by coupling of proton translocation to electron transfer by the cytochrome bc complex. *J. Biol. Chem.*, 265:11409–11412, 1990.

[64] G. Goor, J. Glenneberg, and S. Jacobi. Hydrogen Peroxide. In B. Elvers, editor, *Ullmann's Encyclopedia of Industrial Chemistry*. Wiley-VCH Verlag GmbH & Co. KGaA, Weinheim, Germany, 2007.

[65] B. Yang, L. Hoober-Burkhardt, F. Wang, G. K. Surya Prakash, and S. R. Narayanan. An Inexpensive Aqueous Flow Battery for Large-Scale Electrical Energy Storage Based on Water-Soluble Organic Redox Couples. *J. Electrochem. Soc.*, 161:A1371–A1380, 2014.

[66] M. R. Gerhardt, L. Tong, R. Gómez-Bombarelli, Q. Chen, M. P. Marshak, C. J. Galvin, A. Aspuru-Guzik, R. G. Gordon, and M. J. Aziz. Anthraquinone Derivatives in Aqueous Flow Batteries. *Adv. Energy Mater.*, 7:382–382, 2017.

[67] B. Huskinson, M. P. Marshak, C. Suh, S. Er, M. R. Gerhardt, C. J. Galvin, X. Chen, A. Aspuru-Guzik, R. G. Gordon, and M. J. Aziz. A metal-free organic-inorganic aqueous flow battery. *Nature*, 505:195–198, 2014.

[68] A. Laurent. Ueber verschiedene Verbindungen des Anthracen's. *Justus Liebigs Ann. Chem.*, 34:287–296, 1840.

[69] M. Phillips. The Chemistry of Anthraquinone. *Chem. Rev.*, 6:157–174, 1929.

[70] S.I. Bailey and I.M. Ritchie. A cyclic voltammetric study of the aqueous electrochemistry of some quinones. *Electrochim. Acta*, 30:3–12, 1985.

[71] P. S. Guin, S. Das, and P. C. Mandal. Electrochemical Reduction of Quinones in Different Media: A Review. *int. j. electrochem.*, 2011:1–22, 2011.

[72] E. H. Van Dijk, D. J. T. Myles, M. H. Van Der Veen, and J. C. Hummelen. Synthesis and properties of an anthraquinone-based redox switch for molecular electronics. *Org. Lett.*, 8:2333–2336, 2006.

[73] E. W L Chan and M. N Yousaf. Immobilization of Ligands with Precise Control of Density to Electroactive Surfaces. *Langmuir*, 128:14730–14731, 2006.

[74] A. Artzy-Schnirman, E. Brod, M. Epel, M. Dines, T. Hammer, I. Benhar, Y. Reiter, and U. Sivan. A two-state electronic antigen and an antibody selected to discriminate between these states. *Nano Lett.*, 8:3398–3403, 2008.

[75] Z. Gao and Z. Jiang. Two-Dimensional Structure Induced K+ and Na+ Recognition by Self-Assembled Anthraquinone-Polyether Monolayers on Gold Electrodes. *Electrochem. Solid-State Lett.*, 7:E35–E39, sep 2004.

[76] A. Wieckowska, A. B. Braunschweig, and I. Willner. Electrochemical control of surface properties using a quinone-functionalized monolayer: effects of donorâacceptor complexes. *Chem. Commun.*, 38:3918, 2007.

[77] K. Dai, R. Huang, R. Jiang, H. X. Ke, F. Li, S. Jin, D. Y. Wu, and Z. Q. Tian. Adsorption and reduction reactions of anthraquinone derivatives on gold electrodes studied with electrochemical surface-enhanced Raman spectroscopy. *J. Raman Spectrosc.*, 43:1367–1373, 2012.

[78] H. Ma, M. Sik Kang, Q. M. Xu, K. S. Kim, and A. K. Y. Jen. Thiol-linked anthraquinone anthryl acetylene molecule: Synthesis, Self-assembly, and Photoelectrochemical Properties. *Chem. Mater.*, 17:2896–2903, 2005.

[79] M. Rausch, M. Vogel, and H. Rosenberg. Ferrocene: A Novel Organometallic Compound. *J. Chem. Educ.*, 34:268–272, 1957.

[80] H. Werner. At least 60 years of ferrocene: The discovery and rediscovery of the sandwich complexes. *Angew. chem.*, 51:6052-6058, 2012.

[81] G. Wilkinson, M. Rosenblum, M. C. Whiting, and R. B. Woodward. The Structure of Iron Bis-Cyclopentadienyl. *J. Am. Chem. Soc.*, 74:2125–2126, 1952.

[82] C. Ornelas. Application of ferrocene and its derivatives in cancer research. *New J. Chem.*, 35:1973–1985, 2011.

[83] D. E. Herbert, U. F.J. Mayer, and I. Manners. Strained metallocenophanes and related organometallic rings containing π-hydrocarbon ligands and transition-metal centers. *Angew. Chem. Int. Ed.*, 46:5060–5081, 2007.

[84] N S Neghmouche and T Lanez. Electrochemical properties of ferrocene in aqueous and organic mediums at glassy carbon electrode. *Recent Trends in Physical Chemistry: An International Journal*, 1:1–3, 2013.

[85] K M Kadish and C H Su. Relationships between Electron-Transfer Rate Constants of Bis(ligated)(octaethylporphinato)iron(iii) Perchlorate and the Presence of a Spin Equilibria. *Journal of the American Chemical Society*, 105(2):177–180, 1983.

[86] N. Ito, T. Saji, and S. Aoyagui. Electrochemical formation of stable ferrocene anion and the formal rate constant of the ferrocene0/- electrode. *J. Organomet. Chem.*, 247:301–305, 1983.

[87] A. M. Bond, T. L.E. Henderson, D. R. Mann, T. F. Mann, W. Thormann, and C. G. Zoski. Fast Electron Transfer Rate for the Oxidation of Ferrocene in Acetonitrile or Dichloromethane at Platinum Disk Ultramicroelectrodes. *Anal. Chem.*, 60:1878–1882, 1988.

[88] J. W Diggle and A. J. Parker. Solvation of ions-XX. The ferrocene-ferricinium couple and its role in the estimation of free energies of transfer of single ions. *Electrochim. Acta*, 18:975–979, 1973.

[89] M. Sharp. Determination of the charge-transfer kinetics of ferrocene at platinum and vitreous carbon electrodes by potential steps chronocoulometry. *Electrochim. Acta*, 28:301–308, 1983.

[90] A. B. Mandal. Self-Diffusion Studies on Various Micelles Using Ferrocene as Electrochemical Probe. *Langmuir*, 9: 1932-1933,1993.

[91] R. R. Gagne, C. A. Koval, and G. C. Lisensky. Ferrocene as an Internal Standard for Electrochemical Measurements. *Inorg. Chem.*, 19:2854–2855, 1980.

[92] G Bar, S Rubin, T N Taylor, B I Swanson, T A Zawodzinski Jr, J T Chow, and J P Ferraris. Patterned self â assembled monolayers of ferrocene and methyl terminated alkanethiols on gold : A combined electrochemical , scanning probe microscopy , and surface science study. *J. Vac. Sci. Technol., A*, 14:1794–1800, 1996.

[93] C. E D Chidsey, C. R Bertozzi, T. M. Putvinski, and A. M. Mujsce. Coadsorption of Ferrocene-Terminated and Unsubstituted Alkanethiols on Gold : Electroactive Self-Assembled Monolayers. *J. Am. Chem. Soc.*, 112:4301–4306, 1990.

[94] C. A. Nijhuis, W. F Reus, and G. M Whitesides. Molecular rectification in metal-SAM-metal oxide-metal junctions. *J. Am. Chem. Soc.*, 131:17814–17827, 2009.

[95] E. R Dionne, T. Sultana, L. Norman, V. Toader, and A. Badia. Redox-induced ion pairing of anionic surfactants with ferrocene-terminated self-assembled monolayers: Faradaic electrochemistry and surfactant aggregation at the monolayer/liquid interface. *J. Am. Chem. Soc.*, 135:17457–17468, 2013.

[96] A. Labande, J. Ruiz, and D. Astruc. Supramolecular gold nanoparticles for the redox recognition of oxoanions: Syntheses, Titrations, Stereoelectronic Effects, and Selectivityt. *J. Am. Chem. Soc.*, 124:1782–1789, 2002.

[97] J. Lehr, M. Tropiano, P. D Beer, S. Faulkner, and J. J Davis. Reversible redox modulation of a lanthanide emissive molecular film. *Chem. Commun.*, 51:6515–6517, 2015.

[98] Kosuke Namiki, Aiko Sakamoto, Masaki Murata, Shoko Kume, and Hiroshi Nishihara. Reversible photochromism of a ferrocenylazobenzene monolayer controllable by a single green light source. *Chemical Communications*, (44):4650–4652, 2007.

[99] P. Saint-Cricq, T. Pigot, L. Nicole, C. Sanchez, and S. Lacombe. Hybrid functional mesostructured thin films with photo-oxidative properties in the visible range. *Chem. Commun.*, 0:5281–5283, 2009.

[100] M. Frasconi and F. Mazzei. Electrochemically controlled assembly and logic gates operations of gold nanoparticle arrays. *Langmuir*, 28:3322–3331, 2012.

[101] M. Lestelius, I. Engquist, P. Tengvall, M. K Chaudhury, and B. Liedberg. Order/disorder gradients of n-alkanethiols on gold. *Colloids Surf., B*, 15:57–70, 1999.

[102] J. Casado-Montenegro, E. Marchante, N. Crivillers, C. Rovira, and M. Mas-Torrent. Donor/Acceptor Mixed Self-Assembled Monolayers for Realising a Multi-Redox-State Surface. *ChemPhysChem*, 17:1810–1814, 2016.

[103] X. Qu, Y. Li, L. Li, Y. Wang, J. Liang, and J. Liang. Fluorescent gold nanoclusters: Synthesis and recent biological application. *J. Nanomater.*, 2015:1–23, 2015.

[104] T. Theophanides. Supramolecular Chemistry: Recognition Processes in Nucleic Acid Systems. In *Spectroscopy of Biological Molecules: Modern Trends*, pages 347–350. Springer Netherlands, Dordrecht, 1997.

[105] W. S. Jeon, E. Kim, I. H. Ho, I. Wang, J. W. Lee, S.Y. Kim, H. J. Kim, and K. Kim. Molecular Loop Lock: A Redox-Driven Molecular Machine Based on a Host-Stabilized Charge-Transfer Complex. *Angew. Chem.*, 44:87–91, 2005.

[106] M. Bagheri, M. Yaser Masoomi, A. Morsali, and A. Schoedel. Two Dimensional Host-Guest Metal-Organic Framework Sensor with High Selectivity and Sensitivity to Picric Acid. *ACS Appl. Mater. Interfaces*, 8:21472–21479, 2016.

[107] E. M.Martin Del Valle. Cyclodextrins and their uses: A review. *Process Biochem.*, 39:1033-1046, 2004.

[108] G. Crini. Review: A history of cyclodextrins. *Chem. Rev.*, 114:10940-10975, 2014.

[109] A. E Kaifer. Interplay between molecular recognition and redox chemistry. *Acc. Chem. Res.*, 32:62–71, 1999.

[110] J. Woo Park, H. Eun Song, and S. Y. Lee. Face selectivity of inclusion complexation of viologens with β-cyclodextrin and 6-O-(2-sulfonato-6-naphthyl)-β-cyclodextrin. *J. Phys. Chem. B*, 106:7186–7192, 2002.

[111] W. P. Joon and Y. L. Soo. Bi-directional inclusion complexation of methylalkyl viologens with β-cyclodextrin and naphthyl group-tethered β-cyclodextrins. *J. Incl. Phenom. Macrocycl. Chem.*, 47:143–148, 2003.

[112] F. Kitamura, T. Ohsaka, and K. Tokuda. Effect of complexation by β-cyclodextrins on the voltammetric characteristic of viologens adsorbed on an HMDE. *J. Electroanal. Chem.*, 368:281–284, 1994.

[113] Y. Wang, S. Mendoza, and A. E. Kaifer. Electrochemical Reduction of Cobaltocenium in the Presence of -Cyclodextrin. *Inorg. Chem.*, 37:317–320, 1998.

[114] E. I. Rogers, D. S. Silvester, D. L. Poole, L. Aldous, C. Hardacre, and R. G. Compton. Voltammetric characterization of the ferrocene|ferrocenium and cobaltocenium|cobaltocene redox couples in RTILs. *J. Phys. Chem. C*, 112:2729–2735, 2008.

[115] E. A. Smith, R. R. Lilienthal, R. J. Fonseca, and D. K. Smith. Electrochemical Characterization of a Viologen-Based Redox-Dependent Receptor for Neutral Organic Molecules. *Anal. Chem.*, 66:3013–3020, 1994.

[116] J. S. Wu, K. Toda, A. Tanaka, and I. Sanemasa. Association Constants of Ferrocene with Cyclodextrins in Aqueous Medium Determined by Solubility Measurements of Ferrocene. *Bull. Chem. Soc. Jpn.*, 71:1615–1618, 1998.

[117] V. V. Strelets, I. A. Mamedjarova, M. N. Nefedova, N. I. Pysnograeva, V. I. Sokolov, L. Pospíšil, and J. Hanzlík. Electrochemistry of inclusion complexes of organometallics. Complexation of ferrocene and azaferrocene by cyclodextrins. *J. Electroanal. Chem.*, 310:179–186, 1991.

[118] W. S. Jeon, K. Moon, S. H. Park, H. Chun, Y. H. Ko, J. Y. Lee, E. S. Lee, S. Samal, N. Selvapalam, M. V. Rekharsky, V. Sindelar, D. Sobransingh, Y. Inoue, A. E. Kaifer, and K. Kim. Complexation of Ferrocene Derivatives by the Cucurbit[7]uril Host: A Comparative Study of the Cucurbituril and Cyclodextrin Host Families. *J. Am. Chem. Soc.*, 127:12984–12989, 2005.

[119] X.J. Dang, R. Tong, and H.L. Li. The Electrochemistry of the Inclusion Complex of Anthraquinone With Cyclodextrin Studied by Means of OSWV. *J. Inclusion Phenom. Mol. Recognit. Chem.*, 24:275–286, 1996.

[120] K. Tian, H. Zhang, X. Chen, and Z. Hu. Determination of five anthraquinones in medicinal plants by capillary zone electrophoresis with beta-cyclodextrin addition. *J. Chromatogr. A*, 1123:134–137, 2006.

[121] T. Sun, Y. Li, H. Zhang, J. Li, F. Xin, L. Kong, and A. Hao. PH-reversible vesicles based on the " supramolecular amphiphilies" formed by cyclodextrin and anthraquinone derivate. *Colloids Surf., A*, 375:87–96, 2011.

[122] H. Jiang, H. Sun, S. Zhang, R. Hua, Y. Xu, S. Jin, H. Gong, and L. Li. NMR investigations of inclusion complexes between β-cyclodextrin and naphthalene/anthraquinone derivatives. *J. Inclusion Phenom. Macrocyclic Chem.*, 58:133–138, 2007.

[123] Y. Tang, X. Zeng, and J. Liang. Surface plasmon resonance: An introduction to a surface spectroscopy technique. *J. Chem. Educ.*, 87:742–746, 2010.

[124] E. Samiei, M. Tabrizian, and M. Hoorfar. A review of digital microfluidics as portable platforms for lab-on a-chip applications. *Lab. Chip*, 16:2376–2396, 2016.

[125] J. Biener, A. Wittstock, T. F. Baumann, J. Weissmüller, M. Bäumer, and A. V. Hamza. Surface chemistry in nanoscale materials. *Materials*, 2:2404-2428, 2009.

[126] R. Marek and J. Straub. Origin of thermocapillary convection in subcooled nucleate pool boiling. *Int. J. Heat Mass Transfer*, 44:619–632, 2001.

[127] V. Pretorius, B. J. Hopkins, and J. D. Schieke. Electro-osmosis. A new concept for high-speed liquid chromatography. *J. Chromatogr. A*, 99:23–30, 1974.

[128] Y. Ren, W. Liu, Y. Jia, Y. Tao, J. Shao, Y. Ding, and H. Jiang. Featuring work from the group of Prof Title: Induced-charge electroosmotic trapping of particles As featured in: Induced-charge electroosmotic trapping of particles. *Lab. Chip*, 15:2181–2191, 2015.

[129] M. G. Pollack, R. B. Fair, and A. D. Shenderov. Electrowetting-based actuation of liquid droplets for microfluidic applications. *Appl. Phys. Lett.*, 77:1725–1726, 2000.

[130] W. Liu, Y. Ren, J. Shao, H. Jiang, and Y. Ding. A theoretical and numerical investigation of travelling wave induction microfluidic pumping in a temperature gradient. *J. Phys. D: Appl. Phys.*, 47:075501, 2014.

[131] Y. Ren, H. Jiang, H. Yang, A. Ramos, and P. García-Sánchez. Electrical manipulation of electrolytes with conductivity gradients in microsystems. *J. Electrostat.*, 67:372–376, 2009.

[132] A. Salari, M. Navi, and C. Dalton. A novel alternating current multiple array electrothermal micropump for lab-on-a-chip applications. *Biomicrofluidics*, 9:014113, 2015.

[133] A Ramos, H Morgan, N G Green, and A Castellanos. Ac electrokinetics: a review of forces in microelectrode structures. *J. Phys. D: Appl. Phys.*, 31:2338–2353, 1998.

[134] J. Lee, H. Moon, J. Fowler, T. Schoellhammer, and C. J. Kim. Electrowetting and electrowetting-on-dielectric for microscale liquid handling. *Sens. Actuators, A*, 95:259–268, 2002.

[135] M. G Pollack, R. B. Fair, and A. D. Shenderov. Electrowetting-based actuation of liquid droplets for microfluidic applications. *J. Appl. Phys. Lett.*, 77:1725–244108, 2000.

[136] V. Srinivasan, V. K Pamula, and R. B. Fair. Droplet-based microfluidic lab-on-a-chip for glucose detection. *Anal. Chim. Acta*, 507:145–150, 2004.

[137] D. Mark, S. Haeberle, G. Roth, F. von Stetten, and R. Zengerle. From microfluidic application to nanofluidic phenomena issue. *Chem. Soc. Rev.*, 39:1153–82, 2010.

[138] G. J. Shah, A. T Ohta, E. P. Y Chiou, M. C. Wu, and C. J. âCJâ Kim. EWOD-driven droplet microfluidic device integrated with optoelectronic tweezers as an automated platform for cellular isolation and analysis. *Lab. Chip*, 9:1732, 2009.

[139] I. Barbulovic-Nad, H. Yang, P. S. Park, and A. R Wheeler. Digital microfluidics for cell-based assays. *Lab. Chip*, 8:519, 2008.

[140] W. C Nelson and C. J. C. Kim. Droplet actuation by electrowetting-on-dielectric (EWOD): A review. *J Adhes Sci Technol*, 26:12-17, 2012.

[141] B Berge. Electrocapilarity and wetting of insulator film by water. *C.R Acad. Sci. Paris Ser II.*, 317:157–163, 1993.

[142] F. Saeki, J. Baum, H. Moon, J. Y. Yoon, C. J. Kim, and R. L. Garrell. Electrowetting on dielectrics (EWOD): reducing voltage requirements for microfluidics. *Polym. Mater. Sci. Eng.*, 85:12–13, 2001.

[143] M. Abdelgawad and A. R Wheeler. The digital revolution: A new paradigm for microfluidics. *Adv. Mater.*, 21:920–925, 2009.

[144] Y. Y. Lin, E. R.F. Welch, and R. B Fair. Low voltage picoliter droplet manipulation utilizing electrowetting-on- dielectric platforms. *Sens. Actuators, B*, 173:338–345, 2012.

[145] H. Moon, S. Kwon Cho, and R. L Garrell. Low voltage electrowetting-on-dielectric. *J. Appl. Phys.*, 92:4080–4087, 2002.

[146] S. Casalini, M. Berto, C. A Bortolotti, G. Foschi, A. Operamolla, M. Di Lauro, O. H. Omar, A. Liscio, L. Pasquali, M. Montecchi, G. M Farinola, and M. Borsari. Electrowetting of nitro-functionalized oligoarylene thiols self-assembled on polycrystalline gold. *ACS Appl. Mater. Interfaces.*, 7:3902–3909, 2015.

[147] H. Li, Z. Yin, Q. He, H. Li, X. Huang, G. Lu, D. W. H. Fam, A. I. Y. Tok, Q. Zhang, and H. Zhang. Fabrication of single- and multilayer MoS_2 film-based field-effect transistors for sensing NO at room temperature. *Small*, 8:63–67, 2012.

[148] A. Castellanos-Gomez, R. Van Leeuwen, M. Buscema, H. S J Van Der Zant, G. A. Steele, and W. J. Venstra. Single-layer MoS2 mechanical resonators. *Adv. Mater.*, 25:6719–6723, 2013.

[149] D. Lembke, S. Bertolazzi, and A. Kis. Single-layer MoS_2 electronics. *Acc. Chem. Res.*, 48:100–110, 2015.

[150] V. Pachauri, K. Kern, and K. Balasubramanian. Chemically exfoliated large-area two-dimensional flakes of molybdenum disulfide for device applications. *APL Mater.*, 1:032102, 2013.

[151] H. Li, J. Wu, Z. Yin, and H. Zhang. Preparation and Applications of Mechanically Exfoliated Single-Layer and Multilayer MoS_2 and WSe_2 Nanosheets. *Acc. Chem. Res.*, 47:1067–1075, 2014.

[152] E. Varrla, C. Backes, K. R. Paton, A. Harvey, Z. Gholamvand, J. McCauley, and J. N. Coleman. Large-scale production of size-controlled MoS_2 nanosheets by shear exfoliation. *Chem. Mater.*, 27:1129–1139, 2015.

[153] Arramel, Q. Wang, Y. Zheng, W. Zhang, and A. T. S. Wee. Towards molecular doping effect on the electronic properties of two-dimensional layered materials. *J. Phys. Conf. Ser.*, 739:012014, 2016.

[154] H. Samassekou, A. Alkabsh, M. Wasala, M. Eaton, A. Walber, A. Walker, O. Pitkänen, K. Kordas, S. Talapatra, T. Jayasekera, and D. Mazumdar. Viable route towards large-area 2D MoS_2 using magnetron sputtering. *2D Mater.*, 4:021002, 2017.

[155] B. D. Keller, A. Bertuch, J. Provine, G. Sundaram, N. Ferralis, and J. C. Grossman. Process Control of Atomic Layer Deposition Molybdenum Oxide Nucleation and Sulfidation to Large-Area MoS_2 Monolayers. *Chem. Mater.*, 29:2024–2032, 2017.

[156] R. Browning, N. Kuperman, and R. Solanki. Atomic layer deposition of MoS_2 thin films Large area growth of layered WSe_2 films. *Mat. Res. Express*, 2:035006, 2015.

[157] D. H. Kwon, Z. Jin, S. Shin, W. S. Lee, and Y. S. Min. A comprehensive study on atomic layer deposition of molybdenum sulfide for electrochemical hydrogen evolution. *Nanoscale*, 8:7180–7188, 2016.

[158] Oleg V Yazyev and Andras Kis. MoS2 and semiconductors in the flatland. *Materials Today*, 18:20–30, 2015.

[159] H. Liu and P. D. Ye. MoS_2 Dual-Gate MOSFET with Atomic-Layer-Deposited Al_2O_3 as Top-Gate Dielectric. *Electron Devices Lett.*, 33:1–3, 2012.

[160] J. Hong, Z. Hu, M. Probert, K. Li, D. Lv, X. Yang, L. Gu, N. Mao, Q. Feng, L. Xie, J. Zhang, D. Wu, Z. Zhang, C. Jin, W. Ji, X. Zhang, J. Yuan, and Z. Zhang. Exploring atomic defects in molybdenum disulphide monolayers. *Nat. Commun.*, 6:6293–6300, 2015.

[161] A. Förster, S. Gemming, G. Seifert, and D. Tománek. Chemical and Electronic Repair Mechanism of Defects in MoS2 Monolayers. *ACS Nano*, 11:9989–9996, 2017.

[162] A. M. Van Der Zande, P. Y. Huang, D. A. Chenet, T. C. Berkelbach, Y. You, G. H. Lee, T. F. Heinz, D. R. Reichman, D. A. Muller, and J. C. Hone. Grains and grain boundaries in highly crystalline monolayer molybdenum disulphide. *Nat. Mater.*, 12:554–561, 2013.

[163] J V Lauritsen, M Nyberg, R T Vang, M V Bollinger, B S Clausen, H. Topsøe, K W Jacobsen, E. Lægsgaard, J. K. Nørskov, and F Besenbacher. Chemistry of one-dimensional metallic edge states in MoS_2 nanoclusters. *Nanotechnology*, 14:385–389, 2003.

[164] D. Voiry, M. Salehi, R. Silva, T. Fujita, M. Chen, T. Asefa, V. B. Shenoy, G. Eda, and M. Chhowalla. Conducting MoS_2 nanosheets as catalysts for hydrogen evolution reaction. *Nano Lett.*, 13:6222–6227, dec 2013.

[165] J. Kibsgaard, Z. Chen, B. N Reinecke, and T. F Jaramillo. Engineering the surface structure of MoS_2 to preferentially expose active edge sites for electrocatalysis. *Nat. Mater.*, 11:963–969, 2012.

[166] J. Xie, H. Zhang, S. Li, R. Wang, X. Sun, M. Zhou, J. Zhou, X. W. Lou, and Y. Xie. Defect-rich MoS_2 ultrathin nanosheets with additional active edge sites for enhanced electrocatalytic hydrogen evolution. *Adv. Mater.*, 25:5807–5813, 2013.

[167] N. Yu, L. Wang, M. Li, X. Sun, T. Hou, and Y. Li. Molybdenum disulfide as a highly efficient adsorbent for non-polar gases. *Phys. Chem. Chem. Phys.*, 17:11700–11704, 2015.

[168] S. Chee, C. Oh, M. Son, G. Son, H. Jang, T. J. Yoo, S. Lee, W. Lee, J. Y. Hwang, H. Choi, B. H. Lee, and M.H Ham. Sulfur vacancy-induced reversible doping of transition metal disulfides via hydrazine treatment. *Nanoscale*, 9:9333–9339, 2017.

[169] Q. Li, Y. Zhao, C. Ling, S. Yuan, Q. Chen, and J. Wang. Towards a Comprehensive Understanding of the Reaction Mechanisms Between Defective MoS_2 and Thiol Molecules. *Angew. Chem. Int. Ed.*, 56:10501–10505, 2017.

[170] D. M. Sim, M. Kim, S. Yim, M. J. Choi, J. Choi, S. Yoo, and Y. S. Jung. Controlled Doping of Vacancy-Containing Few-Layer MoS_2 via Highly Stable Thiol-Based Molecular Chemisorption. *ACS Nano*, 9:12115–12123, 2015.

[171] S. Bertolazzi, S. Bonacchi, G. Nan, A. Pershin, D. Beljonne, and Paolo Samorì. Engineering Chemically Active Defects in Monolayer MoS_2 Transistors via Ion-Beam Irradiation and Their Healing via Vapor Deposition of Alkanethiols. *Adv. Mater.*, 29:1606760, 2017.

[172] M. Makarova, Y. Okawa, and M. Aono. Selective adsorption of thiol molecules at sulfur vacancies on $MoS_2(0001)$, followed by vacancy repair via S-C dissociation. *J. Phys. Chem. C*, 116:22411–22416, 2012.

[173] Y. Cai, H. Zhou, G. Zhang, and Y-W. Zhang. Modulating Carrier Density and Transport Properties of MoS_2 by Organic Molecular Doping and Defect Engineering. *Chem. Mater.*, 28:8611–8621, 2016.

[174] Y. Jing, X. Tan, Z. Zhou, and P. Shen. Tuning electronic and optical properties of MoS_2 monolayer via molecular charge transfer. *J. Mater. Chem. A*, 2:16892–16897, 2014.

[175] L. Nagy, G. Gyetvai, L. Kollár, and G. Nagy. Electrochemical behavior of ferrocene in ionic liquid media. *J. Biochem. Biophys. Methods*, 69:121–132, 2006.

[176] W. Zhu, T. Low, Y. H. Lee, H. Wang, D. B. Farmer, J. Kong, F. Xia, and P. Avouris. Electronic transport and device prospects of monolayer molybdenum disulphide grown by chemical vapour deposition. *Nat. Commun.*, 5:3087, 2014.

[177] E. P. Nguyen, B. J. Carey, J. Z. Ou, J. Van Embden, E. D. Gaspera, A. F. Chrimes, M. J. S. Spencer, S. Zhuiykov, K. Kalantar-Zadeh, and T. Daeneke. Electronic Tuning of 2D MoS_2 through Surface Functionalization. *Adv. Mater.*, 27:6225–6229, 2015.

[178] H. Tokuda, K. Hayamizu, K. Ishii, M. A. B. H. Susan, and M. Watanabe. Physicochemical properties and structures of room temperature ionic liquids. 2. variation of alkyl chain length in imidazolium cation. *J. Phys. Chem. B*, 109:6103–6110, 2005.

[179] H. Tokuda, K. Hayamizu, K. Ishii, M. A. B. H. Susan, and M. Watanabe. Physicochemical properties and structures of room temperature ionic liquids. 1. Variation of anionic species. *J. Phys. Chem. B*, 108:16593–16600, 2004.

[180] M. Armand, F. Endres, D. R MacFarlane, H. Ohno, and B. Scrosati. Ionic-liquid materials for the electrochemical challenges of the future. *Nat. Mater*, 8:621-629, 2009.

[181] M. Galiński, A. Lewandowski, and I. Stepniak. Ionic liquids as electrolytes. *Electrochim. Acta*, 51:5567-5580, 2006.

[182] Z. Li, S. W. Chang, C. C. Chen, and S. B Cronin. Enhanced photocurrent and photoluminescence spectra in MoS_2 under ionic liquid gating. *Nano Res.*, 7:973–980, 2014.

[183] M. M. Perera, M. W. Lin, H. J. Chuang, B. P. Chamlagain, C. Wang, X. Tan, M. M. C. Cheng, D. Tománek, and Z. Zhou. Improved carrier mobility in few-layer MoS_2 field-effect transistors with ionic-liquid gating. *ACS Nano*, 7:4449–4458, 2013.

[184] M. J. Lee, C. B. Lee, D. Lee, S. R. Lee, M. Chang, J. H. Hur, Y. B. Kim, C. J. Kim, D. H. Seo, S. Seo, U. I. Chung, I. K. Yoo, and K. Kim. A fast, high-endurance and scalable non-volatile memory device made from asymmetric Ta2O5-xx/TaO2-xbilayer structures. *Nat. Mater.*, 10:625–630, 2011.

[185] R. Waser, R. Dittmann, C. Staikov, and K. Szot. Redox-based resistive switching memories nanoionic mechanisms, prospects, and challenges. *Adv. Mater.*, 21:2632–2663, 2009.

[186] T. Chattopadhyay, J. N. Roy, and A. K. Chakraborty. Polarization encoded all-optical quaternary R-S flip-flop using binary latch. *Opt. Commun.*, 282:1287–1293, 2009.

[187] F. Wudl, G. M. Smith, and E. J. Hufnagel. Bis-1,3-dithiolium chloride: an unusually stable organic radical cation. *J. Chem. Soc. D*, 21:1453, 1970.

[188] M. B. Nielsen and S. P.A. Sauer. On the aromaticity of tetrathiafulvalene cations. *Chem. Phys. Lett.*, 453:136–139, 2008.

[189] E. Gomar-Nadal, C. Rovira, and D. B. Amabilino. Synthesis of optically active amphiphilic tetrathiafulvalene derivatives. *Tetrahedron*, 62:3370–3379, 2006.

[190] A. El-W. A.O. Sarhan. Synthesis and applications of tetrathiafulvalenes and ferrocene-tetrathiafulvalenes and related compounds. *Tetrahedron*, 61:3889–3932, 2005.

[191] J. Nakayama, E. Seki, and M. Hoshino. General Synthesis of Di benzotetrathiafulvalenes. *J. Chem. Soc., Perkin Trans. 1*, pages 468–471, 1978.

[192] M. B. Nielsen, C. Lomholt, and J. Becher. Tetrathiafulvalenes as building blocks in supramolecular chemistry II. *Chem. Soc. Rev.*, 29:153–164, 2000.

[193] F. Wudl, D. Wobschall, and E. J. Hufnagel. Electrical Conductivity by the Bis-1,3-dithiole-Bis-1,3-dithiolium System. *J. Am. Chem. Soc.*, 94:670-672, 1972.

[194] S. M. Rosenfeld, R. G. Lawlert, and H. R. Ward. Electron Transfer in a New Highly Conducting Donor-Acceptor Complex. *J. Am. Chem. SOC*, 95:948, 1973.

[195] E. H. Conwell. Charge Transfer Change With Pressure IN TTFâTCNQ. *Solid State Commun.*, 33:17–19, 1980.

[196] C. Rovira. Bis(ethylenethio)tetrathiafulvalene (BET-TTF) and related dissymmetrical electron donors: From the molecule to functional molecular materials and devices (OFETs). *Chem. Rev.*, 104: 5289-5318, 2004.

[197] M. Iyoda, M. Hasegawa, and Y. Miyake. Bi-TTF, bis-TTF, and related TTF oligomers. *Chem. Rev.*, 104:5085–5113, 2004.

[198] Marta Mas-Torrent. Novel small molecules for organic field-effect transistors: towards processability and high performance. *Chem. Soc. Rev.*, 37:827–838, 2008.

[199] Y. Bando, T. Shirahata, K. Shibata, H. Wada, T. Mori, and T. Imakubo. Organic Field-Effect Transistors Based on Alkyl-Terminated Tetrathiapentalene (TTP) Derivatives. *Chem. Mater.*, 20:5119–5121, 2008.

[200] M. A. Herranz, L. Yu, N. Martín, and L. Echegoyen. Synthesis, Electrochemistry and Self-Assembled Monolayers of Novel Tetrathiafulvalene (TTF) and π-Extended TTF (exTTF) Disulfides. *J. Org. Chem.*, 68:8379–8385, 2003.

[201] P. Y. Blanchard, O. Alévêque, S. Boisard, C. Gautier, A. El-Ghayoury, F. Le Derf, T. Breton, and E. Levillain. Intermolecular interactions in self-assembled monolayers of tetrathiafulvalene derivatives. *Phys. Chem. Chem. Phys.*, 13:2118–2120, 2011.

[202] E. Gomar-Nadal, G. K. Ramachandran, F. Chen, T. Burgin, C. Rovira, D. B. Amabilino, and S. M. Lindsay. Self-assembled monolayers of tetrathiafulvalene derivatives on au(111): Organization and electrical properties. *J. Phys. Chem. B*, 108:7213–7218, 2004.

[203] E. Vargas, M. Gamella, S. Campuzano, A. Guzmán-Vázquez De Prada, M. A. Ruiz, A. J. Reviejo, and J. M. Pingarrón. Development of an integrated electrochemical biosensor for sucrose and its implementation in a continuous flow system for the simultaneous monitoring of sucrose, fructose and glucose. *Talanta*, 105:93–100, 2013.

[204] S. Campuzano, V. Escamilla-Gómez, M. Herranz, M. Pedrero, and J. M. Pingarrón. Development of amperometric biosensors using thiolated tetrathiafulvalene-derivatised self-assembled monolayer modified electrodes. *Sens. Actuators, B*, 134:974–980, 2008.

[205] N. Bouquin, V. L. Malinovskii, X. Guégano, S. X. Liu, S. Decurtins, and R. Häner. TTF-modified DNA. *Chem.âEur. J.*, 14:5732–5736, 2008.

[206] H. Liu, S. Liu, and L. Echegoyen. Remarkably stable self-assembled monolayers of new crown-ether annelated tetrathiafulvalene derivatives and their cation recognition propertiesâ . *Chem. Commun.*, 0:1493–1494, jan 1999.

[207] D. Canevet, M. Sallé, G. Zhang, D. Zhang, and D. Zhub. Tetrathiafulvalene (TTF) derivatives: key building-blocks for switchable processes. *Chem. Commun.*, 0:2245–2269, 2009.

[208] M. R. Bryce. Functionalised tetrathiafulvalenes: new applications as versatile p-electron systems in materials chemistry. *J. Mater. Chem.*, 10:589–598, 2000.

[209] J. L. Segura and N. Martín. New Concepts in Tetrathiafulvalene Chemistry. *Angew. Chem. Int. ed.*, 40:1372–1409, 2001.

[210] M. A. Herranz, L. Yu, N. Martín, and L. Echegoyen. Synthesis, Electrochemistry and Self-Assembled Monolayers of Novel Tetrathiafulvalene (TTF) and π-Extended TTF (exTTF) Disulfides. *J. Org. Chem.*, 68:8379–8385, 2003.

[211] Javier Garin, Jesus Orduna, Santiago Uriel, Adrian J. Moore, Martin R. Brice, Stefan Wagener, Dimitri S. Yufit, and Judith A.K.Howard. Improved Syntheses of Carboxytetrathiafulvalene, Formyltetrathiafulvalene and (Hydroxymethyl)tetrathiafulvalene: Versatile Bulding Blocks for New Functionalised Tetrathiafulvalene Derivatives. *Synthesis*, pages 489–493, 1994.

[212] G. Cooke, F. M. Duclairoir, V. M. Rotello, and J. F. Stoddart. The reversible complexation of a tetrathiafulavene functionalised self-assembled monolayer by cyclobis(paraquat-p-phenylene). *Tetrahedron Lett.*, 41:8163–8166, 2000.

[213] C. A. Nijhuis, W. F. Reus, and G. M. Whitesides. Mechanism of rectification in tunneling junctions based on molecules with asymmetric potential drops. *J. Am. Chem. Soc.*, 132:18386–18401, dec 2010.

[214] C. Jia, D. Zhang, W. Xu, and D. Zhu. A new approach to 4-alkylthio-1,3-dithiole-2-thione: An unusual reaction of a zinc complex of 1,3-dithole-2-thione-4,5-dithiolate. *Org. Lett.*, 3:1941–1943, 2001.

[215] O. Jeannin and M. Fourmigué. One- or two-dimensional fluorine segregation in amphiphilic perfluorinated tetrathiafulvalenes. *C. R. Chim.*, 9:1287–1294, 2006.

[216] J. Nakayama, H. Sugiura, and M. Hoshino. Reaction of 1,3-benzodithiol-2-ylidenes with elemental sulfur and selenium: a convenient preparation of 2-thioxo- and 2-selenoxo-1,3-benzodithioles. *Tetrahedron Lett.*, 24:2585–2588, 1983.

[217] T. K. Tran, Q. Bricaud, M. Oçafrain, P. Blanchard, J. Roncali, S. Lenfant, S. Godey, D. Vuillaume, and D. Rondeau. Thiolate chemistry: A powerful and versatile synthetic tool for immobilization/functionalization of oligothiophenes on a gold surface. *Chem.âEur. J.*, 17:5628–5640, 2011.

[218] E. J. Pacsial, D. Alexander, R. J. Alvarado, M. Tomasulo, and F. M. Raymo. Donor/acceptor interactions in self-assembled monolayers and their consequences on interfacial electron transfer. *J. Phys. Chem. B*, 108:19307–19313, 2004.

[219] O. Alévêque, F. Seladji, C. Gautier, M. Dias, T. Breton, and E. Levillain. Nitroxyl radical self-assembled monolayers on gold: Versatile electroactive centers in aqueous and organic media. *ChemPhysChem*, 10:2401–2404, 2009.

[220] Y. Yokota, A. Miyazaki, K. I. Fukui, T. Enoki, K. Tamada, and M. Hara. Dynamic and Collective Electrochemical Responses of Tetrathiafulvalene Derivative Self-Assembled Monolayers. *J. Phys. Chem.*, 110:20401–20408, 2006.

[221] S. Campuzano, M. Pedrero, C. Montemayor, E. Fatás, and J. M. Pingarrón. Characterization of alkanethiol-self-assembled monolayers-modified gold electrodes by electrochemical impedance spectroscopy. *J. Electroanal. Chem.*, 586:112–121, 2006.

[222] E. Boubour and R B. Lennox. Potential-induced defects in n-alkanethiol self-assembled monolayers monitored by impedance spectroscopy. *J. Phys. Chem. B*, 104:9004–9010, 2000.

[223] E. Katz, O. Lioubashevsky, and I. Willner. Electromechanics of a redox-active rotaxane in a monolayer assembly on an electrode. *J. Am. Chem. Soc.*, 126:15520–32, 2004.

[224] T. M. Nahir and E. F. Bowden. Measurement of the rate of adsorption of electroactive cytochrome c to modified gold electrodes by electrochemical impedance spectroscopy. *Langmuir*, 18:5283–5286, 2002.

[225] Y. Guo, J. Zhao, X. Yin, X. Gao, and Y. Tian. Electrochemistry investigation on protein protection by alkanethiol self-assembled monolayers against urea impact. *J. Phys. Chem. C*, 112:6013–6021, 2008.

[226] M. Druchler, N. Borisenko, J. Wallauer, C. Winter, B. Huber, F. Endres, and B. Roling. New insights into the interface between a single-crystalline metal electrode and an extremely pure ionic liquid: slow interfacial processes and the influence of temperature on interfacial dynamics. *Phys. Chem. Chem. Phys.*, 14:5090–5099, 2012.

[227] Z. Kerner and T. Pajkossy. On the origin of capacitance dispersion of rough electrodes. *Electrochim. Acta*, 46:207–211, 2000.

[228] E. Boubour and R. B. Lennox. Insulating Properties of Self-Assembled Monolayers Monitored by Impedance Spectroscopy. *Langmuir*, 16:4222–4228, may 2000.

[229] P. R. Bueno, G. Mizzon, and J. J. Davis. Capacitance spectroscopy: A versatile approach to resolving the redox density of states and kinetics in redox-active self-assembled monolayers. *J. Phys. Chem. B*, 116:8822–8829, 2012.

[230] M. S. Góes, H. Rahman, J. Ryall, J. J. Davis, and P. R. Bueno. A dielectric model of self-assembled monolayer interfaces by capacitive spectroscopy. *Langmuir*, 28:9689–9699, 2012.

[231] G. Yzambart, B. Fabre, F. Camerel, T. Roisnel, and D. Lorcy. Controlled grafting of tetrathiafulvalene (TTF) containing diacetylenic units on hydrogen-terminated silicon surfaces: From redox-active TTF monolayer to polymer films. *J. Phys. Chem. C*, 116:12093–12102, 2012.

[232] N. Bellec, A. Faucheux, F. Hauquier, D. Lorcy, and B. Fabre. Redox-active organic monolayers deposited on silicon surfaces for the fabrication of molecular scale devices. *Int. J. Nanotechnol.*, 5:741–756, 2008.

[233] V. F. Lvovich. *Impedance Spectroscopy: Applications to Electrochemical and Dielectric Phenomena.* John Wiley & Sons, Inc., Hoboken, NJ, USA, 2012.

[234] M. Singh, M. Y. Mulla, M. V. Santacroce, M. Magliulo, C. Di Franco, K. Manoli, D. Altamura, C. Giannini, N. Cioffi, G. Palazzo, G. Scamarcio, and L. Torsi. Effect of the gate metal work function on water-gated ZnO thin-film transistor performance. *J. Phys. D: Appl. Phys.*, 49:275101, 2016.

[235] L. Kergoat, L. Herlogsson, B. Piro, M. C. Pham, G. Horowitz, X. Crispin, and M. Berggren. Tuning the threshold voltage in electrolyte-gated organic field-effect transistors. *Proc. Natl. Acad. Sci. USA*, 109:8394–8399, 2012.

[236] M. Singh, K. Manoli, A. Tiwari, T. Ligonzo, C. Di Franco, N. Cioffi, G. Palazzo, G. Scamarcio, and L. Torsi. The double layer capacitance of ionic liquids for electrolyte gating of ZnO thin film transistors and effect of gate electrodes. *J. Mater. Chem. C*, 5:3509–3518, 2017.

[237] S. Fabiano, S. Braun, M. Fahlman, X. Crispin, and M. Berggren. Effect of gate electrode work-function on source charge injection in electrolyte-gated organic field-effect transistors. *Adv. Funct. Mater.*, 24:695–700, 2014.

[238] S. Casalini, F. Leonardi, T. Cramer, and F. Biscarini. Organic field-effect transistor for label-free dopamine sensing. *Org. Electron.*, 14:156–163, 2013.

[239] M. Y. Mulla, E. Tuccori, M. Magliulo, G. Lattanzi, G. Palazzo, K. Persaud, and L. Torsi. Capacitance-modulated transistor detects odorant binding protein chiral interactions. *Nat. Commun.*, 6:1–9, 2015.

[240] Q. Zhang, F. Leonardi, S. Casalini, I. Temiño, and M. Mas-Torrent. High performing solution-coated electrolyte-gated organic field-effect transistors for aqueous media operation. *Sci. Rep.*, 6:39623, dec 2016.

[241] I. Temiño, F. G. Del Pozo, M. R. Ajayakumar, S. Galindo, J. Puigdollers, and M. Mas-Torrent. A Rapid, Low-Cost, and Scalable Technique for Printing State-of-the-Art Organic Field-Effect Transistors. *Adv. Mater. Technol.*, 1:1600090, 2016.

[242] M. Kiguchi and S. Kaneko. Electron transport through single p-conjugated molecules bridging between metal electrodes. *ChemPhysChem*, 13:1116–1126, 2012.

[243] H. C. Seong, B. Kim, and C. D. Frisbie. Electrical resistance of long conjugated molecular wires. *Science*, 320:1482–1486, jun 2008.

[244] D. J. Wold, R. Haag, M. A. Rampi, and C. D. Frisbie. Distance dependence of electron tunneling through self-assembled monolayers measured by conducting probe atomic force microscopy: Unsaturated versus saturated molecular junctions. *J. Phys. Chem. B*, 106:2813–2816, 2002.

[245] G. Binnig, H. Rohrer, C. Gerber, and E. Weibel. Tunneling through a controllable vacuum gap. *Appl. Phys. Lett.*, 40:178–180, 1982.

[246] P. A. Lewis, C. E. Inman, Y. Yao, J. M. Tour, J. E. Hutchison, and P. S. Weiss. Mediating stochastic switching of single molecules using chemical functionality. *J. Am. Chem. Soc.*, 126:12214–12215, 2004.

[247] G. Yang and G. Y. Liu. New Insights for Self-Assembled Monolayers of Organothiols on Au(111) Revealed by Scanning Tunneling Microscopy. *J. Phys. Chem. B*, 107:8746–8759, 2003.

[248] G. Wang, S. I. Na, T. W. Kim, Y. Kim, S. Park, and T. Lee. Effect of PEDOT:PSS-molecule interface on the charge transport characteristics of the large-area molecular electronic junctions. *Org. Electron.*, 13:771–777, 2012.

[249] L. A. Bumm, J. J. Arnold, T. D. Dunbar, D. L. Allara, and P. S. Weiss. Electron Transfer through Organic Molecules. *J. Phys. Chem. B*, 103:8122–8127, 1999.

[250] V. B. Engelkes, J. M. Beebe, and C. D. Frisbie. Analysis of the causes of variance in resistance measurements on metal-molecule-metal junctions formed by conducting-probe atomic force microscopy. *J. Phys. Chem. B*, 109:16801–16810, 2005.

[251] H. Haick and D. Cahen. Contacting organic molecules by soft methods: Towards molecule-based electronic devices. *Acc. Chem. Res*, 41:359-366, 2008.

[252] H. B. Akkerman and B. De Boer. Electrical conduction through single molecules and self-assembled monolayers. *J. Phys. Condens. Matter*, 20:013001, 2008.

[253] M. A. Rampi, O. J. A. Schueller, and G. M. Whitesides. Alkanethiol self-assembled monolayers as the dielectric of capacitors with nanoscale thickness. *Appl. Phys. Lett.*, 72:1781–1783, jun 1998.

[254] C. Grave, E. Tran, P. Samorì, G. M. Whitesides, and M. A. Rampi. Correlating electrical properties and molecular structure of SAMs organized between two metal surfaces. In *Synth. Met.*, volume 147, pages 11–18, 2004.

[255] R. C. Chiechi, E. A. Weiss, M. D. Dickey, and G. M. Whitesides. Eutectic gallium-indium (EGaIn): A moldable liquid metal for electrical characterization of self-assembled monolayers. *Angew. Chem. Int. Ed.*, 47:142–144, jan 2008.

[256] R. Haag, M. A. Rampi, R. E. Holmlin, and G. M. Whitesides. Electrical breakdown of aliphatic and aromatic self-assembled monolayers used as nanometer-thick organic dielectrics. *J. Am. Chem. Soc.*, 121:7895–7906, 1999.

[257] M. Galperin, A. Nitzan, S. Sek, and M. Majda. Asymmetric electron transmission across asymmetric alkanethiol bilayer junctions. *J. Electroanal. Chem.*, 550:337–350, jul 2003.

[258] G. J. Ashwell, J. Ewington, and B. J. Robinson. Organic rectifying junctions fabricated by ionic coupling. *Chem. Commun.*, 0:618–620, 2006.

[259] P.E. Kornilovitch, A.M. Bratkovsky, and R. Stanley Williams. Current rectification by molecules with asymmetric tunneling barriers. *Phys. Rev. B*, 66:165436, oct 2002.

[260] R. Liu, S. H. Ke, W. Yang, and H. U. Baranger. Organometallic molecular rectification. *J. Chem. Phys.*, 124:024718, jan 2006.

[261] J. Casado-Montenegro, M. Mas-Torrent, F. Otón, N. Crivillers, J. Veciana, and C. Rovira. Electrochemical and chemical tuning of the surface wettability of tetrathiafulvalene self-assembled monolayers. *Chem. Commun.*, 49:8084–8086, 2013.

[262] M. Hegner, P. Wagner, and G. Semenza. Ultralarge atomically flat template-stripped Au surfaces for scanning probe microscopy. *Surf. Sci.*, 291:39–46, 1993.

[263] E. A. Weiss, G. K. Kaufman, J. K. Kriebel, Z. Li, R. Schalek, and G. M. Whitesides. Si/SiO2-templated formation of ultraflat metal surfaces on glass, polymer, and solder supports: Their use as substrates for self-assembled monolayers. *Langmuir*, 23:9686–9694, 2007.

[264] L. Yuan, L. Jiang, B. Zhang, and C. A. Nijhuis. Dependency of the tunneling decay coefficient in molecular tunneling junctions on the topography of the bottom electrodes. *Angew. Chem. Int. Ed.*, 53:3377–3381, 2014.

[265] M. Ballester, J. Riera, J. Castatier, C. Badfa, and J. M. Monso. Perchlorotriphenylmethyl Radical Series . *J . Am. Chem. Soc.*, 93:2215–2225, 1971.

[266] M. Ballestee. Inert Free Radicals (IFR): A Unique Trivalent Carbon Species. *Acc. Chem. Res*, 18:380–387, 1985.

[267] 0. Armet, J. Veciana, T. C. Rovira, J. Riera, J. Castaiier, E. Molins, J. Rius, C. Miravitlles, S. Olivella, and J. Brichfeus 'l. Inert Carbon Free Radicals. 8. Polychlorotriphenylmethyl Radicals. Synthesis, Structure, and Spin-Density Distributiont. *J . Phys. Chem*, 91:5608–5616, 1987.

[268] M. A. Fox, E. Gaillard, and C. C. Chen. Photochemistry of stable free radicals: the photolysis of perchlorotriphenylmethyl radicals. *J . Am. Chem. Soc.*, 109:7088–7094, 1987.

[269] I. Ratera and J. Veciana. Playing with organic radicals as building blocks for functional molecular materials. *Chem. Soc. Rev.*, 41:303–349, 2012.

[270] J. Guasch, L. Grisanti, S. Jung, D. Morales, G. D'Avino, M. Souto, X. Fontrodona, A. Painelli, F. Renz, I. Ratera, and J. Veciana. Bistability of Fc-PTM-Based Dyads: The Role of the Donor Strength. *Chem. Mater.*, 25:808–814, 2013.

[271] J. Guasch, L. Grisanti, M. Souto, V. Lloveras, J. Vidal-Gancedo, I. Ratera, A. Painelli, C. Rovira, and J. Veciana. Intra- and Intermolecular Charge Transfer in Aggregates of Tetrathiafulvalene-Triphenylmethyl Radical Derivatives in Solution. *J. Am. Chem. Soc.*, 135:6958–6967, 2013.

[272] V. Lloveras, J. Vidal-Gancedo, D. Ruiz-Molina, T. M. Figueira-Duarte, J. F. Nierengarten, J. Veciana, and C. Rovira. Influence of bridge topology and torsion on the intramolecular electron transfer. *Faraday discussions*, 131:291–305, 2006.

[273] A. Heckmann and C. Lambert. Neutral organic mixed-valence compounds: Synthesis and all-optical evaluation of electron-transfer parameters. *J . Am. Chem. Soc.*, 129:5515–5527, 2007.

[274] C. Sporer, I. Ratera, D. Ruiz-Molina, Y. Zhao, J. Vidal-Gancedo, K. Wurst, P. Jaitner, K. Clays, A. Persoons, C. Rovira, and J. Veciana. A Molecular Multiproperty Switching Array Based on the Redox Behavior of a Ferrocenyl Polychlorotriphenylmethyl Radical. *Angew. Chem. Int. Ed.*, 43:5266–5268, 2004.

[275] N. Crivillers, M. Mas-Torrent, J. Vidal-Gancedo, J. Veciana, and C. Rovira. Self-assembled monolayers of electroactive polychlorotriphenylmethyl radicals on Au(111). *J. Am. Chem. Soc.*, 130:5499–5506, 2008.

[276] N. Crivillers, M. Mas-Torrent, S. Perruchas, N. Roques, J. Vidal-Gancedo, J. Veciana, C. Rovira, L. Basabe-Desmonts, B. J. Ravoo, M. Crego-Calama, and D. N. Reinhoudt. Self-Assembled Monolayers of a Multifunctional Organic Radical. *Angew. Chem. Int. Ed*, 46:2215–2219, 2007.

[277] C. Simão, M. Mas-Torrent, N. Crivillers, V. Lloveras, J. M. Artés, P. Gorostiza, J. Veciana, and C. Rovira. A robust molecular platform for non-volatile memory devices with optical and magnetic responses. *Natu Chem.*, 3:359–364, 2011.

[278] M. Souto, M. V. Solano, M. Jensen, D. Bendixen, F. Delchiaro, A. Girlando, A. Painelli, J. O. Jeppesen, C. Rovira, I. Ratera, and J. Veciana. Self-Assembled Architectures with Segregated Donor and Acceptor Units of a Dyad Based on a Monopyrrolo-Annulated TTF-PTM Radical. *Chem.-Eur. J.*, 21:8816–8825, 2015.

[279] M. Ballester, J. Riera, J. Castañer, C. Rovira, and O. Armet. An Easy, High-yield Synthesis of Highly Chlorinated Mono-, Di- and Triarylmethanes. *Synthesis*, 1:64-66, 1986.

[280] S. Chopin, J. Cousseau, E. Levillain, C. Rovira, J. Veciana, A. S. D. Sandanayaka, Y. Araki, and O. Ito. [60]Fullereneâperchlorotriphenylmethide anion triads. Synthesis and study of photoinduced intramolecular electron-transfer processes. *J. Mater. Chem.*, 16:112–121, 2006.

[281] M. Ballester, J. Riera, J. Castañer, C. Rovira, J. Veciana, and C. Onrubia. Inert Carbon Free Radicals. 4. Spin Labeling of Amino Acids and Peptides. *J. Org. Chem.*, 48:3716–3720, 1983.

[282] V. Dang, J. Wang, S. Feng, C. Buron, F. A. Villamena, Peng G. Wang, and P. Kuppusamy. Synthesis and characterization of a perchlorotriphenylmethyl (trityl) triester radical: A potential sensor for superoxide and oxygen in biological systems. *Bioorg. Med. Chem. Lett.*, 17:4062–4065, 2007.

[283] C. Simão. *Surface self-assembly of electroactive molecules as wires and switches.* PhD thesis, UAB Universitat Autonoma de Barcelona, 2011.

[284] S. G. J. Mathijssen, M. J. Spijkman, A. M. Andringa, P. A. Van Hal, I. McCulloch, M. Kemerink, R. A J Janssen, and D. M. De Leeuw. Revealing buried interfaces to understand the origins of threshold voltage shifts in organic field-effect transistors. *Adv. Mater.*, 22:5105–5109, 2010.

[285] S. Kobayashi, T. Nishikawa, T. Takenobu, S. Mori, T. Shimoda, T. Mitani, H. Shimotani, N. Yoshimoto, S. Ogawa, and Y. Iwasa. Control of carrier density by self-assembled monolayers in organic field-effect transistors. *Nat. Mater.*, 3:317–322, 2004.

[286] L. L. Chua, J. Zaumseil, J. F. Chang, E. C. W. Ou, P. K. H. Ho, H. Sirringhaus, and R. H. Friend. General observation of n-type field-effect behaviour in organic semiconductors. *Nature*, 434:194–199, 2005.

[287] J. Veres, S. Ogier, and L. Giles. Gate Insulators in Organic Field-Effect Transistors. *Chem. Mat.*, 16:4543–4555, 2004.

[288] H. Sirringhaus. Reliability of Organic Field-Effect Transistors. *Adv. Mater.*, 21:3859–3873, 2009.

[289] J. T. N. Ng, J.A. Marohn, and M.L. Chabinyc. Comparing the kinetics of bias stress in organic field-effect transistors with different dielectric interfaces. *J. Appl. Phys.*, 100:084505, 2006.

[290] O. Acton, G. G. Ting II, H. Ma, D. Hutchins, Y. Wang, B. Purushothaman, J. E. Anthony, and A. K.Y. Jen. π-σ-Phosphonic acid organic monolayerâamorphous solâgel hafnium oxide hybrid dielectric for low-voltage organic transistors on plastic. *J. Mater. Chem.*, 19:7929, 2009.

[291] H. S. Lee, D. H. Kim, J. H. Cho, M. Hwang, Y. Jang, and K. Cho. Effect of the Phase States of Self-Assembled Monolayers on Pentacene Growth and Thin-Film Transistor Characteristics. *J. Am. Chem. Soc.*, 130:10556–10564, 2008.

[292] S. Y. Yang, K. Shin, and C. E. Park. The Effect of Gate-Dielectric Surface Energy on Pentacene Morphology and Organic Field-Effect Transistor Characteristics. *Adv. Funct. Mater.*, 15:1806–1814, 2005.

[293] R. F. De Oliveira, L. Merces, T. Parra Vello, and C. C. Bof Bufon. Water-gated phthalocyanine transistors: Operation and transduction of the peptide-enzyme interaction. *Org. Electron.*, 31:217–226, 2016.

[294] K. Fukuda, T. Hamamoto, T. Yokota, T. Sekitani, U. Zschieschang, H. Klauk, and T. Someya. Effects of the alkyl chain length in phosphonic acid self-assembled monolayer gate dielectrics on the performance and stability of low-voltage organic thin-film transistors. *Appl. Phys. Lett.*, 95:203301, 2009.

[295] T. Takahashi, T. Takenobu, J. Takeya, and Y. Iwasa. Ambipolar organic field-effect transistors based on rubrene single crystals. *Appl. Phys. Lett.*, 88:1–3, 2006.

[296] B. Park, P. Paoprasert, I. In, J. Zwickey, P. E. Colavita, R. J. Hamers, P. Gopalan, and P. G. Evans. Functional self-assembled monolayers for optimized photoinduced charge transfer in organic field effect transistors. *Adv. Mater.*, 19:4353, 2007.

[297] A. Jedaa, M. Salinas, C. M. Jäger, T. Clark, A. Ebel, A. Hirsch, M. Halik, and C. M. Jä Ger. Mixed self-assembled monolayer of molecules with dipolar and acceptor characterâ Influence on hysteresis and threshold voltage in organic thin-film transistors. *Appl. Phys. Lett.*, 100:063302, 2012.

[298] M. Burkhardt, A. Jedaa, M. Novak, A. Ebel, K. Voïtchovsky, F. Stellacci, A. Hirsch, and M. Halik. Concept of a molecular charge storage dielectric layer for organic thin-film memory transistors. *Adv. Mater.*, 22:2525–2528, 2010.

[299] P. S. Abthagir, Y.G. Ha, E.A. You, S.H. Jeong, H.S. Seo, and J.H. Choi. Studies of tetracene- and pentacene-based organic thin-film transistors fabricated by the neutral cluster beam deposition method. *J. Phys. Chem. B*, 109:23918–23924, 2005.

[300] Y.K. Su, T.S. Huang, and P.C. Wang. The Study of Organic Thin Film Transistor with Polymethylmethacrylate as a Dielectric Layer. *Appl. Phys. Lett.*, 91:1–7, 2007.

[301] S. Henke, K. H. Thürer, J. K. N. Lindner, B. Rauschenbach, B. Stritzker, and K. H. Thtirer. Structural characterization of the temperature dependence of C 60 - thin films on mica (001) by x-ray diffraction Structural characterization of the temperature dependence of C&-thin films on mica (001) by x-ray diffraction. *J. Appl. Phys.*, 76:3337–3340, 1994.

[302] M. Egginger, S. Bauer, R. Schwödiauer, H. Neugebauer, and N. S. Sariciftci. Current versus gate voltage hysteresis in organic field effect transistors. *Monatsh. Chem.*, 140:735–750, 2009.

[303] H. Nishide and K. Oyaizu. Toward flexible batteries *Science*, 319:737-738, 2008.

[304] W. Choi, S. Endo, K. Oyaizu, H. Nishide, and K. E. Geckeler. Robust and efficient charge storage by uniform grafting of TEMPO radical polymer around multi-walled carbon nanotubes. *J. Mater. Chem. A*, 1:2999, 2013.

[305] M. Morita. Advanced Polymers as Active Materials and Electrolytes for Electrochemical Capacitors and Hybrid Capacitor Systems. *Electrochem. Soc. Interface*, 17:44–48, 2008.

[306] R. Thangavel, K. Kaliyappan, D. U. Kim, X. Sun, and Y. S. Lee. All-Organic Sodium Hybrid Capacitor: A New, High-Energy, High-Power Energy Storage System Bridging Batteries and Capacitors. *Chem. Mater.*, 29:7122–7130, 2017.

[307] A. Vlad, N. Singh, S. Melinte, J. F. Gohy, and P. M. Ajayan. Carbon Redox-Polymer-Gel Hybrid Supercapacitors. *Scientific Reports*, 6:1–6, 2016.

[308] S. S. Popova, L.N. Ol'shanskaya, and T.V. Pominova. Electrochemical Intercalation of Lithium into Graphite in Acetonitrile Solutions: The Effect of the Anion Nature. *Russ. J. Electrochem.*, 38:412–418, 2002.

[309] M. Ballester, J. Castafier, J. Riera, A. IbXiez, and J. Pujadas. Inert Carbon Free Radicals. 2. Monofunctionalized Tetradecachlorotriphenylmethyl Radicals and Related Compounds. *J. Org. Chem.*, 47:259–264, 1982.

Publications

- Maria Serena Maglione, Javier Casado-Montenegro, Eva-Corinna Fritz, Núria Crivillers, Bart Jan Ravoo, Concepció Rovira, Marta Mas- Torrent, Chem. Commun., 53, 2018, 3038-3041.
- Maria Serena Maglione, Stefano Casalini, Stamatis Georgakopoulos, Marianna Barbalinardo, Vitaliy Parkula, Núria Crivillers, Concepció Rovira, Pierpaolo Greco andMartaMas-Torrent, Small, 2017, 1703344.
- Elena Marchante, Maria Serena Maglione, Núria Crivillers, Concepció Rovira and Marta Mas-Torrent, RSC Adv, 2017, 7, 5636-5641.